Post-Earthquake Damage Assessment and Residual Capacity of Concrete and RC Beams

A thesis submitted in partial fulfilment of the requirements for the degree of

Doctor of Philosophy in Civil Engineering

By

Amirmasoud Malek

Supervised by

Dr. Allan Scott

Prof. Stefano Pampanin

Assoc. Prof. Greg MacRae

Department of Civil and Natural Resources Engineering

University of Canterbury

January, 2018

Abstract

The assessment of damage and remaining capacity after an earthquake is an immediate measure to determine whether a reinforced concrete (RC) building is usable and safe for occupants. The recent Christchurch earthquake (22 February 2011) caused a uniquely severe level of structural damage to modern buildings, resulting in extensive damage to the building stock. About 60% of damaged multistorey concrete buildings (3 storeys and up) were demolished after the earthquake, and the cost of reconstruction amounted to 40 billion NZD. The aftermath disclosed issues of great complexities regarding the future of the RC buildings damaged by the earthquakes. This highlighted the importance of post-event decision-making, as the outcome will allow the appropriate course of action—demolition, repair or acceptance of the existing building—to be considered. To adopt the proper strategy, accurate assessment of the residual capacity and the level of damage is required.

This doctoral dissertation aims to assess the damage and remaining capacity at constituent material and member level (i.e., concrete material and beams) through a systematic approach in an attempt to address part of an existing gap in the available literature. Since the residual capacity of RC members is not unique and depends on previously applied loading history, post-event residual capacity in this study was assessed in terms of fraction of fatigue life (i.e., the number of cycles required to failure).

This research comprises three main parts: (1) residual capacity and damage assessment at material level (i.e., concrete), (2) post-yield bond deterioration and damage assessment at the interface of steel and concrete, and, finally, (3) residual capacity and damage assessment at member level (i.e., RC beam).

The first part of this research focused on damage assessment and the remaining capacity of concrete from a material point of view. It aimed to employ appropriate and reliable durability-based testing and image-detection techniques to quantify deterioration in the mechanical properties of concrete on the basis that stress-induced damage occurred in the microstructural system of the concrete material. To this end, in the first phase, a feasibility study was conducted in which a combination of oxygen

permeability, electrical resistivity and porosity tests were assessed to determine if they were robust and reliable enough to reveal damage which occurred in the microstructural system of concrete. The results, in terms of change in permeability, electrical resistivity and porosity features of disk samples taken from the middle third of damaged concrete cylinders (200 mm × 100 mm) monotonically pre-loaded to 50%, 70%, 90% and 95% of the ultimate strength (f'_c), showed the permeability test is a reliable tool to identify the degree of damage, due to its high sensitivity to the load-induced microcracking. In parallel, to determine the residual capacity, the companion damaged concrete cylinders already loaded to the same level of compressive strength were reloaded up to failure. Comparing the stress–strain relationship of damaged concrete with intact material, it was also found that the strain capacity of the reloaded pre-damaged concrete cylinders decreases while strength remained virtually unchanged.

In the second phase of the first part, a fluorescent microscopy technique was used to assess the damage and develop a correlation between material degradation, by virtue of the geometrical features, and damage to the concrete.

To account for the effect of confinement and cyclic loading, in the third phase, the residual capacity and damage assessment of unconfined and GFRP confined concrete cylinders subjected to low-cycle fatigue loading, was investigated. Similar to the first phase, permeability testing technique was used to provide an indirect evaluation of fatigue damage. Finally, in the fourth phase of the first part, the suitability of permeability testing technique to assess damage was evaluated for cored concrete taken from three types of RC members: columns, beams and a beam-column joint.

In view of the fact that the composite action of an RC member is highly dependent on the bond between reinforcement and surrounding concrete, understanding the deterioration of the bond in the post-yield range of strain in steel was crucial to assess damage at member level. Therefore, in the second phase of this research, a state-of-the-art distributed fibre optic strain sensor system (DFOSSS) system was used to evaluate bond deterioration in a cantilever RC beam subjected to monotonic lateral loading. The technology allowed the continuous capture of strain, every 2.6 mm along the length, in both reinforcing bars and cover concrete. The strain profile provided a basis by which the slip, axial stress and bond stress distributions were then established.

In the third part, the study focused on the damage assessment and residual capacity of seven half-scale RC beams subjected to a constant-amplitude cyclic loading protocol. In the first stage, the structural performances of three specimens under constant-amplitude fatigue at 1%, 2% and 4% chord rotation (drift) were examined. In parallel, the number of cycles to failure, degradation in strength, stiffness and energy dissipation were characterized. In the second stage, four RC beams were subjected to loading up to 70% and 90% of their fatigue life, at 2% and 4% drift, and then monotonically pulled up to failure. To determine the residual flexural capacity, the lateral force–displacement results of pre-damaged specimens were compared with an undamaged specimen subjected to only monotonic loading. The study showed significant losses in strength, deformability, stiffness and energy dissipation capacity. A nonlinear finite element analysis (FEA) using concrete damage plasticity (CDP) model was also conducted in ABAQUS to numerically investigate the behaviour of the tested specimen. The results of the FE simulations indicated a reasonable response compared with the behaviour of the test specimen in terms of force–displacement and cracking pattern.

During the Christchurch earthquake it was observed that the loading history has a significant influence on structural responses. While in conventional pseudo-static loading protocol, internal forces can be redistributed along the plastic length: there is little chance for structures undergoing high initial loading amplitude to redistribute pertinent stresses. As a result, in the third phase of this part, the effect of high rate of loading on the behaviour of seismically designed RC beams was investigated. Two half-scale cantilever RC beams were subjected to similar constant-amplitude cyclic loading at 2% and 4% drifts, but at a rate of 500 mm/s. Due to the incapability of conventional measuring techniques, a motion-tracking system was employed for data acquisition with the high-speed tests. The effect of rate of loading on the fatigue life of specimens (i.e., the number of cycles required to failure), secant stiffness, failure mode, cracking pattern, beam elongations and bar fracture surface were analysed.

Integrating the results of all parts of this research has resulted in a better understanding of residual capacity and the development of damage at both the material and member level by using a low-cycle fatigue approach.

Acknowledgements

I would like to express my profound gratitude to my supervisors, Senior Lecturer Allan Scott, Professor Stefano Pampanin and Associate Professor Gregory MacRae. Without their guidance, technical discussions, continuous support and encouragement, this work would not have been possible.

Completion of this research would have not been feasible without the financial support provided by the New Zealand Natural Hazard Research Platform with the projects *SAFER Structures* and *Residual Capacity and Repairing Options for RC Structures*, and the Department of Civil and Natural Resources Engineering.

My acknowledgment is also extended to the technicians of the UC Structural Laboratory who have helped me to accomplish the experimental phases of this research. I would also like to thank Elizabeth Ackermann for her support and managing administrative tasks during my PhD study.

Many thanks are due to my friends and colleagues for their support and friendship which made these four years of my life memorable.

To my mother and father for their love, unwavering support, prayers and understanding during my PhD studies. Finally, I am immensely appreciative of my wife, Naeimeh, for being the source of my joy, inspiration and encouragement.

Table of Contents

Table of Figures

Chapter 1 *Introduction*

1.1 Background

The assessment of damage and determination of remaining capacity of RC buildings after a seismic event is not only an imperative task from a post-earthquake remediation plan standpoint, but also it is of vital importance to foster resilience in the community. The Christchurch earthquake (22 February 2011) caused extensive damage to the building stock as well as to other infrastructure. About 60% of damaged multistorey concrete buildings (3 storeys and up) were demolished after the earthquake (Marquis et al. 2017) and the cost of the damage and reconstruction was estimated at 40 billion NZD (Wood et al. 2016). The aftermath revealed some issues of great complexity regarding the future of the RC buildings damaged by the earthquakes as to whether they are sufficiently safe for reoccupation.

This highlighted the importance of post-event decision-making, as the outcome will allow the appropriate course of action to be considered. Three possible strategies can be considered for such decision-making: the building is safe enough, the building should be repaired to the same performance level or even to the higher standard, or in the worst case scenario, the building should be demolished. But, to make such a decision on the future of the building impacted by earthquake, two challenges need to be answered. First, what is the level of damage and secondly how much load carrying capacity remains in the damaged RC buildings? The appraisal of residual capacity will provide a basis by which the functionality of the damaged RC buildings to resist further loading demands (e.g., aftershocks) can be justified.

Residual load-bearing capacity can be investigated at four levels: constituent material (i.e., steel/concrete), components, subassemblies, and, finally, system level. At concrete material level, limited studies are available in the literature (Cornelissen and Reinhardt 1986; Zhang and Wu 1997; Baluch et al. 2003; Meng et al. 2011; Zhu and Li 2011; Kontani et al. 2016). However, due to differences in damage-induced loading protocol and inconsistencies in the damage level, no generalized proposition

on residual capacity with respect to remaining mechanical properties could be drawn. In addition, no incorporation of concrete diagnosis techniques as auxiliary tools to quantify residual capacity of damaged concrete have been proposed. As a result, there is a need to develop a consistent approach to correlate observed damage with material degradation in the concrete using an appropriate testing technique.

At the member level, a few experimental studies investigated the residual capacity of RC columns subjected to lateral loading (Tasai 1999; Mackie 2004; Terzic et al. 2008; Chung et al. 2008; Warn and Unal 2014; Terzic and Stojadinovic 2015). Although these studies provided some information on residual capacity of RC columns, no widely applicable approach to assess residual capacity of RC columns is available. That is because the loading protocol to which specimens were damaged, and also the loading regime by which the residual axial/lateral capacity of columns were investigated, were not consistent. Thus, it is crucial to develop a more harmonized/standardized approach towards evaluating the residual capacity of RC members.

With respect to residual capacity of damaged RC buildings, Maeda et al. (2004) and Maeda and Kang (2009) investigated the residual seismic capacity of RC buildings, and introduced an index and a rating-damage procedure, incorporated in the Japanese guideline for post-earthquake damage evaluation and rehabilitation (JBDPA 2001). Polese et al. (2012) studied a mechanism-based simplified analytical method using pushover curves for residual capacity of earthquake-damaged buildings; however, the method was proposed for preliminary assessment and no experimental validation was included. More recently, seismic residual capacity of RC buildings has been singled out as a most challenging topic to be addressed in New Zealand (Cuevas et al. 2015; Elwood et al. 2016). That is because the lack of comprehensive and robust guidelines to assess the residual capacity of damaged modern buildings resulted in demolition of a huge number of modern RC buildings, which was typically beyond the norms from past experience at international levels (Cuevas and Pampanin 2017).

As the aim of this research is to develop a methodology to assess damage and residual capacity at material (i.e., concrete) and component (i.e., beam) levels, there is a need to quantify the level of damage (i.e., degradation in strength, stiffness, deformation and energy dissipation) in reference to the behaviour of an intact specimen

(i.e., load-deformation relationship) under the same loading protocol. Due to the difference in loading history/protocols to which specimens are partially damaged and also differences in the subsequent re-loading regime, different values for residual capacity of an RC member can be attributed. That is because the structural performance of RC members is not unique and depends on the previously applied cyclic loading history (Krawinkler 2009). This signifies the importance of adopting a more unified and standardized approach to assess damage and residual capacity of concrete and RC members. The implementation of a low-cycle fatigue concept in this study for loading protocol and quantifying damage at any desired fraction of fatigue life (i.e., required number of cycles to failure) seems promising for expediting a more generalized procedure for assessment of damage and residual capacity.

Erberik and Sucuoğlu (2004) showed that earthquake-induced damage in RC buildings can conveniently be investigated in the context of low-cycle fatigue. That is because the low-cycle fatigue concept denotes the application of a few load cycles which are sufficiently significant to incur plastic deformation in the specimen. Under load reversals into the inelastic range the strength of a structure deteriorates, and the structure will no longer be able to carry the same load at the given deformation level. Load-carrying and deformation capacity of an RC member decreases due to the hysteretic energy dissipation of induced seismic forces until failure takes place. The decline in strength in each cycle will depend on the amount by which the critical strain has been exceeded. This phenomenon is generally known as low-cycle fatigue (Fajfar 1992). In terms of the number of cycles, Hsu (1981) ascribed low-cycle fatigue to the range of loading cycles from 1 to approximately 1000 cycles, to which an RC building may be subjected during earthquakes over its lifespan.

Fatigue damage increases with applied cycles in a cumulative manner that eventually leads to fracture. The implication to fatigue damage analysis is that the fatigue life at a prescribed load (or strain level) is not a unique quantity dictated by the magnitude of the loading. Instead, details of prior loadings can alter the fatigue life relationship (Manson and Halford 1986). It is known that in real excitation, loading cycles have great variation in amplitude, number and sequence, which makes it difficult to experimentally test all likely situations. As a result, fatigue-based damage

assessment serves a basis to add all damage produced by any single stress cycle with given characteristics in order to evaluate the total fatigue damage in the specimens.

Therefore, this PhD research intends to assess residual capacity and damage occurred at both material and member level using a low-cycle fatigue approach.

1.2 Research motivations

This research is motivated by the need to provide greater information on the post-event residual capacity and damage assessment of concrete and RC beams due to the limited information currently available in the literature. The outcomes allow the level of damage in terms of degradation in mechanical properties, extent of damage and also remaining load-carrying capacity of damaged concrete and damaged RC beams to be identified. Assessment of residual capacity and damage at material and member level will provide a basis by which the residual capacity of a damaged RC building at system level can be evaluated. This will finally allow an appropriate course of action on the future of the damaged RC building to be taken: reoccupation without repair, repair or demolition.

At material level, the study is highly focused on ascertaining how preloading of concrete can affect its load-carrying capacity (stress–strain curve) and also to correlate such degradation with a damage indicator using an appropriate testing technique. Moreover, since the bond between reinforcement and concrete is a prerequisite for composite action of an RC section, one of the important aspects of this research is to assess bond deterioration in a damaged RC member.

Finally, there is a need to experimentally and numerically assess residual capacity and damage of RC members in the context of low-cycle fatigue. In addition, the effect of high rate of loading on residual capacity and damage evolution of RC beams was studied.

While the need for evaluating post-event residual capacity and damage is well agreed, a standardized approach for uptake has not been developed. This research was motivated by these gaps in literature, and will contribute to the knowledge and highlight the implementation of a low-cycle fatigue loading approach for assessing residual capacity and damage at both material and member level. In order to accomplish these

objectives, comprehensive experimental as well as analytical and numerical investigations have been carried out in this thesis. This research is part of more extensive ongoing research projects at the University of Canterbury focusing on *SAFER Structures* and *Residual Capacity and Repairing Options for RC structures in New Zealand.*

1.3 Research objectives and scope of work

Considering the above-mentioned issues, the objectives of this dissertation were broken down into three main research areas, and for each of these areas, a systematic approach is set out as follows:

(a) Damage assessment and residual capacity at material level

- Develop a durability-based damage assessment methodology to identify the level of load-induced damage in the microstructural system of concrete and make a correlation between observed damage and degradation of the mechanical properties in damaged concrete
- Application of fluorescent microscopy technique) to assess the level of damage in the microstructural system of concrete and provide further quantitative information on the geometrical features of microcracking
- Study the evolution of damage in terms of degradation in the mechanical properties of confined and unconfined concrete subjected to low-cycle fatigue
- Determine the extent of damage occurred in the RC column, beam and a beam-column joint

(b) Damage assessment of bond between deformed bar and concrete in the post-yield region

- Determine bond deterioration in the post-yield region in a real RC beam using distributed fibre-optic strain sensing
- Study the ability of distributed fibre-optic strain sensing to detect crack locations, and the extent of damage in both the reinforcement and concrete

(c) Damage assessment and residual capacity at member level

- Investigate the behaviour of RC beam subjected to low-cycle fatigue, and the evolution of damage in terms of degradation in the strength, deformability and energy-dissipation capacity over the fatigue life of the specimens
- Develop and calibrate a 3D nonlinear finite element (FE) model to simulate fatigue damage of the experimentally test specimens
- Investigate the effect of the rate of loading on the cyclic behaviour and fatigue damage of the specimens

1.4 Organization of thesis

The thesis consists of ten chapters including the Introduction, Conclusions and eight core chapters. Figure 1-1 shows the structure of the thesis.

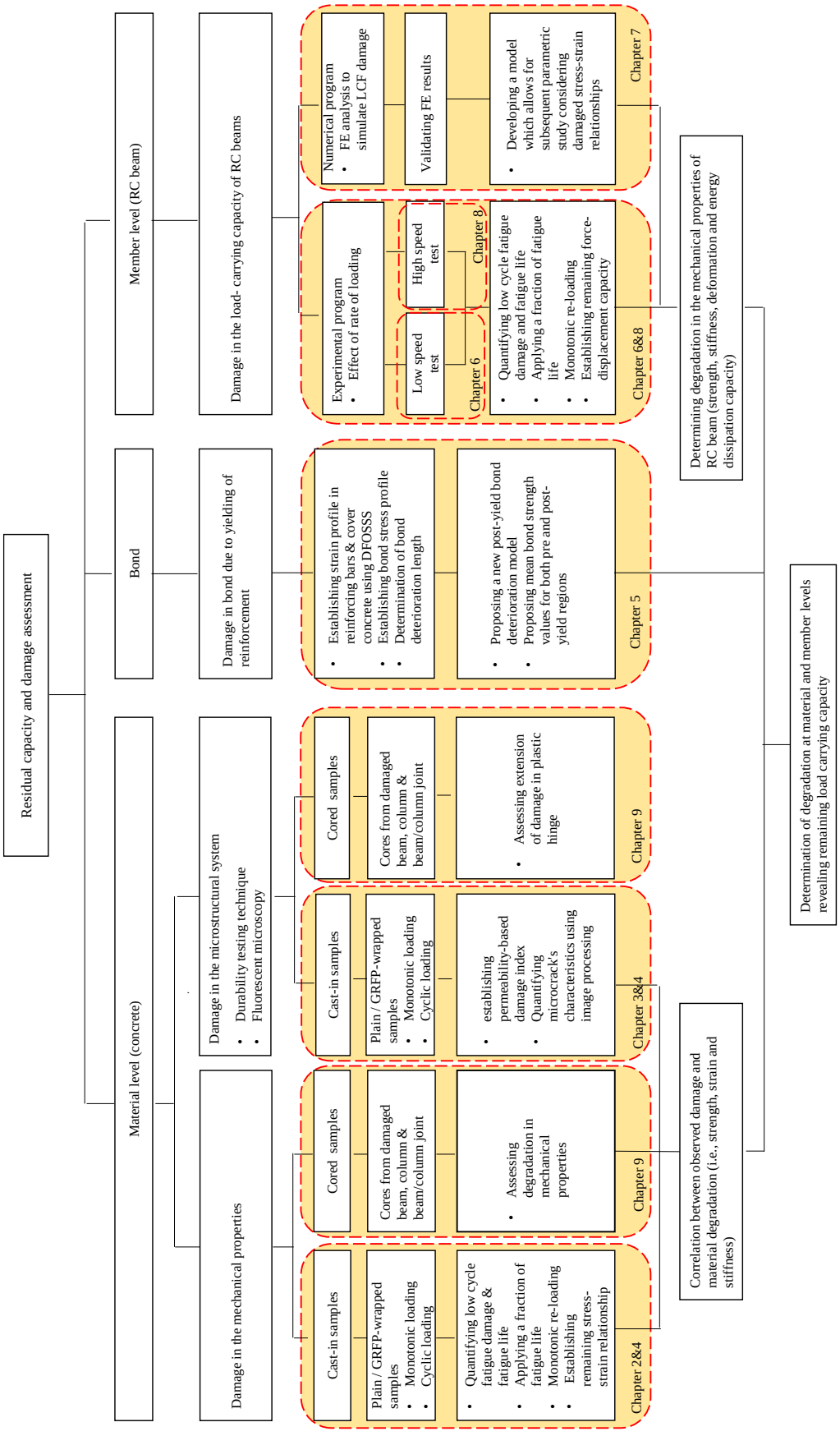

Fig. 1.1 PhD thesis structure

Chapter 2 describes a feasibility study to evaluate the stress-induced damage in concrete cylinders subjected to axial compression by making a correlation between applied stress levels and changes in the durability characteristics of the damaged concrete. Conventional durability testing techniques–oxygen permeability, resistivity and porosity tests–were employed to quantify damage on disk samples taken from the mid-height of concrete cylinders, pre-loaded to 50%, 70%, 90% and 95% of the ultimate strength. In the next stage, the companion damaged concrete cylinders were reloaded up to failure. By comparing the stress–strain relationships of damaged concrete cylinders with intact cylinders, residual capacity was evaluated.

Chapter 3 provides information on the use of a fluorescent microscopy technique to evaluate post-event damage that occurs in the microstructure of concrete material and its possible effects on its mechanical properties. Post image processing was conducted on digital microscopic images obtained from thin petrographic sections to provide quantitative information on the cracks' characteristics. The distribution of geometrical features of the microcracks was determined, and relationships were developed to estimate crack area, crack width and crack length at each stress level. Eventually, a relationship was established to evaluate the residual strain capacity of the damaged concrete, using a relative damage index based on the change in the area of microcracks.

Chapter 4 presents the procedure of determining residual capacity and assessing post-event damage of unconfined and GFRP-wrapped confined concrete cylinders subjected to low-cycle fatigue loading. Monotonic compressive behaviour, including post-peak, strain-softening and strain-hardening responses, were characterized. The number of cycles to failure (i.e., fatigue life), material degradation in terms of development of total and plastic strain, deterioration of elastic modulus and also change in the temperature of concrete cylinders were scrutinized. The evolution of fatigue damage and the residual monotonic capacity were investigated for damaged concrete subjected to 0.3, 0.5, 0.7 and 0.9 of the fatigue life. Finally, the procedure to indirectly quantify damage by means of permeability tests were elaborated.

Chapter 5 focuses on deterioration of bond of an RC section as the only interconnected link that allows concrete and steel to function in a composite action. The aim of the second area of research is to assess deterioration of bond, and level of

damage at each demand level (i.e., drift). Thus, this chapter deals with the design and development of a unique test to enable the exploration of the deterioration of the bond, and the level of damage at each drift level at post-yield ranges of reinforcement in an actual RC member (i.e., beam) subjected to monotonic lateral loading. To this end, an advanced measuring technique, distributed fibre optic strain sensor system (DFOSSS) system, was used to capture strain, every 2.6 mm along the length, in both reinforcing bars and cover concrete, continuously. The strain profile provided a basis by which the slip, axial stress and bond stress distributions were established. Also, the bond deterioration length, strain penetration and locations of cracks were accurately determined. The work reported in this chapter is a contribution to the existing knowledge of the performance of bond and also the damage assessment of an RC beam in the post-yield range of steel strain using the state-of-the-art DFOSSS to measure strain data along the length of specimen.

Chapter 6 presents the results of an experimental investigation into residual capacity and damage assessment of RC beams subjected to low-cycle fatigue loading. In the first stage, the structural performance of specimens under constant-amplitude fatigue at 1%, 2% and 4% drift were examined. In parallel, the number of cycles to failure, degradation in strength, stiffness and energy dissipation were characterized. In the second stage, the RC beams were subjected to 70% and 90% of their fatigue life, at 2% and 4% drift, and then monotonically pulled up to failure. To determine the residual flexural capacity, the lateral force–displacement results of pre-damaged specimens were compared to an undamaged specimen subjected to only monotonic loading.

Chapter 7 describes the numerical simulation of RC beams subjected to low-cycle fatigue with a focus on finite element modelling and analysis. Constitutive material models selected for the concrete (concrete damage plasticity) and steel are explained and calibrated using the experimental investigations and the available literature. To input the proper parameters needed to simulate the fatigue behaviour of steel, a fatigue test was conducted on a reinforcing bar identical to that used in the experiments. Appropriate elements for discretization of the beams are investigated and mesh sensitivity is checked in cyclic analyses. Finally, the seismically important features are extracted from the FE predictions and compared with the experimental results.

Chapter 8 presents the results of experimental investigations into the effect of high rate of loading on the behaviour of test specimens. Two half-scale cantilever RC beams were subjected to constant-amplitude reversed cyclic displacement loading at 2% and 4% drifts, applied at a rate of 500 mm/s. Results were compared with identical specimens subjected to similar loading (discussed in Chapter 6) but at a rate of 0.5 mm/s (quasi-static loading). Due to the incapability of conventional measuring techniques, a motion-tracking system was employed for data acquisition with the high-speed tests. The effect of rate of loading on the fatigue life of specimens (i.e., the number of cycles required to failure), secant stiffness, failure mode, cracking pattern, beam elongations and bar fracture surface were analysed. In addition, so-called effects on degradation of both strength and energy dissipation capacity over fatigue life were examined.

Chapter 9 investigates the applicability of a permeability testing technique, which was found sufficiently sensitive to reveal damage in an actual damaged RC member. The method was applied on cored concrete samples taken from three types of RC members—columns, beams and beam-column joints—to evaluate both residual capacity and the damage of the concrete material. In addition, the extent of damage was identified for the plastic hinge region based on permeability profile.

Chapter 10 presents the overall conclusions to the research and discusses possible extensions and future work.

1.5 References

Baluch, M., Al-Gadhib, A., Khan, A., and Shaalan, A. (2003). "CDM model for residual strength of concrete under cyclic compression." *Cement and Concrete Composites*, 25(4), 503-512.

Chung, Y.-S., Park, C. K., and Meyer, C. (2008). "Residual seismic performance of reinforced concrete bridge piers after moderate earthquakes." *ACI structural journal*, 105(1), 87.

Cornelissen, H., and Reinhardt, H. "Effect of Static and Fatigue Pre-loading on Residual Strength and Stiffness of Plain Concrete." *Proc., ECF6, Amsterdam*

Cuevas, A., and Pampanin, S. (2017). "Post-Seismic Capacity of Damaged and Repaired Reinforced Concrete Plastic Hinges Extracted from a Real Building." *Seventeenth world conference on earthquake engineering* Santiago, Chile.

Cuevas, A., Pampanin, S., Carr, A., and Ozbolt, J. (2015). "Seismic residual capacity of reinforced concrete frames: Part I: General Framework. ." *Research Report UC*

2015-4, Part I, Department of Civil and Natural Resources Engineering, University of Canterbury, Christchurch, New Zealand.

Elwood, K., Marder, K., Pampanin, S., Ramirez, A. C., Kral, M., Smith, P., Cattanach, A., and Stannard, M. (2016). "Draft framework for assessing residual capacity of earthquake-damaged concrete buildings." *NZSEE*Christchurch, New Zealand.

Erberik, A., and Sucuoğlu, H. (2004). "Seismic energy dissipation in deteriorating systems through low-cycle fatigue." *Earthquake engineering & structural dynamics*, 33(1), 49-67.

Fajfar, P. (1992). "Equivalent ductility factors, taking into account low-cycle fatigue." *Earthquake Engineering & Structural Dynamics*, 21(10), 837-848.

Hsu, T. T. (1981). "Fatigue of plain concrete." *Journal Proceedings*, 78(4), 292-305.

JBDPA (2001). "The Japan Building Disaster Prevention Association, Guideline for Post-earthquake Damage Evaluation and Rehabilitation."Japan.

Kontani, O., Ishitobi, N., Kawada, J., Taogoshi, N., Koge, M., and Umeki, Y. (2016). "Residual Static Strength of Concrete Cylinder Specimen and Stud Anchor Specimen after Cyclic Loadings." *Journal of Advanced Concrete Technology*, 14(10), 634-642.

Krawinkler, H. "Loading histories for cyclic tests in support of performance assessment of structural components." *Proc., The 3rd international conference on advances in experimental structural engineering, San Francisco*, Citeseer.

Mackie, K. "Degradation of reinforced concrete column axial strength." *Proc., The 5th International Symposium in Civil Engineering*.

Maeda, M., and Kang, D. E. (2009). "Post-earthquake damage evaluation of reinforced concrete buildings." *Journal of Advanced Concrete Technology*, 7(3), 327-335.

Maeda, M., Nakano, Y., and Lee, K. S. "Post-earthquake damage evaluation for R/C buildings based on residual seismic capacity." *Proc., Proceedings of the 13th World Conference on Earthquake Engineering*.

Manson, S., and Halford, G. R. (1986). "Re-examination of cumulative fatigue damage analysis—an engineering perspective." *Engineering Fracture Mechanics*, 25(5), 539-571.

Marquis, F., Kim, J. J., Elwood, K. J., and Chang, S. E. (2017). "Understanding post-earthquake decisions on multi-storey concrete buildings in Christchurch, New Zealand." *Bulletin of Earthquake Engineering*, 15(2), 731-758.

Meng, X., Wang, W., Zhou, J., and Song, Y. P. "Experimental investigation on residual strength of plain concrete under fatigue biaxial compression with constant confined stress." *Proc., Advanced Materials Research*, Trans Tech Publ, 581-585.

Polese, M., Di Ludovico, M., Prota, A., and Manfredi, G. "Residual capacity of earthquake damaged buildings." *Proc., Proceedings of the 15 th World conference on Earthquake Engineering*, 24-28.

Tasai, A. "Residual axial capacity and restorability of reinforced concrete columns damaged due to earthquake." *Proc., US-Japan Workshop on Performance-Based Earthquake Engineering Methodology for Reinforced Concrete Building Structures*, 191-202.

Terzic, V., Mackie, K., and Stojadinovic, B. "Experimental evaluation of the residual axial load capacity of circular bridge columns." *Proc., 14th World Conference on Earthquake Engineering, Beijing, China*, 1-8.

Terzic, V., and Stojadinovic, B. (2015). "Evaluation of post-earthquake axial load capacity of circular bridge columns." *ACI Structural Journal*, 112(1), 23.

Warn, G., and Unal, M. (2014). "Estimating the Residual Axial Load Capacity of Flexure-dominated Reinforced Concrete Bridge Columns."

Wood, A., Noy, I., and Parker, M. (2016). "The Canterbury rebuild five years on from the Christchurch earthquake." *Reserve Bank of New Zealand Bulletin*, 79, 1-16.

Zhang, B., and Wu, K. (1997). "Residual fatigue strength and stiffness of ordinary concrete under bending." *Cement and Concrete Research*, 27(1), 115-126.

Zhu, H. B., and Li, X. "Experimental research on residual strength of recycled aggregate concrete under compressive fatigue loading." *Proc., Advanced Materials Research*, Trans Tech Publ, 1379-1382.

Chapter 2 *Durability-based damage assessment and residual capacity of concrete*

2.1 Introduction

Assessment of the degree of damage and residual capacity in the concrete component of a structure, in terms of remaining strength, stiffness and deformation capacity is essential information for structural engineers and decision makers following a significant loading demand (i.e., seismic event). The post-event investigation into level of damage and deterioration in mechanical properties can be addressed at the material, member, subassemblies and finally, system level (Elwood et al. 2016). Information on the material characteristics of damaged concrete provides a basis to find out to what extent the concrete can sustain further demands. Currently, there are relatively few tools available to engineers to assess the material damage experienced by the various concrete structural components. Durability testing techniques, which are conventionally used to assess the environmental causes of deterioration, may also provide in-depth knowledge to evaluate damage due to mechanical loading which has occurred in the microstructure of the concrete. The durability of reinforced concrete structures is to a large extent determined by the ability of the concrete cover to limit the movement of gases, liquids or harmful ions such as chlorides. As a result, considerable research has been directed towards not only understanding the various mechanisms of mass transport in concrete, but also to develop suitable test methods to measure the likely performance of the concrete.

There are a large number of testing techniques available for durability studies (Yao et al. 2016) including: oxygen permeability (Grube and Lawrence 1984), alternating current (AC) resistivity (Monfore 1900), and water sorptivity (Hall 1989). The same techniques used to evaluate the durability of concrete should also be capable of assessing the level of damage associated with mechanical loading of a specimen or structure. When concrete is loaded, microcracking initially occurs at the bond between

the aggregate and the cement paste followed by a propagation of the cracks into the mortar. The level of cracking will affect the ease of transport within the concrete.

The permeability of concrete directly governs the ease with which water and gases can penetrate through the concrete. For concrete subject to applied loading, the stress level, rate of loading, and type of stress state (i.e., compression or tension) will significantly affect the transport characteristics of concrete material due to the generation and propagation of cracks (Banthia et al. 2005). The increase in the permeability of concrete due to damage induced by external loading becomes considerably pronounced once loading exceeds a certain threshold stress level. Kermani (Kermani 1991) reported 40% of the ultimate strength (f'_c) as the load level above which a significant increase in permeability occurs. An investigation by Sugiyama et al. (Sugiyama et al. 1996), however, showed that permeability of concrete increases markedly when the concrete samples experience stress beyond $0.69f'_c$, which is similar to the findings of Hearn and Lok (Hearn and Lok 1998) who observed a sharp increase in permeability at $0.71f'_c$. A study by Picandet et al. (Picandet et al. 2001) on the effect of compression loading damage on the gas permeability characteristics of concrete indicated the permeability is approximately 10 times larger once the stress level exceeds $0.9f'_c$ compared with undamaged concrete. A load of $0.9f'_c$ is also reported by Tegguer (Tegguer et al. 2013) to generate considerable cracking and result in a significant increase in the permeability index. Another experimental study carried out by Choinska (Choinska et al. 2007) indicated that $0.8f'_c$ should be considered as the critical stress level that causes considerable change in the permeability of the concrete after unloading.

There appears to be little change in the permeability at stress levels below a critical stress, whereas exceeding the threshold stress level leads to a significant detrimental effect on the permeability properties of concrete. Small changes in the permeability well below threshold stress is an indication of minor cracking at the aggregate-paste interface, while the spread of cracking into mortar triggers significant growth in the permeability (Samaha and Hover 1992).

The electrical properties of concrete – in particular, resistivity or its reciprocal, conductivity – are commonly used to assess likely future durability performance, as they are a measure of the ease with which ions can move through the microstructure of

the material (Alexander et al. 2008; Polder 2001). Concrete can be viewed as two component material consisting of a porous hardened cement matrix, typically either saturated or partially-saturated with pore solution, and solid aggregate. Since the conductivity of the pore solution is significantly greater than that of other parts (i.e., hydration products, cement and aggregate), the electrical properties of concrete are dependent on the movement of ions through the pore networks. Electrical resistivity measurement, which are used to assess the durability properties of concrete, are affected by a number of factors including: the pore solution composition, pore connectivity, and the total porosity (Andrade et al. 2000; McCarter and Garvin 1989). In the majority of previous research electrical resistivity testing was used to evaluate the vulnerability of the concrete to corrosion-related deterioration, and the relationship between electrical resistivity of damaged concrete at different stress levels was not studied.

The durability of concrete can also be quantified by its ability to absorb water, which indicates the total volume of permeable voids and pore size distribution. Studies carried out by Hearn et al. (Hearn et al. 2006) showed the porosity of concrete influences its mechanical properties. The volume of permeable voids should provide an indication of the capillary porosity and potentially micro/macro cracking in the damaged concrete. The measurement of porosity of damaged concrete for the purpose of identification of damage in the microstructural system of concrete unloaded from different levels of stress has not received significant attention.

Regarding residual mechanical properties of damaged concrete, some studies have investigated the residual strength of plain concrete after exposure to fatigue loading (Ali et al. 2010; Meng et al. 2012; Zhang and Wu 1997; Zhu and Li 2011). The residual strength of concrete after static preloading, however, is very rarely examined in the literature. Cornelissen and Reinhardt (Cornelissen and Reinhardt 1986), for instance, reported no significant loss in strength, stiffness, and strain by static compression preloading below $0.8f'_c$.

From previous discussion, this chapter intends develop a testing methodology to quantify not only the level of damage, but also to determine the remaining capacity of the damaged concrete after a significant loading (i.e., earthquake). Although the study of durability aspects of cracked concrete can reveal damage incurred in the

microstructure of the concrete, it has not generally been related to degradation of material due to external mechanical loading. The objectives of this investigation therefore are: (1) to study the capability and robustness of permeability, electrical resistivity and porosity testing techniques to identify the level of load-induced damage in the microstructural system of concrete through their responses to applied loading at certain levels; (2) to determine the critical loading levels that affect durability related properties of concrete; (3) to evaluate the post-event residual capacity of concrete material using a monotonic compression test up to failure on the concrete samples, which had previously pre-loaded up to certain levels; and (4) to make a correlation between the level of damage identified through durability-based techniques and degradation in mechanical properties of concrete.

2.2 Experimental investigations

2.2.1 Materials, mix proportion and specimen details

The concrete mix used in this investigation was prepared using a general purpose (GP) Portland cement with a water cement (w/c) ratio of 0.56. A locally available, semi-crushed Greywacke coarse aggregate with a maximum size of 13 mm and natural river sand with a fineness modulus of 2.76 were used in the mix. The course aggregate was pre-soaked in water to ensure the moisture content was above the saturated-surface dry condition. The water content of the mix was adjusted to compensate for the moisture content of the aggregate. Water reducing admixtures (WRA) were used to achieve a slump of 90 ±20 mm. Table 2-1 presents the mixture proportions per cubic metre of concrete.

Table 2-1 Concrete constituents and mix proportions

Material	
Coarse aggregate, kg/m^3	1050
Fine aggregate, kg/m^3	840
Cement, kg/m^3	304
Water, kg/m^3	170
Average compressive strength at 28 days, MPa	48
Average compressive strength at 90 days, MPa	70

Concrete cylinders of height 200 mm and diameter 100 mm were cast in steel moulds in three layers from a single batch with the use of vibrating table to ensure adequate compaction. All mixing and casting were carried out under ambient laboratory conditions. After casting, the cylindrical specimens were stored in a room maintained at 21 ± 2 ℃ and covered for 24 hours. The cylinders were demoulded and moist-cured in a fog room at 95–100% relative humidity for 28 and 90 days. Prior to testing, the top surface of the cylinders were ground to provide a smooth, flat surface during loading.

2.2.2 Specimen instrumentation

Two strain gauges (PL-60-11 TML Tokyo) were attached using Cyanoacrylate CN-E adhesive in the axial direction and two strain gauges in the transverse direction at the midpoints on opposite sides of the concrete specimens. Prior to attaching the strain gauges, the surface was sanded and any dirt or residue removed using acetone. A two-component, PS polyester adhesive was used as a precoating to provide a smooth surface that is alkali resistant and effectively prevents the movement of moisture from the inside the concrete to the strain gauges. Strain gauges with short gauge lengths are not good candidates to capture strain in concrete surfaces since they are only sensitive to localized strains. For a heterogeneous material like concrete, a gauge length is required that can average out any irregular stresses caused by the coarse aggregate in the material. Thus, the gauge length in this research has a sensing length of 60 mm, which is approximately five times the diameter of the largest aggregate size. Figure 2-1 shows a schematic layout of strain gauges.

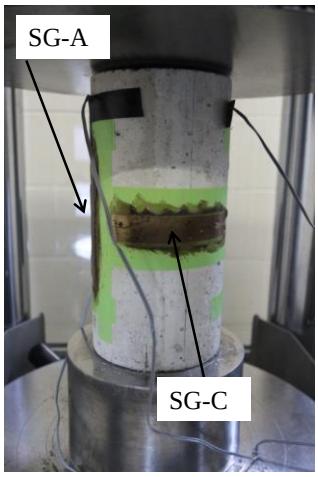

SG-A = Strain gauge-Axial

SG-C = Strain gauge-Circumferential

Figure 2-1 strain gauges' configuration

2.2.3 Uniaxial loading

The concrete cylinders were tested under displacement control at a rate equal to 50 με/min using a compression machine with a capacity of 3000 kN. Figure 2-2 illustrates the full stress-strain behaviour of the average of three cylinders under uniaxial compression up to failure. Each data point on the compression or tension branch is the average reading from two axial or transverse strain gauges attached to each sample. The test was conducted in accordance with ASTM C39/C39M and the post-peak behaviour of specimens was captured until fracture after which, no more strain-softening response was recorded. Having determined the ultimate axial strength of control cylinders, the companion concrete cylinders were subjected to compression loading up to predefined levels. To simulate partial damage, four levels of uniaxial compression: 50%, 70%, 90% and 95% of the average ultimate compressive strength were applied to three cylinders at each level of loading at a rate equal to 2 kN/s.

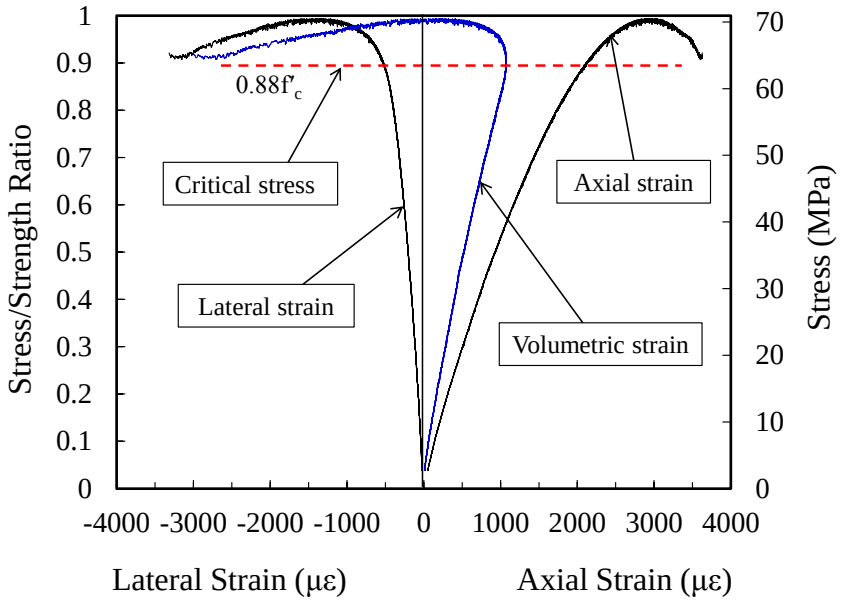

Figure 2-2 Relationship between stress and axial, lateral, and volumetric strain

2.2.4 Specimen preparation for durability testing

After unloading the cylinders from predefined stress levels, two concrete disks of approximately 25 mm in thickness were cut off from the middle third of each of the three damaged cylinders (Figure 2-3). The central portion of the cylinder was selected to supply concrete disks as it represents the most damaged portion of the cylinder and also eliminates any end effect. The thickness of each disk was measured with an accuracy of ± 0.1 mm. The disks were dried in an oven at 50°C (ASTM C1585) for approximately two weeks until the difference in mass between their two consecutive readings was less than 0.1 %.

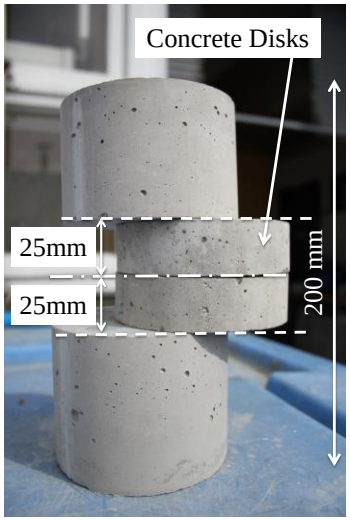

Figure 2-3 Procedure to extract the concrete disks

2.2.5 Oxygen permeability test

A falling head permeameter pressurized with oxygen was used to determine the coefficient of permeability (Ballim 1991; Edvardsen 1999). The cell consists of inlet and outlet valves that allow oxygen flow through the chamber. To ensure a uni-dimensional gas flow, concrete disks were sealed by a tight-fitting silicone rubber collar inside a confining ring. The specimens were secured at the top of the permeability cell, and a pressure head difference up to 100 kPa was applied (Figure 2-4). Permeability measurements were conducted in a climate-controlled room (21 ± 2 ℃ and RH 50 ± 5%).

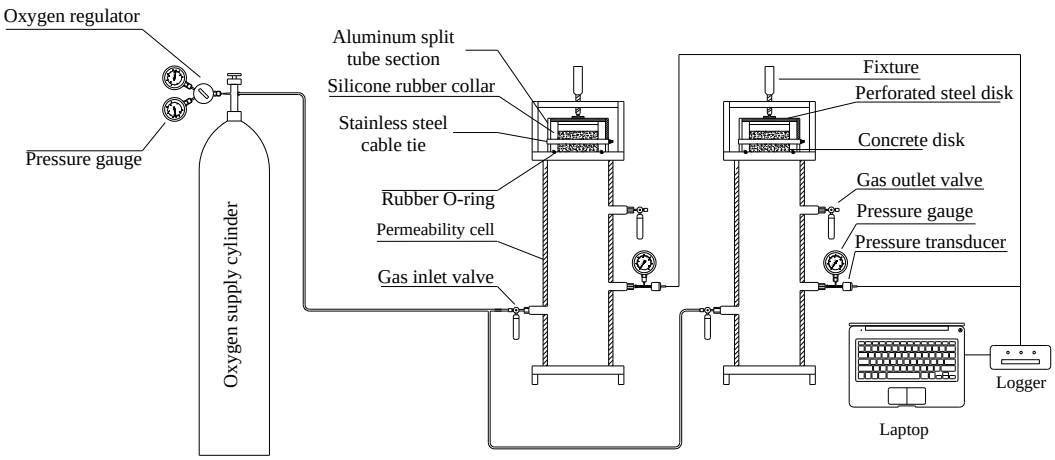

Figure 2-4 Oxygen permeability test apparatus

The pressure decay was recorded by a transducer at five-minute time intervals. The test was terminated either after eight hours or a 50 kPa drop in the pressure. The apparent coefficient of permeability (m/s) is calculated from the expression of Equation (2.1) (Alexander et al. 1999).

$$k = \frac{\omega \, vgtz}{RA\,\theta} \tag{2.1}$$

where ω = molecular mass of oxygen (kg/mol); v = volume of oxygen under pressure (0.00495 m^3); g = acceleration due to gravity (m/s^2); t = sample thickness (m); z = the slope of line $\ln(P_o/P_t)$; R = gas constant; A = cross-sectional area (m^2); θ = absolute temperature (K);P_o is the initial pressure reading at the start of the test (kPa); and P_t = subsequent pressures during experiment obtained at each step (kPa). Figure 2-5 schematically illustrates the oxygen gas flow through concrete disks samples.

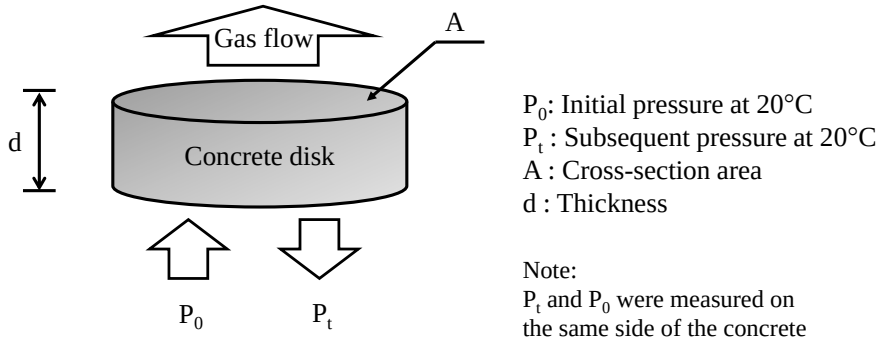

Figure 2-5 Schematic representation of pressure gradient

It is worth mentioning that the durability index test method used in this study has been developed in South Africa and has similar merit in establishing material properties as other internationally accepted methods (Beushausen and Alexander 2008).

2.2.6 Electrical resistivity test

A parallel plate AC resistivity technique, in which the concrete disks are placed between two electrodes, was employed in this study to measure the resistivity of concrete (Smith 2006). To conduct this experiment, all concrete disks were completely water-saturated using the vacuum saturation technique described in ASTM C1202 . The voltage and alternating current across the two stainless steel plates holding the concrete sample were measured. Because the cement paste acts as an insulator, it is

assumed that the current would follow a similar path to movement of ions through the pore solution in the concrete. Figure 2-6 shows the electrical resistivity test apparatus.

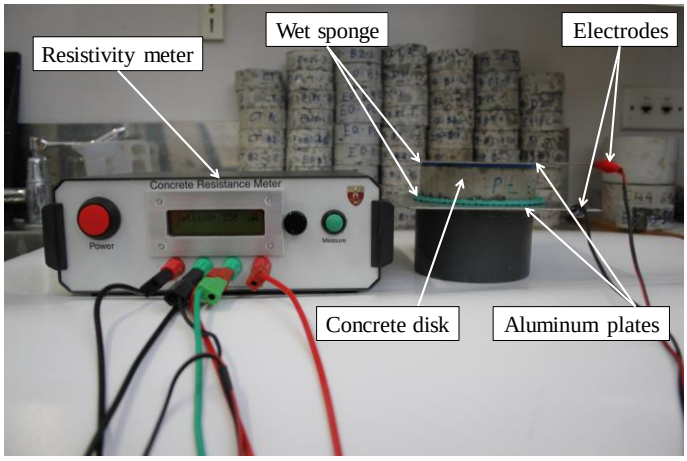

Figure 2-6 Electrical resistivity test apparatus

The electrical resistance of the concrete was calculated for each of six disks at each level of loading using Ohm's law by substituting the voltage and the current measured across the sample, using Equation (2.2):

$$\rho = \frac{VA}{It} \tag{2.2}$$

where ρ = resistivity of concrete (kΩ.cm); I = measured current passed between outer surfaces (μA); t = thickness of the specimen (cm);V = applied voltage (mV); and A = cross-sectional area of the specimen (cm^2).

2.2.7 Porosity test

A test method described by ASTM C642 was adopted to measure absorption in the hardened concrete, using the vacuum saturation method. The vacuum saturation technique is considered sufficiently rigorous to ensure all microcracks are thoroughly filled (Safiuddin and Hearn 2005). Thus, in the present study the vacuum saturated porosity test was used as a further measure of the damage in the concrete. The specimens were dried in the oven at 50°C until two successive values of mass of the sample at intervals of one day showed no decrease in mass beyond 0.1%. The concrete disks were removed from the oven and allowed to cool under laboratory conditions of 20–25°C, after which the oven-dry mass was obtained. Concrete disks, 100 mm in

diameter and 25 mm in thickness were placed under vacuum for three hours after which de-aerated tap water was allowed to enter the chamber, submerging the test specimens. The vacuum was maintained for one further hour, after which the chamber was opened to the atmosphere. The specimens were immersed and kept under water for an additional 20 hours, at which point both the saturated mass and the immersed apparent mass (buoyant mass) were determined. Figure 2-7 shows the configuration of porosity test set-up.

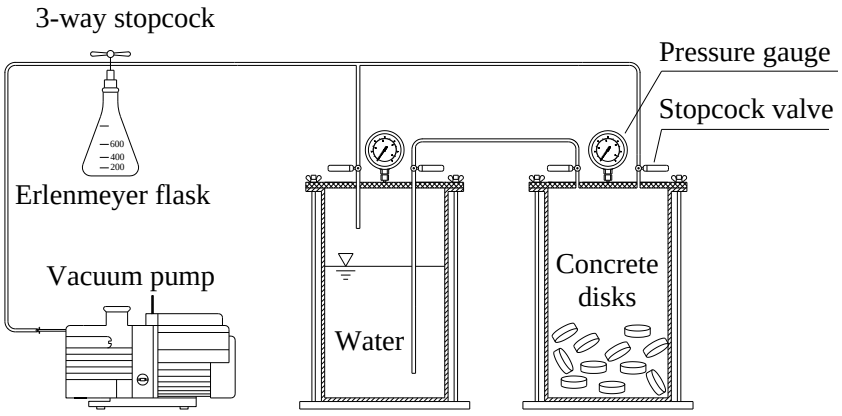

Figure 2-7 Porosity test set-up

2.3 Results and discussion

2.3.1 Volumetric strain-based damage assessment

The volumetric strain of concrete material (ε_v) is represented by the ratio of the change in the volume of the concrete sample to the original volume, which is equal to the summation of the principal strains (ε_1, ε_2, ε_3). Measuring three principal strains in a concrete cylinder requires axial (ε_a), circumferential (ε_c) and radial strain (ε_r) to be captured. In a cylindrical concrete sample under uniaxial compression, the circumferential strain measurement is related to the radial strain, as is shown in Equation (2.3).

$$\varepsilon_c = \frac{2\pi\Delta r}{2\pi r} = \frac{\Delta r}{r} = \varepsilon_r \tag{2.3}$$

where r = radius of the specimen; and Δr = change in radius. As a result, to determine the volumetric strain, readings from axial and circumferential strain gauges (SG-A and SG-T) were considered as given in Equation (2.4).

$$\varepsilon_v = \varepsilon_1 + \varepsilon_2 + \varepsilon_3 = \varepsilon_a + \varepsilon_c + \varepsilon_r = \varepsilon_a + 2\varepsilon_c \quad (2.4)$$

As illustrated in Fig. 1b, the volumetric strain of the concrete material reduced nearly linearly up to a stress level of about $0.7f'_c$, above which a nonlinear trend up to a stress level of $0.88f'_c$ was observed. At $0.88f'_c$ the rate of increase in lateral strain exceeded the rate of increase in axial strain such that the change in volume was reversed. The volume of the specimen at $0.88f'_c$ is therefore at a minimum. At stress levels just beyond this, the specimens dilate as the lateral cracks open, increasing the specimen volume despite the significant axial compaction. This level of stress is referred to as "critical stress", when deterioration in the internal integrity of the material suddenly occurs (Richart et al. 1928). Having exceeded the critical stress, interconnected channels form in the damaged concrete that do not completely close after unloading. The damage at this condition is mainly attributed to the onset of unstable fracture propagation, below which no collapse of concrete under short term loading is expected, while above that, given sufficient time, collapse will be unavoidable (Kotsovos 1979).

2.3.2 Effect of mechanical stress and age on durability features

Figure 2-8 illustrates the relationship between the change in the permeability coefficient, as an indicator of damage, and the level of applied stress in terms of percentage of the ultimate strength. The result of the permeability test on the damaged concrete samples showed that as the load increased, the coefficient of permeability increased also. There is a very slight increase in permeability when the compressive load is below $0.5f'_c$, reflecting only limited damage in the material. At this stage, the crack network becomes more interconnected. However, the stress is not sufficient to result in a significant change in the permeability. The transitional zone, in which minor microstructural damage turns into significant macrocracking of the binder system, is associated with stress levels of $0.5\text{-}0.7f'_c$.

At a stress level of $0.7f'_c$ and beyond, in which "continuous cracks", as classified by Shah and Chandra 1968 are formed, a noticeable ascending trend in the permeability

was observed. The permeability coefficient of the samples loaded to $0.95f'_c$ at 28 days was approximately 2.5 times greater than the average value of 2.4×10^{-11} m/s associated with the intact samples. The significant increase in permeability happens because of the extensive propagation of microcracks throughout the matrix connecting with other mortar cracks as well as bond cracks. At such a stress level, the bond cracks increase in length, width and number, which is in general agreement with results reported by Hsu et al. (1963). At 95 % of the ultimate strength, the maximum increase in the permeability coefficient was recorded.

Considering volumetric strain variation over the applied range of stress, it is understood that the pores network that already exists in the concrete becomes more condensed at a very initial stage of compression loading, which hinders a noticable increase in the permeability. However, the coalescence of microcracking above the threshold stress facilitates the flow conveyance in partially damaged concrete, resulting in a rapid rise in the permeability. The test did not proceed for stress levels higher than $0.95f'_c$ owing to variability in the ultimate strength results.

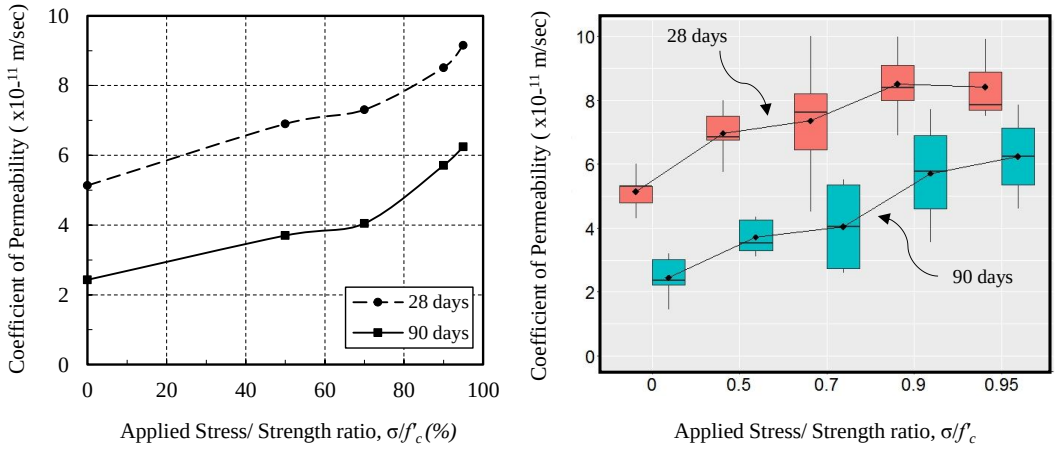

Figure 2-8 Relationship between applied stress level and permeability coefficient: (a) line chart; (b) box plot

The average measurements of permeability coefficient on 60 disks at both 28 and 90 days are provided in Table 2-2.

Table 2-2 Permeability test results

Stress to strength ratio, σ/f'_c	28 days		90 days	
	Permeability* $\times 10^{-11}$ m/s	Standard deviation	Permeability* $\times 10^{-11}$ m/s	Standard deviation
0	5.13	0.29	2.43	0.50
0.50	6.91	1.41	3.70	0.37
0.7	7.30	2.85	4.04	1.58
0.9	8.51	4.69	5.71	1.83
0.95	9.15	4.75	6.24	2.45

* the permeability described at each stress level is the average of measurements of six disks

Figure 2-9 indicates the relationship between the change in electrical resistivity with respect to the applied stress levels. Similar to the permeability coefficient, a slight increase in the resistivity occurred up to $0.5f'_c$. The increase in resistivity might be associated with the compression of the pre-existing pore spaces, which limits the ionic movement through concrete that is not highly damaged. However, an increase in stress level between 0.5–$0.7f'_c$, which results in the initiation and propagation of cracking, leads to a decrease in resistivity that is associated with a greater ease of ionic movement.

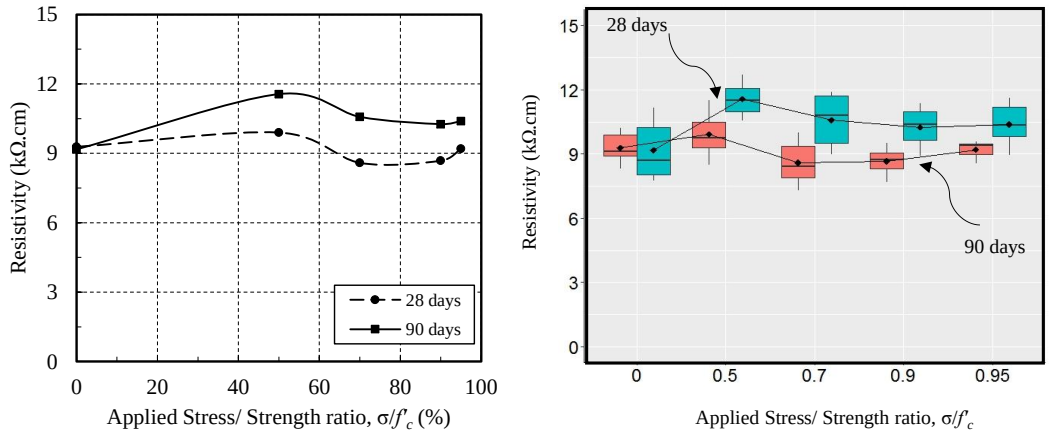

Figure 2-9 Relationship between applied stress level and electrical resistance: (a) line chart; (b) box plot

The resistivity of concrete at $0.9f'_c$ is nearly the same as that before loading, which is consistent with the results reported by Saito and Ishimori (Saito and Ishimori 1995). Once the stress exceeded $0.95f'_c$, the resistivity showed only a small increase, despite this level of stress being associated with a highly connected network of cracking and pores. Considering the behaviour of resistivity over the applied stress range, no discernible trend could be found, which implies this test is not a good candidate for durability-based damage assessment of concrete material. The average results of the resistivity test on 6 disks at each stress level for both 28 and 90 days are summarized in Table 2-3.

Table 2-3 Resistivity test results

Stress to strength ratio, σ/f'_c	28 days		90 days	
	Resistivity* kΩ·cm	Standard deviation	Resistivity* kΩ·cm	Standard deviation
0	9.28	0.28	9.17	1.47
0.5	9.90	0.67	11.56	0.83
0.7	8.59	0.57	10.58	1.39
0.9	8.68	0.15	10.26	1.48
0.95	9.20	0.42	10.39	2.13

* the resistivity described at each stress level is the average of measurements of six disks

The results of porosity tests are provided in Figure 2-10. In spite of significant damage in the microstructure of the concrete material, once the samples were loaded up to 95 % of their ultimate strength, no significant change is seen in the porosity. The porosity test is primarily designed to measure the volume of the voids and capillary pores that are many times larger than the volume of microcracks formed during loading. The porosity test therefore is not sensitive enough to detect changes in the microstructure of the concrete associated with mechanical loading.

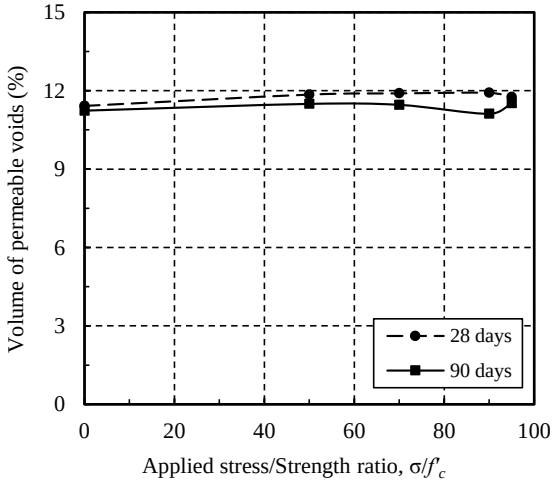

Figure 2-10 Relationship between applied stress level and porosity

With the aging of concrete, there is a potential change in the microstructure of concrete which is expected to be reflected in durability-based tests. However, in this investigation, the effect of age of the concrete, was more pronounced in the permeability test, rather than electrical resistivity or porosity tests. As the cement continues to hydrate with time, there is a densification of the microstructure, which is evident in the decrease in permeability and porosity and the increase in resistivity.

Those tests which were able to differentiate between applied stress levels in the concrete at 28 days were just as effective at 90 days, while those tests which showed only a minor change in response to mechanical loading at 28 days were similarly incapable of distinguishing the level of applied stress at 90 days. Table 2-4 shows the results of the porosity readings and standard deviation values associated with six concrete disks at each stress level for 28 and 90 days.

Table 2-4 Porosity test results

Applied stress to strength ratio	28 days		90 days	
	Porosity (%)*	Standard deviation	Porosity (%)*	Standard deviation
0	11.4	0.18	11.2	0.39
0.5	11.8	0.34	11.4	0.45
0.7	11.9	0.42	11.4	0.49
0.9	11.9	0.45	11.1	0.34
0.95	11.7	0.14	11.5	0.37

* the porosity described at each stress level is the average of measurements of six disks

2.3.3 Permeability-based damage assessment

The damage denoted in this study is a post-event measurement of microcracks that occurred in the damaged concrete disks, which is analogous to the damage model reported by Løland (1980). The damage model introduced by Løland defines damage as a measure of the relative portion of pores and cracks (nominal fracture area) in the concrete material. Løland's model attributes the increase in the damage to the decrease in elastic modulus. Since only the oxygen permeability test was found to be sensitive and reliable enough to reveal damage in concrete samples, a permeability damage index (PDI) was introduced to account for relative change in the permeability characteristics of the damaged concrete, as follows:

$$\text{PDI}\ (\%) = \frac{k - k_0}{k_{peak}} \times 100 \tag{2.5}$$

where k = coefficient of the permeability of concrete disk at any damage level; k_{peak} = the maximum coefficient of permeability achieved amongst disk samples (in this current investigation measured at $0.95f'_c$); and k_0 = coefficient of permeability of the intact concrete disk (undamaged).

Using Equation (2.5), the concrete samples are considered undamaged when the coefficient of permeability of the concrete disk under examination is equal to the coefficient of permeability of the concrete in its intact condition (PDI=0%). At fully damaged status, where there is no resistance to flow in the damaged sample, k and k_{peak} acquire large identical values. This implies denominator and numerator are approximately equal causing PDI to tend to unity (PDI=100%). Although it is practically impossible to measure the permeability of fully damaged disks, owing to disintegration, the proposed damage index is applicable for the level of damage observed in this study.

It should be noted that since the value of PDI is relative, it is possible to obtain a high value of PDI for members that have only minor damage. This means that the intensity of permeability-based damage represented by PDI does not necessarily represents the same level of damage in the mechanical properties of the damage concrete. The relationship between PDI and applied level of stress can be estimated using Equation (2.6) with a coefficient of determination (R^2) of 0.98. It should be noted

that, this equation has been deduced from data associated with the concrete at the age of 90 days. Although the general form of equation can be adopted for any other type of concrete at any age, the numerical constants would be different.

$$\text{PDI}(\%) = 5.8e^{\left(\frac{\sigma}{f'_c}\right)} - 4.6 \tag{2.6}$$

where f'_c = ultimate compressive strength; and σ = applied stress. Figure 2-11 shows the relationship between PDI and applied stress level for disks taken from previously loaded cylinders. Since for practical purposes, the damage assessment of the aged concrete is of interest, the PDI associated with the samples at 90 days is shown. It should be noted that the data points represented in each plot are the average test results from six disks taken from the middle third of the three concrete cylinders tested at any desired loading level.

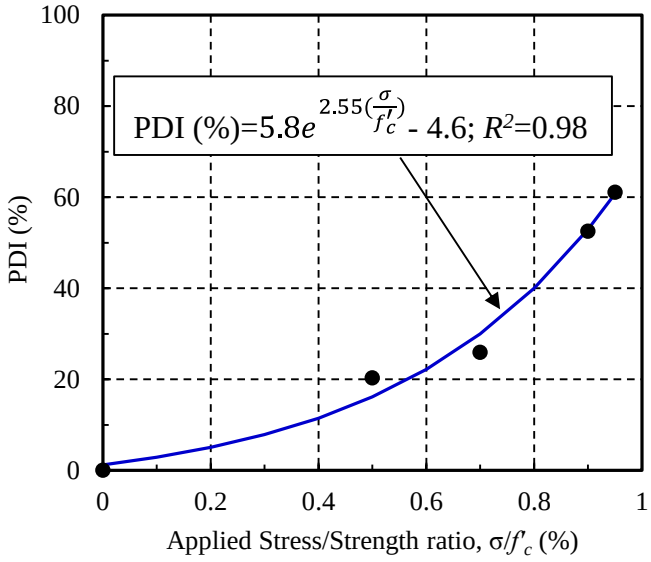

Figure 2-11 Permeability damage index versus stress/strength ratio

2.3.4 Mechanical -based damage assessment

To determine the residual capacity of the damaged cylinders, twelve concrete cylinders were initially loaded in compression to 0.5, 0.7, 0.9 and 0.95f'_c, three cylinders at each level. The cylinders were instrumented, as previously described, following the partial loading to avoid damage on strain gauges and possible permanent strain associated with the initial loading sequence. In the next step, all damaged

cylinders were reloaded up to failure to capture their remaining stress-strain behaviour. The re-loading was conducted immediately after employing pre-defined loading with no rest time to avoid any self-healing. The mechanical properties of damaged concrete material including elastic modulus, ultimate compressive strength and maximum strain capacity were precisely measured and the losses in the material characteristics were captured.

The residual stress-strain responses of the partially damaged concrete cylinders at the age of 90 days, reloaded after exposure to predefined monotonic compressive stress levels are provided in Figure 2-12 The effect of damage on the ultimate bearing capacity after reloading. All graphs are representative of the average of three experiments at each level of loading. The results indicate a noticeable reduction in the strain capacity; however, no significant reduction in strength was observed. Having compared the average strain capacity of intact concrete cylinders cured in a fog room with samples preloaded to 70–95% of ultimate strength, about 900 με reduction in the strain of damaged concrete was observed, which is equivalent to approximately a 24% loss in strain capacity. The same reduction in post-damaged strain capacity was not found for cylinders loaded up to 50% of the ultimate strength, since continuous cracking in the paste and at the aggregate interface are not significant until the stress levels reaches 0.7–0.95f'_c. For stress levels up to 0.5f'_c, primarily interfacial cracks are expected to occur. This implies that when the concrete microstructure is damaged and significant microcracking occurs, the damaged concrete is less ductile and tolerates less deformation demand. With respect to strength capacity, the comparison between strengths of cylinders preloaded up to 0.95f'_c and undamaged cylinders showed only a 9.5% difference, which may partially be attributed to the normal scatter of strength amongst specimens.

The elastic modulus was not significantly different between the various samples. Although the strength and elastic modulus of the damaged concrete cylinders did not substantially decrease, there is a high risk of strain deterioration beyond the critical stress level. The reduction in strain capacity can be attributed to the increase in permanent strain associated with the formation of a network of imperfectly closed cracks in the microstructural system of the concrete. In fact, energy absorbed by the specimen during the first compressive load excursion induces some permanent deformation, resulting in a reduction in pore space and the concrete becoming more compacted. After the initial loading there is a reduction in the subsequent deformability (strain capacity) of the concrete, causing a more brittle mode of failure. This phenomenon causes a decrease in the stress peaks occurring within the material and a redistribution of stresses that results in little overall change in strength. As preloading occurs at stress levels below peak stress, it does not significantly undermine the integrity and load-carrying capacity of the concrete, indicating load paths are still functional to carry compressive load. The findings from this investigation are consistent with those of Shah and Winter (1966) who reported that the application of five cycles of excursion at 0.83–0.88 of the ultimate strength did not affect the ultimate strength of specimens on monotonic failure reloading.

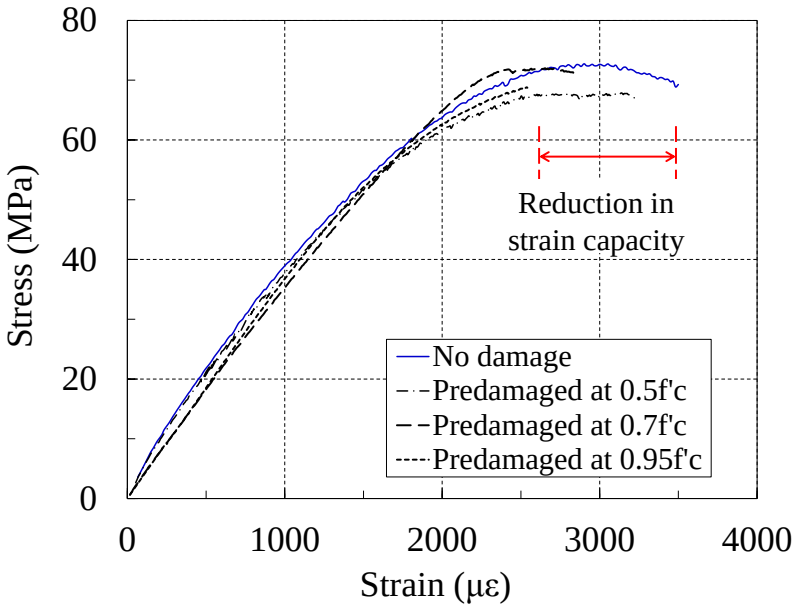

Figure 2-12 The effect of damage on the ultimate bearing capacity after reloading

2.3.5 Residual strain capacity estimation

Considering strain as the mechanical parameter that undergoes the most degradation, a proper estimation of the remaining strain capacity of damaged concrete is needed for quantitative assessment of damaged concrete. The key factor affecting the remaining strain capacity of a damaged concrete sample is the stress level already experienced, which can be found through experimental relationships established between permeability and damage level. When the coefficient of permeability is measured, the material degradation in terms of ultimate monotonic loading strain can then be evaluated. Equation (2.7) represents a prediction model based on a PDI-based approach to estimate the residual strain in uniaxial damaged concrete.

$$\varepsilon_{res} = \varepsilon_{ult}(0.5+0.48\ e^{-1.25\ PDI}) \tag{2.7}$$

where ε_{res} = residual strain of the damaged concrete; and ε_{ult} = strain of the undamaged concrete.

As can be seen in Figure 2-13, an increase in the PDI results in a deterioration of the strain capacity. Having assigned k_{peak} to the most damaged area of a concrete member and k_0 to the least damaged area, PDI can be determined appropriately for any concrete construction at any age. Once PDI is calculated, the residual strain capacity can be predicted using a PDI-based estimator. To determine the level of damage in previously stressed concrete, a simple strength test of damaged concrete is not adequate. An accurate estimate of the residual strain capacity is what needs to be precisely measured, as it reveals the level of the damage. Therefore, the relationship has been developed to evaluate residual strain, not strength, because the loss in strain is more dominant, and it also affects the ductility of the concrete.

It should be noted that Equations 7 has been developed based on the current range of experimental results in this investigation and may not be applicable for predicting ultimate failure in the post-peak area. The maximum level of stress demand considered herein is equal to peak stress (strength) while the actual failure occurs beyond ultimate strength.

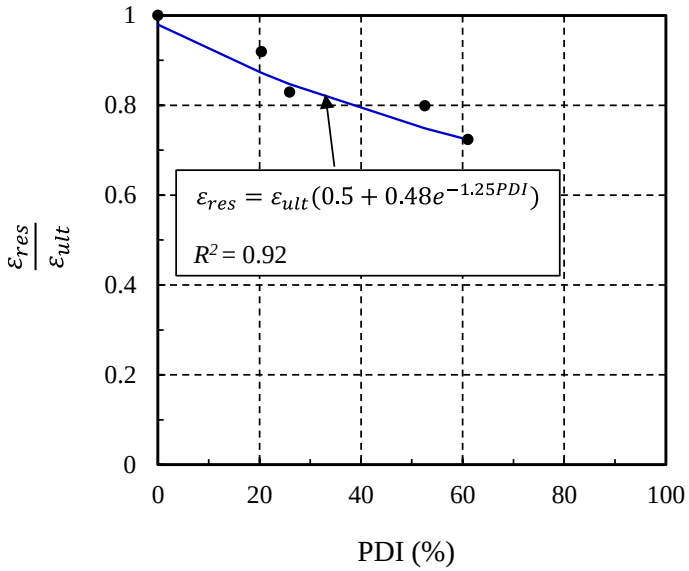

Figure 2-13 PDI-based prediction of residual strain

2.3.6 Limitations on permeability-based damage assessment

The value of permeability coefficient is not constant and varies over the time. The introduced permeability damage index (PDI), is a relative value which depends on k_0 and k_{peak}. While k_0 is associated with the intact concrete sample or a sample which is taken from a region of RC member with the minimum level of damage, k_{peak} is representative of the most stressed concrete sample or a sample taken from the severest damaged region of RC member (i.e., plastic hinge region). Hence, the value of k_0 can be determined with acceptable level of uncertainty, while determination of k_{peak} is a big challenge. That is because, concrete in the regions with significant damage is crushed, making it impossible to take a sample and to measure the permeability coefficient. As a result, assessment will be limited to the range of stresses over which the concrete can retain its integrity. This implies, Equation 2.6 represents the PDI values which are considerably higher than PDI value if there would be possible to determine real value

of k_{peak}. That is why, for the range of stress levels considered in this study, a big value of PDI of 60% resulted in only 30% deterioration in strain capacity. Although the value of PDI is not absolute, it is a good indication of damage in microstructural system of concrete due to external loading. Since the value of PDI calculated herein is related to one excursion of compressive loading, its application to estimate the residual strain capacity suggests the minimum strain degradation. Thus, it can be concluded that increase of 50% of PDI potentially causes a minimum of 20% loss in strain capacity.

It should be also mentioned that due to relative nature of PDI and its dependency on k_{peak}, it is possible to obtain high value of PDI even for the concrete samples that experienced minor damage. Thus, there is a need to expand database in future works in an attempt to conduct more reliable quantitative permeability-based damage assessment.

2.4 Conclusions

Three alternative durability testing techniques were used to assess concrete material damaged by external uniaxial compression. In the first stage, an attempt was made to develop a relationship between the level of the stress and the damage that occurred in the microstructure of the concrete material. The second stage investigated the reloaded stress-strain behaviour of the damaged concrete cylinders to reveal the residual strain and strength capacity of the damaged material. Based on this work, the following conclusions can be drawn:

1. Of the three durability testing techniques studied in this work– oxygen permeability tests, electrical resistivity tests, and porosity tests – only the oxygen permeability testing was found to be sufficiently robust and sensitive to identify the level of damage with respect to applied stress. Neither the resistivity nor the volume of permeable voids tests were able to distinguish varying degrees of damage in the concrete microstructure.
2. In the present study, the oxygen permeability coefficient of the concrete disks taken from cylinders loaded up to $0.7f'_c$ showed only a slight increase in permeability. At loads great than $0.7f'_c$ the permeability increased drastically. For specimens loaded to $0.95f'_c$ the oxygen permeability coefficient was

approximately three times greater compared with an undamaged sample. In the present study, the critical stress, i.e. the point at which oxygen permeability coefficient dramatically increase for small increase in stress is found to be exceeded when the concrete cylinders were loaded to stress level between $0.7f'_c$ and $0.95f'_c$. This is line with the critical stress value ($0.88f'_c$) obtained from the volumetric strain diagram. In fact, when the applied load exceeds the critical stress, interconnected channels formed in the damaged concrete do not completely close after unloading. Results showed the effect of these irreversible cracks can be efficiently identified using permeability test.

3. From the experimental results for monotonic loading, as the pre-applied stress level increased, the residual strains of the damaged samples decreased. The experiments showed an average reduction of about 24% in strain capacity associated with preloaded samples up to $0.7\text{-}0.95f'_c$, while no significant degradation in the strength was observed. The loss in deformability of concrete implies that damage (e.g., crushing) would occur earlier if the damaged member were subject to the next loading demand (i.e., earthquake aftershock). Although the application of one time pre-loading does not reflects the damage induced during seismic event, this study successfully showed the feasibility and capability of permeability test to reveal damage. Although the level of damage determined in this condition is less than what is expected under significant cyclic loading, it denotes for non-use of stress-strain diagrams related to intact concrete for the purpose of determining the residual capacity of a damaged RC member. In fact, adopting an undamaged stress-strain behaviour of concrete material for the purpose of assessment in a damaged RC structure leads to overestimating the residual capacity.
4. A permeability-based damage index was proposed along with a PDI-based model to estimate the residual strain in uniaxial damaged concrete.

2.5 References

Alexander, M., Ballim, Y., and Mackechnie, J. (1999). "Concrete durability index testing manual." *Research monograph*, 4.

Alexander, M., Ballim, Y., and Stanish, K. (2008). "A framework for use of durability indexes in performance-based design and specifications for reinforced concrete structures." *Materials and structures*, 41(5), 921-936.

Ali, M., Oehlers, D., and Griffith, M. (2010). "The residual strength of confined concrete." *Advances in Structural Engineering*, 13(4), 603-618.

Andrade, C., Alsonso, C., Arteaga, A., and Tanner, P. "Methodology based on the electrical resistivity for calculation of reinforcement service life, 683 in: Malhotra (Ed.) proceedings of the 5th CANMET." *Proc., ACI International Conference on Durability of Concrete, Barcelona, Spain*, 899-684.

ASTM C39/C39M (2017). "Standard Test Method for Compressive Strength of Cylindrical Concrete Specimens." *ASTM International, West Conshohocken, PA*.

ASTM C642 (2013). "Standard Test Method for Density, Absorption, and Voids in Hardened Concrete." *ASTM International, West Conshohocken, PA*.

ASTM C1202 (2012). "Standard Test Method for Electrical Indication of Concrete's Ability to Resist Chloride Ion Penetration." *ASTM International, West Conshohocken, PA*.

ASTM C1585 (2013). "Standard Test Method for Measurement of Rate of Absorption of Water by Hydraulic-Cement Concretes." ASTM International, West Conshohocken, PA.

Ballim, Y. (1991). "A low cost falling head permeameter for measuring concrete gas permeability." *Concrete Beton*, 61, 13-18.

Banthia, N., Biparva, A., and Mindess, S. (2005). "Permeability of concrete under stress." *Cement and Concrete Research*, 35(9), 1651-1655.

Beushausen, H., and Alexander, M. (2008). "The South African durability index tests in an international comparison." *Journal of the South African institution of civil engineering*, 50(1), 25-31.

Choinska, M., Khelidj, A., Chatzigeorgiou, G., and Pijaudier-Cabot, G. (2007). "Effects and interactions of temperature and stress-level related damage on permeability of concrete." *Cement and Concrete Research*, 37(1), 79-88.

Cornelissen, H., and Reinhardt, H. "Effect of Static and Fatigue Pre-loading on Residual Strength and Stiffness of Plain Concrete." *Proc., ECF6, Amsterdam*

Edvardsen, C. (1999). "Water permeability and autogenous healing of cracks in concrete." *ACI Materials Journal-American Concrete Institute*, 96(4), 448-454.

Elwood, K., Marder, K., Pampanin, S., Ramirez, A. C., Kral, M., Smith, P., Cattanach, A., and Stannard, M. (2016). "Draft framework for assessing residual capacity of earthquake-damaged concrete buildings." *NZSEE*Christchurch, New Zealand.

Grube, H., and Lawrence, C. (1984). *Permeability of concrete to oxygen*, Cement and Concrete Association.

Hall, C. (1989). "Water sorptivity of mortars and concretes: a review." *Magazine of concrete research*, 41(147), 51-61.

Hearn, N., Hooton, R. D., and Nokken, M. R. (2006). "Pore structure, permeability, and penetration resistance characteristics of concrete." *Significance of Tests and Properties of Concrete and Concrete-Making Materials*, ASTM International.

Hearn, N., and Lok, G. (1998). "Measurement of permeability under uniaxial compression: a test method." *Materials Journal*, 95(6), 691-694.

Hsu, T. T., Slate, F. O., Sturman, G. M., and Winter, G. (1963). "Microcracking of plain concrete and the shape of the stress-strain curve." *Journal of the American Concrete Institute*, 60(2), 209-224.

Kermani, A. (1991). "Permeability of stressed concrete: Steady-state method of measuring permeability of hardened concrete studies in relation to the change in structure of concrete under various short-term stress levels." *Building research and information*, 19(6), 360-366.

Kotsovos, M. (1979). "Fracture processes of concrete under generalised stress states." *Materiaux et Construction*, 12(6), 431-437.

Løland, K. (1980). "Continuous damage model for load-response estimation of concrete." *Cement and Concrete Research*, 10(3), 395-402.

McCarter, W., and Garvin, S. (1989). "Dependence of electrical impedance of cement-based materials on their moisture condition." *Journal of Physics D: Applied Physics*, 22(11), 1773.

Meng, X. H., Zhang, Y. X., and Zhou, J. H. "A Prediction Model of Concrete Fatigue Residual Strength." *Proc., Advanced Materials Research*, Trans Tech Publ, 1843-1846.

Monfore, G. (1900). "The electrical resistivity of concrete."

Picandet, V., Khelidj, A., and Bastian, G. (2001). "Effect of axial compressive damage on gas permeability of ordinary and high-performance concrete." *Cement and Concrete Research*, 31(11), 1525-1532.

Polder, R. B. (2001). "Test methods for on site measurement of resistivity of concrete—a RILEM TC-154 technical recommendation." *Construction and building materials*, 15(2), 125-131.

Richart, F. E., Brandtzaeg, A., and Brown, R. L. (1928). "A study of the failure of concrete under combined compressive stresses." *University of Illinois Bulletin; v. 26, no. 12*.

Safiuddin, M., and Hearn, N. (2005). "Comparison of ASTM saturation techniques for measuring the permeable porosity of concrete." *Cement and Concrete Research*, 35(5), 1008-1013.

Saito, M., and Ishimori, H. (1995). "Chloride permeability of concrete under static and repeated compressive loading." *Cement and Concrete Research*, 25(4), 803-808.

Samaha, H. R., and Hover, K. C. (1992). "Influence of microcracking on the mass transport properties of concrete." *Materials Journal*, 89(4), 416-424.

Shah, S. P., and Chandra, S. "Critical stress, volume change, and microcracking of concrete." *Proc., Journal Proceedings*, 770-780.

Shah, S. P., and Winter, G. "Response of concrete to repeated loading." *Proc., RILEM Proceedings of International Symposium on the Effects of Repeated Loading on Materials and Structural Elements, Mexico City, Mexico*.

Smith, D. (2006). "The development of a rapid test for determining the transport properties of concrete."

Sugiyama, T., Bremner, T. W., and Holm, T. A. (1996). "Effect of stress on gas permeability in concrete." *Materials Journal*, 93(5), 443-450.

Tegguer, A. D., Bonnet, S., Khelidj, A., and Baroghel-Bouny, V. (2013). "Effect of uniaxial compressive loading on gas permeability and chloride diffusion coefficient of concrete and their relationship." *Cement and concrete research*, 52, 131-139.

Yao, Y., Wang, L., Wittmann, F. H., De Belie, N., Schlangen, E., Eguez Alava, H., Wang, Z., Kessler, S., Gehlen, C., Yunus, B. M., Li, J., Li, W., Setzer, M. J., Xing, F., and Cao, Y. (2016). "Test methods to determine durability of concrete under combined environmental actions and mechanical load: final report of RILEM TC 246-TDC." *Materials and Structures*, 50(2), 123.

Zhang, B., and Wu, K. (1997). "Residual fatigue strength and stiffness of ordinary concrete under bending." *Cement and Concrete Research*, 27(1), 115-126.

Zhu, H. B., and Li, X. "Experimental research on residual strength of recycled aggregate concrete under compressive fatigue loading." *Proc., Advanced Materials Research*, Trans Tech Publ, 1379-1382.

Chapter 3 *Microcrack monitoring-based damage assessment and residual capacity of concrete*

3.1 Introduction

Damage to concrete is often associated with the formation of cracks, which causes not only degradation in the long-term durability of material, but also jeopardizes its functionality from a structural standpoint. Regardless of the cause of the cracking, it substantially affects the mechanical properties of the concrete, which in turn plays a key role in post-event behaviour of the damaged concrete. Evaluation of damage in the concrete from a material standpoint involves investigations into the initiation, progression and configuration of cracking in the microstructure to identify to what extent the material has deteriorated. This appraisal is of vital importance to provide understanding into deterioration and the failure processes of the concrete structures, particularly after a seismic event.

Several techniques have been used over the past 50 years to detect and to examine cracks in the concrete material. Commonly used methods are acoustic emission (AE) (Carpinteri et al. 2004; Ohno and Ohtsu 2010; Ohtsu et al. 2007), X-ray techniques (Landis et al. 2003; Mullins and Pearson 1949; Slate and Olsefski 1963), ultrasonic tomography (Hoegh et al. 2011) and computational tomography (CT) (Karihaloo and Jefferson 2001). Despite AE being an effective technique for analyzing damage, it is an active technique that measures the released energy during the material deformation process and as such is not used for post-event material assessment. X-ray methods can accurately show the level of cracking, but have limitations associated with bulky and expensive equipment, in addition to the detrimental side effects associated with radiation. In the case of CT scanning techniques, the sophistication of software required for analysis, and a lack of in-situ applications makes it difficult for practical purposes. Ultrasonic tomography mainly provides a general appreciation of damage, but cannot adequately reveal the microcrack network.

The most widely used microscopic techniques to examine the cracking in the concrete at microstructural level are scanning electron microscopy (SEM) and optical microscopy (Ollivier 1985). The key parameters in choosing the appropriate microscopic method are: the goal of the investigation, the level of the observation (micro, meso or macro), and the required resolution. SEM utilizes focused beams of electrons to capture images with a magnification varying from 15 times to over 50 000 times and can be used on specimens such as fragments, polished surfaces, or powders. These images provide a basis from which chemical composition, topographical variations, degree of hydration of cement and also morphological information about the specimen can be determined (ASTM C1723). SEMs are very specialized instruments that are typically expensive, large and requiring controlled operational environments. Samples used for SEM analysis need to be conductive and are usually coated with carbon, gold or iridium to allow for the proper imaging when the SEM is operated in high-vacuum mode. However, non-coated samples can be easily examined using variable pressure or low pressure capable SEMs. The optical microscopy method has drawn increasing attention as a low-cost practical type of examination with no need for highly advanced equipment. Hsu et al. (1963) conducted the very first stereoscopic microscopic study on thin concrete slices taken from axially loaded concrete cylinders. Although the geometrical characteristics of cracks were not reported, the method provided sufficient resolution to reveal cracking in cement paste and at the interface of coarse aggregate and mortar.

Fluorescent microscopy is similar to conventional light microscopy, with added features that enhance its capabilities to illuminate and produce more highly magnified images of a sample of interest. It is a very powerful tool that uses a much higher intensity light source compared with conventional optical microscopy (Murphy and Davidson 2012). The light source excites the fluorescent molecule, which then emits lower energy light with longer wavelength; this light, not the original light source, produces the magnified micrographs. The captured fluorescent optical micrographs allow the visualization of the location or pattern of fluorescence in microcracks that have been stained with fluorescent molecules. Fluorescent microscopy has shown great potential when reliable quantitative information about concrete is needed. Knab et al. (1984) reported one of the first applications of fluorescent microscopy on thin sections

for the study of the fracture zone in mortar. It has also turned into one of the standard methods for assessing capillary pores, and for the determination of water/cement ratios of hardened cement pastes and mortars (Gran 1995; Jakobsen and Brown 2006; Mayfield 1990). Litorowicz (2006) and Glinicki and Litorowicz (2006) implemented a fluorescent microscopy technique to examine development of crack patterns on impregnated samples damaged by freezing action. Shuguang et al. (2013) quantitatively examined microcrack characteristics on fluorescent-epoxy impregnated concrete that had suffered various degrees of alkali aggregate reaction (AAR) damage. In addition, a qualitative application of fluorescent microscopy for crack identification in concrete after uniaxial tensile testing has shown the efficiency of this method to visualize failure processes in concrete material (Alterman et al. 2011).

One of the objectives of this study was to investigate whether or not fluorescent microscopy is sufficiently robust and capable to detect the level of external load-induced damage and to provide further quantitative information on the geometrical features of microcracking, such as crack length and width. Because the majority of fluorescent microscopic work previously conducted has tended to focus on cracks induced by freezing or (AAR), there is a need to scrutinize cracks induced by different levels of external loading. Due to a lack of relationships for evaluating geometry-based damage parameters, it is desirable to develop a correlation between material degradation by virtue of the geometrical features of the damaged concrete, and the level of damage for concrete cylinders subjected to one excursion of compression loading. To assess damage as precisely as possible, the study was conducted on the relatively large petrographic thin sections covering a significant portion of the cross-sectional areas of specimen. The thin sections provided accurate and detailed information about the microstructural system of concrete and identified, by means of optical fluorescent microscopy, different types of microcraking at each stress level.

3.2 Experimental investigations

3.2.1 Materials, mixture proportion and specimen details

The concrete mixture used general purpose (GP) Portland cement with a water-to-cement (w/c) ratio of 0.56. Semicrushed Greywacke coarse aggregate with a maximum

size of 13 mm, and natural river sand with a fineness modulus of 2.76 were used in the mix. The quantities of the mix proportions per cubic metre of concrete could be found in Table 2-1. Concrete cylinders of height 200 mm and diameter100 mm were cast in steel moulds in three layers from a single batch and compacted using a vibrating table after pouring each layer. Cylinders were demoulded after 24 hours and then stored in a controlled fog room, at 20°C and 95–100% RH until the age of 90 days.

3.2.2 Uniaxial compression

To determine mechanical properties and stress–strain relationships of the concrete, three cylinders aged 90 days were prepared for compression test. Two PL-60-11 strain gauges (TML Tokyo) were attached in the axial direction and two strain gauges in the transverse direction on both sides of each cylinder to capture both axial and circumferential strains. The average of typical compressive behaviour of three concrete cylinders in uniaxial compression up to failure –axial strain, lateral strain and volumetric strain (the difference between axial strain and 2 × lateral strain) – plotted in section 2.2.3.

Having determined the stress–strain curves, the concrete specimens were subjected to uniaxial compressive loading at the rate of 2kN/s up to predefined load levels equal to 50%, 70% and 90% of the ultimate strength. Figure 3-1 shows the average stress–strain responses of three concrete cylinders subjected to 50%, 70% and 90% of the ultimate strength considering loading-unloading branches.

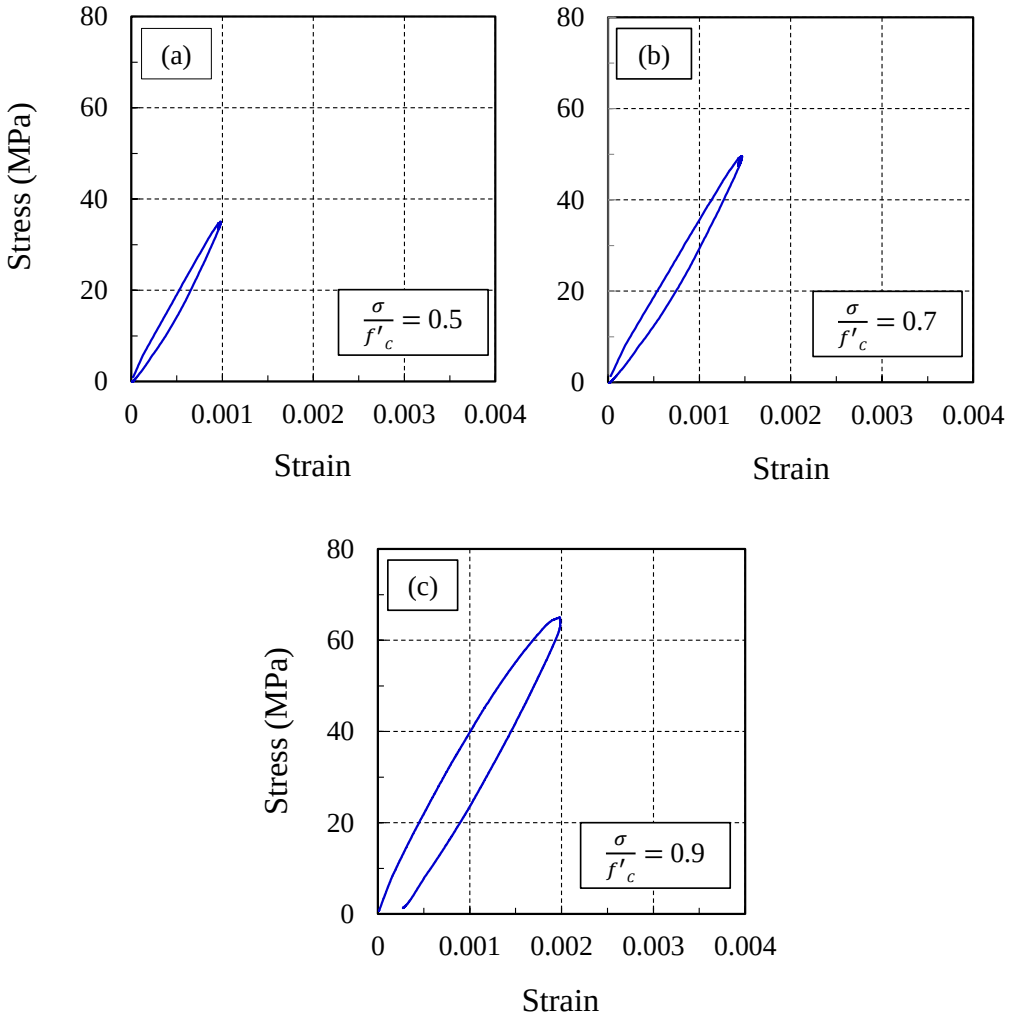

Figure 3-1 Stress–strain responses of concrete subjected to (a) 50%; (b) 70%; and (c) 90% of the ultimate strength

3.2.3 Sample preparation for microscopic investigations

In the current study a fluorescent epoxy vacuum-impregnation technique was implemented for the investigation of concrete microcracks through fluorescent microscopy. Special attention was paid to prevent the formation of any additional cracks over the entire specimen preparation process. For this purpose, once the concrete cylinders were unloaded, a concrete disk 25 mm in thickness was cut off from the mid-height of each of the damaged cylinders. The central portion of the cylinder was selected to supply concrete disks as it represents the highest damage status and also eliminated any end effect. The surfaces of the disks were ground and polished to

remove any residue of dust and irregularities, resulting in a smooth, flat surface. The disks were rinsed, cleaned and finally dried in an oven at 50°C until the difference between their two consecutive mass values became less than 0.1% of the greater value. The dried disks were placed in a vacuum chamber (desiccator) and subjected to a constant pressure of −100 kPa for 24 hours. Figure 3-3 shows the ingredients needed for fluorescent impregnation.

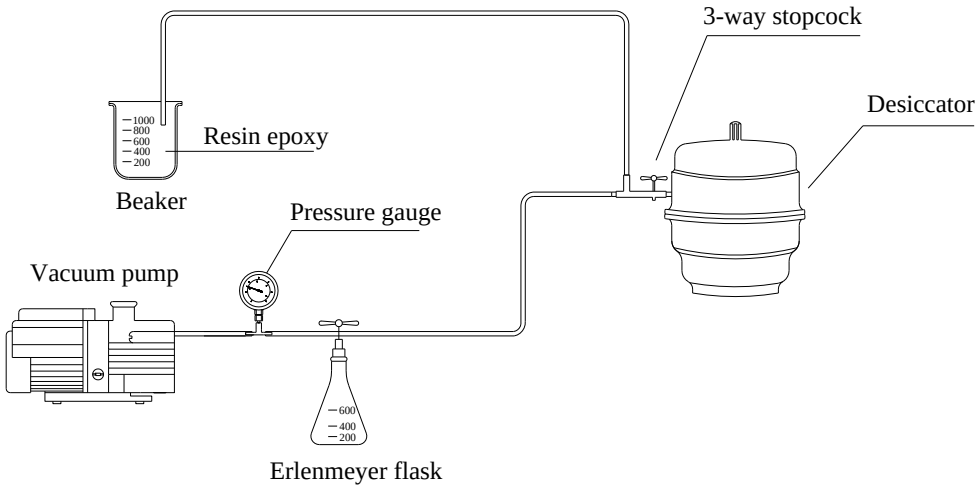

Figure 3-2 Configuration of vacuum impregnation

(a) (b) (c)

Figure 3-3 ingredients for fluorescent impregnation (a) fluorescent dye (b) epoxy resin (c) hardener

Five gram of fluorescent dye (Struers EpoDye) was added to a litre of low viscosity epoxy resin (Robnor RX771C/NC) and mixed in a beaker to achieve a

homogenous solution. The valve of the desiccator was opened, allowing the solution to enter the desiccator. The concrete disks were left in the desiccator for a day to let the epoxy penetrate into the cracks and other defects inside the disk (Figure 3-4a). In the next step, the negative pressure inside the chamber was released, the lid was removed and the hardener (Araldite HY951) with a mix ratio of 10:1 (resin to hardener) was added to the resin. The mix was thoroughly stirred with spatula and was put aside. The mix started to solidify in 40 minutes and was hard after about 2 hours. Before the solution completely hardened and while it was still somewhat sticky, the disk specimens were taken out and were allowed to dry completely. Once the excess resin on the surface of the specimen was removed by grinding, the specimens were transferred to an oven at a temperature of 50°C for 24 hours (Figure 3-4b). At this stage impregnated concrete disks were used to prepare petrographic thin sections in accordance with method given in ASTM C856 . An 8-mm thick section of concrete was then cut from the impregnated disks with a diamond saw and mounted on glass slides with dimensions of 76 mm × 51 mm (Figure 3-4c). The concrete thin sections were ground further until they reached a thickness of approximately 30 μm. Figure 3-4d shows the final status of a prepared thin section.

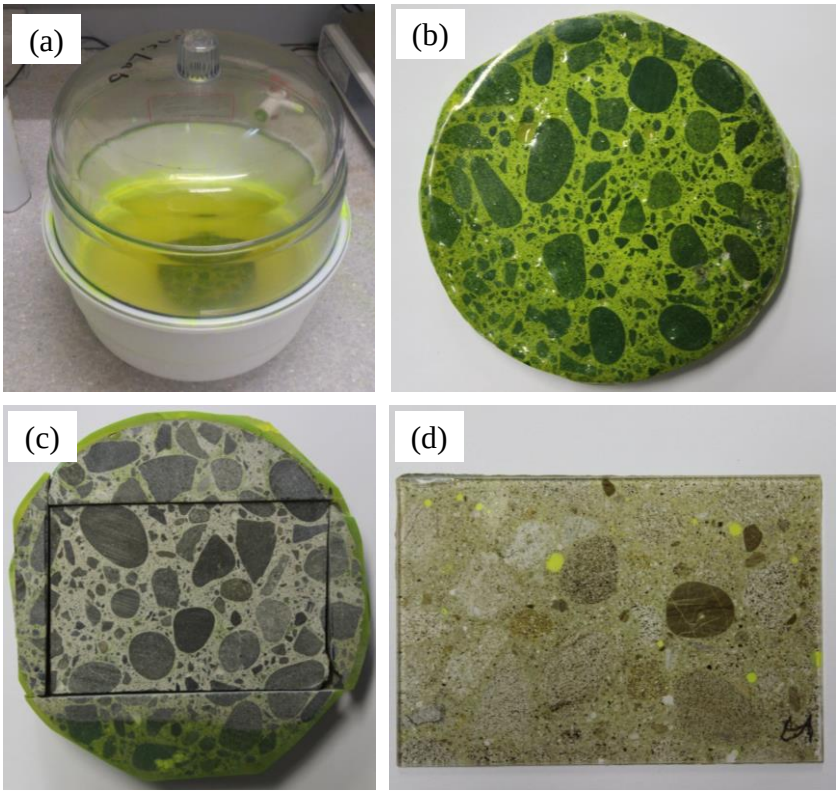

Figure 3-4 Immersed concrete disks in fluorescent dye solution (b) hardened epoxy-impregnated preloaded concrete disk (c) a sliver of concrete disk (d) epoxy-impregnated petrographic thin sections

3.2.4 Quantitative microscopic analysis

Digital photomicrography investigation was used for monitoring flaws inside the concrete. In this method a magnified digital image was taken of the concrete thin sections by using a stereomicroscope to visualize the internal structure of the concrete. Regarding the magnification at which the examination was carried out, a decision was made to partition the thin section into a number of regions of such a size that allowed analysis of each area. In the current study, a grid pattern on each slide was devised to sequentially investigate each region of 3.1 mm × 2.4 mm, as shown in Figure 3-5. This segment size allows the objects under the applied magnification to be easily viewed and provides reference areas for counting and locating the microcracks.

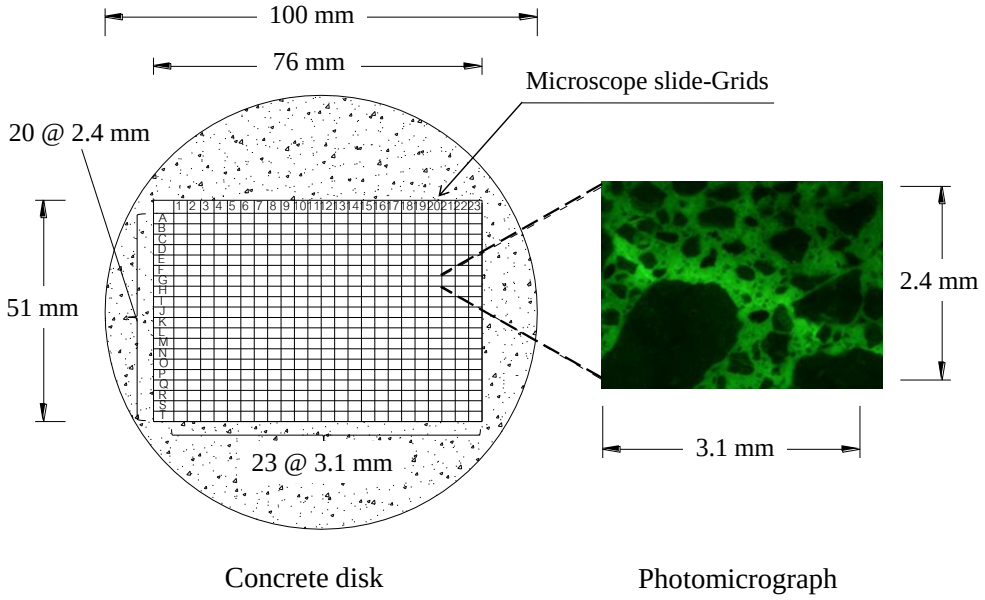

Figure 3-5 Microscopic slide partitioning

The impregnated petrographic thin sections were precisely scanned, segment by segment, at a total magnification of 40x (microscope objective with 4x magnification multiply by the ocular magnification caused by 10x eyepiece), which was sufficient to detect microcracks as narrow as 0.002 mm in width. Images were captured using NIS-Element F at the exposure time of 1/40s with enhanced contrast mode at highest quality to obtain the high resolution images. Contrast is one the camera's setting that affects dynamics of how the luminosity is rendered. There are several modes for different illumination (contrast) scene situations. In the case of fluorescence microscopy, the

contrast enhancement procedure sets a lower offset setting which creates a black background and thus helps to enhance the images thumbnails.

Figure 3-6 displays the set-up for the digital fluorescent microscopic investigations used in this work. Observations were performed with a stereo Nikon Eclipse 80i microscope using a fluorescence filter cube (B-2A) under blue excitation color with long-pass barrier and wideband excitation bandwidth (i.e., 30 to 50 nm). It is worth mentioning that, using a filter with blue color excitation results in blocking out the UV portion of the high pressure mercury lamp, so the visible blue light portion of the spectrum is used to excite the dye. To capture digital images, a PC-use control unit (DS-U2) along with a high-definition cooled 5 MP charged-coupled device color camera head (DS-5Mc) was used. Utilizing a 5 MP camera head allowed to record images with a resolution quality of 2560 pixels wide by 1920 pixels high. The images were stored sequentially in the computer using their unique tag named with a combination of letter and numbers. The letter denotes the horizontal row and the number indicates the vertical row (e.g., G17).

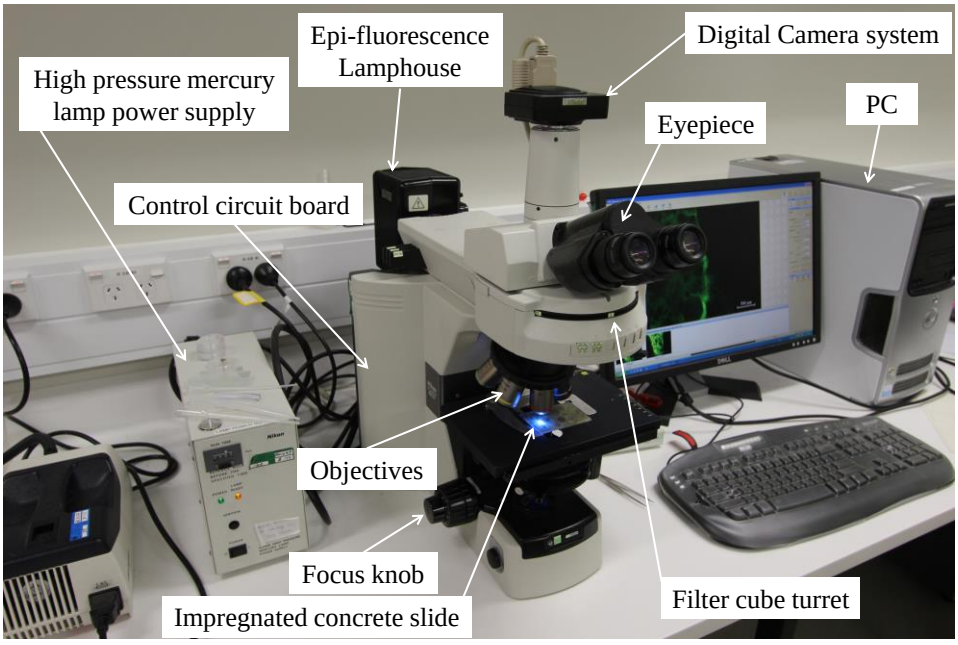

Figure 3-6 Fluorescent microscopic test set-up

Having captured all micrographs associated with each slide (460 micrographs), image processing followed using postprocessing software (Image Pro Plus). Prior to capturing micrographs, a calibration was conducted using a stage micrometer with 1 mm scale subdivided into 0.01 mm divisions (S8 Pyser-SGI), to provide a scale bar which is sufficiently accurate for subsequent physical measurements.

To determine the total length of cracking in each thin section, the lengths of any existing cracks in each individual micrograph were measured and stratified based on the average width dimension. This involves the capture of all images with a displayed calibrated scale bar during monitoring of every micrograph. To measure the length of crack in postprocessing software, first the length of the scale bar shown on the images needed to be measured. For this, a line was drawn over the entire length of the scale bar, and the length was found by the software in term of pixels. Since the physical length of the scale bar was already known (i.e., 500μm in this study), the equivalent length of each pixel in terms of mm was calculated, and entered and adjusted in the software (i.e., 0.0012 mm/pixel).

To measure the length of any chosen crack, a continuous line was drawn on the crack at appropriate intervals to follow its track between the start and end point as precisely as possible in the software. This allows the measurement of crack length in terms of pixels and finally converts to any desired unit of length (millimeter in this study). To measure the width of cracks, the same procedure was conducted and an average width was introduced. It is worth mentioning that, to avoid loss of some data during opening, editing or resaving, all images were saved in a lossless format of TIFF. Over the testing at four stress levels, 1840 micrographs were individually analyzed, as described earlier, to characterize the geometrical features of cracks.

It should be noted that, for the cases in which cracks were extended between adjacent micrographs, image stitching was performed in postprocessing software to combine multiple images with overlapping fields of view. To ensure the best match up for each pair of images, "full Fourier correction" technique, for tiling method was used. For stitching method, "gradient blend" technique was utilized to make a smooth weighted blend from one side of the overlapping tiles to the other. This results in reducing issues which is related to varying background intensities and providing smoothest edge transitions between tiles.

3.2.5 Microcrack formation and failure mechanism

The formation and evolution of microcracks in the concrete material is attributed to two main factors: mechanical loading or environmental factors connected with internal effects (e.g., carbonation, AAR, sulfate attack, freeze-thaw). Concrete suffers from microcracking even before the application of external loading. Differences in the mechanical properties of constituents as well as shrinkage can result in cracks at the interface of coarse aggregate and the bulk cement paste. The existence of these microcracks form weak points in the heterogeneous nature of the concrete, which result in low tensile strength. By applying external loading up to failure, new microcracks emerge predominantly from preexisting defects. Once microcracking occurs, four types of cracking can be distinguished: cracks at the interface between coarse aggregates and mortar (bond cracks), cracks in the cement paste (mortar cracks), combined bond and mortar cracks connected to each other when bond cracks are bridged by one or more mortar cracks (continuous cracks), and cracks through the aggregates. The occurrence of the latter is strongly dependent on the stiffness ratios and strength difference between cement paste and the aggregate. In the case where the aggregate stiffness is comparatively lower than cement paste stiffness, tensile splitting resistance of the aggregate is reduced, causing aggregates to crack.

For the purpose of damage evaluation, it is of vital importance to identify which categories the microcracks belong to, as it implicitly denotes the load/stress history the concrete experienced. Figure 3-7a shows the microstructural system of undamaged concrete. Microcracks that are isolated and not coalesced are indications of lower stress levels. The formation of bond cracks at the interface of coarse aggregates and the cement matrix is the first sign of damage, followed by the emergence of mortar cracks at higher level of loading (Mazars 1986, Perry and Gillott 1977) .The increase of bond cracks was not significant up to $0.5f'_c$, which corresponds to the upper bound of the linear part of the stress–strain curve (Figure 3-7b). At $0.7f'_c$, a marked increase in mortar cracks was observed, resulting in the appearance of continuous cracks (Figure 3-7c). At $0.9f'_c$, mortar cracks bridged nearby bond cracks, especially where the distance between coarse aggregates was small, which caused bond cracks to extend into the cement paste, leading to continuous cracks (Figure 3-7d). Interestingly, mortar cracks mostly bridged large aggregates compared to small aggregates, indicating that the

larger aggregate acquires the weaker bond strength, confirming the observation of (Alexander and Wardlaw 1960).

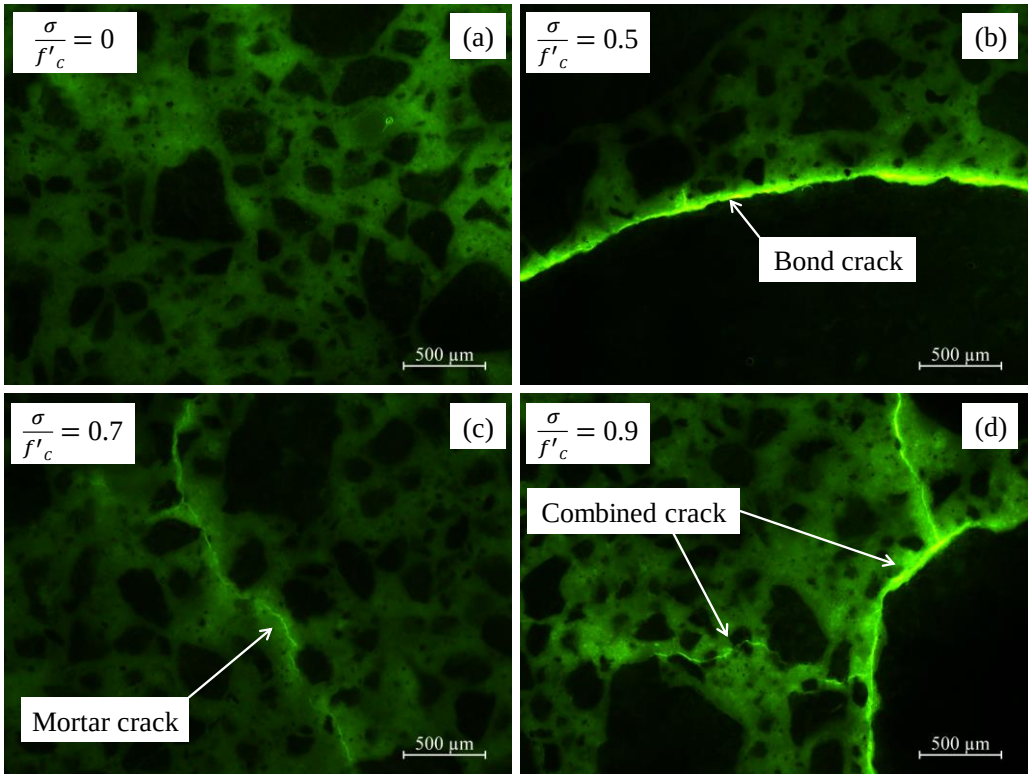

Figure 3-7 Micrographs of thin petrographic section illustrating microcracks maps at four stress levels (a) undamaged (b) 0.5f'_c (c) 0.7f'_c (d) 0.9f'_c

Tracing microcracks pattern at the maximum level of loading indicated that the load bearing capacity of the concrete degrades, mainly due to the growth of mortar microcracking. In other words, the development of mortar cracks is the key factor which leads to a deterioration of the concrete's capability to withstand external loading. Under this circumstance, the available consecutive load paths are no longer functional, which in turn alters load paths through the entire mortar, or partly through mortar and partly through aggregate. This causes a proliferation in cracking, which induces a decrease in the number of load paths. Such reductions incur extra stress and strain values on the remaining load paths, which are inadequate to carry the additional loading demand. A structural representation of this is the progressive increase in the curvature of the stress–strain curve in the vicinity of peak stress.

3.3 Damage assessment

3.3.1 Microscopic-based damage assessment

The evolution of the crack length and crack width with respect to different degrees of damage level is shown in Figure 3-8. As illustrated, with the increase in loading demand (level of damage), the crack width distribution shows a gradual move from cracks with smaller width towards cracks with greater width, leading to wider range of crack width. Figure 3-8a shows the distribution of crack width and associated crack length before the application of external loading. Although the concrete is mechanically undamaged, there are still a few microcracks, located particularly at the interface between coarse aggregate and mortar, with a maximum width of 0.0061 mm. The existence of these microcracks can be attributed to the paste shrinkage, which implies that the bond is the weakest link in the concrete material (Giaccio and Zerbino 1998, Grassl et al. 2010).

It is well known that the Interfacial Transition Zone (ITZ) between cement paste and aggregate is relatively porous with a high concentration of calcium hydroxide (CH) and a low proportion of calcium silicate hydrates (CSH) compared with the bulk paste (Scrivener et al. 2004). With increasing compression loading up to $0.5f'_c$, the microcracking increased significantly in length, width, and number (Figure 3-8b). The substantial increase in microcracking is associated with the point where the stress–strain curve begins to deviate from straight line. Despite increasing the level of loading to 70% of the ultimate strength, only a slight change in crack width was observed; however, the total crack length increased by 31% (Figure 3-8c). Figure 3-8d represents the distribution of crack width and length at the most severe condition investigated in the current study. As can be seen, significant growth in crack width and crack length occurred once the "critical stress" was reached, at 88% of the ultimate strength in this study. Beyond this threshold, the concrete volume starts to expand instead of contracting in compression, indicating the emergence of continuous cracks as discussed earlier.

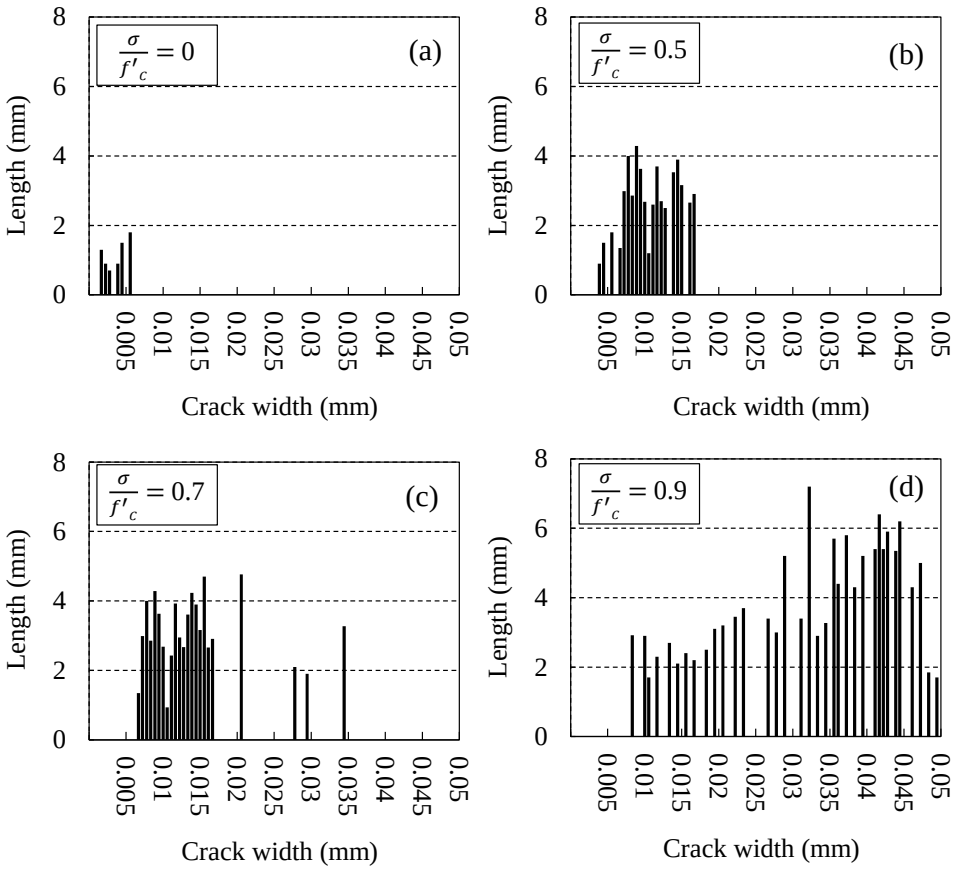

Figure 3-8 Distribution of microcracking

Figure 3-9 shows the cumulative distribution of microcracks, where each bar represents the percentage of the total length of microcracking accumulated at any particular bin over the range of measured crack width, at the four levels of stress. The value of each bar was determined by the ratio of total length of accumulated narrow bars stratified to each interval to the total length of microcracks observed in the thin section. For concrete in pristine condition, about 74% of microcracking acquires crack widths below 0.005 mm (Figure 3-9a). At $0.5f'_c$, 85% of the observed microcracks are concentrated between widths of 0.005 mm to 0.015 mm (Figure 3-9b). By increasing the stress level to $0.7f'_c$, the microcracks increase in width, though microcracks with crack width in the range of 0.01 mm to 0.015 mm are dominant (Figure 3-9c). Figure 3-9d shows microcrack width growth up to 0.05 mm in the case of applying $0.9f'c$. It can be seen that about 25% of microcracks belong to the category with width of 0.04 mm to 0.045 mm. Generally, the higher the level of damage, the greater the diversity in microcrack pattern that was observed.

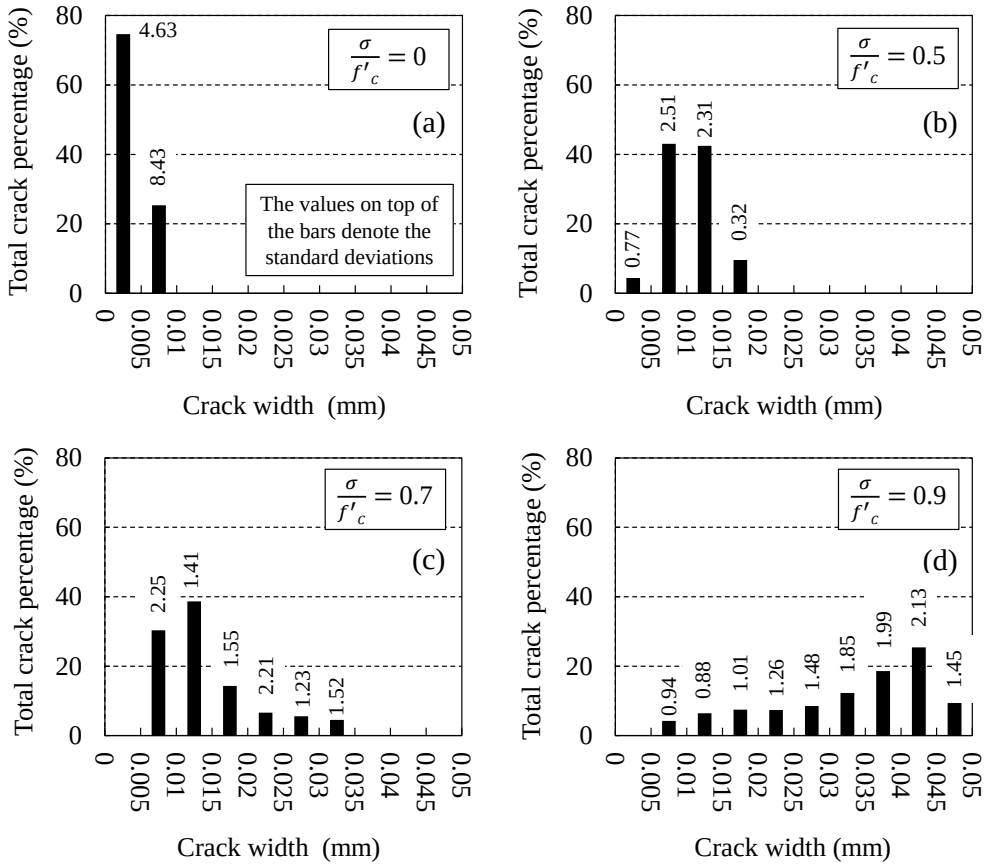

Figure 3-9 Cumulative distribution of microcracking

The relationships between the crack lengths, crack width and area of cracks, and the applied stress to strength ratio, are shown in Figure 3-10. The high determination coefficient (R^2) of relationships established between microcracks characteristics and level of damage, indicates that degradation in microcracks geometrical features, considered as microscopic parameters, provide a good quantitative indication of the damage incurred in the microstructural system of the concrete. To assess the accuracy of the predictions models, the standard error of the estimate is determined using Equation (3.1).

$$Err_{est} = \sqrt{\frac{\sum_{i=1}^{n}(Y_i - \hat{Y}_i)^2}{n}} \tag{3.1}$$

where Err_{est} = standard error of the estimate; Y_i = measured value of desired quantity (i.e., length, width or area of crack); $\hat{Y}_i$ = predicted value of desired quantity by the model; and n = number of pairs of data.

It can be seen that, all the microcracks geometric parameters increase with increasing level of damage induced by stress level with the greatest changes occurring from 0.5$f'c$ and higher. In spite of a slight change in the status of microcracks over the range of 0.5$f'c$ to 0.7f'_c, increasing stress level up to 0.7f'_c causes a concave in the graphs, implying a threshold beyond that a significant damage is expected to happen. At 0.9f'_c, a dramatic increase in geometrical characteristics of microcracks occurs which denotes for formation of continuous cracks. At this damage level, area of cracks shows the greatest increase compared to cracks width and length.

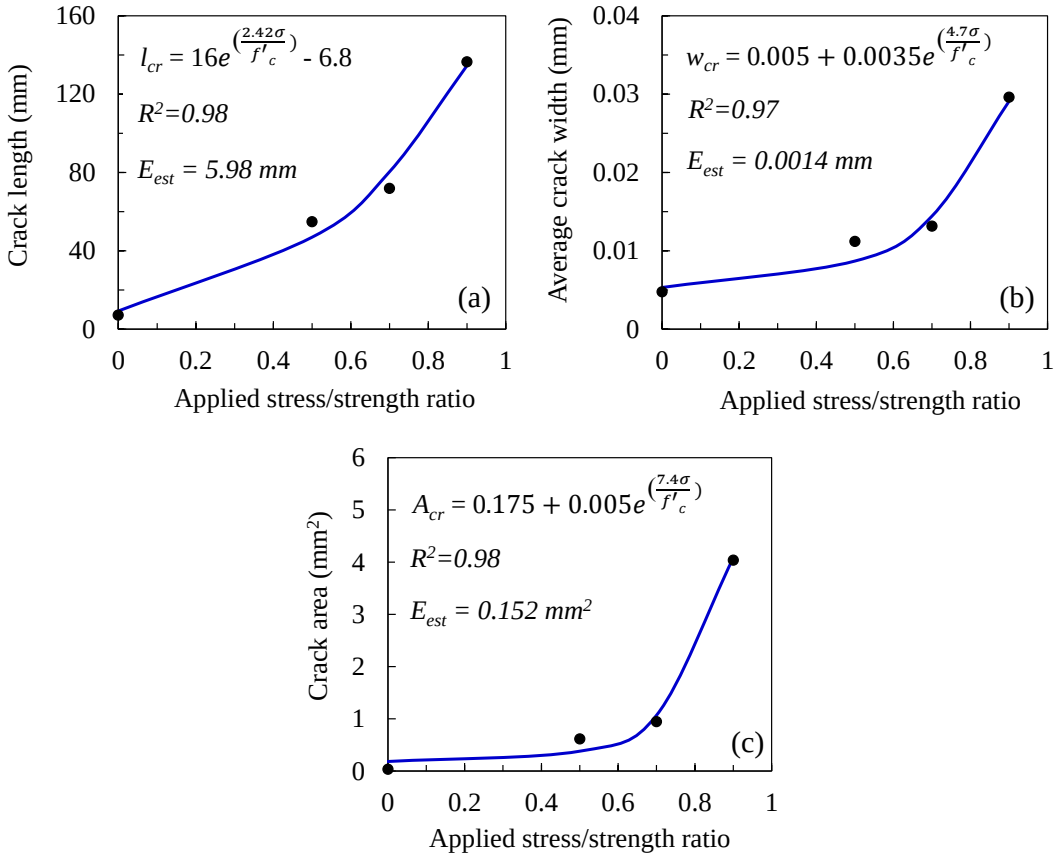

Figure 3-10 The relationships between microcrack characteristics and applied stress

3.3.2 Mechanical properties-based damage assessment

Compression tests were conducted on companion concrete cylinders, to correlate damage occurring in the micro structure of the concrete specimens – represented by change in the geometrical features of damaged concrete – to the degradation in its mechanical properties. This will allow the material characteristics of damaged concrete

at macro level, which is more relevant from the structural point of view, to be estimated through information obtained at micro level. For this purpose, the concrete cylinders previously subjected to one compression excursion and the same level of stress, were reloaded monotonically to failure to capture the post-event stress–strain relationships. They were instrumented using two axial and two transverse strain gauges (PL-60-11 TML), Figure 3-11 shows the stress–strain behaviours of predamaged concrete cylinders in comparison with intact specimen up to failure. The residual strength, even after experiencing 0.9*f'c*, showed almost no degradation compared to the ultimate strength of specimens loaded to failure without any previous damage. However, results associated with strain showed a maximum deterioration of 29% in the case of the cylinder subjected to 0.9*f'c*. The significant degradation in strain capacity was found to occur when the stress level exceeded 0.7*f'c*, the threshold above which combined microcracks are expected to be formed.

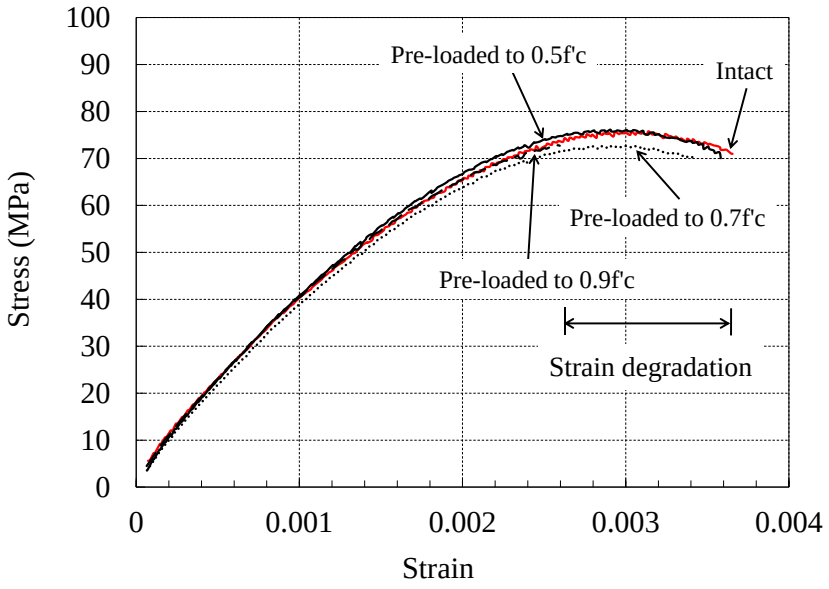

Figure 3-11 The effect of microcracking damage on residual capacity of companion concrete cylinders after reloading

Considering the area enclosed under the stress–strain response of the concrete cylinders as dissipated energy (Chrisp et al. 1993), the dissipated energy of hysteresis loop of pre-loaded concrete cylinders, as illustrated in Figure 3-1, was calculated. Table 3-1 summarizes the value of the dissipated energy, averaged for three specimens pre-loaded at each level of loading (i.e., 50%, 70% and 90% of ultimate

strength). The study showed that as the area of cracks increases, the associated dissipation energy also increases. This indicates the more the specimen is damaged, the larger hysteresis loop is produced.

Table 3-1 Dissipated energy calculated for three level of loadings

Stress/strength ratio	Dissipated energy (KJ/m^3)	Standard deviation	Coefficient of variation (%)
50%	3.631	0.782	21.5
70%	9.106	1.102	12.1
90%	24.821	1.074	4.32

3.3.3 Correlation between degradation in material properties and area of crack

A relative damage index based on increase in area of microcracks (DI_A) was introduced to represent load-induced damage in the geometrical characteristics of the damaged concrete. The damage index implicitly accounts for change in both the length and width of microcracking, as follows:

$$DI_A = \frac{A_{cr} - A_0}{A_{max}} \times 100 \quad (3.1)$$

where A_{cr} = area of microcracks at any damage level; A_{max} = the maximum area of microcracks (in this study measured at $0.9f'c$); and A_0 = area of microcracks at zero loading (intact). Using Equation (3.1), the concrete samples are considered undamaged when the area of microcracks under examination is equal to the maximum area of microcracks in its intact condition (DI_A = 0%). At fully damaged status, A_{cr} and A_{max} acquire large, identical values. This implies the denominator and numerator are approximately equal causing DI_A to tend to unity (DI_A = 100%). Nevertheless, it is practically impossible to measure the area of microcracks of fully damaged concrete, owing to disintegration; the proposed damage index is applicable for the level of damage observed in this study (below ultimate strength). Equation 3.2 represents a prediction model to estimate the residual strain capacity of damaged concrete in terms of DI_A, with a coefficient of determination (R^2) of 0.98.

$$\varepsilon_{res} = \varepsilon_{ult}\,(1.2e^{-0.28DI_A} - 0.2) \tag{3.2}$$

where ε_{res} = residual strain of the damaged concrete, ε_{ult} = ultimate strain of the intact concrete. As shown in Figure 3-12, the increase in DI_A results in strain deterioration. It should also be noted that the development of this model has been based on the current range of experimental results and may not be applicable for predicting ultimate failure in the postpeak area.

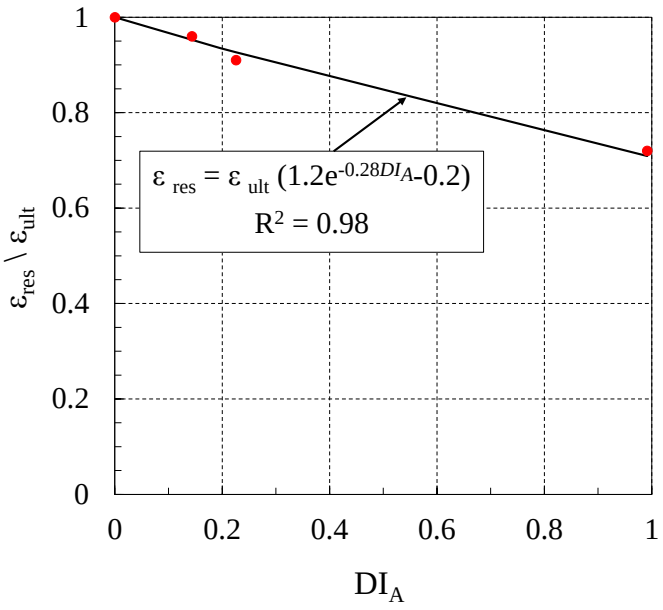

Figure 3-12 Residual strain prediction in terms of area of microcrack damage index

3.4 Conclusions

Based on the experimental outcomes and quantitative microcrack analysis reported in this chapter, the following conclusions can be drawn.

1. Using a fluorescent microscopy technique along with supplementary image analysis on petrographic thin sections it is possible to identify and also quantify the microcrack pattern. The applied impregnation method was successful in creating images with excellent contrast, which facilitated the quantitative analysis procedure. Observation of the thin petrographic sections in ultraviolet light using a stereomicroscope at a magnification of 4 times was sufficient to detect the microcracks.

2. Microcracks, attributed to environmental conditions and possible shrinkage of the cement paste, were present in the concrete prior to the application of load. Most of the preexisting crack widths were below 0.005 mm. At $0.5f'_c$, while bond cracks were clearly observed, no noticeable sign of mortar cracks were present. At $0.7f'_c$ the first mortar cracks were measured, indicating that mortar cracks develop in the range from $0.5f'_c$ to $0.7f'_c$. At $0.9f'_c$, bond cracking increased considerably and the coalescence of the microcrack network resulted in the formation of continuous cracks by bridging action between adjacent bond cracks.
3. Although the failure of concrete is attributed to the development of a network of microcracks due to the increase in the level of damage, the formation of continuous cracks does not by itself lead to loss in the bearing capacity of concrete. Concrete can still sustain considerable strain capacity beyond $0.9f'_c$ and retain its short-term stability, prior reaching the fracture point where the concrete cannot support further loading demand. Furthermore, the distribution of microcrack width showed that at $0.9f'_c$, microcrack width generally did not exceed 0.05 mm, which is still hard to identify without the aid of microscope.
4. The length, area and the width of microcracks all increased with an increase in level of damage. The investigation revealed a good correlation between the damage represented as geometrical characteristics of microcracks and the applied compressive stress.
5. Quantitative microcrack analysis is not only a powerful tool to evaluate damage in concrete but also provides a basis to quantify stress-induced damage by microcrack characteristics. Area of cracks, which implicitly accounts for length and width, is highly sensitive to stress-induced damage and could be used as an indicative parameter to assess the degree of damage in concrete members that were subject to loading.

3.5 References

Alexander, K., and Wardlaw, J. (1960). "Dependence of cement-aggregate bond-strength on size of aggregate." *Nature*, 187(4733), 230-231.

Alterman, D., Akita, H., Neitzert, T., and Alterman, J. "An Impregnation Technique for Crack Identification Following Uniaxial Tension Tests." *Proc., Advanced Materials Research*, Trans Tech Publ, 51-54.

ASTM C856 (2017). "Standard Practice for Petrographic Examination of Hardened Concrete. ." ASTM International, West Conshohocken, PA, .

ASTM C1723 (2016). "Standard guide for examination of hardened concrete using scanning electron microscopy." ASTM International, West Conshohocken, PA.

Carpinteri, A., Lacidogna, G., and Pugno, N. "Damage diagnosis and life-time assessment of concrete and masonry structures by an acoustic emission technique." *Proc., Proc of 5th int conf on fracture mechanics of concrete and concrete structures (FraMCos-5), Vail, Colorado-USA*, 31-40.

Chrisp, T., Waldron, P., and Wood, J. (1993). "Development of a non-destructive test to quantify damage in deteriorated concrete." *Magazine of Concrete Research*, 45(165), 247-256.

Giaccio, G., and Zerbino, R. (1998). "Failure mechanism of concrete: combined effects of coarse aggregates and strength level." *Advanced Cement Based Materials*, 7(2), 41-48.

Glinicki, M., and Litorowicz, A. (2006). "Crack system evaluation in concrete elements at mesoscale." *Bulletin of the Polish Academy of Sciences-Technical Sciences*, 54(4).

Gran, H. C. (1995). "Fluorescent liquid replacement technique. A means of crack detection and water: binder ratio determination in high strength concretes." *Cement and concrete research*, 25(5), 1063-1074.

Grassl, P., Wong, H. S., and Buenfeld, N. R. (2010). "Influence of aggregate size and volume fraction on shrinkage induced micro-cracking of concrete and mortar." *Cement and concrete research*, 40(1), 85-93.

Hoegh, K., Khazanovich, L., and Yu, H. T. (2011). "Ultrasonic Tomography for Evaluation of Concrete Pavements." *Transportation Research Record: Journal of the Transportation Research Board*, 2232(1), 85-94.

Hsu, T. T., Slate, F. O., Sturman, G. M., and Winter, G. (1963). "Microcracking of plain concrete and the shape of the stress-strain curve." *Journal of the American Concrete Institute*, 60(2), 209-224.

Jakobsen, U., and Brown, D. (2006). "Reproducibility of w/c ratio determination from fluorescent impregnated thin sections." *Cement and concrete research*, 36(8), 1567-1573.

Karihaloo, B., and Jefferson, A. (2001). "Looking into concrete." *Magazine of Concrete Research*, 53(2), 135-147.

Knab, L., Walker, H., Clifton, J., and Fuller, E. (1984). "Fluorescent thin sections to observe the fracture zone in mortar." *Cement and concrete research*, 14(3), 339-344.

Landis, E. N., Nagy, E. N., and Keane, D. T. (2003). "Microstructure and fracture in three dimensions." *Engineering Fracture Mechanics*, 70(7), 911-925.

Litorowicz, A. (2006). "Identification and quantification of cracks in concrete by optical fluorescent microscopy." *Cement and concrete Research*, 36(8), 1508-1515.

Mayfield, B. (1990). "The quantitative evaluation of the water/cement ratio using fluorescence microscopy." *Magazine of Concrete Research*, 42(150), 45-49.

Mazars, J. (1986). "A description of micro-and macroscale damage of concrete structures." *Engineering Fracture Mechanics*, 25(5), 729-737.

Mullins, L., and Pearson, H. (1949). "The X-Ray Examination of Concrete." *Civil Engineering and Public Works Review*, 44(515), 256-258.

Murphy, D. B., and Davidson, M. W. (2012). *Fundamentals of Light Microscopy and Electronic Imaging*, John Wiley & Sons, Hoboken, NJ, USA. .

Ohno, K., and Ohtsu, M. (2010). "Crack classification in concrete based on acoustic emission." *Construction and Building Materials*, 24(12), 2339-2346.

Ohtsu, M., Isoda, T., and Tomoda, Y. (2007). "Acoustic emission techniques standardized for concrete structures." *Journal of Acoustic Emission*, 25, 21-32.

Ollivier, J. (1985). "A non destructive procedure to observe the microcracks of concrete by scanning electron microscopy." *Cement and Concrete Research*, 15(6), 1055-1060.

Perry, C., and Gillott, J. (1977). "The influence of mortar-aggregate bond strength on the behaviour of concrete in uniaxial compression." *Cement and Concrete Research*, 7(5), 553-564.

Scrivener, K. L., Crumbie, A. K., and Laugesen, P. (2004). "The interfacial transition zone (ITZ) between cement paste and aggregate in concrete." *Interface Science*, 12(4), 411-421.

Shuguang, L., Yihui, L., and Gaixin, C. (2013). "Quantitative damage evaluation of AAR-affected concrete by DIP technique." *Magazine of Concrete Research*, 65(5), 332-342.

Slate, F. O., and Olsefski, S. "X-rays for study of internal structure and microcracking of concrete." *Proc., Journal Proceedings*, 575-588.

Chapter 4 *Damage assessment and residual capacity of confined and unconfined concrete subjected to low-cycle fatigue*

4.1 Introduction

Assessment of damage and residual capacity of concrete material after an earthquake is a crucial task. The evaluation provides invaluable piece of information on possible deterioration in mechanical properties of the constituent material (i.e., strength, stiffness, deformation and energy dissipation) which is of vital importance for any further analytical or numerical analyses associated with the component or system level. The residual capacity of concrete material is not unique and depends on previously applied cyclic loading history. Therefore, there is a need to assess post-event residual capacity and damage in a standardized way.

Erberik and Sucuoğlu (2004) showed that earthquake-induced damage in RC buildings can conveniently be investigated in the context of low-cycle fatigue. That is because, low-cycle fatigue concept denotes to application of a few number of load cycles which are sufficiently significant to incur plastic deformation in the specimen. In terms of the number of cycles, Hsu (1981) ascribed low-cycle fatigue to the range of loading cycles from 1 to approximately 1000 cycles, to which an RC building may be subjected during earthquakes over its lifespan.

With respect to remaining strength and deformation capacity of previously cyclically loaded concrete specimens, limited studies are avaible in the literature. Mehmel and Kern (1962) found that the strength of concrete improves by 10% if the concrete specimens are subjected to a limited number of low intensity compressive cycles. Bennett and Muir (1967) reported a 1% to 23% increase in strength with an average of 11% after repetition of 1 million cycles at a stress range of 0.66–0.71f'_c. Note that although the applied stress level was high, the magnitude of stress level was small. A study conducted by Awad (1971) on prism specimens showed only a 5%

increase at a fatigue life ratio of 0.3, and 0.9% and 5% decrease at fatigue life ratios of 0.6 and 0.9, respectively. Observations by Ballatore and Bocca (1997) on cored cylinders tested at stress levels of 0.02 to 0.2f'_c also showed 10% to 15% increase in strength, and degradation values of 22% and 86% in deformability, dependent on the concrete mix. Most recently, Kontani et al. (2016) reported 1% to 9% increase in residual strength of concrete specimens previously cyclically loaded between 0.05 to 0.33, 0.65 and 0.75f'_c.

In this chapter the post-event investigation on remaining mechanical capacity, as well as the change in the permeability feature of the confined and unconfined damaged concrete cylinders subjected to low-cycle fatigue loading is presented for the first time. The information provided can help to form a basis to determine whether damaged concrete can undergo further loading demand to aid in the prediction of residual capacity of RC members.

4.1.1 Background to fatigue damage

Fatigue damage denotes the deterioration in the mechanical properties of the concrete under reversals of loading. This is mainly attributed to the formation, growth, coalescence and propagation of microcracking in the microstructural system of the concrete. Concrete substantially consists of various flaws and microcracks, formed in the hydration and/or shrinkage process. Having loaded concrete, the stresses at the tip of these internal microcracks have a great tendency to extend and eventually exceed the cohesive strength of cement paste or the interfacial transition zone (ITZ). In fact, failure is caused by localization of damage at or near the peak load, which disturbs the uniform distribution of strain along the length of concrete specimen. After localization, stress–strain behaviour is governed by continuous damage accumulation in the damage zone (Mu et al. 2004).

In the case of plain concrete, literature shows some inconsistencies with respect to stress limit below which no fatigue failure occurs. Nordby (1958) reported 47–60% of ultimate strength (f'_c) as a threshold stress level in this regard; however, Karsan and Jirsa (1969) considered 0.63f'_c as a fatigue limit, where stresses exceeding that may cause failure. Currently, it is generally accepted that stress level of about 0.75f'_c is liable

to cause significant changes in the properties of concrete (L'Hermite 1954; Newman 1968; Jones 1968).

4.1.2 Current indirect methods for fatigue damage assessment

During cyclic loading, the propagation and growth of internal microcracking causes a progressive and permanent damage to the microstructural system of the concrete. Damage jeopardizes the integrity of the concrete and consequently results in a significant increase in the irrecoverable strain. Degradation in the mechanical properties is an indication of such breakdown, which is exacerbated as the number of cycles increases. The deterioration process, however, may leave no visible damage at macrolevel before failure. Although it is well accepted that material degradation associated with fatigue damage is related to the emergence of microcracking, the precise and direct measurement of microcracks is still hard and requires huge effort. Thus, the importance of using a reliable testing method to assess the damage indirectly, by measuring the alteration in the microstructural system of the material, is highlighted.

To date, different types of diagnosis tools have been used to indirectly assess fatigue damage in the concrete. In indirect methods, the degradation in mechanical properties of the concrete under fatigue loading is investigated by change in an appropriate indicator of the test. Muguruma and Fumio (1986) employed Acoustic Emission (AE) techniques to examine the local fracture of concrete cylinders subjected to low-cycle fatigue tests. The AE technique was also used by Shah and Kishen (2012) to study the fatigue behaviour of concrete under variable and increasing amplitude. Findings showed that the number of AE events, as an indicator of damage, increases with crack growth towards incipient fatigue failure. The drawback with using this technique is that AE is a passive technique, which means it is only applicable for real-time monitoring when concrete is under loading; it does not allow for post-event damage assessment. The applicability of ultrasonic (US) techniques to capture the process of fatigue in concrete has also been investigated in the past (Wagner et al. 2012; Urban et al. 2014). Using this technique, the reduction in US velocity is representative of internal fatigue damage of the concrete.

The fatigue damage of concrete may also be examined from a durability perspective. Gontar et al. (2000) implemented a chloride-permeability testing technique

to investigate the effects of high-amplitude cyclic flexural loading on the chloride penetration of notched concrete beams at a frequency of 1Hz. A study conducted by Fu et al. (2016) showed that regardless of the magnitude of loads, fatigue damage accelerates the chloride penetration in concrete by a factor of 1.5–3.0. Tawfiq et al. (1996) measured the real-time air-permeability of the single-edge notched beams under cyclic loading. Results showed that in the stressed zone, the permeability values decrease exponentially as the number of cycles increases. The application of water permeability was also examined by Desmettre and Charron (2013); however, the self-healing phenomenon that occurred in the presence of water mitigated some of the microcracking damage caused by cyclic loading.

A review of the literature shows paucity of information on the state of the art on residual capacity and permeability-based damage assessment of confined and unconfined concrete using low cycle fatigue approach. With the aim of providing further information, this chapter reports the results of experimental investigations to address the following objectives (1) to characterize the behaviour of confined and unconfined concrete under monotonic loading; (2) to establish a life cycle diagram (*S-N curves*) along with an investigation into the effect of confinement on fatigue life; (3) to study the evolution of damage in terms of degradation in the mechanical properties of concrete as well as variation of temperature over the low-cycle fatigue life of the specimens; (4) to estimate the post-event residual capacity of concrete material using a monotonic compression test up to failure on the concrete samples, which had previously experienced fatigue damage up to certain levels of their fatigue life at different stress levels; (5) to assess damage on the basis of the change in the microstructural system of the concrete using a permeability test; and (6) to make a correlation between material degradation and observed damage.

4.2 Experimental program

4.2.1 Unconfined concrete cylinders

The concrete mix design and casting process for unconfined concrete specimens was similar to the concrete used for specimen described in chapter 2.

4.2.2 Confined concrete cylinders

SikaWrap® Hex-100 G, classified as glass-fibre reinforced polymer (GFRP), was used as a wrapping fabric. It is a unidirectional, woven, glass-fibre fabric, designed for installation using the wet application process mainly targeting the structural strengthening of reinforced concrete. Table 4-1 provides the technical reported data of the GFRP sheets in the longitudinal direction of the fibres, provided by the supplier.

Table 4-1 Properties of GFRP fibre sheets as provided by Manufacturer

Nominal thickness (mm)	Fibre density (kg/m^3)	Tensile strength (MPa)	Ultimate tensile strain (%)	Elastic modulus (GPa)
0.359	2540	2276	2.8	72.4

Two parameters needed to be checked at the time of wrapping: the moisture content of the surface of the concrete cylinders, which is suggested to be less than 4%, and the ambient temperature, which should exceed the dew point. The concrete cylinders were taken from the fog room once they were 90 days old, and stored at room temperature for two weeks. The surface humidity was measured using a Proceq moisture meter to ensure it met the criterion, otherwise there might have been a risk of the fabric not fully bonding to the concrete surface. Figure 4-1 shows the preparation process of GFRP-confined concrete cylinders.

The GFRP fabric sheet was cut into rectangular strips (1000 mm × 300 mm). This length was enough to provide two continuous wrap layers around the perimeter (471mm) of each sample, with an overlap of 60 mm over second round (Figure 4-1a). A two-component high-strength, high-modulus and moisture-tolerant epoxy impregnation resin (Sikadur Hex-300) was used in this test. To saturate GFRP fabrics, 1490 g resin (part A) and 510 g hardener (part B) were thoroughly mixed. Strips of GFRP were laid down with onto the working table and resin was spread out back and forth continuously on both sides to facilitate the penetration of resin into the fabrics. The perimeter surface of the cylinders, which had already been cleaned, was also coated before attaching the GFRP fabric. It is worth mention that, before wrapping fully saturated GFRP fabrics around the precoated concrete cylinders, all possible voids

remaining on the surface of cylinders were filled with a mixture consisted of the same proportion of part A and part B as well as equal volume of hydrophilic fumed silica (Aerosil 200) (Figure 4-1b). The wrapped specimens were maintained at room temperature for one year (Figure 4-1c).

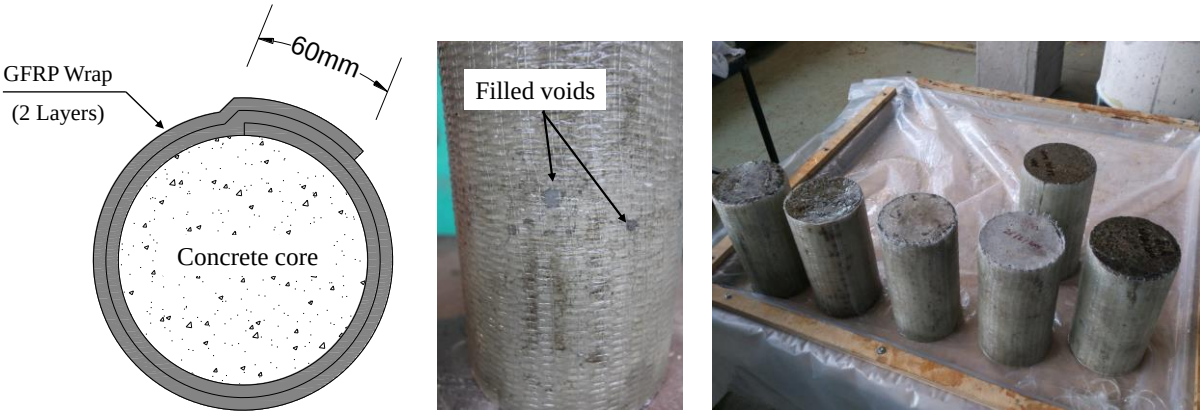

Figure 4-1 Preparation of GFRP-confined concrete cylinders (a) Overlapping layout (b) Filling voids (c) Wrapped specimens

4.2.3 Testing apparatus and instrumentation

A servo-hydraulic testing machine with a capacity of 2500 kN was used for the fatigue tests. The testing apparatus and data acquisition system allowed the application of various types of loading protocols (waveforms), loading frequencies and readings of axial deformations of the specimens, up to a frequency of 300 Hz.

The laser-distance sensor, used for capturing strain in the concrete, was compared with conventional stain gauges to verify it's suitability for use in this investigation. Two cylinders were incorporated with two axial and two circumferential strain gauges (PL-60-11 TML), which were attached to the surface of the cylinders using cyanoacrylate CN-E adhesive. Prior to attaching the strain gauges, and once the surface was sanded and any dirt or residue removed, a two-component, PS polyester adhesive was used as a precoating substance to provide a smooth surface. For the companion cylinders, no specific preparation was needed and the axial deformations were measured using three laser-distance sensors which were positioned every 120° around the specimen. Compression tests on the concrete cylinders showed, before peak

strength, the stress-strain responses obtained from both instruments were in excellent agreement. However, for the post-peak region, because of the intensive rate of change in strain and the need for super-fast communication between strain gauge logger and machine, it is practically impossible to capture the associated behaviour using strain gauges in spite of a displacement-control platform.

It should be noted that after the peak stress, significant amounts of cracking and damage occur, particularly in the midheight of the cylinder where the strain gauges are attached. The damage in the midheight is responsible for stress concentration and subsequently breakage of the strain gauges, leaving no opportunity to measure the strain. But, in the case of laser-distance sensors, even after formation of severe cracks, and delamination and spalling of the surface concrete, the sensors are still functional. The capability of laser-distance sensors allows precise and continuous measurement of the entire stress-strain behaviour. Additionally, data recorded by virtue of this technology are associated with the global behaviour of concrete samples as the laser measures the displacement between upper and bottom jaw plates (total length of the specimen) while information associated with strain gauges are limited to local strain readings.

The available advanced measuring technique showed promise of gaining not only more accurate data, but also obtaining enough information in the post-peak region compared with earlier investigations. Thus, the measurements for all experiments were conducted using laser sensors; the only limitation, however, of using laser sensors is their inability to measure transverse strain, which was out of the scope of this study. In addition, the temperature of the specimen's surface was also measured at top, mid and bottom points of each cylinder using three infrared thermometers. Figure 4-2 shows the test set-up, including the instrumented specimen.

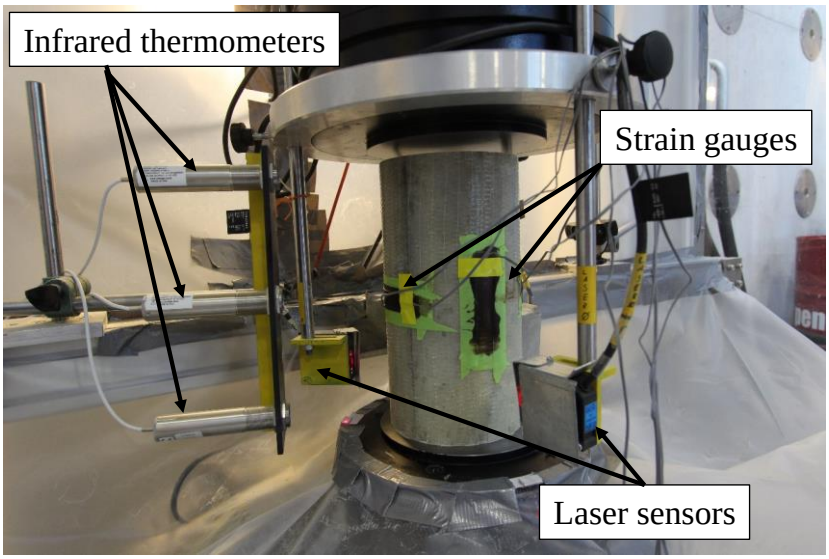

Figure 4-2 Compression test and measurement set-up

4.2.4 Compression test-monotonic behaviour

Conducting monotonic compression test was essential as it provides a benchmark for subsequent comparisons to be made with damaged specimens. The compression test was conducted to precisely characterize monotonic behaviour of specimens. The concrete ultimate strength (f'_c), was calculated, based on the mean value of compressive strengths of three cylindrical specimens. The reference cylinders from the same batch were tested, just prior to commencing the fatigue testing, under monotonic displacement-control at the rate of 0.01 mm/s. The ultimate strength values were found to be 52.2 MPa and 86.3 MPa for unconfined and confined concrete specimens, respectively.

4.2.5 Fatigue test

Fatigue loading was applied as a sinusoidal waveform with a frequency of 0.5 Hz. The rate of loading was decided on as a compromise between cyclic loading under static condition and the total time needed to complete the experimental test campaign. The change in displacement was measured continuously over the test at a rate of 10 times per second. This was found to provide accurate and sufficient samplings with respect to the loading frequency in the range of the maximum and minimum stresses (σ_{max}, σ_{min}). The minimum stress level was kept constant for all the fatigue tests for

both confined and unconfined concrete cylinders at $0.01f'_c$. With respect to maximum compressive stresses, three levels, $0.75f'_c$, $0.85f'_c$ and $0.95f'_c$, were considered in this study. The fatigue tests were started with a force-controlled preloading at a constant loading rate of 4 kN/s until the average stress (σ_{ave}) was reached. Then cyclic loading followed, the sinusoidal pattern alternating between maximum and minimum stresses with an amplitude of $(\sigma_{max} - \sigma_{min})/2$ as shown in Figure 4-3. Table 4.2 presents the tests matrix, fatigue loading characteristics, number of fatigue tests and results related to the total number of cycles to failure.

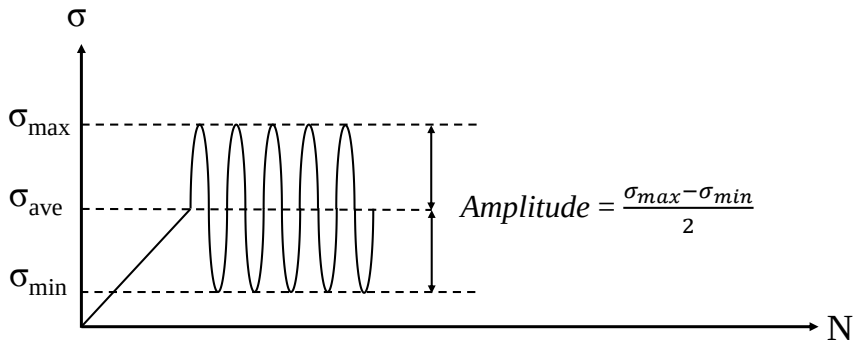

Figure 4-3 Loading protocol

4.2.6 Compression test - Residual capacity

Having determined the total number of cycles to failure for each type of specimen at the desired stress levels, the new series of specimens were subjected to 30%, 50%, 70% and 90% of the number of cycles required to obtain fatigue life. This allowed the degradation process in the form of damage in strength and strain capacity to be traced throughout the fatigue life at stress levels of 0.75f'c, 0.85f'c and 0.95f'c. Compression tests were, subsequently conducted on the specimens previously subjected to pre-defined ratios of fatigue life, to capture the monotonic stress–strain relationships associated with damaged specimens up to failure. Comparing the compressive behaviour of intact (benchmark) and damaged specimens, the remaining load–deformation bearing capacity of cyclically damaged specimens were determined, as will be discussed later.

Table 4. 2 Fatigue test matrix and loading characteristics

Stress level	Unconfined concrete cylinders							Confined concrete cylinders				
σ_{max}/f'_c *or* σ_{max}/f'_{cc}[a]	F_{max} (kN)	F_{min}[b] (kN)	Amp (kN)	F_{ave} (kN)	Specimen	$N_{f,i}$[c]	N_f[d]	F_{max} (kN)	F_{min} (kN)	Amp (kN)	F_{ave} (kN)	Specimen
0.95	876	9	433	442	1 2 3	46 37 63	49	1443	15	714	729	1 2 3
0.90[e]	830	9	410	419	1 2 3	184 158 217	187	1367	15	676	691	1 2 3
0.85	784	9	387	396	1 2 3	511 543 468	501	1291	15	638	653	1 2 3
0.75	692	9	341	350	1 2 3	2001 1912 1809	1908	1139	15	562	577	1 2 3

Note: F_{max} = maximum applied force; F_{min} = minimum applied force; Amp = amplitude of loading; F_{ave} = Average of applied force; N_f = number of cycles to failure.

[a]f'_c and f'_{cc} denote the mean value of compressive strengths of three unconfined and GFRP-confined concrete cylinders.

[b]Calculated based on minimum stress level equal to 0.01 f'_c for unconfined and $0.01\,f'_{cc}$ for confined cylinders.

[c]The number of cycles associated with each specimen.

[d]The mean value.

[e]This level of stress was considered just to capture more data point for *S-N* curve and no further investigation was conducted.

1

4.2.7 Oxygen permeability test

In an attempt to indirectly assess fatigue damage through changes occurring in the microstructural system of the concrete, an oxygen-permeability testing technique was employed. After applying fatigue loading at predefined level of fatigue life similar to the levels considered for the residual capacity test, but only at stress levels equal to $0.85f'_c$ and $0.95f'_c$, the specimens were unloaded and cut into three equal pieces. A diamond core bit with nominal outer diameter of 100 mm was then used on the core drill machine to take cores perpendicular to the surface of the middle piece of each specimen (Figure 4-4a). Two concrete disks, 25 mm in thickness and 93 mm in diameter, were then sawn with an accuracy of 0.1 mm from the central part of each core. For permeability measurement, the disks were oven-dried at 50°C until the disks reached a steady state moisture content where the difference between their mass measured between two consecutive days was less than 0.1% (Figure 4-4b). It should be noted that the photo was just taken after cutting to show how the disks look like at this stage while further works for smoothing the surface by means of rubbing stone and sand paper were carried out to come up with fine finish of the surface. The procedure to calculate the coefficient of permeability has been previously described in section 2.2.5.

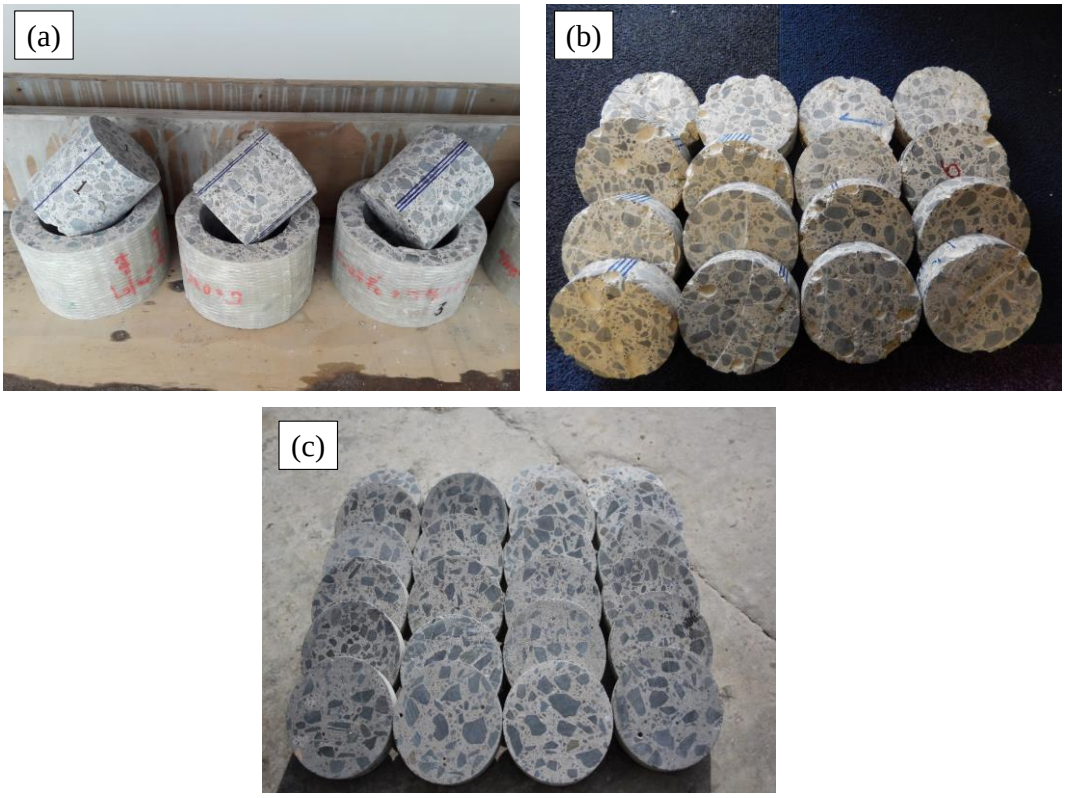

Figure 4-4 (a) Cored cylinders (b) Concrete disks (c) prepared concrete disk

4.3 Results and discussion

4.3.1 Monotonic compression test

The average stress–strain behaviours for both GFRP-confined and unconfined concrete specimens is provided in Figure 4-5a. While unconfined concrete specimens showed softening after reaching the peak stress, f'_c, confined concrete showed strain hardening once stress levels exceeded the strength of confined concrete at the onset of the pseudo-plastic branch, f_p. This resulted in significant increase in ductility and load-bearing capacity, which means the level of confinement provided was high enough for continuous increasing pressure on the core concrete until the rupture of GFRP. The confined concrete showed bilinear behaviour, in which the slope of the first branch is similar to plain concrete. The behaviour of confined specimens in the first part is mainly attributed to the mechanical properties of core concrete, while in the second branch, the properties of GFRP sheets play a fundamental role. In the first branch, the bond between concrete and wrapped material is functional, which ensures the integrity of

specimens, whereas in the subsequent branch the core concrete is damaged and the tensile strength of GFRP allows for extra load-deformation capacity. Moreover, no indication of sliding of GFRP layers occurred during testing, which is a big advantage of continuous wrapping. Figure 4-5b illustrates the implementation of a bilinear approach to characterize the behaviour of confined concrete. For the number of confining layers considered in this study, the ultimate GFRP-confined strength of concrete (f_{cu}) increased from an average value of 52.2 MPa to 86.2 MPa –an increase of about 65%. However, the confined strength of concrete was 32% greater than the strength of confined concrete at the onset of the pseudo plastic branch (f_p). This demonstrates that merely two layers of wrapping have a significant influence at increasing compressive capacity of concrete cylinders. It can be also shown that the ultimate strain of confined concrete (ε_{cu}) increased about 6 times compared to the strain of confined concrete at the onset of the pseudo-plastic branch (ε_p). In terms of ultimate strain endured by both types of specimens, the confined concrete allowed for an average strain value of 0.0183, that is, about 74% more strain capacity compared with the average strain value of unconfined concrete (0.0105). The tangent modulus of confined concrete in the pseudoplastic branch (E_p) decreases markedly to about 7.1% of the tangent modulus of confined concrete in the first branch (E_c). This confirms the results of a study conducted by Valdmanis et al. (2007), which found that the tangent modulus in the second branch is between 7.6% and 20% of the tangent modulus in the first branch.

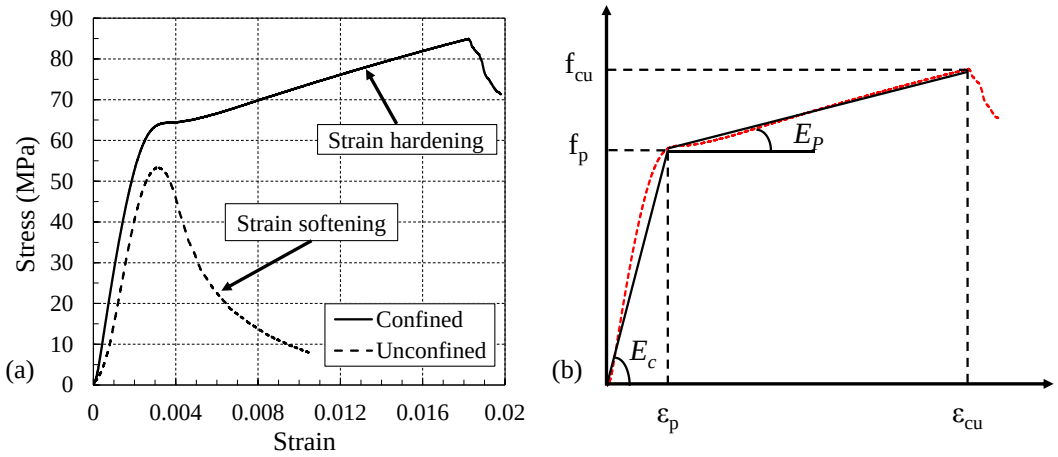

Figure 4-5 (a) Experimental stress–strain curves for confined and unconfined concrete (b) bilinear illustration of stress–strain relationship of confined concrete

4.3.2 Fatigue test-life

The number of cycles that concrete specimen endured to failure (N_f) is referred to as fatigue life (Graf and Brenner 1934). The value of N_f was found to be influenced by the loading frequency, loading conditions and characteristics of concrete specimens (Mordock 1965). The relationship between the fatigue life of concrete and the stress level is conventionally displayed in logarithmic scale graphs and referred to as *S-N* curves (or *Wöhler* curve). Generally, the applied stress is normalized to ultimate static strength, resulting in an *S-N* curves which is believed to be independent of the concrete strength, specimen shape, age and the moisture conditions (Hsu 1981).

The average test results used to predict the fatigue life of both confined and unconfined concrete specimens under cyclic compression are shown in Figure 4-6. It can be seen that the effect of stress level on the fatigue life of concrete is significant: the fatigue life decreased with increasing stress level. Unlike the beneficial effect associated with ultimate strength and strain, confinement was found to have little influence very on the fatigue life of the concrete. Equations 4.1–4.2 express the best prediction model for the fatigue life of both unconfined and confined concrete specimens, as follows:

$$\frac{\sigma}{f'_c} = -0.055\ln(N_f) + 1.176 \tag{4.1}$$

$$\frac{\sigma}{f'_{cu}} = -0.05\ln(N_f) + 1.144 \tag{4.2}$$

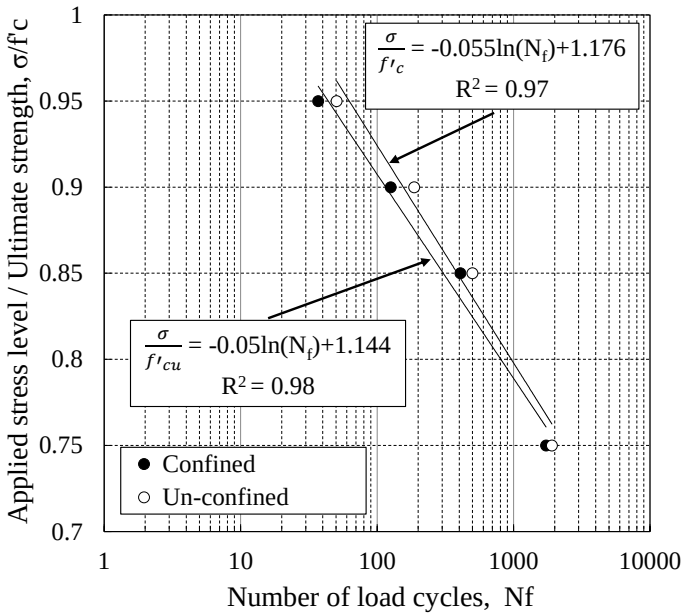

Figure 4-6 The relationship between fatigue life, N_f, and stress level of concrete

4.3.3 Fatigue test-damage evolution

Figure 4-7 shows the fatigue stress–strain curves of confined and unconfined concrete specimens. Stress–strain curves are measured at three stress levels corresponding to 75%, 85% and 95% of the ultimate strength for each type of concrete. It should be noted that the level of stress applied to the confined concrete is comparatively higher than the ultimate strength of plain concrete. For unconfined specimens, the strain, accumulated swiftly during the initial cycles, decelerated during the intermediate cycles, and escalated again for the final cycles up to failure (Figure 4-7(a)-(c)).

The confined specimens did not show similar behaviour. Damage showed a high level of development in terms of significant increase in plastic strain, just in a few initial cycles. However, the rate of increase slowed down for the remaining fatigue life cycles. Although the shape of the stress–strain curves of confined concrete changed from convexity to concavity, as is normally observed in plain concrete, confined specimens did not show the classical three, well-defined regions associated with plain concrete. It can be seen that the hysteresis areas formed in the case of confined concrete exhibit

huge potential for energy dissipation, showing the great advantage of GFRP-wrapped confinement (Figure 4-7(e)-(f)).

For confined specimens, the difference between the total and plastic strains is significantly higher than for unconfined specimens. This recoverable strain increases by increasing the number of load cycles, particularly over the last cycles. The reason is related to the presence of GFRP-sheets, producing confining pressure that tends to restore the extra lateral expansion made during loading to its previous position, once the load is removed. That is why there is a distinctive convex shape at the end of confined concrete specimens. As a result, the unloading branch in plain concrete intersects with the horizontal axis more rapidly, compared to confined concrete.

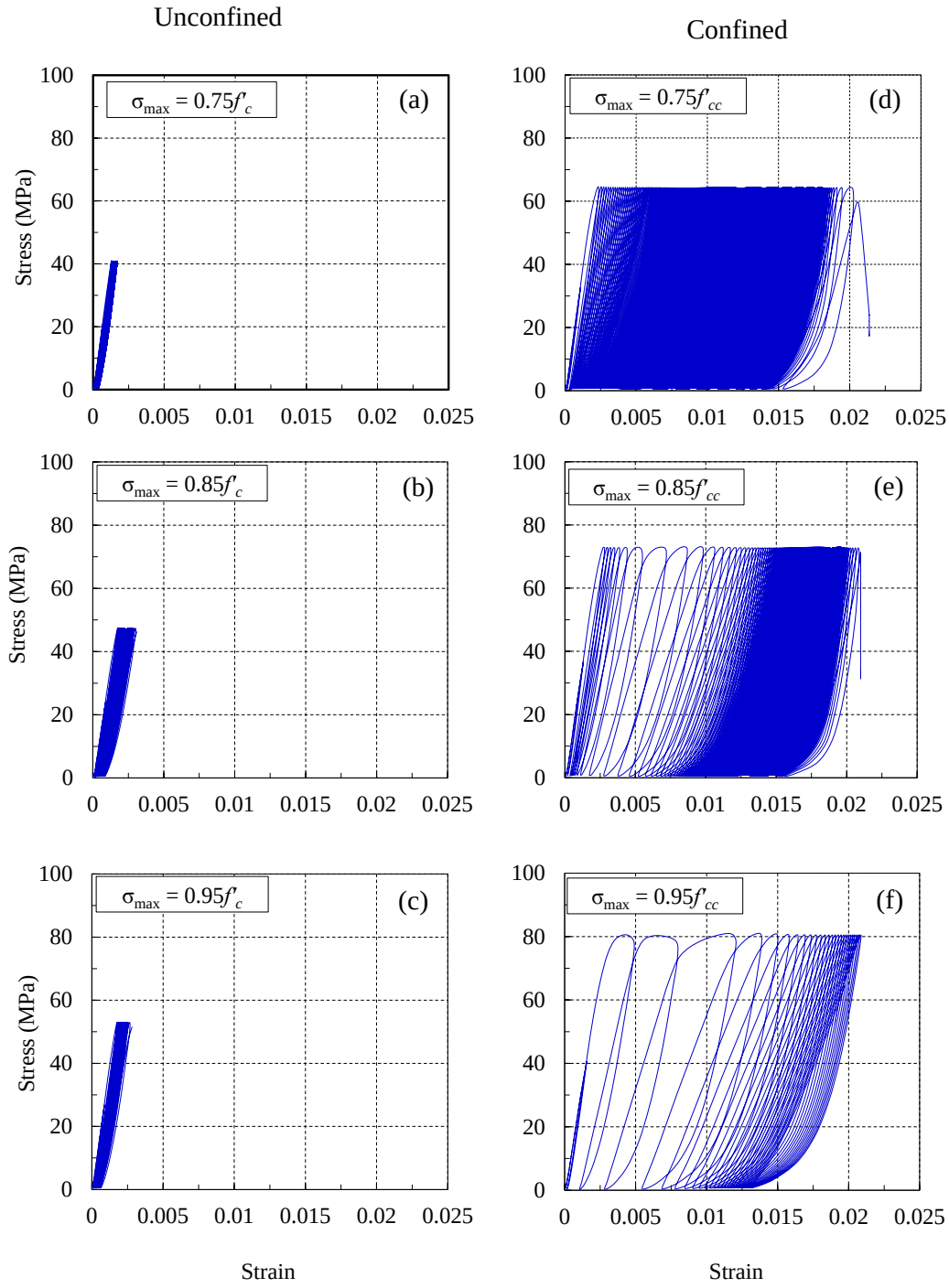

Figure 4-7 Stress–strain curves for confined and unconfined concrete cylinders under fatigue loading

Figure 4-8 shows the typical history of fatigue cycle of concrete in compression, in which the total strain (ε_{total}) is defined as the sum of plastic strain (ε_{pl}) and recoverable strain (ε_r). The total strain corresponds to the strain of the maximum stress level at a certain loading cycle. The plastic strain is defined as the irrecoverable permanent strain corresponding to the intersection point of the unloading branch with the minimum stress axis, at any loading cycle. The value of ε_r is therefore the difference between total strain and plastic strain.

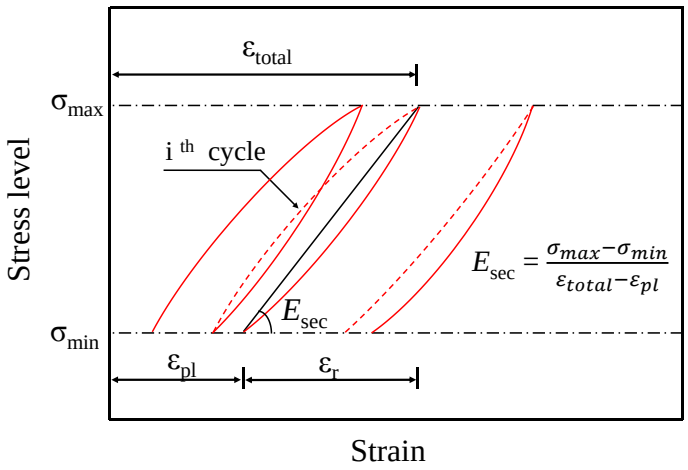

Figure 4-8 Illustration of total, plastic and recoverable strain

Figure 4-9 shows the total and plastic strain (normalized to the ultimate strain of monotonic test ($\varepsilon_{ult,mono}$) obtained from the monotonic test) plotted against the cycle ratio n/N_f for both confined and unconfined concrete specimens under the three stress levels considered in this study. Generally, for unconfined concrete, strain development comprises three regions, the first of which starts with a rapid growth with decreasing slope during the first stage, up to 5% of total fatigue life. This is followed by a shallow and almost constant slope in the second phase, up to 95% of total fatigue life, and the final phase with rapid increasing slope until failure.

The results associated with unconfined specimens formed classical S-shaped spectrum, in line with previous studies (Linger and Gillespie 1966; Holmen 1982; Gao and Hsu 1998). The first stage mainly accommodates the propagation of microcracks at the interface between aggregates and cement paste. During the second stage, the rate of damage is slow and progressive growth of microcracking occurs, followed by accumulation of microcracks already formed during the first and second stages, which

merge into a sufficient number of unstable macrocracks, resulting in the failure of concrete in the final stage.

Note that the failure mechanism of low-cycle fatigue differs from high-cycle fatigue loading. While the formation of mortar cracks, which subsequently lead to continuous cracked networks, are dominant failure mechanisms in the former, under high-cycle fatigue the slow and gradual development of microcracks in the form of bond cracks are the main source of failure (Hsu 1984). However, Kolluru et al. (2000) considered two phases for crack development under constant-amplitude fatigue loading: the "slow-down" phase in which, in spite of increase in the crack length, the rate of crack growth decreases; and the second stage – the "speed-up" stage – where the rate of crack growth increases at a steady rate.

For confined concrete, the development of total and plastic strain did not show the similar classical stretched S-shape pattern of unconfined specimens. The strain showed a significant rise up to 10% of fatigue life, followed by a gradual nonlinear ascending trend up to 95% of fatigue life and eventually a rapid surge to failure. During the first phase, since the level of applied stress is considerbly higher than the ultimate strength of plain concrete, a high level of damage occurs, resulting in a marked development of total strain. In the second phase, the rate of degradation decreases because of more stabilized compaction of dislocated aggregates in the core concrete. In the final region, the GFRP-sheets start to deteriorate, and rupture of sheets leads to failure of specimens.

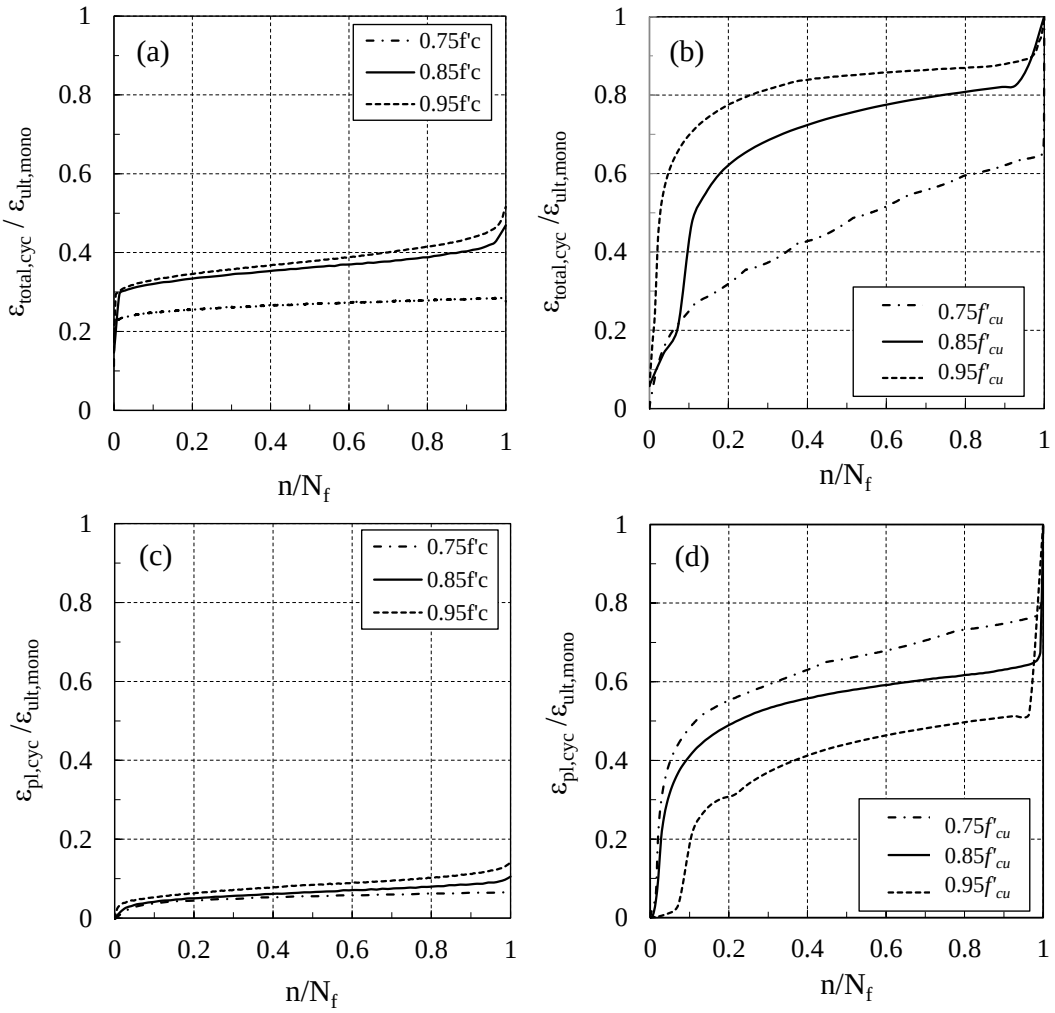

Figure 4-9 Development of: total strain (a) unconfined, (c) confined; and plastic strain (b) unconfined, (d) confined

The spectrums of total and plastic strain associated with confined concrete showed high dependency on applied stress level, whereas in the case of unconfined concrete, stress levels affected the results only slightly. Applying a stress level equal to $0.95f'_{cu}$ developed the total strain up to $0.7\varepsilon_{ult,mono}$, while the total strain spectrum related to $0.75f'_{cu}$ only developed up to $0.25\varepsilon_{ult,mono}$ during the first stage. Compared to unconfined concrete specimens, higher values of total and plastic strain were generated in confined specimens, which can be ascribed to the confinement. Interestingly, the level of damage for confined specimens is such that it caused the normalized total and plastic strain to reach unity, while for unconfined concrete it increases to maximum value of 0.52. Furthermore, results also showed that in the case of unconfined concrete, at the same

cycle ratio, the total and plastic strains developed under higher stress levels were greater than under lower stress. This confirms the results reported by Pang et al. (2012). Similarly, higher stress levels caused higher total strain in confined concrete specimens; however, in the case of plastic strain, as the stress level increases, the produced plastic strain decreases.

Figure 4-10 shows the typical failure of confined and unconfined test specimens. The failure of confined specimens occurred by tensile GFRP-sheet failure and was initiated by the rupture of the inner layers near the mid-height of specimens, propagating toward both ends. Failure by debonding or shear of GFRP-wraps was not observed. Failure of concrete in this case happens before the GFRP-wraps reached their ultimate fatigue capacity, which suggests the premature failure of the concrete component for stress levels well below the ultimate strength of composite structure. In fact, once the level of applied stress exceeds the ultimate strength of plain concrete, aggregates lose their cohesion to cement paste and segregates. This was confirmed by highly crushed concrete material at the end of the test compared to unconfined specimens.

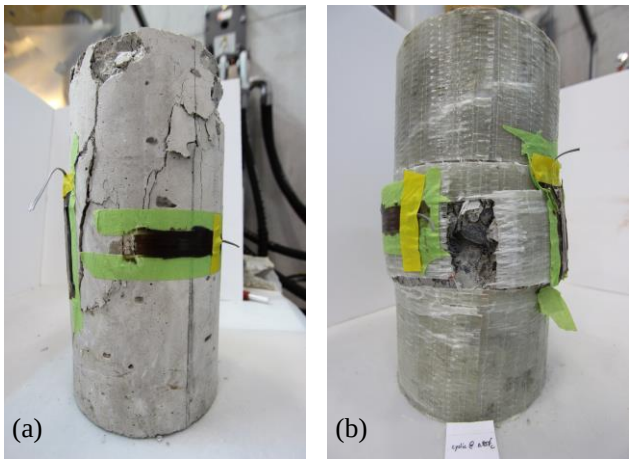

Figure 4-10 Typical failure modes under fatigue loading: (a) Unconfined (b) Confined concrete

The fatigue damage of concrete can generally be represented by introducing characteristic parameters of secant modulus (Gao and Hsu 1998). It was found that during cyclic loading in compression, the response of the stress–strain diagram exhibit three forms of tendency, particularly in the case of unconfined concrete. At the

macroscopic level, the fatigue process results in progressive damage resulting in a marked degradation in stiffness of concrete. This reduction is usually described by using the secant modulus as an appropriate indicator of material degradation. The evaluation of secant modulus for each load cycle to failure leads to the development of the secant modulus over the test period. Owing to constant stress maxima and minima in the fatigue test, a reduction in secant modulus means an increase in strain difference for each load cycle.

It is widely accepted that elastic modulus, which implicitly accounts for stiffness of concrete, deteriorates with an increase in the number of cycles during constant amplitude cyclic loading (Linger and Gillespie 1966; Raju 1969). The secant modulus is calculated as the ratio of stress range to strain range, as illustrated earlier in Figure 4-8. The average secant modulus values determined for three stress levels are shown in Figure 4-11. As seen in Figure 4-11a, in the case of unconfined concrete, subjecting to 10% of fatigue life at any of three stress level considered in this study, causes a 10% decrease in the stiffness of the specimens. During the second phase, it showed a gradual decrease up to 90% of fatigue life, whereupon a significant degradation in stiffness was observed. As the ratio of fatigue life increases further, the impact of the level of applied stress becomes more important, because the higher stress level incur more degradation.

As seen in Figure 4-11b, for confined concrete, about 80% deterioration in secant modulus occurred up to 10% of fatigue life, followed by a slight descending trend up to failure. By introducing a damage index in terms of degradation in secant modulus, DI_E, the evolution of material deterioration at each consecutive cycle of loading can be expressed as follows:

$$DI_E = 1 - \frac{E_{secant}}{E_0} \tag{4.3}$$

where E_{secant} = the secant modulus at cycle of interest; E_0 = the initial tangent modulus coefficient. As shown in Figure 4-11, while the secant modulus-based damage index developed only 40% in the case of unconfined concrete, the degradation in secant modulus reached 100% for confined concrete. Applying 10% of fatigue life of the confined concrete specimens, induced 80% reduction in secant modulus. After that, no considerable difference between the stress levels for the specimens were found. Also, the higher stress levels resulted in a higher level of damage. Although these results

confirm the findings by Petkovic et al. (1990) and Chen et al. (2017), which reported that stiffness degrades more under a higher stress level, it contradicts the results reported by Holmen (1982) and von der Haar and Marx (2016), in which the modulus of elasticity was shown to be degraded more at lower stress levels. This may be related to the fact that for concrete samples subjected to high-cycle fatigue, higher crack density is produced under lower stress levels up to failure, compared with low-cycle fatigue loading.

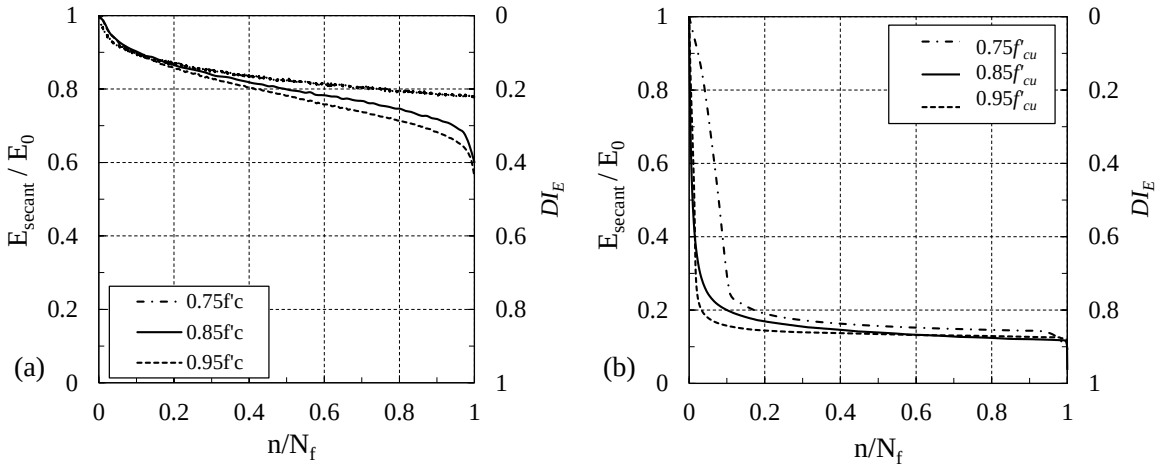

Figure 4-11 Degradation of secant modulus: (a) Unconfined (b) Confined concrete

4.3.4 Temperature development during fatigue loading

The surface temperatures of all test specimens were recorded during fatigue loading at three positions of the specimen (bottom, middle, top). Figure 4-12 shows the typical average variation of temperature in confined and unconfined specimens over fatigue life at each stress level.

As the number of cycles increase, the temperature increases; however, the rate of increase in temperature depends on the total number of cycles experienced. The highest increase is related to the stress level of 0.75, in which temperature rises from ambient temperature of 29°C to 33°C, and from 25°C to 43°C for unconfined and confined specimens, respectively.

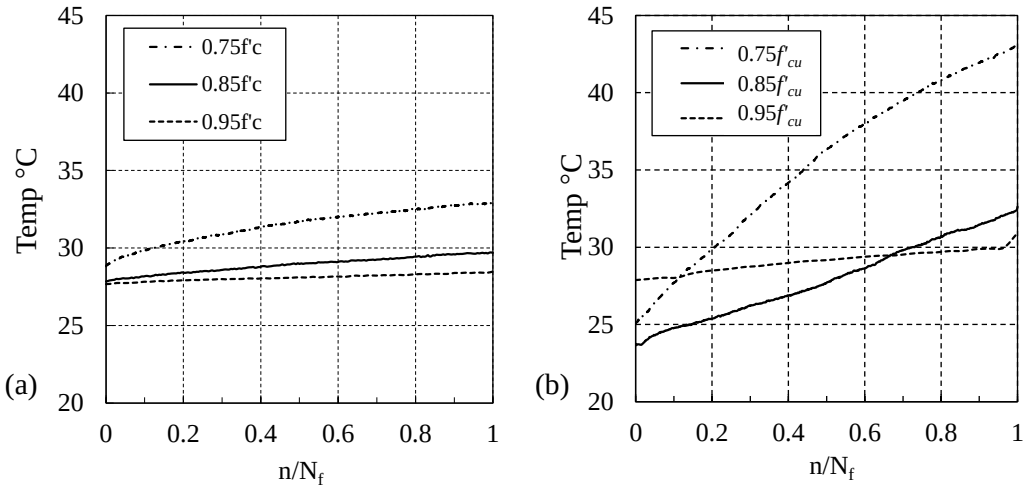

Figure 4-12 The average surface temperature over fatigue life: (a) Unconfined (b) Confined concrete

The minimum increases in temperature were found to be 4% and 14% for unconfined and confined specimens, respectively, and were associated with applying maximum stress level, as it requires the minimum number of cycles. Although the total number of cycles to failure were approximately the same for both types of concrete, temperature increased more markedly for confined specimens. This is mainly attributed to the kinetic energy generated during dislocation of separated aggregates in core concrete.

4.3.5 Residual capacity

Following the procedure described earlier, the residual compressive capacities of partially damaged specimens were captured. The residual stress–strain relationships of damaged specimens reloaded after fatigue loading are shown in Figure 4-13. The compressive behaviour of an intact specimen is also shown for comparison purposes. As shown, for both confined and unconfined concrete, as the number of cycles increases, the residual strain decreases. Although the reduction in strain capacity is well accepted, the effect of previous fatigue loading on strength can be argued. Table 4.3 shows the test matrix, number of load cycles, residual strength and residual strain that have been extracted from so-called damaged responses.

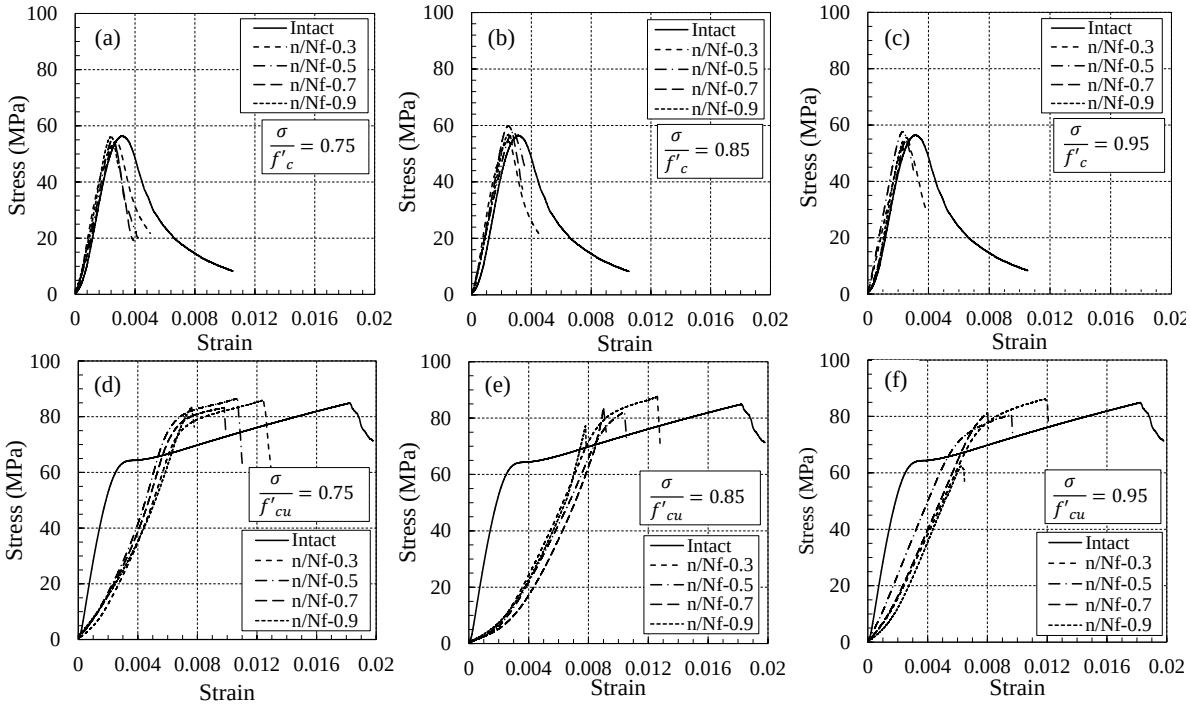

Figure 4-13 Stress–strain relationships of damaged specimens (a–c) Unconfined concrete; (d–e) Confined concrete

Table 4.3 Test matrix, number of load cycles, residual strength and residual strain

Stress level σ/f'_c or σ/f_{cc}	Unconfined					Confined				
	N_f	n/N_f	n	Residual strength, σ_{res}	Residual strain ε_{res}	N_f	n/N_f	n	Residual strength σ_{res}	Residual strain ε_{res}
0.75	1908	0.3	572	56.1	0.0049	1730	0.3	519	85.7	0.0134
		0.5	954	53.8	0.0042		0.5	865	86.3	0.0112
		0.7	1335	53.3	0.0039		0.7	1211	83.1	0.0098
		0.9	1717	55.8	0.0029		0.9	1557	82.7	0.0078
0.85	501	0.3	150	54.2	0.0045	408	0.3	122	87.6	0.0128
		0.5	250	57.6	0.0036		0.5	204	81.9	0.0104
		0.7	351	59.8	0.0034		0.7	285	83.2	0.0091
		0.9	451	56.8	0.0026		0.9	367	77.3	0.0072
0.95	49	0.3	15	54.1	0.0039	37	0.3	11	85.8	0.0119
		0.5	24	57.8	0.0031		0.5	18	80.5	0.0096
		0.7	34	55.6	0.0028		0.7	26	80.9	0.0082
		0.9	44	54.4	0.0023		0.9	33	62.2	0.0064

In this study the residual strength did not show significant change, and the variation in results were in a range of ± 9% which is in the normal range of scatter when calculating ultimate strength. Only in the case of applying 90% of fatigue life at stress level of $0.95f'_c$, was a 26% reduction in strength capacity was observed. That no major loss occurs in strength capacity might be ascribed to the cyclic creep and compaction in the material, which results in reduction in pore spaces. This subsequently causes a permanent deformation, which reduces strain capacity, but in the meantime benefits the still functional load carrying paths. That is why, in spite of the reduction in deformation capacity, little degradation in strength was observed.

It was found that the highest level of reduction in strain capacity is produced by stress levels corresponding to $0.95f'_c$ or $0.95f'_{cu}$. It is also seen, as the level of damage increases the confined concrete tends to lose its bi-linearity attribute. Figure 4-14 provides spectrums by which the material degradation in terms of reduction in strain capacity at each stress level can be evaluated over fatigue life.

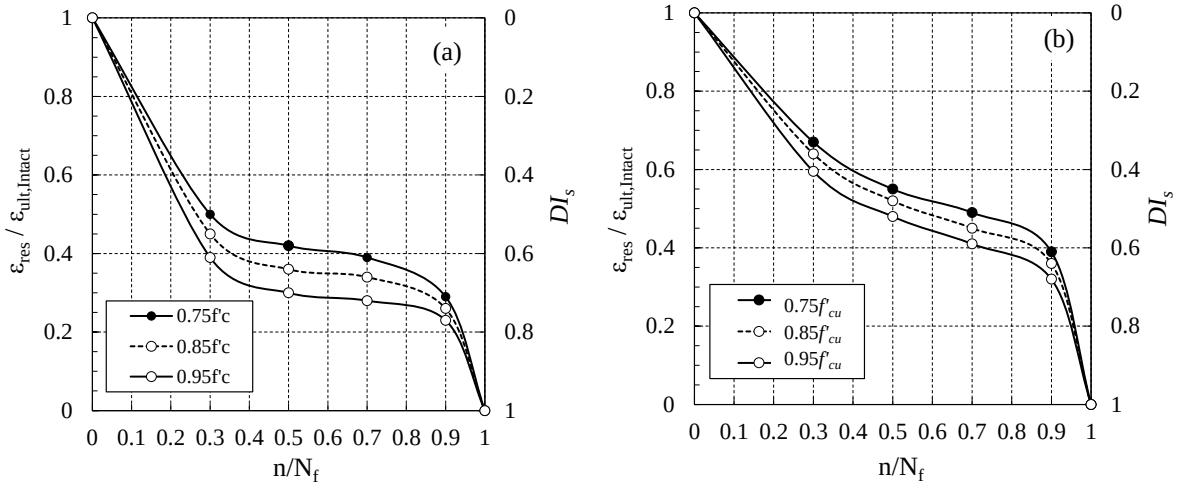

Figure 4-14 Residual strain capacity spectrums (a) Unconfined (b) Confined specimens

The spectrum exhibits a significant drop in residual strain up to 30% of fatigue life, beyond which a gradual decrease up to 90% of fatigue life occurs. In the last region, the spectrum shows a sharp reduction, which is an indication of huge loss in strain capacity. The spectrum showed a stretched S-shape with three different phases, all following a descending trend. Equation 4.5 expresses a strain damage index, DI_s, to quantify damage occurring in the residual strain capacity.

$$DI_s = 1 - \frac{\varepsilon_{res}}{\varepsilon_{ult,intact}} \quad (4.5)$$

where ε_{res} = residual strain after re-loading; $\varepsilon_{ult,intact}$ = ultimate strain capacity of intact specimen subjected to compression test. Comparatively, at any ratio of fatigue life, the strain damage index in unconfined concrete is higher than in confined concrete.

4.3.6 Permeability-based assessment of fatigue damage

Having extracted the concrete disks from both damaged confined and unconfined specimens, the coefficients of permeability were calculated. Figure 4-15 indicates the change in the coefficient of permeability over fatigue life. This spectrum consists of three phases, and is similar to classical responses under fatigue loading. As seen in Figure 4-15a, for unconfined concrete subjected to $0.95f'_c$, the first phase starts with a gradual increase in coefficient of permeability from 2.4×10^{-11} m/s to 4.9×10^{-11} m/s until 30% of fatigue life, indicating an average increase of two and half times in the coefficients of permeability. In the second phase, lasting up to 70% of fatigue life, a slight increase was observed. During the last phase, an ascending trend was again followed, resulting in a six-fold increase, reaching a coefficient of permeability of 16.2×10^{-11} m/s.

Similar to unconfined concrete, in the case of confined concrete, permeability spectrums over fatigue life of the specimens consisted of three phases. As shown in Figure 4-15b, for specimen subjected to $0.95f'_{cu}$ the first phase includes a significant surge in the coefficient of permeability, from 2.4×10^{-11} m/s to 2390×10^{-11} m/s, an increase of 1000 times. This rate appreciably decreased during the second phase, in which the coefficient of permeability reached 5010×10^{-11} m/s, showing an average of only a two-fold increase. During the last phase, an ascending trend was again followed, reaching a coefficient of permeability of 8230×10^{-11} m/s.

It is worth noting that the investigation was carried out up to level of damage corresponding to 90% of fatigue life, since the coefficient of permeability was not measured for the ratios exceeding that limit. That is because beyond such a level, the concrete is highly damaged, leaving no possibility of taking concrete disks for the experiments. If it were possible to measure coefficient of permeability, it would offer little or no resistance to flow, resulting in considerably large, off-scale values.

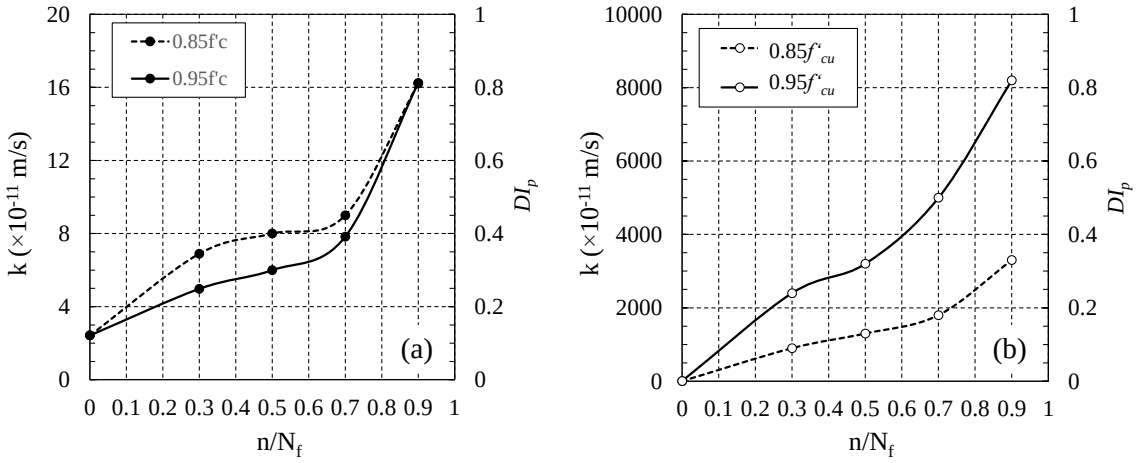

Figure 4-15 Permeability spectrum over fatigue life (a) Unconfined (b) Confined specimens

Comparing the spectrums for both type of concrete, the confined specimens showed significantly higher values, as was expected. This is mainly due to the experiencing higher levels of stress, far beyond their strength under unconfined conditions, resulting in the formation of severe cracking. Interestingly, spectrums associated with permeability of unconfined concrete, showed application of higher stress level (i.e, $0.95f'_c$), caused less damage in the coefficient of permeability compared to the specimens subjected to lower stress level (i.e., $0.85f'_c$).

This shows the dependency on number of load cycle rather than stress level, and is in line with the results of plastic strain in which the lower stress level produced higher plastic strain. However, in the case of confined concrete, the higher stress level leads to more damage in the coefficient of permeability. A relative permeability damage index, DI_p, was established to estimate relative change in the permeability as an indicator of material deterioration as follows:

$$DI_p = \frac{k-k_0}{k_{peak}} \tag{4.6}$$

where k = coefficient of permeability of the concrete disk taken from specimen subjected to fatigue loading; k_{peak} = the maximum coefficient of permeability of the concrete disk measured during experiments, and k_0 = the coefficient of permeability of the concrete disk taken from the unloaded specimen.

Note that, theoretically, the maximum coefficient of permeability is related to the fatigue life ratio of n/N_f = 1. But it was experimentally impossible to determine this coefficient of permeability, as the level of damage was such that no concrete disk could be obtained. It is not feasible to derive DI_p = 1. Thus, the maximum value of the coefficient of permeability in this study was associated with the fatigue life ratio of n/N_f =0.9. The minimum of damage index (DI_p = 0) was calculated for the disks taken from zero-loaded concrete cylinders. It should be also noted that k_0 was the same for both types of concrete; however, the value of k_{peak} were derived appropriately for each type of concrete.

Figure 4-16 indicates a correlation between changes that occurred in the strain capacity and damage in the microstructure of specimens, represented by change in the permeability damage index of concrete. Such a correlation can provide a feasibility to indirectly estimate damage in mechanical properties by measuring only the permeability damage index. Considering the deterioration of strain in terms of the damage that occurs in the permeability of concrete, it might be interpreted that the occurrence of 50% damage in the permeability of concrete may cause a minimum of 52% loss in the axial strain capacity, in the case of confined concrete subjected to 0.85f'_{cu}. However, for unconfined concrete, it reaches 74% for a stress level of 0.95f'_c.

As can be seen, the graphs show a rapid change in strain when increasing the level of permeabilty up to a certain level, followed by a gradual increase. That is because DI_p, is a relative damage index in the range of stress level studied herein. In fact, the real values of DI_p would be much lower if the denominator in Equation 6 tends to infinity, which is the permeability coefficient of highly crushed concrete that shows no resistance to gas flow. Conversely, to calculate DI_s, the denominator used is the ultimate strain applicable value obtained from the compression test.

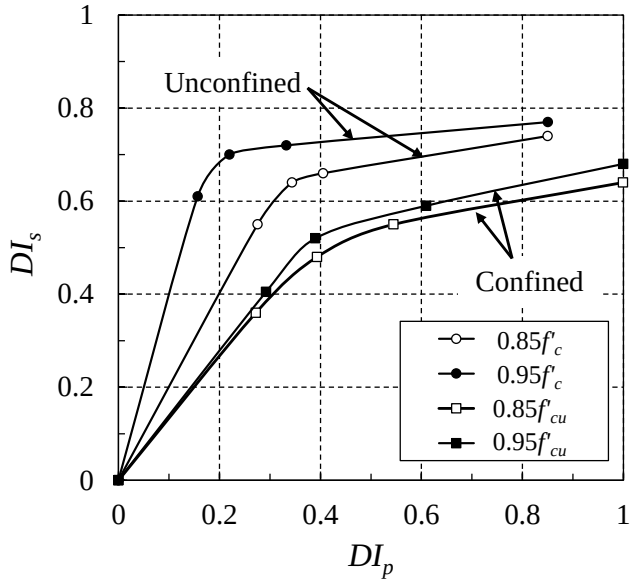

Figure 4-16 Strain damage index DIs against permeability damage index DIp

4.4 Conclusions

This chapter presented the results of an extensive investigation into the development of damage, material degradation, residual mechanical capacity and permeability damage assessment of confined and unconfined cylinders subjected to fatigue loading. The following conclusions can be drawn based on the results of this study:

1. Two different trends: softening in the case of unconfined and hardening in the case of confined concrete, were observed based on well-established stress–strain behaviours. The slope of hardening branch for tested specimens was found to be 7.1% of the tangent modulus of confined concrete in the first branch. The presence of GFRP-wrap confinement increased the strength and strain capacity by 65% and 74%, respectively.

   The use of laser distance sensors to accurately measure deformation (strain) showed great promise and allowed not only to capture the global behaviour of the test specimen, but also the post-peak response precisely, which is practically impossible using conventional strain gauges. It also requires no extra effort regarding surface preparation. However, the only disadvantage is

the inability to measure transverse strain, which was out of the scope of this work.

2. The fatigue life (S–N curve) was drawn and the relationships that best predict it were established for both types of concrete. The confinement showed no significant effect on the number of cycles that a specimen can withstand at each stress level.
3. The development of total and plastic strain during fatigue loading associated with unconfined concrete showed a classical, three phase, S-shape spectrum. In the case of confined concrete, the rate of damage was comparatively higher particularly in the first phase, reaching the ultimate damage state at fatigue loading ratio of $n/N_f = 1$. The damage in the mechanical properties of concrete in terms of degradation in secant modulus of unconfined concrete also followed three distinct parts. Conversely, the confined concrete in practice showed two stages: a significant drop followed by a gradual decrease with trivial dependency on stress level. During fatigue loading, part of the kinetic energy is converted to heat which was measured by a rise in temperature at the surface of specimens. Results showed as the level of stress increase, the rate of increase in surface temperature decreases. This indicates the amount of heat is mainly dependent on the number of cycles and rate of loading rather than stress level. Moreover, the experiments showed the amount of heat generated in confined concrete is considerably higher than unconfined concrete. This is mainly due to severe dislocation of aggregates at stress levels far beyond the strength of unconfined concrete.
4. Having monotonically reloaded partially damaged specimens, previously subjected to different ratios of fatigue and three different stress levels, the residual stress–strain relationships were established. While strength was found to be insignificantly affected by previous fatigue loading, strain showed a marked loss in its capacity compared with an intact specimen subjected to one excursion of compression loading. Subsequently, the spectrums were provided to estimate the residual axial strain capacity for both type of specimens. It was also found that as the effect of stress level increases, the post-event residual load-deformation bearing capacity of concrete decreases. Results indicated that

to determine the residual capacity of a damaged RC member, stress–strain diagrams related to intact concrete are no longer valid and a revised relationship should be used.

5. The oxygen permeability test on concrete disks showed great potential to measure the damage incurred. Using the permeability spectrum over the fatigue life of the damaged concrete, the level of damage was identified. The fatigue damage always accelerated the flow of permeable substance in concrete by a factor of 6 and 300 times for unconfined and confined concrete, respectively.
6. A correlation was made between damage in the microstructure of the concrete represented by permeability damage index, and damage in the mechanical properties of concrete shown by degradation in strain capacity. This may provide a basis to estimate residual strain indirectly through permeability damage, without a need for compression tests on specimens that have previously experienced a fatigue loading demand. This is of great benefit for post-event damage assessment of real concrete building where there is typically no possibility to take cores in the critical regions for determining the residual mechanical characteristics of the material.

4.5 References

Awad, M. E. (1971). "Strength and deformation characteristics of plain concrete subjected to high repeated and sustained loads." University of Illinois Engineering Experiment Station. College of Engineering. University of Illinois at Urbana-Champaign.

Ballatore, E., and Bocca, P. (1997). "Variations in the mechanical properties of concrete subjected to low cyclic loads." *Cement and concrete research*, 27(3), 453-462.

Bennett, E., and Muir, S. S. J. (1967). "Some fatigue tests of high-strength concrete in axial compression." *Magazine of Concrete Research*, 19(59), 113-117.

Chen, X., Bu, J., Fan, X., Lu, J., and Xu, L. (2017). "Effect of loading frequency and stress level on low cycle fatigue behavior of plain concrete in direct tension." *Construction and Building Materials*, 133, 367-375.

Desmettre, C., and Charron, J.-P. (2013). "Water Permeability of Reinforced Concrete Subjected to Cyclic Tensile Loading." *ACI Materials Journal*, 110(1).

Erberik, A., and Sucuoğlu, H. (2004). "Seismic energy dissipation in deteriorating systems through low-cycle fatigue." *Earthquake engineering & structural dynamics*, 33(1), 49-67.

Fu, C., Ye, H., Jin, X., Yan, D., Jin, N., and Peng, Z. (2016). "Chloride penetration into concrete damaged by uniaxial tensile fatigue loading." *Construction and Building Materials*, 125, 714-723.

Gao, L., and Hsu, C.-T. T. (1998). "Fatigue of concrete under uniaxial compression cyclic loading." *Materials Journal*, 95(5), 575-581.

Gontar, W. A., Martin, J. P., and Popovics, J. S. (2000). "Effects of cyclic loading on chloride permeability of plain concrete." *Condition Monitoring of Materials and Structures*, 1, 95-109.

Graf, O., and Brenner, E. (1934). "Experiments for investigating the resistance of concrete under often repeated compression loads." *Bulletin*(76).

Holmen, J. O. (1982). "Fatigue of concrete by constant and variable amplitude loading." *Special Publication*, 75, 71-110.

Hsu, T. T. (1981). "Fatigue of plain concrete." *Journal Proceedings*, 78(4), 292-305.

Hsu, T. T. (1984). "Fatigue and microcracking of concrete." *Materials and Structures*, 17(1), 51-54.

Jones, R. (1968). "Cracking and failure of concrete test specimens under uniaxial quasi-static loading."

Karsan, I. D., and Jirsa, J. O. (1969). "Behavior of concrete under compressive loadings." *Journal of the Structural Division*.

Kolluru, S. V., O'Neil, E. F., Popovics, J. S., and Shah, S. P. (2000). "Crack propagation in flexural fatigue of concrete." *Journal of Engineering mechanics*, 126(9), 891-898.

Kontani, O., Ishitobi, N., Kawada, J., Taogoshi, N., Koge, M., and Umeki, Y. (2016). "Residual Static Strength of Concrete Cylinder Specimen and Stud Anchor Specimen after Cyclic Loadings." *Journal of Advanced Concrete Technology*, 14(10), 634-642.

L'Hermite, R. (1954). "Present Day Ideas in Concrete Technology, Part 3: The Failure of Concrete." *RILEM Bulletin*, 18, 27-38.

Linger, D., and Gillespie, H. (1966). "A Study of the Mechanism of Concrete Fatigue and Fracture." *Highway Research News*.

Mordock, J. (1965). "A Critical Review of Research on the Fatigue of Plain Concrete." *Illinois Univ Eng Exp Sta Bulletin*.

Mu, B., Subramaniam, K. V., and Shah, S. (2004). "Failure mechanism of concrete under fatigue compressive load." *Journal of materials in civil engineering*, 16(6), 566-572.

Muguruma, H., and Fumio, W. "Low-cycle fatigue behavior of concrete and ae monitoring under submerged condition." *Proc., Proceedings of the Japan Congress on Materials Research*, Society of Materials Science, Japan, 151.

Newman, K. (1968). "Criteria for the behaviour of plain concrete under complex states of stress."

Nordby, G. M. "Fatigue of concrete-A review of research." *Proc., Journal Proceedings*, 191-219.

Pang, X., Darbe, R., Ravi, K., and Meyer, C. (2012). "Low-Cycle Fatigue of Oil Well Cements in Compression." *ACI Materials Journal*, 109(2).

Petkovic, G., Lenschow, R., Stemland, H., and Rosseland, S. (1990). "Fatigue of high-strength concrete." *Special Publication*, 121, 505-526.

Raju, N. (1969). "Deformation characteristics of concrete under repeated compressive loads." *Building Science*, 4(3), 151-157.

Shah, S. G., and Kishen, J. C. (2012). "Use of acoustic emissions in flexural fatigue crack growth studies on concrete." *Engineering Fracture Mechanics*, 87, 36-47.

Tawfiq, K., Armaghani, J., and Vysyaraju, J. (1996). "Permeability of concrete subjected to cyclic loading." *Transportation Research Record: Journal of the Transportation Research Board*(1532), 51-59.

Urban, S., Strauss, A., Schütz, R., Bergmeister, K., and Dehlinger, C. (2014). "Dynamically loaded concrete structures–monitoring-based assessment of the real degree of fatigue deterioration." *Structural Concrete*, 15(4), 530-542.

Valdmanis, V., De Lorenzis, L., Rousakis, T., and Tepfers, R. (2007). "Behaviour and capacity of CFRP-confined concrete cylinders subjected to monotonic and cyclic axial compressive load." *STRUCTURAL CONCRETE-LONDON-THOMAS TELFORD LIMITED-*, 8(4), 187.

von der Haar, C., and Marx, S. (2016). "Development of stiffness and ultrasonic pulse velocity of dynamically loaded concrete." *Structural Concrete*(4), 630-636.

Wagner, R., Reiterer, M., Strauss, A., and Urban, S. (2012). "Fatigue Monitoring of High Strength Concrete Using Acoustic Emission and Ultrasonic Techniques." *Proceedings of the 6th EWSHM*, 46-53.

Awad, M. E. (1971). "Strength and deformation characteristics of plain concrete subjected to high repeated and sustained loads." University of Illinois Engineering Experiment Station. College of Engineering. University of Illinois at Urbana-Champaign.

Ballatore, E., and Bocca, P. (1997). "Variations in the mechanical properties of concrete subjected to low cyclic loads." *Cement and concrete research*, 27(3), 453-462.

Bennett, E., and Muir, S. S. J. (1967). "Some fatigue tests of high-strength concrete in axial compression." *Magazine of Concrete Research*, 19(59), 113-117.

Chen, X., Bu, J., Fan, X., Lu, J., and Xu, L. (2017). "Effect of loading frequency and stress level on low cycle fatigue behavior of plain concrete in direct tension." *Construction and Building Materials*, 133, 367-375.

Desmettre, C., and Charron, J.-P. (2013). "Water Permeability of Reinforced Concrete Subjected to Cyclic Tensile Loading." *ACI Materials Journal*, 110(1).

Erberik, A., and Sucuoğlu, H. (2004). "Seismic energy dissipation in deteriorating systems through low-cycle fatigue." *Earthquake engineering & structural dynamics*, 33(1), 49-67.

Fu, C., Ye, H., Jin, X., Yan, D., Jin, N., and Peng, Z. (2016). "Chloride penetration into concrete damaged by uniaxial tensile fatigue loading." *Construction and Building Materials*, 125, 714-723.

Gao, L., and Hsu, C.-T. T. (1998). "Fatigue of concrete under uniaxial compression cyclic loading." *Materials Journal*, 95(5), 575-581.

Gontar, W. A., Martin, J. P., and Popovics, J. S. (2000). "Effects of cyclic loading on chloride permeability of plain concrete." *Condition Monitoring of Materials and Structures*, 1, 95-109.

Graf, O., and Brenner, E. (1934). "Experiments for investigating the resistance of concrete under often repeated compression loads." *Bulletin*(76).

Holmen, J. O. (1982). "Fatigue of concrete by constant and variable amplitude loading." *Special Publication*, 75, 71-110.

Hsu, T. T. (1981). "Fatigue of plain concrete." *Journal Proceedings*, 78(4), 292-305.

Hsu, T. T. (1984). "Fatigue and microcracking of concrete." *Materials and Structures*, 17(1), 51-54.

Jones, R. (1968). "Cracking and failure of concrete test specimens under uniaxial quasi-static loading."

Karsan, I. D., and Jirsa, J. O. (1969). "Behavior of concrete under compressive loadings." *Journal of the Structural Division*.

Kolluru, S. V., O'Neil, E. F., Popovics, J. S., and Shah, S. P. (2000). "Crack propagation in flexural fatigue of concrete." *Journal of Engineering mechanics*, 126(9), 891-898.

Kontani, O., Ishitobi, N., Kawada, J., Taogoshi, N., Koge, M., and Umeki, Y. (2016). "Residual Static Strength of Concrete Cylinder Specimen and Stud Anchor Specimen after Cyclic Loadings." *Journal of Advanced Concrete Technology*, 14(10), 634-642.

L'Hermite, R. (1954). "Present Day Ideas in Concrete Technology, Part 3: The Failure of Concrete." *RILEM Bulletin*, 18, 27-38.

Linger, D., and Gillespie, H. (1966). "A Study of the Mechanism of Concrete Fatigue and Fracture." *Highway Research News*.

Mordock, J. (1965). "A Critical Review of Research on the Fatigue of Plain Concrete." *Illinois Univ Eng Exp Sta Bulletin*.

Mu, B., Subramaniam, K. V., and Shah, S. (2004). "Failure mechanism of concrete under fatigue compressive load." *Journal of materials in civil engineering*, 16(6), 566-572.

Muguruma, H., and Fumio, W. "Low-cycle fatigue behavior of concrete and ae monitoring under submerged condition." *Proc., Proceedings of the Japan Congress on Materials Research*, Society of Materials Science, Japan, 151.

Newman, K. (1968). "Criteria for the behaviour of plain concrete under complex states of stress."

Nordby, G. M. "Fatigue of concrete-A review of research." *Proc., Journal Proceedings*, 191-219.

Pang, X., Darbe, R., Ravi, K., and Meyer, C. (2012). "Low-Cycle Fatigue of Oil Well Cements in Compression." *ACI Materials Journal*, 109(2).

Petkovic, G., Lenschow, R., Stemland, H., and Rosseland, S. (1990). "Fatigue of high-strength concrete." *Special Publication*, 121, 505-526.

Raju, N. (1969). "Deformation characteristics of concrete under repeated compressive loads." *Building Science*, 4(3), 151-157.

Shah, S. G., and Kishen, J. C. (2012). "Use of acoustic emissions in flexural fatigue crack growth studies on concrete." *Engineering Fracture Mechanics*, 87, 36-47.

Tawfiq, K., Armaghani, J., and Vysyaraju, J. (1996). "Permeability of concrete subjected to cyclic loading." *Transportation Research Record: Journal of the Transportation Research Board*(1532), 51-59.

Urban, S., Strauss, A., Schütz, R., Bergmeister, K., and Dehlinger, C. (2014). "Dynamically loaded concrete structures–monitoring-based assessment of the real degree of fatigue deterioration." *Structural Concrete*, 15(4), 530-542.

Valdmanis, V., De Lorenzis, L., Rousakis, T., and Tepfers, R. (2007). "Behaviour and capacity of CFRP-confined concrete cylinders subjected to monotonic and cyclic axial compressive load." *STRUCTURAL CONCRETE-LONDON-THOMAS TELFORD LIMITED-*, 8(4), 187.

von der Haar, C., and Marx, S. (2016). "Development of stiffness and ultrasonic pulse velocity of dynamically loaded concrete." *Structural Concrete*(4), 630-636.

Wagner, R., Reiterer, M., Strauss, A., and Urban, S. (2012). "Fatigue Monitoring of High Strength Concrete Using Acoustic Emission and Ultrasonic Techniques." *Proceedings of the 6th EWSHM*, 46-53.

Awad, M. E. (1971). "Strength and deformation characteristics of plain concrete subjected to high repeated and sustained loads." University of Illinois Engineering Experiment Station. College of Engineering. University of Illinois at Urbana-Champaign.

Ballatore, E., and Bocca, P. (1997). "Variations in the mechanical properties of concrete subjected to low cyclic loads." *Cement and concrete research*, 27(3), 453-462.

Bennett, E., and Muir, S. S. J. (1967). "Some fatigue tests of high-strength concrete in axial compression." *Magazine of Concrete Research*, 19(59), 113-117.

Chen, X., Bu, J., Fan, X., Lu, J., and Xu, L. (2017). "Effect of loading frequency and stress level on low cycle fatigue behavior of plain concrete in direct tension." *Construction and Building Materials*, 133, 367-375.

Desmettre, C., and Charron, J.-P. (2013). "Water Permeability of Reinforced Concrete Subjected to Cyclic Tensile Loading." *ACI Materials Journal*, 110(1).

Erberik, A., and Sucuoğlu, H. (2004). "Seismic energy dissipation in deteriorating systems through low-cycle fatigue." *Earthquake engineering & structural dynamics*, 33(1), 49-67.

Fu, C., Ye, H., Jin, X., Yan, D., Jin, N., and Peng, Z. (2016). "Chloride penetration into concrete damaged by uniaxial tensile fatigue loading." *Construction and Building Materials*, 125, 714-723.

Gao, L., and Hsu, C.-T. T. (1998). "Fatigue of concrete under uniaxial compression cyclic loading." *Materials Journal*, 95(5), 575-581.

Gontar, W. A., Martin, J. P., and Popovics, J. S. (2000). "Effects of cyclic loading on chloride permeability of plain concrete." *Condition Monitoring of Materials and Structures*, 1, 95-109.

Graf, O., and Brenner, E. (1934). "Experiments for investigating the resistance of concrete under often repeated compression loads." *Bulletin*(76).

Holmen, J. O. (1982). "Fatigue of concrete by constant and variable amplitude loading." *Special Publication*, 75, 71-110.

Hsu, T. T. (1981). "Fatigue of plain concrete." *Journal Proceedings*, 78(4), 292-305.

Hsu, T. T. (1984). "Fatigue and microcracking of concrete." *Materials and Structures*, 17(1), 51-54.

Jones, R. (1968). "Cracking and failure of concrete test specimens under uniaxial quasi-static loading."

Karsan, I. D., and Jirsa, J. O. (1969). "Behavior of concrete under compressive loadings." *Journal of the Structural Division*.

Kolluru, S. V., O'Neil, E. F., Popovics, J. S., and Shah, S. P. (2000). "Crack propagation in flexural fatigue of concrete." *Journal of Engineering mechanics*, 126(9), 891-898.

Kontani, O., Ishitobi, N., Kawada, J., Taogoshi, N., Koge, M., and Umeki, Y. (2016). "Residual Static Strength of Concrete Cylinder Specimen and Stud Anchor Specimen after Cyclic Loadings." *Journal of Advanced Concrete Technology*, 14(10), 634-642.

L'Hermite, R. (1954). "Present Day Ideas in Concrete Technology, Part 3: The Failure of Concrete." *RILEM Bulletin*, 18, 27-38.

Linger, D., and Gillespie, H. (1966). "A Study of the Mechanism of Concrete Fatigue and Fracture." *Highway Research News*.

Mordock, J. (1965). "A Critical Review of Research on the Fatigue of Plain Concrete." *Illinois Univ Eng Exp Sta Bulletin*.

Mu, B., Subramaniam, K. V., and Shah, S. (2004). "Failure mechanism of concrete under fatigue compressive load." *Journal of materials in civil engineering*, 16(6), 566-572.

Muguruma, H., and Fumio, W. "Low-cycle fatigue behavior of concrete and ae monitoring under submerged condition." *Proc., Proceedings of the Japan Congress on Materials Research*, Society of Materials Science, Japan, 151.

Newman, K. (1968). "Criteria for the behaviour of plain concrete under complex states of stress."

Nordby, G. M. "Fatigue of concrete-A review of research." *Proc., Journal Proceedings*, 191-219.

Pang, X., Darbe, R., Ravi, K., and Meyer, C. (2012). "Low-Cycle Fatigue of Oil Well Cements in Compression." *ACI Materials Journal*, 109(2).

Petkovic, G., Lenschow, R., Stemland, H., and Rosseland, S. (1990). "Fatigue of high-strength concrete." *Special Publication*, 121, 505-526.

Raju, N. (1969). "Deformation characteristics of concrete under repeated compressive loads." *Building Science*, 4(3), 151-157.

Shah, S. G., and Kishen, J. C. (2012). "Use of acoustic emissions in flexural fatigue crack growth studies on concrete." *Engineering Fracture Mechanics*, 87, 36-47.

Tawfiq, K., Armaghani, J., and Vysyaraju, J. (1996). "Permeability of concrete subjected to cyclic loading." *Transportation Research Record: Journal of the Transportation Research Board*(1532), 51-59.

Urban, S., Strauss, A., Schütz, R., Bergmeister, K., and Dehlinger, C. (2014). "Dynamically loaded concrete structures–monitoring-based assessment of the real degree of fatigue deterioration." *Structural Concrete*, 15(4), 530-542.

Valdmanis, V., De Lorenzis, L., Rousakis, T., and Tepfers, R. (2007). "Behaviour and capacity of CFRP-confined concrete cylinders subjected to monotonic and cyclic axial compressive load." *STRUCTURAL CONCRETE-LONDON-THOMAS TELFORD LIMITED-*, 8(4), 187.

von der Haar, C., and Marx, S. (2016). "Development of stiffness and ultrasonic pulse velocity of dynamically loaded concrete." *Structural Concrete*(4), 630-636.

Wagner, R., Reiterer, M., Strauss, A., and Urban, S. (2012). "Fatigue Monitoring of High Strength Concrete Using Acoustic Emission and Ultrasonic Techniques." *Proceedings of the 6th EWSHM*, 46-53.

Chapter 5 *Experimental damage assessment of bond between deformed bar and concrete using distributed fibre-optic strain sensing*

5.1 Introduction

During an earthquake, reinforcement bars yield, so the bond between reinforcing bar and concrete in the post-yield range of the steel possibly deteriorates. Bond deterioration is of great importance in the context of modern capacity seismic design of RC buildings since it not only affects the extent of damage, but also jeopardizes the structural performance, as it is responsible for the composite behaviour of an RC member. That is because in capacity design, the dissipation of input energy depends on ductility capacity of the RC members after yielding. Ductility requires plastic deformation through incurring more plastic strain in the steel bar, but this will cause significant damage that lowers the ability of the bond to transfer force from the reinforcement to the concrete. Although the ductility and bond are both essential for the survival of RC buildings during an earthquake, these requirements appear not to be in line with each other. From a capacity design perspective, at a high level of loading demand, a more ductile behaviour from an RC member is expected. To ensure such behaviour occurs, the bond strength deteriorates once the steel strain exceeds the yield strain, which is a compromise for the optimum performance of an RC member.

Ismail and Jirsa (1972), and Tada and Takeda (1991) reported degradation of strength and stiffness in the load-deformation response of RC members due to bond deterioration. A study conducted by Filippou et al. (1983) showed that, in the plastic hinges, bond deterioration in the region adjacent to the crack contributes to crack opening. In fact, once the yield strength of the reinforcement is exceeded at a cracked section, the bond deteriorates markedly. It is well understood that bond deterioration under significant cyclic loading demands cannot be prevented, except by the use of very long anchorage lengths and substantial transverse reinforcement. Even in this case,

full elimination of bond damage near the most highly stressed areas is impossible (ACI 408.2R-92 2005).

Although the performance of the bond in the post-yield range of steel strain completely differs from its behaviour in the elastic range, the behaviour of bond-slip in the post-yield region has been the topic of very few studies. Hassan and Hawkins (1977) proposed an analytical model to predict the pullout of an anchored steel bar even in the post-yield range, but no measurement was conducted in support of the assumed bond stress distribution. Viwathanatepa et al. (1979) reported values of bond stress before and after yielding of steel from the bond test of a beam-column joint, but the bond behaviour in the post-yield range was not investigated. Ueda et al. (1986) used a bond-slip model obtained in the elastic range to predict the load–pullout relationship for reinforcing bars extending from beams into exterior columns that were subjected to inelastic loading. Murayama et al. (1986) studied both bond-slip; however, no formulated relationship was reported. Shima et al. (1987) carried out a landmark study to investigate how the bond characteristics are affected in the post-yield range of steel bars and formulated a model to express bond behaviour in this region. The experiments were tested in pullout fashion with very long bond lengths (50 times bar diameter), and different steel grades. Mayer (2001) also studied the bond behaviour of ribbed bars at inelastic steel strain in RC columns subjected to uniaxial loading. Recently, in experiments conducted by Ashtiani et al. (2013) the performance of bonds in the post-yield range of steel was studied through pullout tests on two grades of steel bar embedded in high-strength self-compacting concrete. However, no bond stress measurement was made along the length of reinforcement, and bond stress–slip relationships were established based on measuring the load on the loaded end, and slip on the unloaded end of a steel bar protruding from a concrete block.

The experimental studies mentioned above, on the post-yield behaviour of bond, suffer from one or more of the following items: (a) the slip was measured at the unloaded end and no continuous strain measurement was obtained throughout the length of reinforcement; (b) the bond test specimen was a concrete block with one reinforcing bar in the middle, and no bond test resembling the real RC structural component was conducted; (c) the location along the bar where yielding occurs was not accurately determined; (d) the effects of stirrups and confinement in real situations

was not considered; (e) there is no study that correlated the bond deterioration with applied drift levels.

The current study is the first, reporting the use of a DFOSSS system for the investigation of bond deterioration and damage assessment through a measured strain profile along the length of reinforcing bar, and the surface of cover concrete, in a seismically designed cantilever RC beam, subjected to lateral load. Based on the needs discussed previously, this chapter addresses the following objectives: (1) to measure strain in steel and concrete continuously along the length of the specimen; (2) to determine the distribution of bond along the entire length of reinforcement with the least possible interference and damage to the bond; (3) to determine bond deterioration and investigate the behaviour of the bond in the post-yield region; (4) to determine the level and extent of bond deterioration with respect to the drift level; (5) to study the ability of distributed fibre-optic strain sensing to detect crack locations, and the extent of damage in both the reinforcement and concrete.

5.1.1 Global and local bond performance

When the bonded length is relatively small ($L \leq 5d_b$) (Eligehausen et al. 1982), and a force is applied at one end, the relative slip between the steel and concrete can be considered constant in the longitudinal direction. In this case, rigid body sliding of the bar inside concrete occurs (i.e., global slip), and a typical bond stress-slip response regardless of the type of bond test (i.e., pull-out or push-in test) is achieved. For short embedment length, the average bond stress is assumed to be approximately equal to the local bond stress (Figure 5-1a). The typical monotonic bond stress-slip behaviour is then characterized by an ascending branch up to a certain slip where the force reaches its maximum, followed by a constant value and finally a descending branch (Figure 5-1b).

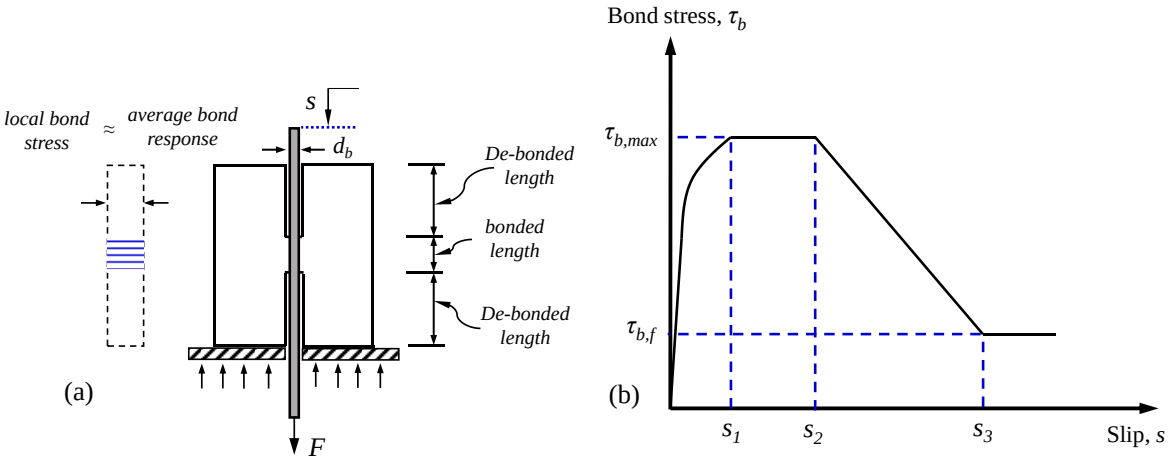

Figure 5-1 Global bond performance (a) typical pull-out test on short anchored bar (b) bond stress-slip behaviour

In contrast, when the bonded length is relatively large ($L > 10d_b$) (Ruiz et al. 2007), which is the case for a typical real RC member, the bond stress distribution is not uniform and the slip between the bar and the concrete is no longer constant (i.e., local slip), so the steel strains should be taken into account. In fact, in the case of long anchored bars, the local response of bond at any location is affected by the axial strain state of the bar. Figure 5-2 shows the local bond stress distribution along the reinforcement including the deterioration of bond in the post-yield range of the reinforcing bar.

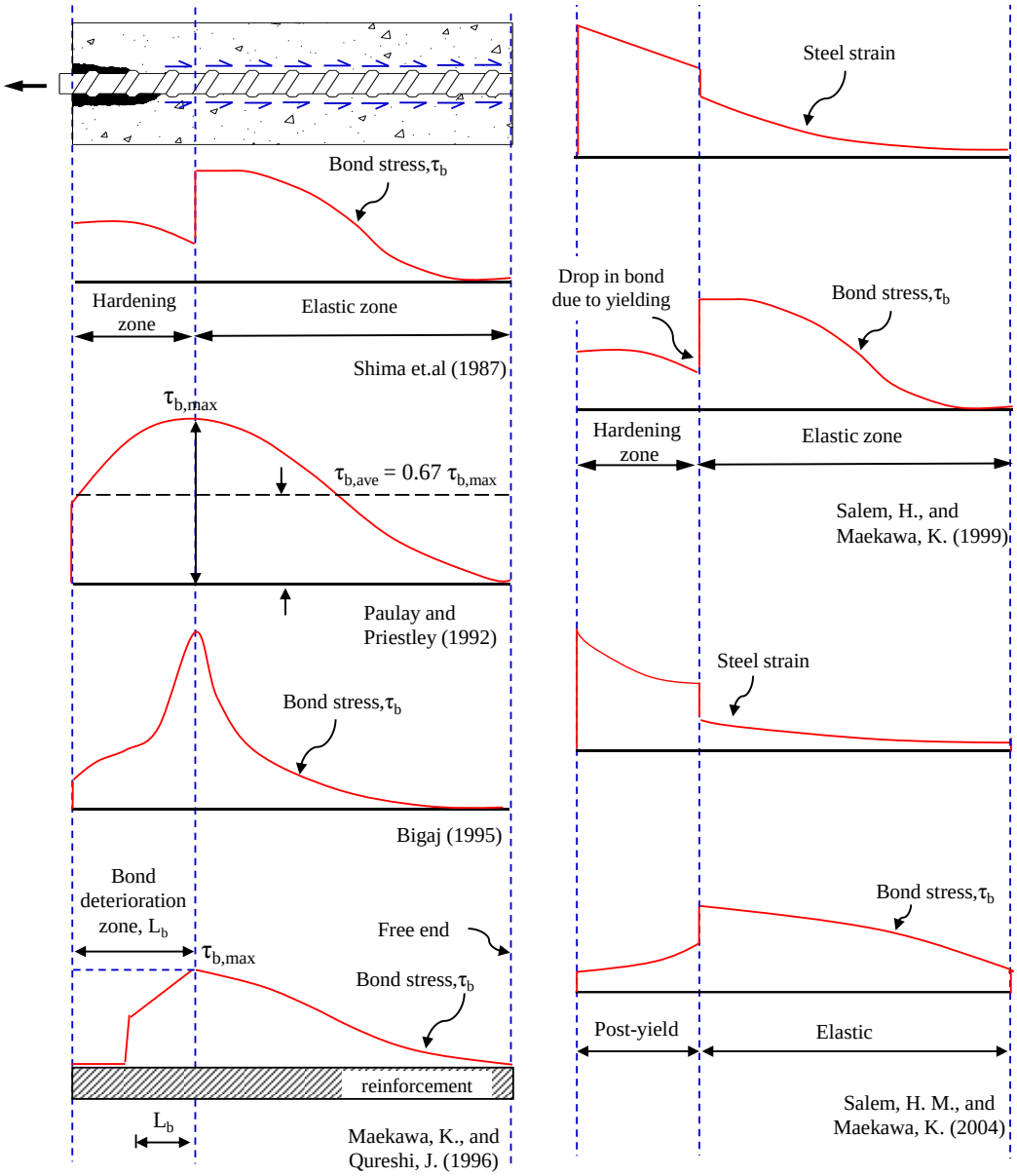

Figure 5-2 Local bond stress distribution allowing for inelasticity

5.1.2 Post-yield bond deterioration models

Although the performance of the bond in the post-yield range of steel strain completely differs from its behaviour in the elastic range, the behaviour of bond-slip in the post-yield region has been the topic of very few studies. Hassan and Hawkins (1977) proposed relationships to predict the pullout strength of an anchored steel bar in the post-yield range, but no measurement was conducted in support of the assumed bond stress distribution. Moreover, no explicit analytical bond stress model in terms of

strain in reinforcement was proposed. Viwathanatepa et al. (1979) reported values of bond stress before and after yielding of steel from the bond test of a beam-column joint, but the bond behaviour in the post-yield range was not investigated. Murayama et al. (1986) studied bond-slip in the post-yield range of reinforcing bars embedded in a concrete footing; however, no formulated relationship was reported. A review of available post-yield bond deterioration models is presented in Table 5-1.

Table 5-1 The review of available post-yield bond deterioration models

Resource	Model	Remarks
Shima et al. (1987)	$\tau(f_c', s, d_b, \varepsilon_s) = \tau(f_c', s, d_b).\, g(\varepsilon_s)$ $\tau(f_c', s, d_b) = 0.73 f_c' \left[\ln(1 + 5000\frac{s}{d_b})\right]^3$ $g(\varepsilon_s) = \frac{1}{1 + \varepsilon_s \times 10^5}$ $s = \begin{cases} \varepsilon_s(2 + 3500\varepsilon_s) & \varepsilon_s \le \varepsilon_y \\ \varepsilon_y(2 + 3500\varepsilon_y) & \varepsilon_y < \varepsilon_s \le \varepsilon_{sh} \\ \varepsilon_y(2 + 3500\varepsilon_y) + 0.047(f_u - f_y)(\varepsilon_s - \varepsilon_{sh}) & \varepsilon_s > \varepsilon_{sh} \end{cases}$	The experiments involved pull-out tests with long bond lengths (50 times the bar diameter), and different steel grades.
Sigrist and Marti (1994)	$\tau(f_c', \varepsilon_s) = \begin{cases} 0.6(f_c')^{2/3} & \varepsilon_s \le \varepsilon_y \\ 0.3(f_c')^{2/3} & \varepsilon_s > \varepsilon_y \end{cases}$	Mean bond stresses for both the pre- and post-yield range of steel strain, obtained based on a non-linear bond slip relationship, dismissing the yielding influence of bond according to force equilibrium.
[a]Bigaj (1995)	$\frac{\tau}{\sqrt{f_c'}} = \begin{cases} 8\left(\frac{s}{d_b}\right)^{0.4} & s \le s_y \\ -80\left(\frac{s}{d_b}\right) + 4.3 & s_y < s \le 0.043 d_b \\ -2\left(\frac{s}{d_b}\right) + 0.95 & s > 0.043 d_b \end{cases}$	The model was developed in terms of slip and did not account for steel strain explicitly.
Engstrom et al. (1998)	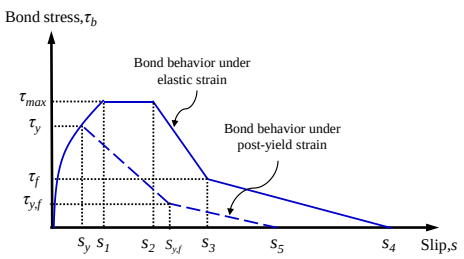	Model adapted from the global response of the anchorage region using pull-out test in which the falling branch starts at the point of the yielding of steel. The values of onset points (τ_y,s_y) are

Resource	Model	Remarks
		dependent on the solution of compatibility and equilibrium equations and could not be predetermined.
Lowes et al. (2004)	$\Gamma(\varepsilon_s) = \begin{cases} 1.0 & \varepsilon_s \le \varepsilon_y \\ 0.1 + 0.9e^{0.4(1-\frac{\varepsilon_s}{\varepsilon_y})} & \varepsilon_s > \varepsilon_y \end{cases}$ $\tau_{post-yield} = \Gamma(\varepsilon_s) \times 1.25\sqrt{f_c'}$	The reduction parameter was calibrated based on experimental pull-out tests from Shima et al. (1987); however, it could not capture the significant drop of bond due to yielding as was observed in the experiment.
Ruiz et al. (2007)	$\tau = \begin{cases} \tau_{b,max}\sqrt{\frac{\varepsilon_s}{\varepsilon_y}}\lambda\left(\frac{x}{d_b}\right) & \varepsilon_s \le \varepsilon_y \\ \tau_{b,max}\frac{\varepsilon_{bu}-\varepsilon_s}{\varepsilon_{bu}-\varepsilon_y}\lambda\left(\frac{x}{d_b}\right) & \varepsilon_s > \varepsilon_y \\ \tau_{b,max} = (f_c')^{2/3} \end{cases}$ square-root model $\tau = \begin{cases} \tau_0\lambda\left(\frac{x}{d_b}\right) & \varepsilon_s \le \varepsilon_y \\ \tau_0 e^{10(\varepsilon_y-\varepsilon_s)}\lambda\left(\frac{x}{d_b}\right) & \varepsilon_s > \varepsilon_y \\ \tau_0 = 0.6(f_c')^{\frac{2}{3}} \end{cases}$ rigid-plastic model	The model was generalized for a long anchorage length on the assumption of the affinity of slip distribution in both short and fully anchored bars at any desired load level.
Wu and Gilbert (2009)	$\lambda(\sigma_s) = \begin{cases} 1 & \sigma_s < 250\ MPa \\ 2 - 0.004\sigma_s & 250\ MPa \le \sigma_s \le 500\ MPa \\ 0 & \sigma_s > 500 MPa \end{cases}$ $\tau_{post-yield} = \lambda(\sigma_s) \times \tau_{b,max}$ $\tau_{b,max} = 2.5\sqrt{f_c'}$	The reduction factor does not take into account the steel strain and is defined based on specific steel material used in the study (i.e., grade 500 normal ductility steel with nominal characteristic yield stress of 500 MPa).
[b]Model Code 2010 (MC 2010)	$\Omega_y = \begin{cases} 1 & \varepsilon_s \le \varepsilon_y \\ 1 - 0.85(1 - e^{-5\left(\frac{\varepsilon-\varepsilon_y}{\varepsilon_u-\varepsilon_y}\right)^b}); b = \left(2 - \frac{\sigma_t}{\sigma_y}\right)^2 & \varepsilon_s > \varepsilon_y \end{cases}$ $\tau_{post-yield} = \Omega_y \times \tau_{b,max}$ $\tau_{b,max} = f(bond\ condition, confinement\ and\ failure\ mode)$	The first code-based relationship to account for the influence of yielding of reinforcement on bond behaviour. The value of maximum bond stress ($\tau_{b,max}$) ranges from a minimum value of $5(f'_c/25)^{0.25}$ for unconfined concrete under splitting mode to $2.5(f'_c)^{0.5}$ for good bond condition under pull-out failure mode.

Resource	Model	Remarks
Ashtiani et al. (2013)	$\tau = \begin{cases} \tau_y \left(\frac{s}{s_y}\right)^{\alpha} & 0 \le s \le s_y \\ \tau_y & s_y < s \le s_{sh} \\ (\tau_{max} - \tau_y) \times \left(\frac{s - s_y}{s_1 - s_{sh}}\right)^{\beta} + \tau_y & s_{sh} < s \le s_1 \\ \tau_{max} & s_1 < s \le s_2 \\ \tau_{max} - (\tau_{max} - \tau_f) \times \left(\frac{s - s_2}{s_3 - s_2}\right) & s_2 < s \le s_3 \\ \tau_y & s > s_3 \end{cases}$	The model was developed from the pull-out test in terms of slip and did not account for steel strain explicitly. No bond stress measurement was made along the length of the reinforcement, and bond stress-slip relationships were established based on measuring the load on the loaded end, and slip on the unloaded end of a steel bar protruding from a concrete block.
Santos and Henriques (2015)	$f(\varepsilon_s) = \begin{cases} 1 & \varepsilon_s \le \varepsilon_y \\ e^{-50\varepsilon_s} \ge 0.25 & \varepsilon_s \ge \varepsilon_y \end{cases}$ $\tau_{post-yield} = f(\varepsilon_s) \times 1.25\sqrt{f_c'}$	The model was calibrated from experimental results by Mayer and Eligehausen (1998) who had studied inelastic bond behaviour of RC columns subjected to monotonic tension only axial loading.
Zhou et al. (2017)	$\tau(\varepsilon_s) = \begin{cases} \tau_y \left[\frac{\varepsilon_s(2+3500\varepsilon_s)}{\varepsilon_y(2+3500\varepsilon_y)}\right]^{\alpha} & \varepsilon_s \le \varepsilon_y \\ \frac{\tau_y}{\left(e^{\left(1-\frac{\varepsilon_u-\varepsilon_s}{\varepsilon_u-\varepsilon_y}\right)}\right)^{c}}; c = 2 + \left(\frac{600}{(f_c')^2}\right)^{\pi} & \varepsilon_s > \varepsilon_y \end{cases}$ $\tau_{post-yield} = \tau(\varepsilon_s) \times 1.1(f_c')^{2/3}$	The model adopted from Shima et al.

Note:

[a]the model is presented for good confinement condition

[b]different values for the maximum bond stress with respect to bond conditions and failure modes (i.e., pull-out or splitting)

a = height of lug

d_b = bar diameter (mm)

f_y = yield strength of steel (MPa)

f_u = tensile strength of steel (MPa)

f'_c = compressive strength of concrete (MPa)

$g(\varepsilon_s)$ = reduction function to account for the effect of steel strain

s = slip between concrete and bar (mm)

s_y = slip value at onset of steel yielding

Ω_y = reduction factor due to yielding

ε_{bu} = bond ultimate strain ($\varepsilon_{bu} = 4a/d_b$)

ε_y = yield strain of steel

ε_s = steel strain

ε_{sh} = steel strain at the onset of strain hardening

σ_y = yield stress of steel bar

σ_t = tensile strength of steel bar

τ = bond stress (MPa)

All the previously mentioned studies recognize the deterioration of bond due to yielding of the reinforcing bars; however, most focus on axial push/pull-out of rebar in a RC component and there are some inconsistencies in the value of τ_{max}. In addition, there are some gaps regarding one or more of the following items: (a) the slip was measured at the unloaded end and no continuous strain measurement was obtained throughout the length of reinforcement; (b) the bond test specimen was a concrete block with one reinforcing bar in the middle, and no bond test resembling the real RC structural component was conducted; (c) due to limitations with the measuring instruments, the location along the bar where yielding occurs was not accurately determined; (d) the effects of stirrups and confinement were not considered; (e) there is no study that correlated the bond deterioration with applied drift levels.

5.1.3 Current Methods for Assessing Bond

To evaluate bond deterioration, some indirect and direct techniques have been developed in the past. Indirect methods consist of a range of nondestructive testing techniques: acoustic emission (AE) techniques (Balázs et al. 1993), contact electrical resistance (Cao and Chung 2001), and piezoelectric elements (Wu and Chang 2006) to assess damage to the bond. The shortcoming of indirect techniques is that they merely evaluate bond deterioration qualitatively, while for quantitative investigations, there is a need for strain measurements on reinforcement. Appendix A provides a thorough description of different methods.

Direct techniques use strain measurement in the reinforcement for bond evaluation (Figure 5-3). In the first method, as illustrated in Figure 5-3a, the relative displacement between concrete and steel is measured using a dial gauge or spring-loaded potentiometer attached to the protruding portion of the steel bar at the unloaded end of the test specimen (Abrams 1913). In the second method, the slip of reinforcement against concrete can be measured using an extensometer positioned between two fixed points along the steel bar (Figure 5-3b) (Watstein 1947; Hawkes and Evans 1951). The third method measures strain on the reinforcing bar using strain gauges rather than using displacement measurements (Mains 1951; Bernander 1957; Perry and Jundi 1969; Nilson 1972; Mirza and Houde 1979; Viwathanatepa et al. 1979; Lahnert et al.

1986; Maekawa and Qureshi 1996; Kankam 1997). Different configurations of strain gauges on reinforcement are illustrated in Figure 5-3c.

The first method is used to measure the displacement of the unloaded end, providing global slip information. The second technique is also implemented for determination of global slip because the long gauge length does not allow for the detection of local variations of stress and deformation.

In the case of the third method, although the use of strain gauges closely spaced on the reinforcing bars showed great potential to measure strain locally, it has disadvantages which cannot be fully eliminated in practice. Strain gauges are limited in the amount of data they can collect, the cumbersome installation process, and bulky wiring. As point sensors, strain gauges can only obtain data about critical points, and no data can be collected between these points. Besides, inability to provide reliable strain in the plastic region due to separation from reinforcement (Motra et al. 2014), and the need for a bundle of cables in the case of using a large number of strain gauges, makes it less favorable for accurate bond measurement in an actual RC member. In addition, as seen in Figure 5-3c, due to milling and grooves, the projected rib areas are reduced, resulting in partial loss of cross section and loss of bond between the bars and surrounding concrete. Moreover, in the case of studies in which reinforcements were longitudinally sliced and re-attached, the behaviour seems not to be representative of real performance of intact reinforcing bars.

Having reviewed the capabilities of conventional measuring techniques, many were found to be unsatisfactory for the goals of this study. Therefore, state-of-the-art technology, based on fibre-optic sensing, was used to capture a continuous strain profile in both the reinforcement and concrete along the length of the RC specimens. The technique offers unique benefits including: the ability to directly measure strain in steel and concrete; the small size of fibres, which significantly reduces the loss of bond area; high measurement accuracy (±25με); corrosion resistance; low cost of the fibre; and insensitivity to humidity.

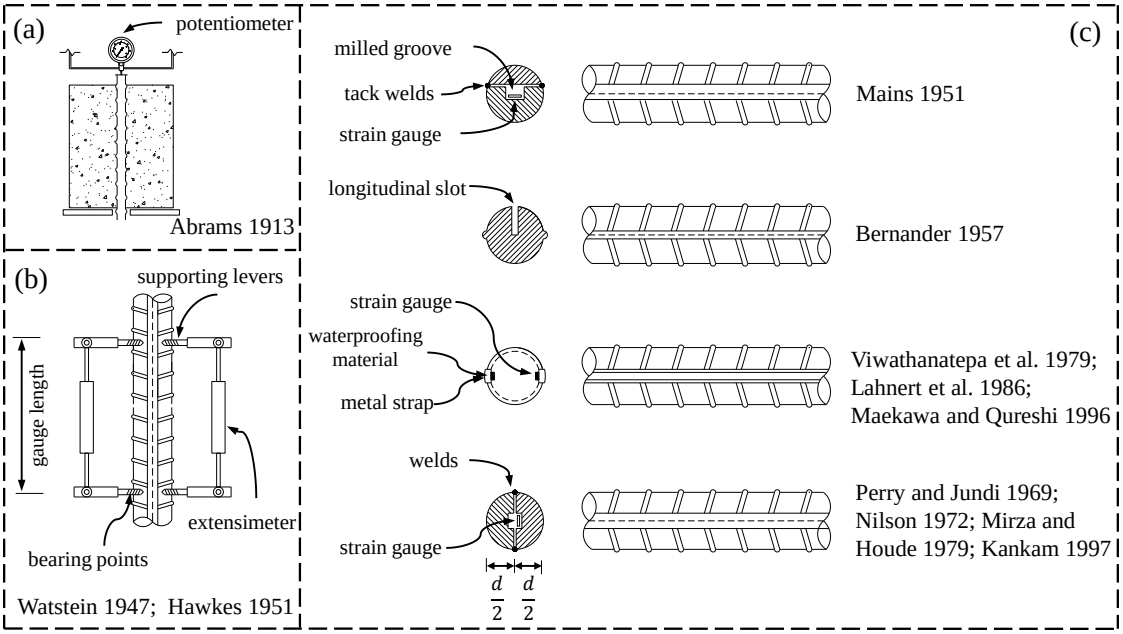

Figure 5-3 Techniques to measure displacement/strain in reinforcing bars for bond calculation

5.1.4 Background to fibre-optic strain sensing

Fibre-optic strain-sensing systems (FOSSS) employ optical fibres as the sensing elements (i.e., sensor) to measure strain. By applying loading demand, the fibres are subjected to extension or contraction. The deformation of the fibres will cause the distance between the imperfections to change, which subsequently alters the frequency of the backscattered light. The characteristics of the backscattered light are measured before and after applying loading, analyzed and then converted to strain data.

A wide variety of fibre-optic strain-sensing systems (FOSSS) have developed over recent decades. FOSs are mainly recognized under two main categories: discrete and distributed strain-sensing systems. Discrete FOSs such as fibre–Bragg gratings (FBG) (Maaskant and Alavie 1998, Sirkis 1998) and Fabry–Perot fibre sensors (Claus et al. 1993) measure strain at specific positions, resulting in single-point strain readings similar to conventional strain gauges. Alternatively, distributed strain-sensing systems, based on the concept of measuring light backscatter, can provide continuous measurements along the entire length of the fibres.

For distributed strain-sensing systems, when a light pulse is sent along an optical fibre, the pulse interacts with the fibre core and a portion of the light is reflected back at every point. Once the light is backscattered, it is decomposed into three distinct spectral components: Rayleigh, Raman and Brillouin. Rayleigh scattering is due to the interaction of light with imperfections in the fibre core, while Raman backscattering is caused by thermal molecular vibration. In the case of the third spectral component, Brillouin backscattering is attributed to photon–phonon interactions (Henault et al. 2012). By applying loading demand, fibres are subjected to extension or contraction. The deformation of the fibre will cause the distance between the imperfections to change, which subsequently alters the frequency of the backscattered light. The characteristics of the backscattered light are measured before (as a reference) and after applying loading, are analyzed and then converted to strain data.

There are two main distributed sensing technologies with respect to using either Brillouin or Rayleigh backscatter techniques. Brillouin-based systems employ the frequency of the returning light wave and offer strain measurement along kilometers of fibre, up to 200 km in length (Connolly 2006). Brillouin-based systems generally utilize two main methodologies for interrogating data: Brillouin optical time domain analysis (BOTDA) (Horiguchi and Tateda 1989), or Brillouin optical time domain reflectometry (BOTDR) (Horiguchi et al. 1995). The significant disadvantage of a BOTDR-based system that restricts its application for localized degradation detection, is its strain and spatial resolution. Depending on the cable, method of installation and length of measurement, the spatial resolution can vary from 1 to 4 m (Connolly 2006). A study conducted by Klar et al. (2006) reported, in the case of BODTR, that although the readings were recorded every 5 cm, the analyzer measured the average of strain along about one metre of gauge length. Mohamad et al. (2011) also reported spatial resolution of every half meter for inclinometers to derive shear force data. In the case of BOTDA, accuracy and spatial resolution, is much better, however, the main downside to BOTDA is the requirement for access to both sides of the cable. Rayleigh-based systems measure Rayleigh backscattered light— using an optical backscatter reflectometer (OBR). OBR-based systems have shown great potential to deliver high levels of strain accuracy (spatial resolutions better than 10 cm for sensing lengths greater than 1 km of

optical fibre), which gives them an advantage when detection of localized change in strain is needed (Kreger et al. 2007).

The implementation of an OBR-based system for damage detection purposes in civil structures is quite new and instances in the literature are limited. Güemes et al. (2010) reported the first successful application of this technology to detect the location and the load corresponding to the onset of buckling, as well as the results of delamination detection in a composite plate of a 40 m long wind turbine blade. Villalba and Casas (2013) also investigated the potential of OBR-based systems for the detection of cracks in the concrete slab. Regier and Hoult (2014) investigated the performance of distributed fibre-optic strain-measurement technology during a load test on an RC bridge. In another study by Regier and Hoult (2015), this technology was effectively used to detect simulated pitting corrosion. Most recently, Davis et al. (2016), Davis et al. (2017) and Davis et al. (2017) used distributed strain sensing to investigate the effect of corrosion on bond performance of singly reinforced RC specimens under tension.

5.2 Experimental program

5.2.1 Background to fibre-optic strain sensing

The specimen was built at half scale, representative of a typical RC beam designed according to New Zealand code of practice for the design of concrete structures (NZS 3101:1982). Figure 5-4 shows the configuration of reinforcing bars, stirrups and fibre optics in the test beam. The sizes of the fibres were enlarged to be visible and are not to scale. As seen, stirrups were placed closer at support side to provide more ductility and seismic performance. This configuration results in better confinement, enhancement of carrying capacity, and reduction in the spalling of concrete. The cross section of the beam was 350 mm in depth by 250 mm in width. The longitudinal and transverse reinforcement used in the specimen were D16 and D10 grade 300E deformed bars, respectively. The stirrups for the test specimen were closed with 135° hooks on both ends. The yield strength was determined from a tensile test on the coupon rebar as 293 MPa. The concrete compressive strength (f'_c) was found to be 35 MPa at

the age of 28 days. Table 5-2 provides the properties of steel and concrete used in this study.

Table 5-2 material properties

Material	
Concrete compressive strength at 28 days, f'_c (MPa)	35
Yield strength of reinforcing bar (Grade 300E), f_y (MPa)	293
Ultimate strength of reinforcing bar (Grade 300E), f_u (MPa)	487
Yield strain, ε_y	0.00147
Strain at the onset of strain hardening, ε_{sh}	0.0242
Ultimate strain, ε_u	0.215

Note: all strain/stress values are associated with engineering stress-strain curve

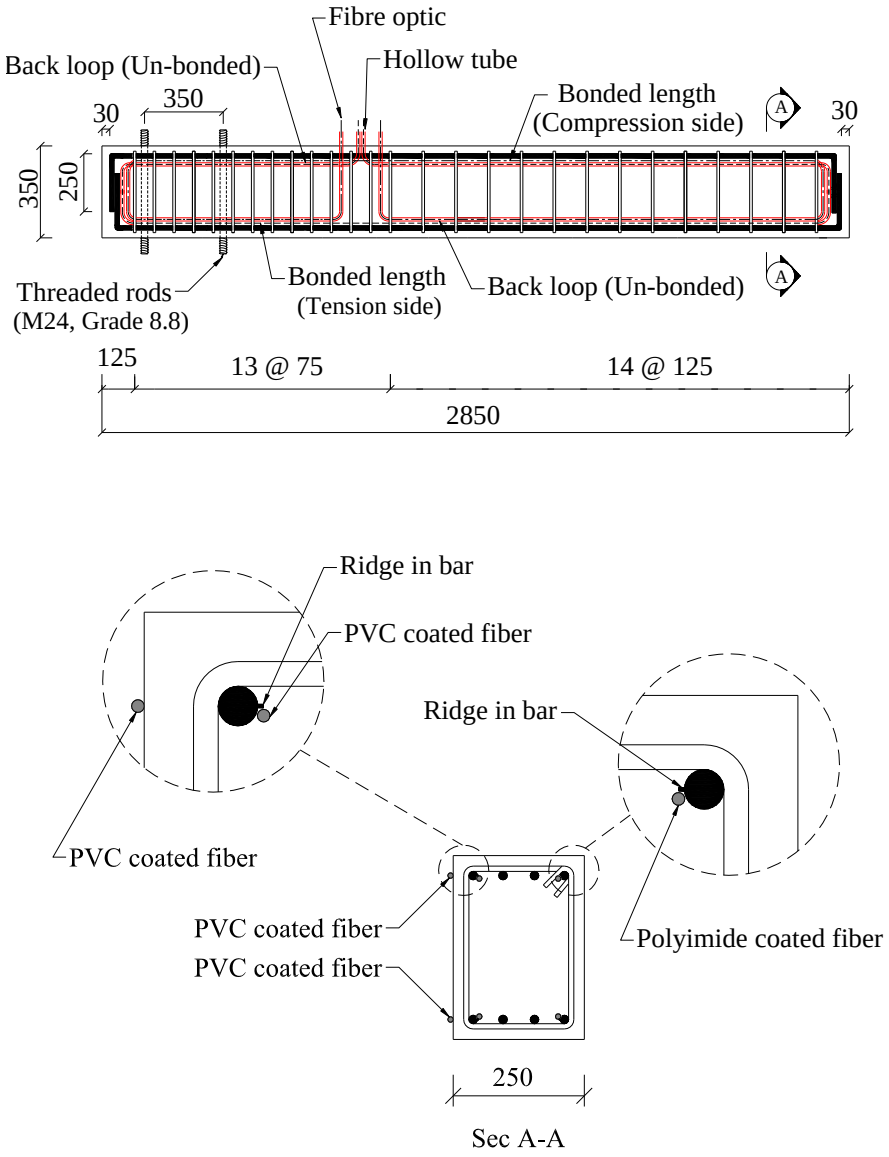

Figure 5-4 Test specimen and fibre optic arrangement

5.2.2 Fibre sensing

Two different types of optical fibres were used in this study: PVC-coated, tight buffer fibre optic cable (TLC tight buffer) and Polyimide-coated fibre (OFS ClearLite® POLY 1310). The former consists of a laser-optimized optical fibre (Corning InfiniCor 300), jacketed with a flame retardant PVC. The former was used for strain

measurements both on the concrete surface and the reinforcement, while the latter was only used on the reinforcement.

The PVC-coated optical fibre consists of five parts: glass core, glass cladding, inner primary coating, outer primary coating and PVC jacket. In the case of polyimide-coated fibre, the core and cladding are manufactured similar to PVC-coated fibre; however, the fibres are covered with the coating consisting of acrylate or PyroCoat. The core allows light to run along the fibre's length. The cladding causes light to be confined to the core and prevents any refraction while transmitting light. The coating shields the cladding coated core to protect against abrasion, environmental exposure and mechanical loading. The coating enhances the strength of the assembly to withstand applied forces, particularly for practical purposes.

Previous studies (Regier and Hoult (2014), Hoult et al. 2014) have reported that the PVC-coated fibres were the most appropriate option for strain measurement on a concrete surface. However, the nylon coating and the core are not chemically bonded to each other. Thus, the strain is transferred through shear that is dependent on friction between the core and coating, which can result in localized slipping of the coating over the core during applied loading. This subsequently introduces inaccuracy in the strain measurements at points of strain concentration. Although incompatibility in strain transfer is a substantial drawback for this type of fibre, it is exactly what justifies its application for strain monitoring in concrete. That is because it is less vulnerable to physical damage due to steep strain gradients, which makes it functional even at crack locations. In the polyimide-coated fibre, strain is transferred between the coating and core reasonably well, so it can offer precise strain measurement even at localized areas of deterioration. The main disadvantage of this type of fibre relates to the cross-sectional area and its second moment of area, which are fractions of a millimetre. This makes the fibre extremely fragile and delicate, requiring care in handling and installation to prevent breakage. The polyimide-coated fibres are also costly, approximately 20 times more expensive than the PVC-coated fibres per unit length (which are about 5.1 NZD versus 0.25 NZD per meter). Figure 5-5 shows a cross section and the geometry of layers for typical optical fibres used in this study.

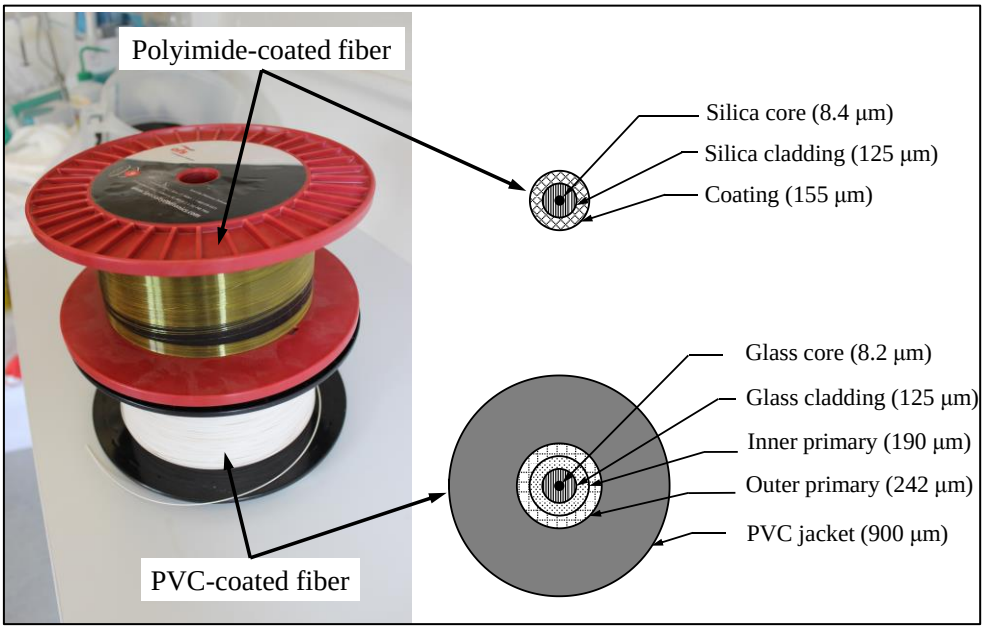

Figure 5-5 Schematic of fibre optic components (a) PVC -coated (b) polyimide-coated

5.2.3 Instrumentation

Figure 5-6 illustrates the whole sequence of steps for instrumentation in this research. It should be noted that photos used in this figure are associated with the PVC-coating as it provides a white surface which is more visible for explanation purposes. The same process was also carried out for the polyimide-coated fibres. To fully capture strain along the length of reinforcement, the fibres were attached to each longitudinal bar, prior to making the reinforcement cage, otherwise, there would be no possibility of gluing the optical fibres to the longitudinal bars because of the presence of the stirrups.

Four longitudinal corner reinforcement bars were individually equipped with fibre optics. To provide an even and smooth surface, each longitudinal bar was secured in a table clamp, and a hand linisher was used to clean any coatings or rust along the longitudinal ridge of the steel bar. The surface was then wiped with acetone to remove oil and dust (Figure 5-6a). As previously illustrated in Figure 5-4, two types of fibre optics (i.e., PVC-coated fibre and polyimide-coated fibre) used to measure strain of the longitudinal bars, positioned in the corners of the beam section. A cyanoacrylate

adhesive (Loctite 435) was used to glue the fibre to the surface along the full length of the reinforcement (Figure 5-6b).

To protect the optical fibre during the making of the cages and the casting on the concrete, a layer of two-component epoxy (JB weld) was subsequently used, and maintained at room temperature for 24 hours to provide a layer of cover over the fibres to protect them from being damaged (Figure 5-6c). The spare lengths of fibres were coiled at each end of the reinforcing bar and safely stored for later splicing and connection purposes (Figure 5-6d). Once the attachment of fibres was completed, the reinforcing -bars were assembled into a cage. The stirrups were positioned such that hooks were located every 90° for seismic considerations. To avoid pinching of the optical fibre, a piece of rubber mastic tape (Scotch 2228) was used at the top of the protective coat where a tie wire secured the stirrups (Figure 5-6e). At both ends of each bar, where the fibres were no longer attached to the bar, plastic tubes were taped (SB-tape) on the fibre to protect it (Figure 5-6f). Finally, the fibres were exited from the mid-height, protected in narrow, hollow plastic tubes, looped from each end. It should be noted that gluing fibre to reinforcement and covering it by protection layer is not perfectly ideal for measuring bond. However, the level of interference introduced by fibre compared to conventional techniques used for measuring strain in bar such as strain gauges is minimal. Each strip of epoxy coating covered approximately 10% of the bar circumference but was installed so that the ribs were still exposed. This is in line with the procedure reported by Davis et. Al (2017). This effect will be further reduced by increase in the bar size.

The longitudinal bars to which optical fibres had already been attached were caged such that the ridges were positioned in parallel to the strong axis of the RC beam specimen. This technique provided more protection during the pouring of fresh concrete. Once the cage was completed, the soundness of fibres was examined using a fault locator, in case of breaks, bends or any other causes of signal loss. If the laser pulse sent from one end of the fibre was seen from the other end, it was considered physically undamaged. However, it was later found that a physically sound fibre may not always serve as a fibre sensor. So, the physical intactness is a requisite condition, but not sufficient for serving as a fibre sensor.

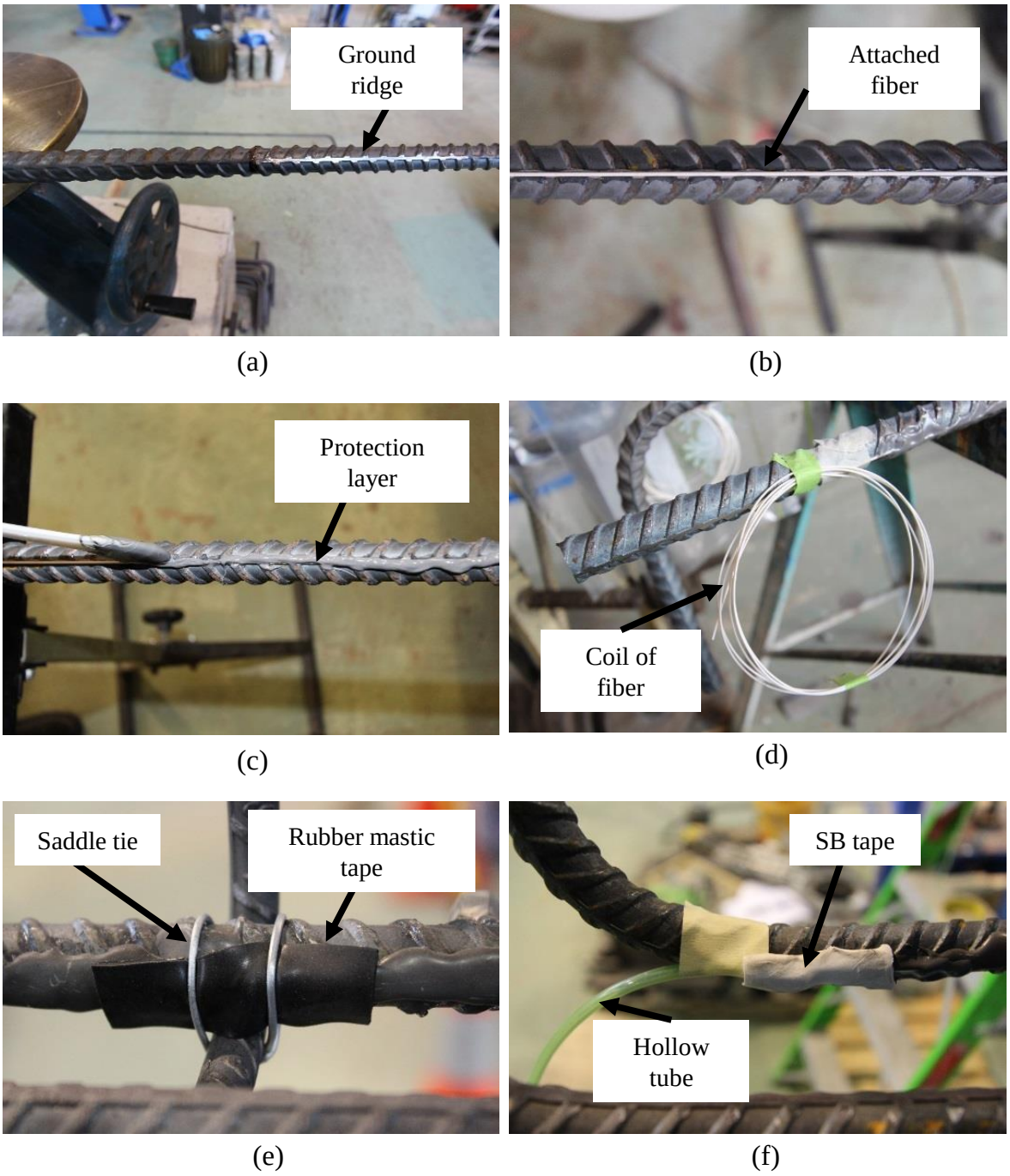

Figure 5-6 Fibre optic installation

Once the RC beam was cast, PVC -coated fibres were attached to the concrete surface on both the tension and compression sides, at the same position as the internal top and bottom reinforcement were located, using a two-part epoxy (Loctite E-20HP).

In the next stage, splicing were conducted to connect either two optical fibres or to make a connection between an optical fibre and a patch cable, which is essential for plugging into a logger. For this, the fibres end were initially cleaved using high precision cleaver (Fujikura CT-30) and then spliced using arc fusion splicer (Fujikura-FSM-60S). Once splicing was completed, two criteria— loss and likelihood of formation of bubble—were checked to see if the splicing was acceptable. The splicing was redone either if the loss estimated on the screen was above 0.1 dB or if there was a warning of a bubble in the fibre.

5.2.4 Strain measurement

The strain was measured using an optical distributed sensor interrogator (LUNA ODiSI-B) along the length of fibres previously attached to the test specimen. The ODiSI-B employs swept-wavelength coherent interferometry to measure strain by means of an optical fibre as the sensor. The system allows for strain measurement as fine as 0.65 mm along the fibre length with a sample acquisition rate up to 250 Hz. For the current study, measurement was conducted every 2.6 mm with an acquisition rate of 50 Hz, and a maximum sensing length of 20 m. Once the sensors were configured, a scan was made just before starting the test, and the strain measurements were zeroed. This provided a reference readings to which subsequent measurements at each step of loading were compared.

It is worth mentioning that the quality of cross-correlation between strain measurements at each step and the reference scan is evaluated by the spectral shift. When the fibre undergoes a change in strain, the reflection spectrum at that location in the fibre will experience a shift in the optical frequency. This shift is proportional to the strain change at that location. The spectral shift quality varies from 0 to 1 where 1 denotes a perfect correlation, and 0 means no correlation. The validity of the spectral shift measurement is described by the quality threshold. Any data point that did not have a quality above the specified value (0.38 by default) was considered erroneous (Luna Innovations Incorporated 2016). Figure 5-7 shows Optical Distributed Sensor Interrogator (ODiSI-B) system employed in this research.

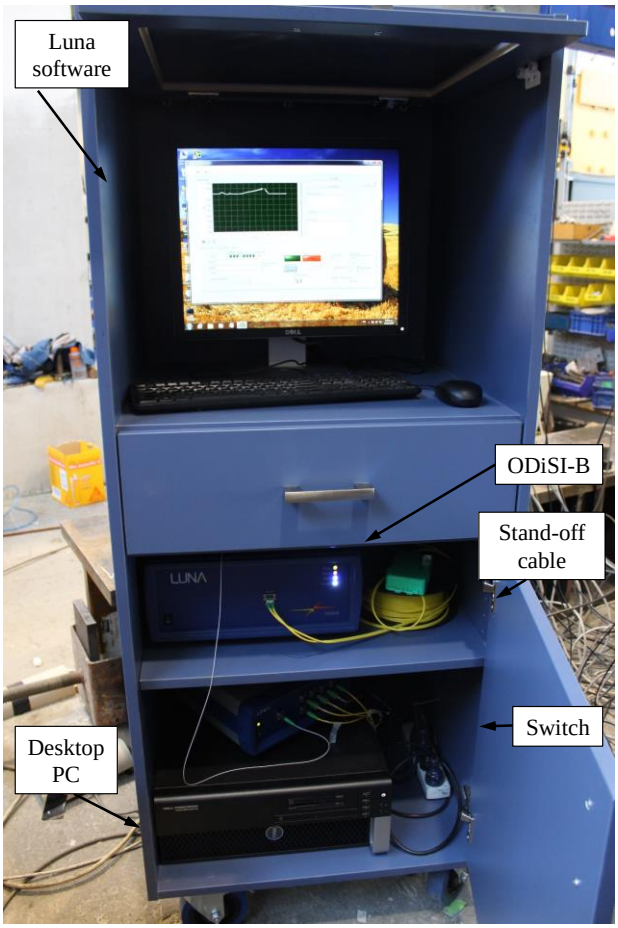

Figure 5-7 Optical Distributed Sensor Interrogator (ODiSI-B) system

Despite the FOS logger configuration offering a 50 Hz sensing frequency, the strains were just measured on a displacement-change basis, at each increment of 0.1% in drift level. It is also worth mentioning that, the optical distributed sensor interrogator used here (i.e., ODiSI-B) is able to measure strain in a tared sensor up to 0.01 of strain. Thus, to measure strain at higher value reached in this experiment, sensors were re-tared at some stages during strain readings. Strains were then accumulated to produce strain profile at desired drift level.

Figure 5-8 illustrates the configurations and components of the data acquisition system used in this study. As seen, the distributed sensing system requires a termination to provide a low reflection at the end of the sensor, which is of great importance for good performance. The fibre was therefore looped in such a way as to reduce the end reflection of the sensor with loop diameter required to be less than 5 mm.

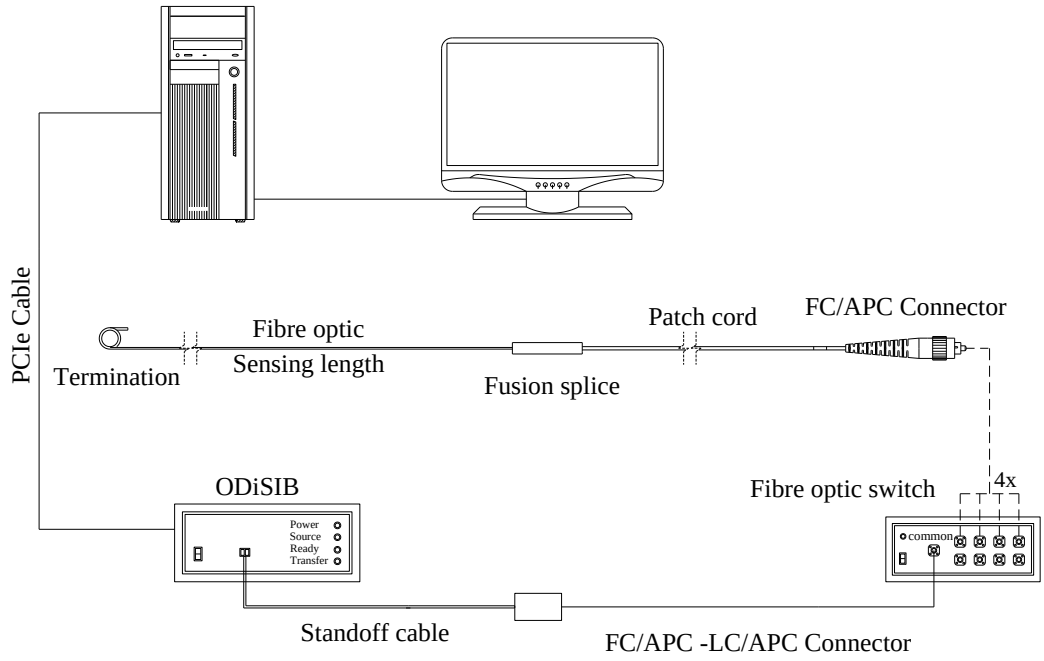

Figure 5-8 Illustration of data acquisition system

The specimen was also instrumented with linear variable displacement transducers (LVDTs) and strain gauges in an attempt to compare results of all three measuring methods. Strain gauges (FLA-3-11-3L TML) were attached using CN cyanoacrylate adhesive on specified spots on the longitudinal reinforcement. The ridge of reinforcing bar was ground and prepared using a grade 180 sandchapter chapter, and finally cleaned with acetone. Strain gauges were coated by applying hot melted microcrystalline solid wax over the area with a brush to provide moisture-proofing, and covered by 3M silicone rubber for mechanical protection (Figure 5-9a). In the case of LVDTs, to measure strain in reinforcement as accurately as possible, a coupler was welded to bar prior to casting protruding from cage to allow for appropriate steel elongation measurement. This ensured the strain readings are associated with embedded steel (Figure 5-9b).

(a) (b)

Figure 5-9 Instrumentation (a) strain gauge; (b) LVDTs

5.2.5 Test setup and loading protocol

The test setup consisted of reaction frames made from hollow steel sections, including lateral bracing in the direction of the loading. To prevent any out-of-plane movement during testing, horizontal beams were attached to the testing frame on either side of the specimen.. It is worth mentioning that the RC cantilever beam was tested vertically because of the actuator orientation. The specimen was supported in a steel footing, made of a wide flange I-shaped high capacity column section with the depth of 500 mm and flange width of 490 mm (500 HCC 413, New Zealand steel). The specimen was secured between two steel blocks, using four threaded rods (M24, Grade 8.8), already cast into the specimen. Once the specimen was fastened to steel footings, each block was secured to the strong floor using four high-strength M36 bolts. Hilti RE-500 epoxy was then used to fully fill the gap between the end plate (welded to footings) and outer face of the specimen.

The lateral quasi-static monotonic pulling loading was applied at the clear height of 1570 mm above the steel footings. The beam was subjected to drift ratio, starting from zero with 0.025% drift step size, up to 1.0% drift, followed by increments of 0.05% until failure. A string potentiometer was used to record the displacement occurring at the level of applied loading. A 400 kN capacity hydraulic actuator with stroke of ±210 mm was employed to apply lateral loading. The applied load was measured using the load cell positioned in the head of actuator. Figure 5-10 shows the configuration of the test setup and experiment.

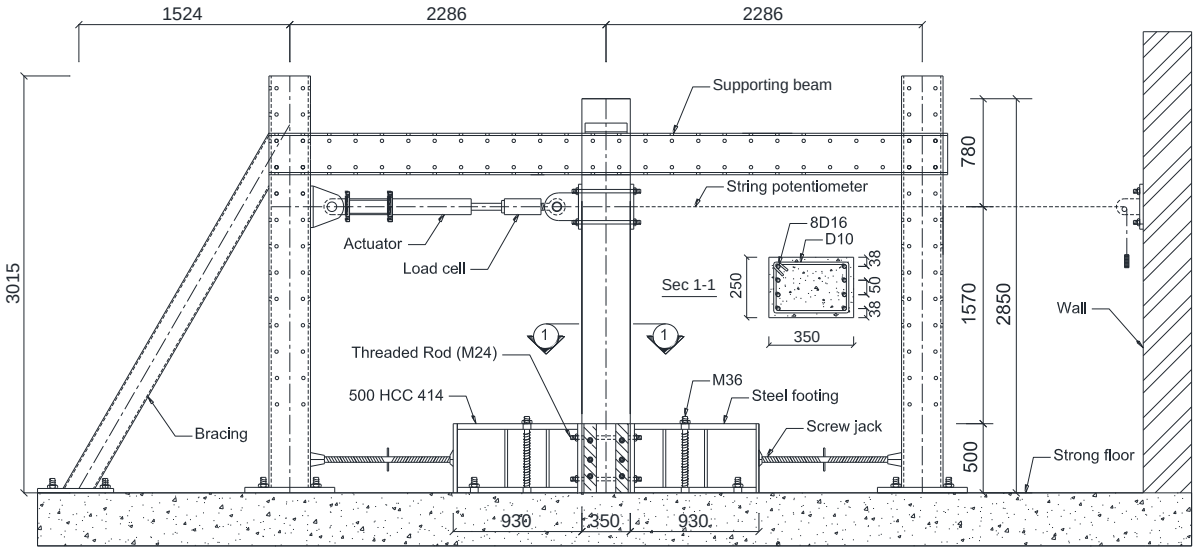

Figure 5-10 Test setup and specimen details

5.3 Results and discussion

5.3.1 Strain profile in reinforcement

Figure 5-11 shows the measured strains from the embedded fibres, bonded along the length of the tensile reinforcement, at 1%, 2%, 3% and 4% drift levels, studied in this investigation. The strain values increase from almost zero at the tip of the beam to the peak value at the datum (i.e., where the strain reaches its maximum value) exactly above the steel footing, which is representative of a fixed-end support. Strain then decreases continuously beyond this point, confirming the concept of strain penetration at the interface between a structural member and its supporting element. Strains in the tensile reinforcement decrease gradually up to the base at which longitudinal bars bent into the shape of a hook. When the drift level is low, the strain distribution almost follows a linear triangle pattern; however, with an increase in the loading demand, the strain profile tends to be a nonlinear distribution. It should be noted that strains were not measured beyond 4% drift as the fibres failure occurred.

As seen in Figure 5-11, the yield length (l_y)—the length over which strain exceeds yield strain (ε_y)— is not constant and increases as the drift level increases. The yield length associated with lateral movement of the specimen at 1%, 2%, 3% and 4% drift, with reference to datum, were measured to 580 mm, 730 mm, 790 mm and 960 mm,

respectively. The yield length is, in fact a length over which actual plasticity spreads, and affects the extent of damage along the length of the specimen. In addition, the yield length influences not only the load carrying-deformation capacities of an RC member, but also influence its plastic rotation capacity. That is why, it is critical to ensure ductile behaviour of an RC structure under seismic loading. It is worth mention that, the yield length measured in the current study, is not equal to the plastic hinge length (L_p) which is used to determine plastic rotation and deflection of an RC member on the basis of constant plastic curvature assumption over equivalent length (Park and Paulay 1975).

The extent of yielding that has penetrated the length encased in steel footing, is also shown in Figure 5-11. The maximum length of strain penetration—the length over which strain decreases from peak (i.e., at datum) to zero—was not determined; however, it can be seen that as the drift level increases, the strain penetration length increases. Results show that, the gradient of strain profile below the datum is less steep than that above the datum, possibly due to the close spacing of longitudinal bars and the existence of strain distribution in the hook.

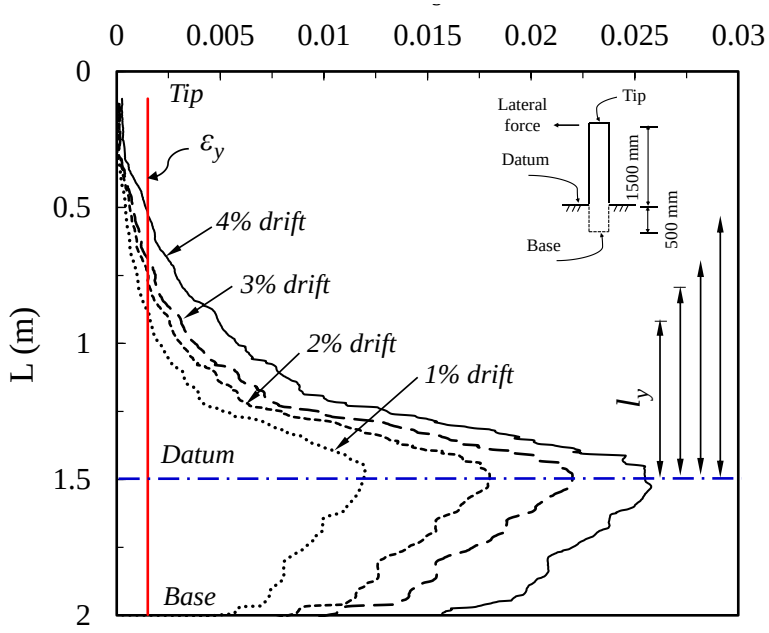

Figure 5-11 Strain profile measured in tensile reinforcement

5.3.2 Strain profile in concrete

Figure 5-12 illustrates tensile strain, compressive strain and crack distribution in concrete surface at four drift levels–1%, 2%, 3% and 4% – over the height of the RC beam. The strain can be seen to increase at the bottom, where the level of damage is significant. The distribution of strain on the compressive side (Figure 5-12a), is less changeable, which implies there is no significant cracking on the compression side In contrast, the strain profile on the tension side (Figure 5-12c), rises and falls, caused by cracks opening over which strain was bridged. The local spikes in the tensile strain profile denote the locations of cracks (C_1–C_{11}), which is in excellent agreement with the experimental crack mapping observed during testing (Figure 7-15b).

The use of polymeric-coated fibres showed great promise in identifying the location and the number of cracks in the specimen. That is because of the higher ductility provided by this type of fibre, which allows for some limited bridging over cracks. However, the value of strain across the crack cannot be precisely measured due to the slippage of the inner sensing core and rubber coating, as highlighted by Hoult et al. (2014). It is worth mentioning that in the areas where cracks were formed too closely (1.25 m to 1.35 m), it is as if merging occurs, and one peak might then appear in the strain profile rather than independent peaks. This happens for the same slipping reason, so the location at which a peak is captured may be a little different from the exact

location of the actual crack. The graph has been plotted up to the top of the steel foundation (0–1.5 m) as the strain in the concrete surface was not measured below that.

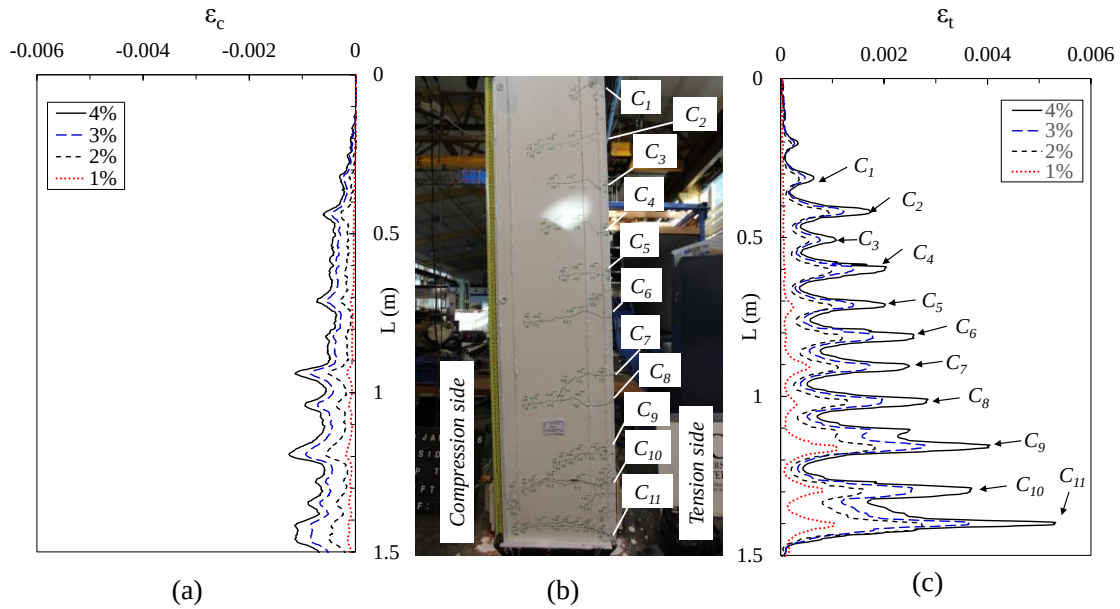

Figure 5-12 Strain profile on concrete surface (a) compression side (b) crack distribution at 4% drift (c) tension side

5.3.3 Assessment of local slipslip

In this study, the local internal slip at any drift level, was defined as the difference between the elongation of the steel bars and the concrete as expressed by Equation 5.1. Based on this definition, the local slip between any two points can be calculated by trapezoidal numerical integration of the strain distribution in tensile steel subtracting the concrete strain over this same length.

$$S = \int_{x=0}^{x=2.6\ mm} (\varepsilon_s - \varepsilon_c)\, dx \tag{5.1}$$

where ε_s = strain in steel bar; ε_c = strain on concrete surface.

Figure 5-13a shows the distribution of local slip along the height of the specimen calculated over each segment of 2.6 mm. It should be noted that no pullout of the tensile reinforcement, in the form of rigid body motion of the bars, occurred in this experiment due to the hooked ends and embedment length provided for the reinforcement bars. Figure 5-13b displays the area enclosed by the strain profile, at each drift level, which is approximately equal to the total elongation of the beam.

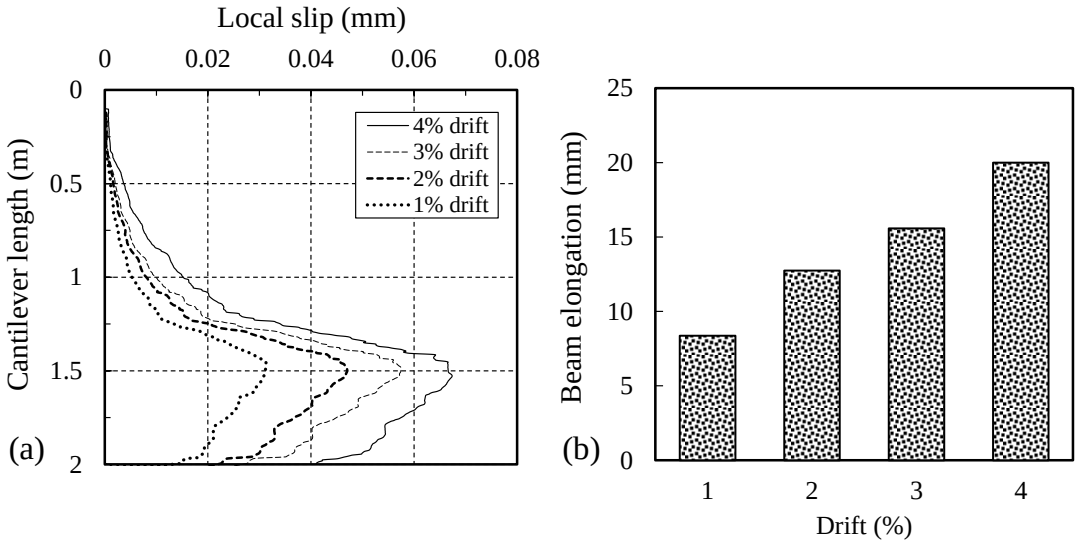

Figure 5-13 Internal slip distribution

5.3.4 Post-yield bond deterioration

To assess deterioration of bond in the post-yield range of steel strain, bond stress, as a first step, needs to be accurately calculated. To calculate bond stresses along the embedment length of a reinforcing bar, three approaches have been used in the past: calculating bond stress based on the slope of force generated in a steel bar (Mains 1951 and Lahnert et al. 1986); calculating bond stress on the basis of the slope of the steel strain curve (Nilson 1972); or calculating bond stress on the basis of the slope of steel stress curve (Shima et al. 1987). Although these approaches may seem similar in the sense that they all rely on direct strain measurements in steel rebar, their applicability is different. While the first two are only appropriate for evaluating bond stress in the elastic range of steel strain, the last is applicable to calculate bond stress in the inelastic

range of steel strain. That is because, in post-yield range of steel, the stress is no longer proportional to strain and the slope of the strain profile does not indicate the bond stress. So, stress profile is needed for bond stress calculation.

Figure 5-14 shows the status of internal forces in a short element along the steel bar. Considering the equilibrium of axial internal forces for this finite segment (dx) will lead to bond stress. In this study, the local bond stress distribution at any location along the reinforcing bar was calculated using the slope of the steel stress distribution at that point using Equation (5.2).

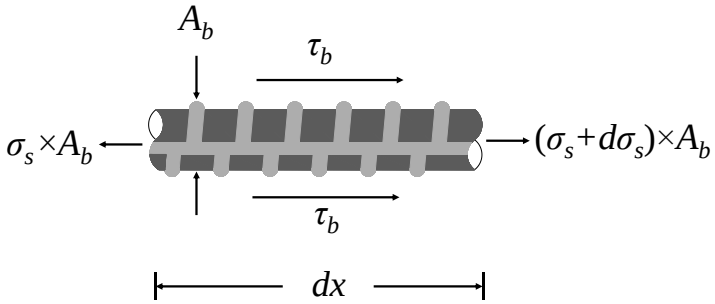

Figure 5-14 Illustration of local bond stress in reinforcement

$$\tau_b = \frac{A_b}{P_b}\frac{d\sigma_s}{dx} = \frac{d_b}{4}\frac{d\sigma_s}{dx} \tag{5.2}$$

where τ_b = local bond stress (MPa); A_b = the reinforcing bar cross-sectional area (mm^2); P_b = the reinforcing bar perimeter (mm); σ_s= axial steel stress; and $d\sigma_s/dx$ = the slope of the steel stress curve at any point.

To determine the axial stress distribution along the entire length of reinforcement, the corresponding stress value for any strain, measured every 2.6 mm, was calculated using the average stress–strain relationship of steel. Using the stress–strain relationship of bare steel for this purpose seemed to be inappropriate. That is because the stress–strain relationship of bare bar obtained from tensile tests in the laboratory is not representative of the stress–strain relationship of steel in an RC member under a combination of internal stresses. Available studies in the literature confirm that the behaviour of steel bar while it is embedded in concrete is distinct from its behaviour when it is tested bare. In fact, while the stress–strain curve of a steel bar tested in a bare

condition shows a significant yield plateau, the average stress–strain curve of steel bar embedded in concrete displays no such yield plateau. Furthermore, the yield stress shifts down compared with the yield stress of a bare bar (Shima et al. 1987; Belarbi and Hsu 1994; Maekawa et al. 2003).

In this work, the analytical model proposed by Belarbi and Hsu (1994) was used to construct the average stress–strain curve of embedded steel bar from the stress–strain curve obtained from a tensile test on a coupon bar identical to longitudinal bars. Figure 5-15 shows the measured stress–strain relationships, as well as the constructed average bilinear stress–strain relationships. Note that, even though the implementation of the average stress–strain curve results in a significant difference in steel stress (up to 2.5 times) at failure, in the range of strain to which an RC member was subjected in this investigation (0.026), the difference in stress values acquired from the two curves was limited to 20%.

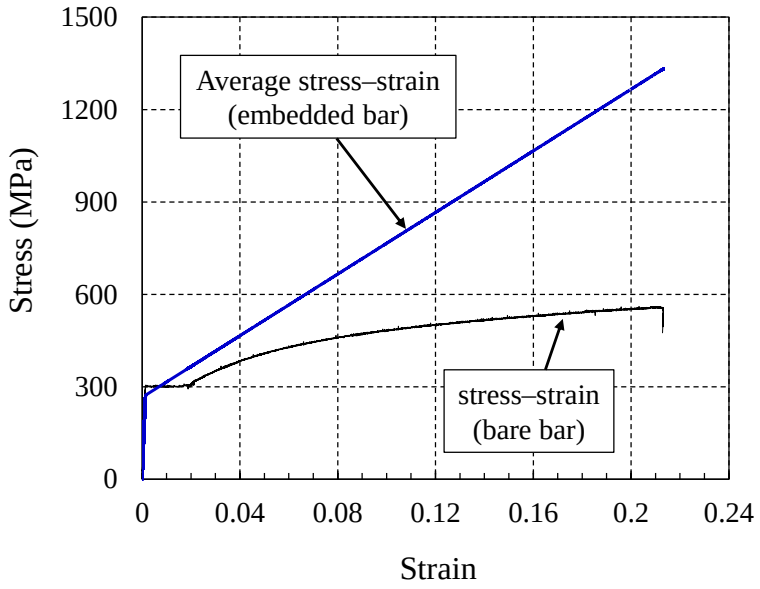

Figure 5-15 Average stress–strain relationship for embedded bars and bare bars

The distribution of the calculated axial stress in the reinforcement over the height of the RC beam at four drift levels is provided in Figure 5-16(a)-(d). There is a significant increase in stress of the steel from the tip of the beam to where yielding of the reinforcing starts. Once the yield stress (σ_y) is exceeded, the stress in the reinforcement continues to increase, but at a lower rate based on the slope of the plastic portion of the bilinear stress–strain relationship adopted in this study. The maximum

stress is reached at the datum where the beam is secured to the connection. After the peak, the stress shows a descending trend due to the diminishing loading demand.

Using Equation 5.2, the bond stress for the various drift levels were calculated and shown in Figure 5-16(e)-(h). As seen, the bond stress increases until the bond strength in the elastic range (i.e., τ_{max}) is attained. Since the slope of the steel stress in the elastic range is higher than the slope of the steel stress in the post-yield range, the bond stress values in the elastic range are much higher than those in the post-yield range. Additionally, once yielding occurs, bond capacity deteriorates and bond stress decreases significantly. As the drift level increases, there is an increase in the yield length which results in an increase in the bond deterioration length (l_{bd}) from $36d_b$ at 1% drift to $45d_b$, $49d_b$ and $60d_b$, for 2%, 3% and 4% drift, respectively. This is significantly higher than the range proposed in the literature described earlier (i.e., $2d_b$ to $5d_b$). The variation in bond deterioration length indicates that the corresponding length depends on the level of applied drift which is associated with the level of inelastic strain in the reinforcement.

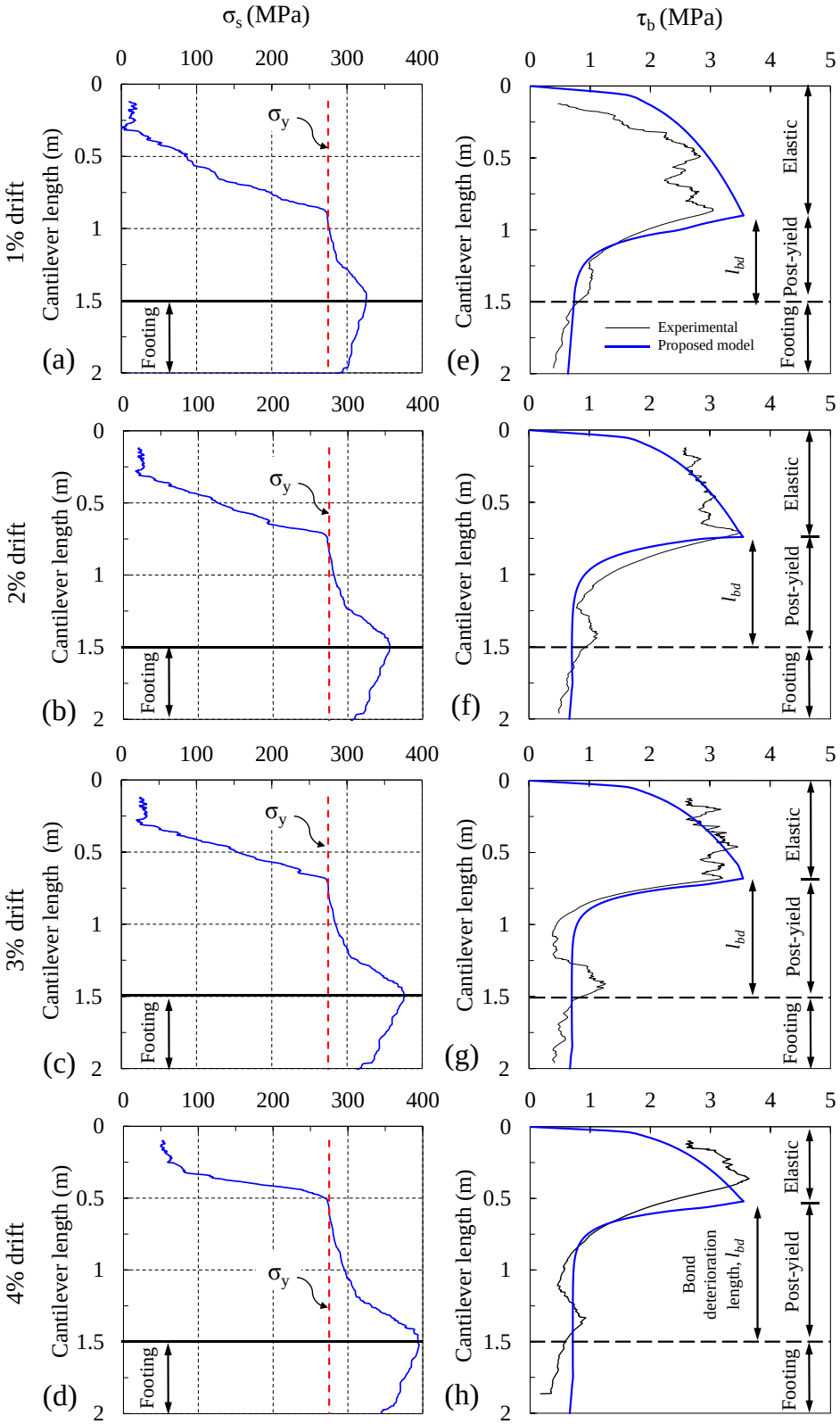

Figure 5-16 Steel stress and bond stress distribution over the height of the RC beam

According to the results of this study, a potential model is tentatively proposed in order to predict more accurately the actual bond stress response along the embedded length of steel bars in a RC member subjected to flexure as follows:

$$\tau_b = \begin{cases} \tau_{max} \left(\frac{\varepsilon}{\varepsilon_y}\right)^{0.3} & \varepsilon_s \leq \varepsilon_y \\ \tau_{max} \cdot \Gamma_y & \varepsilon_s > \varepsilon_y \end{cases} \quad (5.3)$$

$$\Gamma_y = 1 - 0.8\left(1 - e^{0.7\left(1-\frac{\varepsilon_s}{\varepsilon_y}\right)}\right) \quad (5.4)$$

$$\tau_{max} = 0.6\sqrt{f_c'} \quad (5.5)$$

5.3.5 Comparisons of available post-yield bond deterioration models

Figure 5-17 shows the comparison between the proposed models with available post-yield bond deterioration models presented earlier in Table 1. For the purposes of comparison, the following values were used in the models: $\varepsilon_y = 0.0015$; $\varepsilon_u = 0.21$; $\varepsilon_{sh} = 0.019$; $f_y = 293$ MPa; $f_u = 558$ MPa; and $f'_c = 35$ MPa. Note that the value of τ_{max} was calculated based on the individual requirements of each model.

As seen in Figure 5-17 the behaviour of the bond after yielding has a descending trend, so the constant value proposed by Marti et al. (1998) may not be representative of post-yield bond behaviour. Having compared the functions, it seems that the models proposed by Lowes et al. (2004), Ruiz et al. (2007), Wu and Gilbert (2009), Santos and Henriques (2015) and Zhou et al. (2017) overestimate the bond stresses after yielding for a RC member under flexure, while the model proposed by Shima et al. (1987) seems to underestimate bond stress in the post-yield range. Designating the minimum value of bond strength proposed by MC 2010 for splitting failure mode and unconfined condition (i.e., $5(f'_c/20)^{0.25}$), this model seems to have better correlation with the proposed bond deterioration model in this study in terms of start point; however, it does not consider the initial drop in bond stresses in the post-yield range. This also results in an underestimation of the bond deterioration length.

It should be noted that the values of maximum bond stress (i.e., τ_{max}) proposed in the literature are considerably different from each other and range from $0.6f'^{2/3}_c$(Ruiz et al. 2007) to as high as $2.5f'^{1/2}_c$(Wu and Gilbert 2009; MC2010). This discrepancy

affects the rate of decay in the bond stress with the level of strain in the steel, and also it affects the length of bond deterioration. This study showed the maximum bond stress attained in a RC member under flexure can be represented by $0.6f'_c{}^{1/2}$, which is considerably lower than the proposed values of τ_{max} in the literature.

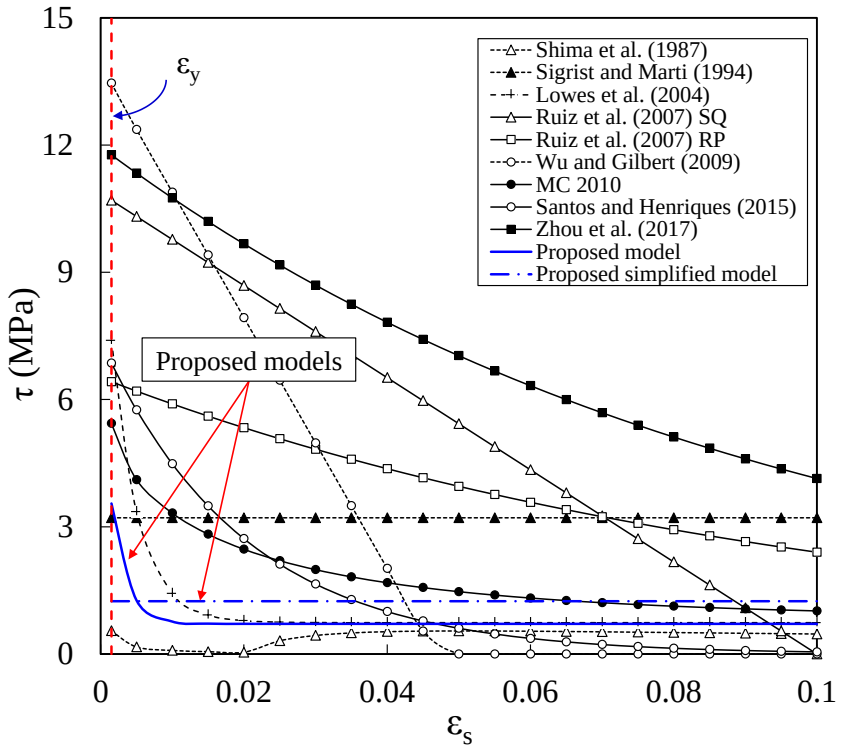

Figure 5-17 Comparison of post-yield bond deterioration models

5.3.6 Simplified assessment of bond using mean stress values

Providing a unique value of bond stress in both pre- and post-yield range of strain without a need for the strain distribution and reduction functions, is of great value from a design perspective. The use of the interfacial fracture energy concept (Haskett et al. 2008) provides the so-called mean bond stress. Figure 5-18a shows the general behaviour of bond in terms of steel strain in the pre- and post-yield range. The area enclosed by the bond stress function (i.e., the hatched area) is referred to as the interfacial fracture energy, and can be determined for any strain (ε^*) using Equation (5.6).

$$G = \int_{\varepsilon=0}^{\varepsilon=\varepsilon^*} \tau(\varepsilon) d\varepsilon \tag{5.6}$$

Using Equation 5.6 and considering the general form of Equation 5.3, the interfacial fracture energy in pre- and pot-yield range is expressed as follows:

$$G_{pre-yield} = \int_{\varepsilon=0}^{\varepsilon=\varepsilon_y} \tau_{max} \left(\frac{\varepsilon}{\varepsilon_y}\right)^{\alpha} d\varepsilon = \frac{\tau_{max}}{\alpha+1} \varepsilon_y \tag{5.7}$$

$$G_{post-yield} = \int_{\varepsilon=\varepsilon_y}^{\varepsilon=\varepsilon_u} \left[\tau_{max} \left(1 - 0.8(1 - e^{0.7\left(1-\frac{\varepsilon}{\varepsilon_y}\right)})\right)\right] d\varepsilon = 0.2\varepsilon - \frac{8}{7}\varepsilon_y e^{0.7(1-\frac{\varepsilon}{\varepsilon_y})} \tag{5.8}$$

Considering the constant mean bond stress for pre- (i.e., $\bar{\tau_1}$) and post-yield range (i.e., $\bar{\tau_2}$), as illustrated in Figure 5-18b, the mean interfacial fracture energy is expressed by Eqs. (5.9)-(5.10).

$$\bar{G_1} = \bar{\tau}_1(\varepsilon_y) \tag{5.9}$$

$$\bar{G_2} = \bar{\tau}_2(\varepsilon_u - \varepsilon_y) \tag{5.10}$$

Equalizing Eqs. (5.7) and (5.9), and (5.8) and (5.10), and substituting characteristic parameters for this study (i.e., α =0.3, ε_y = 0.0015, ε_u = 0.21 and τ_{max} = 0.6 $f'_c{}^{1/2}$), the mean bond stresses are given by Eqs. (5.11)-(5.12).

$$\bar{\tau}_1 = 0.46\sqrt{f_c'} \tag{5.11}$$

$$\bar{\tau}_2 = 0.21\sqrt{f_c'} \tag{5.12}$$

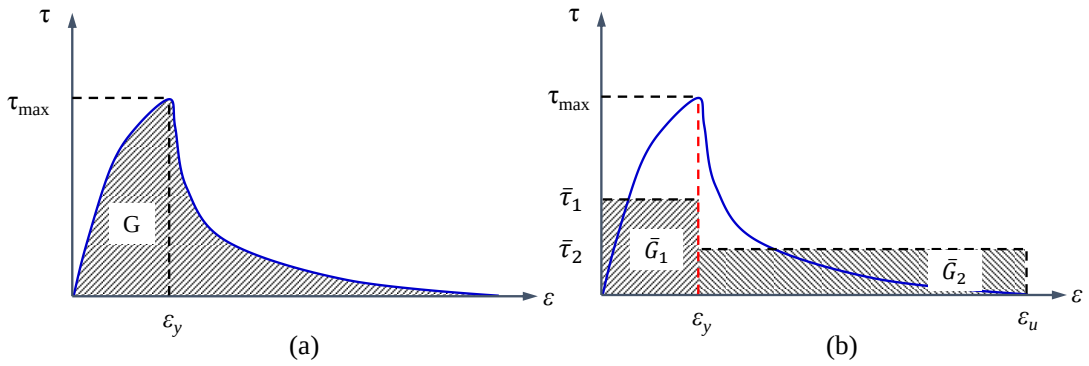

Figure 5-18 Schematic behaviour of bond at pre- and post-yield range of steel strain

5.3.7 Comparison with conventional measuring instrument

Figure 5-19shows the results of strain measurement by means of strain gauges, LVDTs and fibre optics at 3% drift. In the case of LVDTs, strains are the average values calculated by the displacement recorded by LVDT divided by the gauge length (the length between two fixed points that LVDT is located).

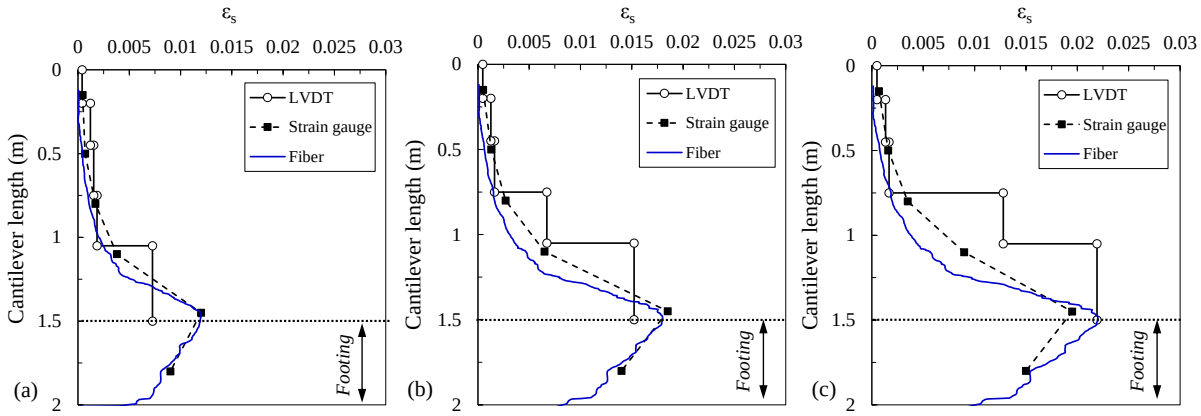

Figure 5-19 Comparison of strain distributions at (a) 1% drift (b) 2% drift (c) 3% drift

As can be seen in Figure 5-19 strain values obtained from LVDT did not represent the real profile along the length of the specimen. For strain gauges, the values of local strain showed generally good agreement with fibre optics, however, the results showed that the strain gauges were functional to measure strain up to 0.02, which is far away from its operational limit of 5%. Beyond that limit the recorded strain values through strain gauges showed no further increase. This may be due to the severe friction

between concrete and steel that may have resulted in damage and peeling off of the strain gauges.

5.4 Conclusions

The work reported in this chapter is a contribution to the existing knowledge of the performance of bond and also the damage assessment of an RC beam in the post-yield range of steel reinforcement using state of the art DFOSSS to measure strain, with sensor spacing of 2.6 mm along the length of the specimens. The study showed the DFOSSS has the potential to provide continuous strain measurements along the length of the specimen. The technology reduces the error associated with instrumentation of the specimen as the size and the installation method of the fibres imposed little damage to the reinforcing bars, compared with measuring techniques used in the past. The measured strain profiles in steel and concrete provide a solid foundation for further damage assessment, monitoring or even the design of structures. The following conclusions are drawn:

1. Once the strain profile was established, a bilinear average stress–strain curve was used to obtain the axial stress values corresponding to the strain at any location. Thereby, the bond stress distribution along the reinforcement was determined using the slope of the axial steel stress profile. Mechanical properties of the reinforcement were found to have a significant influence on the bond behaviour particularly in the post-yield range.
2. The bond deterioration length was found to vary from 36db at 1% drift to 45db, 49db and 60db, for 2%, 3% and 4% drift, respectively. The bond deterioration length increases as the applied drift levels increases.
3. The review of bond deterioration models indicated that the available models either overestimate or underestimate the deterioration of bond after yielding and cannot accurately represent the rate of decay for a member under flexure. Thus, a new strain-based model was proposed to accurately predict the behaviour of bond in pre- and post-yield range of steel strain in a RC beam subjected to flexure. The proposed model shows good agreement with experimental results. The study showed that once yielding occurs, irrespective of drift level, almost 80% degradation in bond capacity is expected. The study

also showed that for a RC cantilever beam subjected to flexure, the maximum bond stress in elastic range can be considered $0.6 f'_c{}^{1/2}$, which is comparatively lower than proposed values in the literature.

4. The mean bond stress was found to be $0.47 f'_c{}^{1/2}$ and $0.21 f'_c{}^{1/2}$, for pre- and post-yield range, respectively. These values were obtained on the basis of the interfacial fracture energy concept and can be used to simplify the evaluation of bond stress in both pre- and post-yield regions.
5. The distributed strain profiles obtained using DFOS allowed for quantification of localized damage in concrete in terms of the location of cracks and extent of cracking. The DFOS also offered the potential capability to reveal the extent of damage in reinforcement in terms of yield length, at different levels of drift, which is of great importance in the context of damage assessment.

5.5 References

Abrams, D. A. (1913). "Tests of bond between concrete and steel." University of Illinois at Urbana Champaign, College of Engineering. Engineering Experiment Station.

ACI 408.2R-92 (2005). "State-of-the-art report on bond under cyclic loads." American Concrete Institute.

Ashtiani, M. S., Dhakal, R. P., and Scott, A. N. (2013). "Post-yield bond behaviour of deformed bars in high-strength self-compacting concrete." *Construction and Building Materials*, 44, 236-248.

Balázs, G., Grosse, C., Koch, R., and Reinhardt, H. (1993). "Titel: Acoustic emission monitoring on steel-concrete interaction Zeitschriftentitel: Otto-Graf-Journal." *Otto-Graf-Journal*.

Belarbi, A., and Hsu, T. T. (1994). "Constitutive laws of concrete in tension and reinforcing bars stiffened by concrete." *Structural Journal*, 91(4), 465-474.

Bernander, K. "An investigation of bond by means of strain measurement in high tensile bars embedded in long cylindrical pullout specimens." *Proc., RILEM Symposium on Bond and Crack Formation in Reinforced Concrete*, 205.

Cao, J., and Chung, D. (2001). "Degradation of the bond between concrete and steel under cyclic shear loading, monitored by contact electrical resistance measurement." *Cement and concrete research*, 31(4), 669-671.

Claus, R., Gunther, M., Wang, A., Murphy, K., and Sun, D. "Extrinsic Fabry-Perot sensor for structural evaluation." *Proc., Applications of fiber optic sensors in engineering mechanics*, ASCE, 60-71.

Connolly, C. (2006). "Fibre-optic-based sensors bring new capabilities to structural monitoring." *Sensor Review*, 26(3), 236-243.

Davis, M., Hoult, N. A., and Scott, A. (2016). "Distributed strain sensing to determine the impact of corrosion on bond performance in reinforced concrete." *Construction and Building Materials*, 114, 481-491.

Davis, M., Hoult, N. A., and Scott, A. (2017). "Distributed strain sensing to assess corroded RC beams." *Engineering Structures*, 140, 473-482.

Eligehausen, R., Popov, E. P., and Bertero, V. V. (1982). "Local bond stress-slip relationships of deformed bars under generalized excitations." *Report No. UCB/EERC-83/23, Earthquake Engineering Research Center, University of California, Berkeley, 162 pp*

Filippou, F. C., Bertero, V. V., and Popov, E. P. (1983). "Effects of bond deterioration on hysteretic behavior of reinforced concrete joints." *UCB/EERC-83/19*, Earthquake Engineering Research Center.

Güemes, A., Fernández-López, A., and Soller, B. (2010). "Optical fiber distributed sensing-physical principles and applications." *Structural Health Monitoring*, 9(3), 233-245.

Haskett, M., Oehlers, D. J., and Ali, M. M. (2008). "Local and global bond characteristics of steel reinforcing bars." *Engineering Structures*, 30(2), 376-383.

Hassan, F. M., and Hawkins, N. M. (1977). "Prediction of the seismic loading anchorage characteristics of reinforced bars." *Special Publication*, 53, 417-438.

Hawkes, J., and Evans, R. (1951). "Bond stresses in reinforced concrete columns and beams." *Journal of the Institute of Structural Engineers*, 24(10), 323-327.

Henault, J.-M., Quiertant, M., Delepine-Lesoille, S., Salin, J., Moreau, G., Taillade, F., and Benzarti, K. (2012). "Quantitative strain measurement and crack detection in RC structures using a truly distributed fiber optic sensing system." *Construction and Building Materials*, 37, 916-923.

Horiguchi, T., Shimizu, K., Kurashima, T., Tateda, M., and Koyamada, Y. (1995). "Development of a distributed sensing technique using Brillouin scattering." *Journal of lightwave technology*, 13(7), 1296-1302.

Horiguchi, T., and Tateda, M. (1989). "BOTDA-nondestructive measurement of single-mode optical fiber attenuation characteristics using Brillouin interaction: Theory." *Journal of lightwave technology*, 7(8), 1170-1176.

Hoult, N. A., Ekim, O., and Regier, R. (2014). "Damage/deterioration detection for steel structures using distributed fiber optic strain sensors." *Journal of Engineering Mechanics*, 140(12), 04014097.

Ismail, M., and Jirsa, J. O. "Behavior of anchored bars under low cycle overloads producing inelastic strains." *Proc., Journal Proceedings*, 433-438.

Kankam, C. K. (1997). "Relationship of bond stress, steel stress, and slip in reinforced concrete." *Journal of Structural Engineering*, 123(1), 79-85.

Klar, A., Bennett, P. J., Soga, K., Mair, R. J., Tester, P., Fernie, R., St John, H. D., and Rail, C. L. (2006). "Civil Engineers Geotechnical Engineering 159 July 2006 Issue GE3."

Kreger, S. T., Gifford, D. K., Froggatt, M. E., Sang, A. K., Duncan, R. G., Wolfe, M. S., and Soller, B. J. "High-resolution extended distance distributed fiber-optic sensing using Rayleigh backscatter." *Proc., The 14th International Symposium on: Smart*

Structures and Materials & Nondestructive Evaluation and Health Monitoring, International Society for Optics and Photonics, 65301R-65301R-65310.

Lahnert, B. J., Houde, J., and Gerstle, K. H. "Measurement of slip between steel and concrete core." *Proc., Journal Proceedings*, 974-982.

Lowes, L. N., Moehle, J. P., and Govindjee, S. (2004). "Concrete-steel bond model for use in finite element modeling of reinforced concrete structures." *Structural Journal*, 101(4), 501-511.

Luna (2016). "Optical Distributed Sensor Interrogator Model ODiSI-B: User's Guide." *Blacksburg, VA*.

Maaskant, R., and Alavie, A. "A recent experience in bridge strain monitoring with fiber grating sensors." *Proc., FIBER OPTICS SENSORS FOR CONSTRUCTION MATERIALS AND BRIDGES-PROCEEDINGS OF THE INTERNATIONAL WORKSHOP HELD MAY 1998*.

Maekawa, K., Okamura, H., and Pimanmas, A. (2003). *Non-linear mechanics of reinforced concrete*, CRC Press.

Maekawa, K., and Qureshi, J. (1996). "Embedded bar behavior in concrete under combined axial pullout and transverse displacement." *Doboku Gakkai Ronbunshu*, 1996(532), 183-195.

Mains, R. M. "Measurement of the distribution of tensile and bond stresses along reinforcing bars." *Proc., Journal Proceedings*, 225-252.

Marti, P., Alvarez, M., Kaufmann, W., and Sigrist, V. (1998). "Tension chord model for structural concrete." *Structural Engineering International*, 8(4), 287-298.

Mayer, U. (2001). "Zum Einfluß der Oberflächengestalt von Rippenstählen auf das Trag- und Verformungsverhalten von Stahlbetonbauteilen."

Mirza, S. M., and Houde, J. "Study of bond stress-slip relationships in reinforced concrete." *Proc., Journal Proceedings*, 19-46.

Model Code 2010 (2013). "fib model code for concrete structures " *du Béton Fédération Internationale*, Ernst & Sohn, Berlin, Germany.

Mohamad, H., Soga, K., Pellew, A., and Bennett, P. J. (2011). "Performance monitoring of a secant-piled wall using distributed fiber optic strain sensing." *Journal of Geotechnical and Geoenvironmental Engineering*, 137(12), 1236-1243.

Murayama, Y., Suda, K., and Mimura, C. "Post-yielding bond-slip and stress-strain relationships of reinforcing bars embedded in massive concrete." *Proc., Proceedings of the 8th Japan Concrete Institute (JCI) Conference (in Japanese)*.

Nilson, A. H. "Internal measurement of bond slip." *Proc., Journal Proceedings*, 439-441.

NZS:3101 (1982). "New Zealand code of practice for the design of concrete structures ", Concrete Structures Standard, New Zealand Standard, Wellington/New Zealand.

Park, R., and Paulay, T. (1975). *Reinforced concrete structures*, John Wiley & Sons.

Perry, E. S., and Jundi, N. "Pullout bond stress distribution under static and dynamic repeated loadings." *Proc., Journal Proceedings*, 377-380.

Regier, R., and Hoult, N. A. (2014). "Distributed strain behavior of a reinforced concrete bridge: Case study." *Journal of Bridge Engineering*, 19(12), 05014007.

Regier, R., and Hoult, N. A. (2015). "Concrete deterioration detection using distributed sensors." *Proceedings of the Institution of Civil Engineers-Structures and Buildings*, 168(2), 118-126.

Ruiz, M. F., Muttoni, A., and Gambarova, P. (2007). "Analytical modeling of the pre-and postyield behavior of bond in reinforced concrete." *Journal of Structural Engineering*, 133(10), 1364-1372.

Santos, J., and Henriques, A. A. (2015). "New finite element to model bond–slip with steel strain effect for the analysis of reinforced concrete structures." *Engineering Structures*, 86, 72-83.

Shima, H., Chou, L.-L., and Okamura, H. (1987). "Micro and macro models for bond in reinforced concrete." *Journal of the Faculty of Engineering*, 39(2), 133-194.

Sirkis, J. "Using Bragg grating sensor systems in construction materials and bridges: perspectives and challenges." *Proc., FIBER OPTICS SENSORS FOR CONSTRUCTION MATERIALS AND BRIDGES-PROCEEDINGS OF THE INTERNATIONAL WORKSHOP HELD MAY 1998*.

Tada, T., and Takeda, T. (1991). "Analysis of Bond Deterioration Process in Reinforced Concrete Beam-Column Joints Subjected to Seismic Loading." *Special Publication*, 123, 443-464.

Ueda, T., Lin, I., and Hawkins, N. "Beam bar anchorage in exterior column-beam connections." *Proc., Journal Proceedings*, 412-422.

Villalba, S., and Casas, J. R. (2013). "Application of optical fiber distributed sensing to health monitoring of concrete structures." *Mechanical Systems and Signal Processing*, 39(1), 441-451.

Viwathanatepa, S., Popov, E. P., and Bertero, V. V. (1979). *Effects of generalized loadings on bond of reinforcing bars embedded in confined concrete blocks*, University of California, Earthquake Engineering Research Center.

Watstein, D. "Distribution of bond stress in concrete pull-out specimens." *Proc., Journal Proceedings*, 1041-1052.

Wu, F., and Chang, F.-K. (2006). "Debond detection using embedded piezoelectric elements in reinforced concrete structures-part I: experiment." *Structural Health Monitoring*, 5(1), 5-15.

Wu, H., and Gilbert, R. (2009). "Modeling short-term tension stiffening in reinforced concrete prisms using a continuum-based finite element model." *Engineering Structures*, 31(10), 2380-2391.

Zhou, B., Wu, R., and Feng, J. (2017). "Two models for evaluating the bond behavior in pre-and post-yield phases of reinforced concrete." *Construction and Building Materials*, 147, 847-857.

Chapter 6 *Damage assessment and Residual capacity of RC beams subjected to low-cycle fatigue*

6.1 Introduction

Post-earthquake damage assessment is a crucial measure for not only remediation plans, but also to foster resilience in the community. Such evaluation will determine whether RC buildings are sufficiently safe for reoccupation. During the Christchurch earthquake (22 February 2011), there was extensive damage with almost 60% of multistory RC buildings (3 storeys and up) being demolished, and 40 billion NZD was spent on the rebuild (Marquis et al. 2017; Wood et al. 2016). This called significant attention to the importance of post-event decision-making as the outcome will allow appropriate courses of action to be considered: demolition, repair or even reoccupation of the existing concrete building without any further action. To adopt a proper strategy, an accurate assessment of the residual capacity and the level of damage is required. From a structural standpoint, this implies scrutiny of the degradations in strength, stiffness, ductility, and energy dissipation capacity, which can each be addressed at material, member and eventually system level.

Tasai (1999) experimentally investigated the residual axial capacity of half-scale RC columns which had been previously subjected to antisymmetric bending reversals through applying axial loading. Maeda et al. (2004) and Maeda and Kang (2009) investigated the residual seismic capacity of RC buildings. They introduced an index and a rating-damage procedure, incorporated in the JBDPA (2001), to account for post-earthquake damage of an RC building. Mackie (2004) studied the residual axial load-carrying capacity of quarter-scale RC columns, after subjecting them to unidirectional incremental cyclic displacement patterns, and then axially loading damaged specimens under zero lateral load conditions. To estimate the residual capacity, the force–displacement results were compared to the force–displacement results of intact columns that were only tested in the axial direction up to failure. Similarly, Terzic et al. (2008) investigated the post-event residual axial load capacity of circular RC bridge columns. The specimens were initially subjected to bidirectional incremental lateral

displacement control up to different ductility targets, recentered and then monotonically forced up to failure. The comparison was finally made between these piers and undamaged piers tested monotonically to failure, to determine residual capacity. Chung et al. (2008) conducted an experimental test to evaluate the residual seismic performance of previously damaged RC bridge piers. They first applied ground motions on specimens, scaled to different peak ground accelerations (PGA), and then examined the residual seismic performance of the pre-damaged piers by employing incremental cyclic loading protocols. However, the residual capacity could not be explicitly interpreted as the comparison was made between the envelopes of the force–displacement responses of specimens that experienced both ground motions and incremental cyclic loading protocol with the envelopes of specimens that only experienced the incremental cyclic loading protocol. More recently, seismic residual capacity of RC buildings has been singled out as an important topic to be addressed in New Zealand (Cuevas et al. 2015; Elwood et al. 2016).

Earthquake-induced damage in RC buildings can conveniently be studied in the context of low-cycle fatigue. That is because seismic loading causes a limited number of relatively large inelastic cycles along with cycles with much smaller demands that are in line with the concept of low-cycle fatigue. Low-cycle fatigue is particularly relevant to the range of loading cycles from 1 to approximately 1000 cycles, to which an RC building may be subjected during earthquakes over its lifespan (Hsu 1981). Since the elements of RC buildings located in earthquake-prone areas are expected to experience such loading reversals, it is of great interest to scrutinize the performance, degradation and eventually the residual capacity of RC beams from a fatigue perspective.

Fatigue life, test-specimen behaviours under fatigue, and fatigue-related damage for both low- and high-cycles conditions have been extensively studied in the literature from a mechanical engineering standpoint (Miner 1945; Manson 1953; Coffin and Fo 1954). However, there are limited studies on the damage assessment and structural performance of earthquake-resistant structures that use a low-cycle fatigue approach. Studies by Suidan and Eubanks (1973) were the earliest that investigated the viability of fatigue damage as a design criterion for shear-type steel seismic frames. Krawinkler and Zohrei (1983) carried out low-cycle fatigue tests to study the failure modes of local

buckling and fracture at weldments of wide-flange-shape cantilever specimens, welded to a column stub. McCabe and Hall (1989) adopted a low-cycle fatigue concept to assess seismic structural damage analytically. Chai and Romstad (1997) proposed a low-cycle fatigue-based model to predict cumulative damage of structures under seismic loadings.

All the studies previously mentioned investigated low-cycle fatigue damage in steel structural elements. It is generally accepted that steel members show stable hysteretic behaviour with little or no deterioration with an increase in the number of cycles. However, in the case of RC members, it is more complicated to study the low-cycle fatigue behaviour, as there is uncertainty in the concrete material's characteristics, reinforcement detailing and associated failure mode. Kunnath et al. (1997) and El-Bahy et al. (1999) conducted landmark studies to evaluate the cumulative seismic damage of circular bridge piers subjected to low-cycle fatigue loading. They used the constant-amplitude cyclic test data as a benchmark to establish the fatigue-life relationship for the tested columns, and then used this data to obtain the damage parameters under variable-amplitude loading using Miner's linear damage rule. However, the fatigue-life relationship was proposed based on the number of cycles at drift levels that were too high to be endured by a seismically designed RC member from a buildings' code perspective (4%, 5.5% and 7% drift), and then extrapolated to 2% drift. Erberik and Sucuoğlu (2004) studied the low-cycle fatigue behaviour of one-third-scale exterior beam-column joints under constant and variable amplitudes. However, because of using plain bars for both longitudinal and stirrups, perfect bond between reinforcement and the surrounding concrete was not provided. In addition, no fatigue life prediction was proposed in terms of the applied drift level.

Based on what discussed above, there is a need to address the residual capacity of RC beams in a more standardized way in terms of fractions of their fatigue life. Since the structural performance of RC members is not unique and depends on previously applied cyclic loading history (Krawinkler 2009), the most logical way seems to express post-event residual capacity in terms of fraction of fatigue life. In this study, the fatigue-life relationship and damage evolution in three specimens under constant-amplitude cyclic loading were first established. Then, another four specimens were subjected to 70% and 90% of the required number of cycles to failure (fatigue life) at

two different drift levels (2% and 4% drift), recentered and then monotonically pulled until failure. Finally, the monotonic results of pre-damaged specimens were compared to the behaviour of an intact specimen loaded monotonically up to failure. To the authors' knowledge, this study is the first reporting the residual flexural capacity of RC beams in terms of the fraction of fatigue life. The objectives of the study described in this chapter are (1) to establish the fatigue-life relationship, and the evolution of damage in terms of degradation in the strength, deformability and energy-dissipation capacity over the fatigue life of the specimens; (2) to estimate the residual flexural capacity of previously damaged beams by applying monotonic lateral load up to failure and comparing with an intact beam.

6.2 Experimental program

6.2.1 Test specimen

Figure 6-1 shows the configuration of reinforcing bars and stirrups in the test beam.

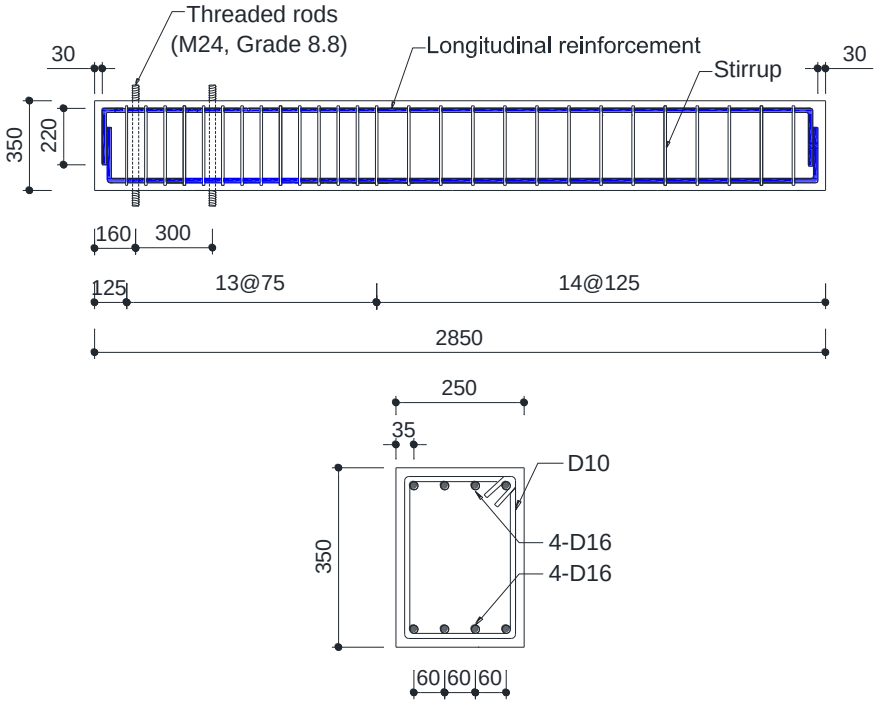

Figure 6-1 Test specimen and reinforcement arrangement

The specimen was built at half scale, representative of a typical RC beam designed according to NZS3101:1982. The cross section of the beam was 350 mm in depth by 250 mm in width. The longitudinal and lateral reinforcement used in the specimen was D16 and D10 Grade 300E deformed bars, respectively. The stirrups for the test specimen were closed with 135° hooks on both ends. The properties of steel reinforcement and concrete used in these experiments showed in Table 5-2.

6.2.2 Test setup

The test setup consisted of reaction frames made from hollow steel sections, including lateral bracing in the direction of the loading. To prevent any out-of-plane movement during testing, horizontal beams were attached to the testing frame on either side of the specimen. It is worth mentioning that the RC cantilever beams were tested vertically because of the ease of applying a lateral load and erecting the experiment. The beam specimen was secured by a steel footing, 500 HCC 413 wide flange steel sections, by bolting four threaded bars (M24, Grade 8.8), already cast into the specimen. Four high-strength M36 bolts were then used to fasten steel blocks to the strong floor. Hilti RE-500 epoxy was used to fully fill the gap between the end plate (welded to footings) and the outer face of the specimen. A 400 kN capacity hydraulic actuator with stroke of ±210 mm was employed to apply lateral loading. The applied load was measured using the load cell positioned in the head of actuator. The configuration of the test setup was shown in Figure 5-10.

6.2.3 Benchmark tests and loading protocols

Two types of benchmark tests – monotonic and low-cycle fatigue – were conducted in this study. In the case of the low-cycle fatigue test, three beams were subjected to three constant-displacement amplitudes, corresponding to 1%, 2% and 4% drift levels at a rate of 0.5 mm/s. This provided a basis to determine the low-cycle fatigue characteristics of the test beams until a fracture of the bar happened.

Monotonic testing was also conducted on one undamaged beam to capture its monotonic flexural capacity. The quasi-static lateral pulling loading was applied at the clear height of 1570 mm above the steel footing. The beam was subjected to drift ratio,

starting from 0.025% drift with the same step size, up to 1.0% drift, followed by increments of 0.05% until failure. A string potentiometer was used to record the displacement occurring at the level of applied loading.

Table 6-1 loading protocol of benchmark and subsequent tests

Specimen ID	Loading pattern	Purpose	n/N_f	Displacement history
M	Monotonic	Monotonic behaviour	N/A	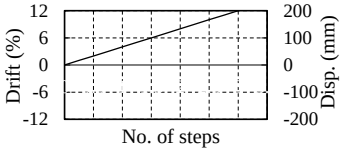
F-1%[a]	Constant cyclic	Fatigue behaviour	1	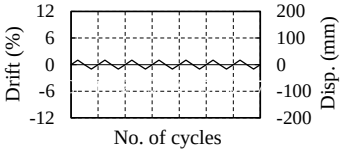
F-2%[a]	Constant cyclic	Fatigue behaviour	1	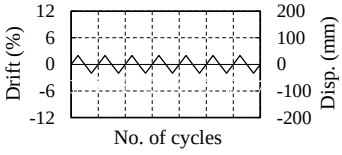
F-4%[a]	Constant cyclic	Fatigue behaviour	1	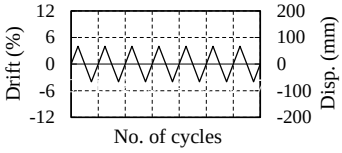
[b]R-0.7-2%	Constant cyclic + Monotonic	Residual capacity	0.7[c]	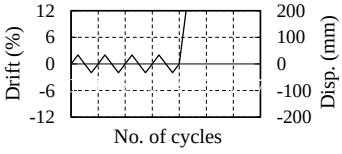
[b]R-0.9-2%	Constant cyclic + Monotonic	Residual capacity	0.9[c]	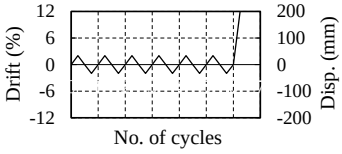

Specimen ID	Loading pattern	Purpose	n/N_f	Displacement history
[b]R-0.7-4%	Constant cyclic + Monotonic	Residual capacity	0.7[c]	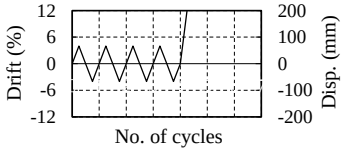
[b]R-0.9-4%	Constant cyclic + Monotonic	Residual capacity	0.9[c]	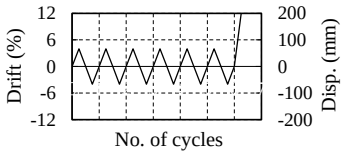

Note: M = Monotonic test; F = Fatigue test; R = Residual capacity of previously damaged specimens;

[a]1%, 2% and 4% denote drift levels at which the RC beams were subjected to constant amplitude cyclic loading

[b]to capture residual monotonic capacity of RC beams, all measuring instrumentations were zeroed before start testing.

[c]0.7 or 0.9 refers to the ratio of fatigue life (n/N_f) to which the RC beam has been previously subjected

6.3 Results and discussion

6.3.1 Monotonic test

The first sign of flexural cracks was captured at 0.2% drift, followed by the emergence of more cracking up to 0.75% drift, where a significant increase in maximum crack size, up to 0.45 mm, was observed. This drift level is very distinct, since it corresponds to yielding of bars that results in an increase in crack width. Beyond this point, the rate of increase in crack width increased considerably. At 2.8% drift, vertical cracking emerged on the compression side; however, no sign of noticeable spalling of cover concrete appeared during the test.

Figure 6-2 shows the monotonic load–deformation capacity of the RC beam. The specimen behaved approximately linearly and elastically up to 52.6 kN (0.75% drift) and then showed a gradual increase over the post-yield range, reaching the maximum lateral load of 72 kN at 13% drift. No indication of bar buckling or fracture of reinforcement was observed on either the compression or tension side. Stirrups

underwent significant deformations; but no fracture occurred. Although at high levels of drift, even without any reversal, a significant amount of strain was generated in the steel bars, no threshold was found to define the failure in the test. The test was terminated at a lateral displacement of 203 mm, due to the limitation in the stroke capacity of the actuator. Figure 6-3 shows the evolution of damage in the test beam at different drift levels.

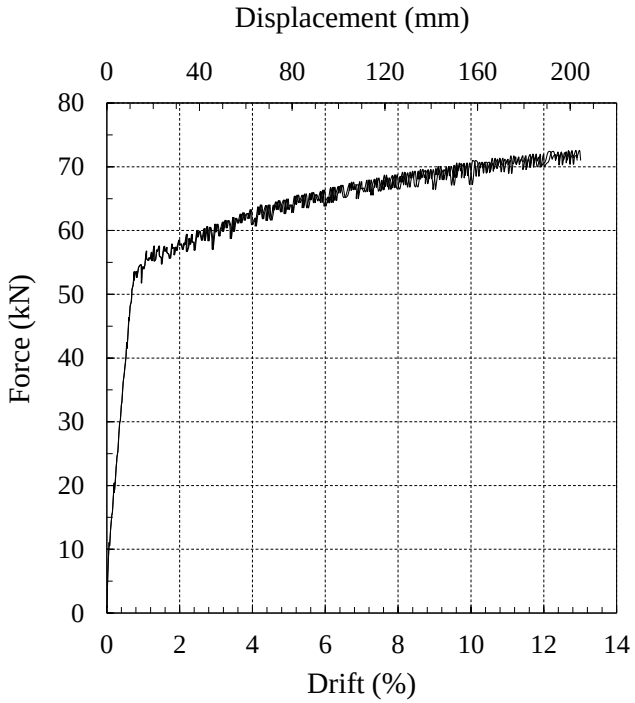

Figure 6-2 Monotonic behaviour of test beam

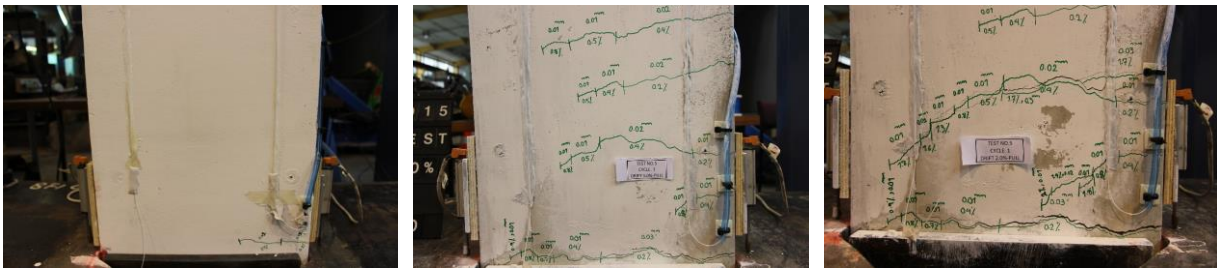

Drift 0.2% Drift 1.0% Drift 2.0%

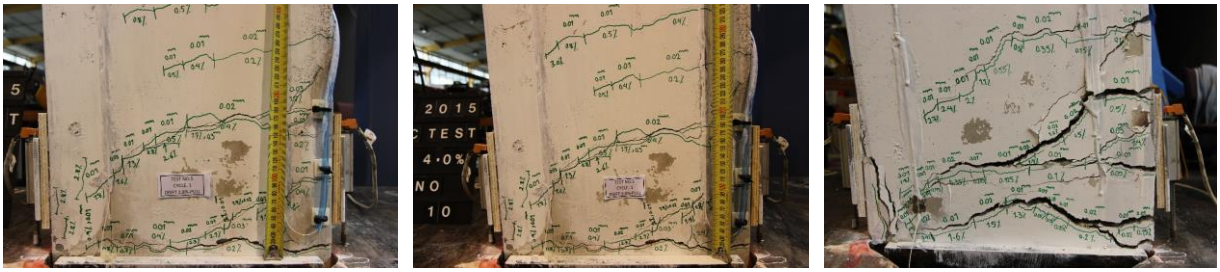

Drift 2.8% Drift 3.0% Drift 12.0%

Figure 6-3 Pictures of damage condition at different drift levels

6.3.2 Fatigue test-life

The number of cycles that the test specimen endured to failure (N_f) is referred to as fatigue life (Graf and Brenner 1934). In this study, N_f at each drift level was counted, corresponding to the failure status at which the force–displacement of the RC beams (hysteresis loop) were flattened, and which is accompanied by the fracture of longitudinal reinforcement. The values for N_f at 1%, 2% and 4% drift levels were found to be 1401, 239 and 37 cycles, respectively. The relationship between the fatigue life of the test specimen and the drift level (chord rotation) is conventionally displayed in logarithmic scale graphs and referred to as *S-N* curves (or Wöhler curve), as illustrated in Figure 6-4a. This relationship has been also shown in non-logarithmic scale (Figure 6-4b). It can be seen that the effect of drift level on the fatigue life of RC beams is significant: the fatigue life decreases with increasing drift level. Equations 7.1a and 7.1b express the best prediction models for the fatigue life following the curve-fitting exercise, as follows:

$$\theta\,(\%) = -0.82 \ln (N_f) + 6.8 \quad (6.1a)$$

$$\theta\,(\%) = 15.65\,(N_f)^{-0.378} \quad (6.1b)$$

where θ = drift (chord rotation); and N_f =total number of cycles required to failure.

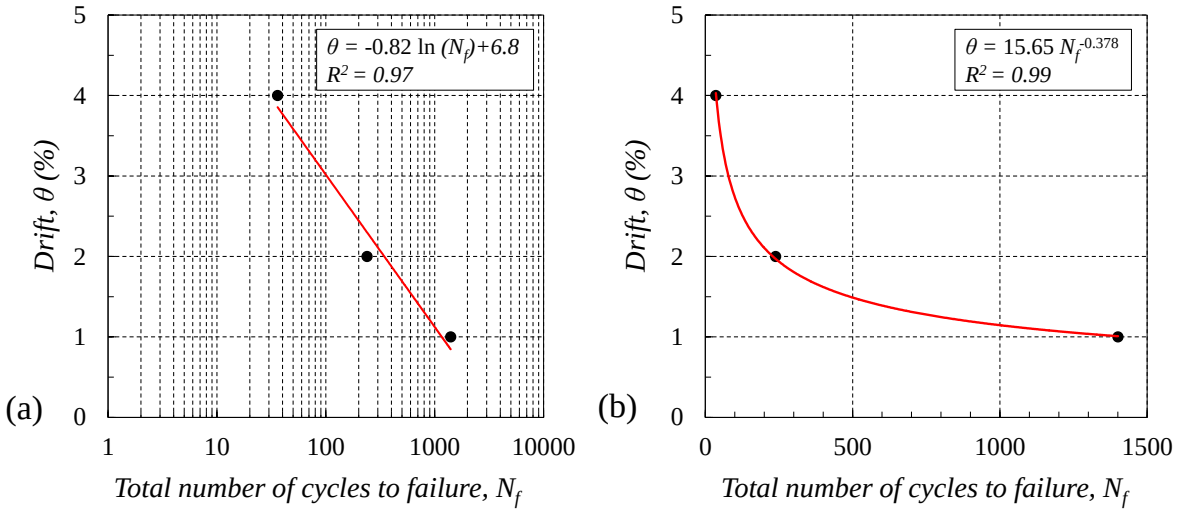

Figure 6-4 Fatigue life relationship: (a) logarithmic scale; (b) non-logarithmic scale

6.3.3 Fatigue test- damage evolution

Fatigue damage denotes the deterioration in the mechanical properties of the RC beam under reversals of loading. The merit of damage evaluation in the context of fatigue is that the degradation in the strength, stiffness and energy-dissipation capacity at any fraction of the fatigue life (n/N_f) can be accurately determined.

For the beam tested cyclically at constant amplitude of 1% drift, the first cycle resulted in a limited dispersion of cracking. The maximum measured crack widths on either side were between 0.85 and 0.95 mm. The maximum crack width in the highly damaged region of the tested beam (i.e., 300 mm above steel footing) increased to approximately 1.9 mm at the end of cycle 1050 (n/N_f =0.75), showing a gradual increase in the crack width even up to 75% of the fatigue life. However, the length of cracks showed no marked growth over this percentage of fatigue life. It should be noted that, in this experiment, the process of mapping and measuring the width of cracks was conducted every 50 cycles.

At 250 cycles, some loose aggregates were picked off; however, no significant spalling, significant crushing or visual damage was observed, even at failure. At the end of cycle 1400, the maximum crack size reached 5 mm. Figure 6-5(a) shows the

lateral force–displacement response of the beam at 1% drift. The maximum lateral load endured by the specimen (F_{max}), the yielding load (F_y) and the maximum displacement associated with applied drift level (Δ_{max}) are also illustrated. It can be seen that stiffness degradation occurs continuously over the entire fatigue life resulting in less strength being achieved at the same level of drift. Stiffness degradation becomes particularly prominent at fatigue life ratios of 0.75 and beyond. Similarly, pinching is observed in the consecutive hysteresis loops; however, the most significant pinching happens during the first cycle.

In fact, when the shear accompanying the moment is considerable, sliding along the "through-depth" crack(s) can occur (Naeim 1989). The sliding (i.e., shear displacement) is mainly resisted by "dowel action" of the longitudinal reinforcing bars, and is reflected through pinching of in the hysteresis loops near the region. Pinching results in not only degradation in the strength but also reduction in the energy-dissipation capacity of the beam. It is worth mentioning that strength deterioration at the desired displacement showed no symmetric pattern in the push and pull directions. This indicates how the damage occurring during the first half-cycle can affect the sequence of hysteresis loops.

In the case of the beam subjected to 2% drift, the first cycle was sufficient to develop well-dispersed cracks along the length of the specimen. The maximum measured crack widths on either side were between 3.1 and 3.2 mm. Crack mapping and crack measurement were conducted every 30 cycles in this test. At the end of 90th cycle (n/N_f =0.39), significant spalling of concrete cover in a length of 260 mm occurred on the compression side. This caused stirrups to be exposed and become visible. As shown in Figure 6-5(b), strength and stiffness degradation occur at a considerably higher rate compared with the previous experiment. Apart from the first cycle, in which the marked pinching starts, during cycles 60–90 (i.e., n/N_f =0.07) significant pinching was also observed.

For the case of beam tests at 4% drift, significant damage, spalling and crushing, was observed on the very first cycle. Cracks propagated along the height of the datum level (top of steel footing), and deformation of hoops and buckling of longitudinal bars started. The maximum crack width was measured as 7.5 mm. The process related to the crack measurement and crack mapping was carried out every 10 cycles. As seen in

Figure 6-5(c), deterioration in strength in this case happens more drastically. At cycle 6 (16% fatigue life), obvious buckling and hoop deformation in the plastic hinge zone was observed, and spalling had extended to about 300 mm on both sides of the specimen. During the first 4 cycles, about 40% reduction in strength was observed. During cycles 21–30, the hysteresis loop showed more stable behaviour and less degradation compared with the two previous sets of 10 cycles, which is an indication of more-balanced internal forces and also redistribution of internal forces. Despite significant deformation of stirrups, no fracture of stirrup was observed.

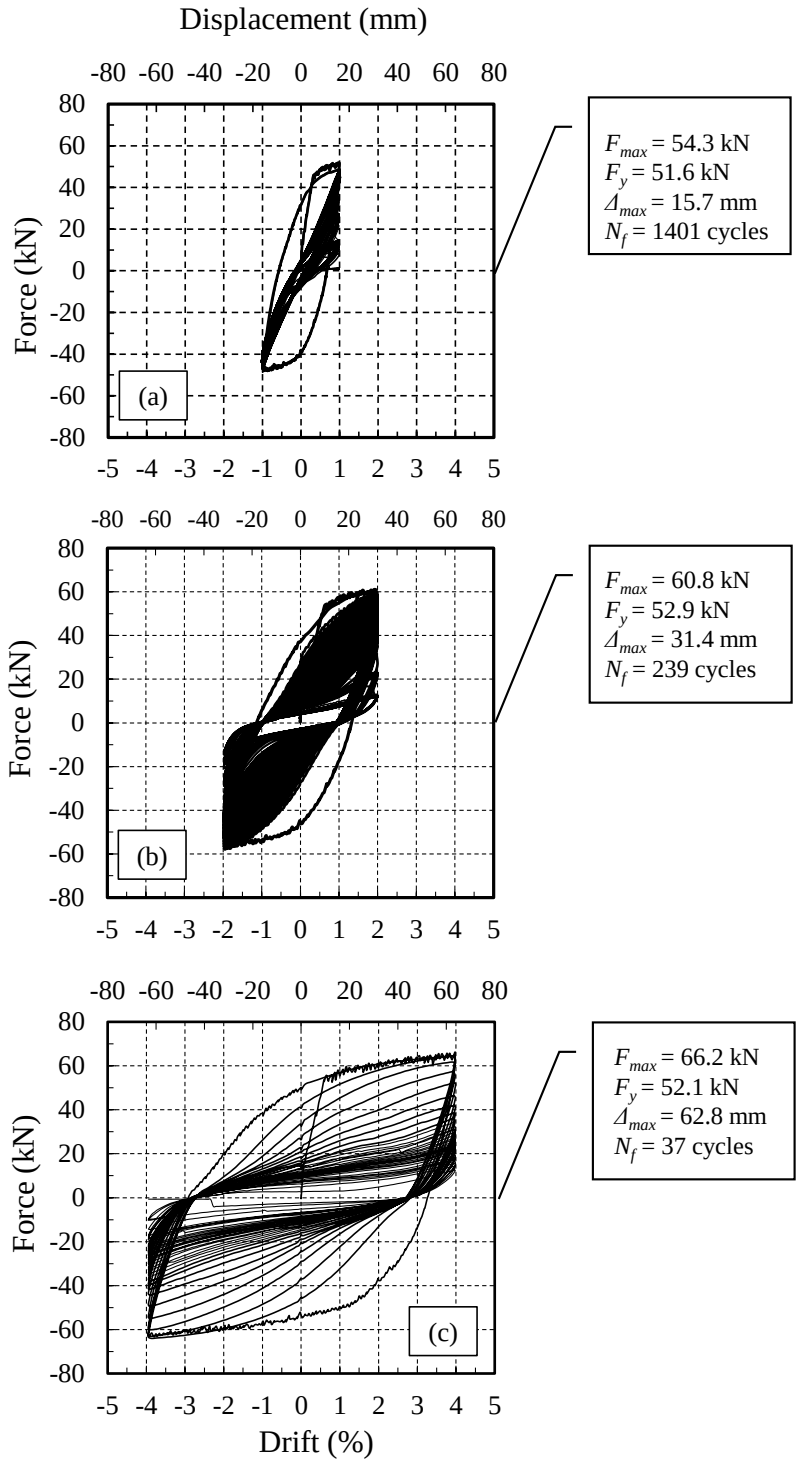

Figure 6-5 Force–displacement responses of RC beams (a) 1% drift; (b) 2% drift; (c) 4% drift

Figure 6-6 shows the evolution of damage at four ratios of fatigue life at two different drift levels. It should be noted that, since the value of N_f is not evident when

the test is started, the photos were captured every 50, 30 and 10 cycles, similar to the data collection in the crack measurement stages. As a result, the damage status is shown at ratios as close as possible to every quarter of the fatigue life. Interestingly, although the visual damage status of the specimen at 75% fatigue life at 2% drift is lower than the one subjected to 27% of its fatigue life at 4% drift, only 25% of the capacity of the former has remained, while the latter has only used about a quarter of its life. This implies that making a judgement based solely on appearance might lead to underestimation of the residual capacity of the RC beam and its capability to undergo extra cycles (demand).

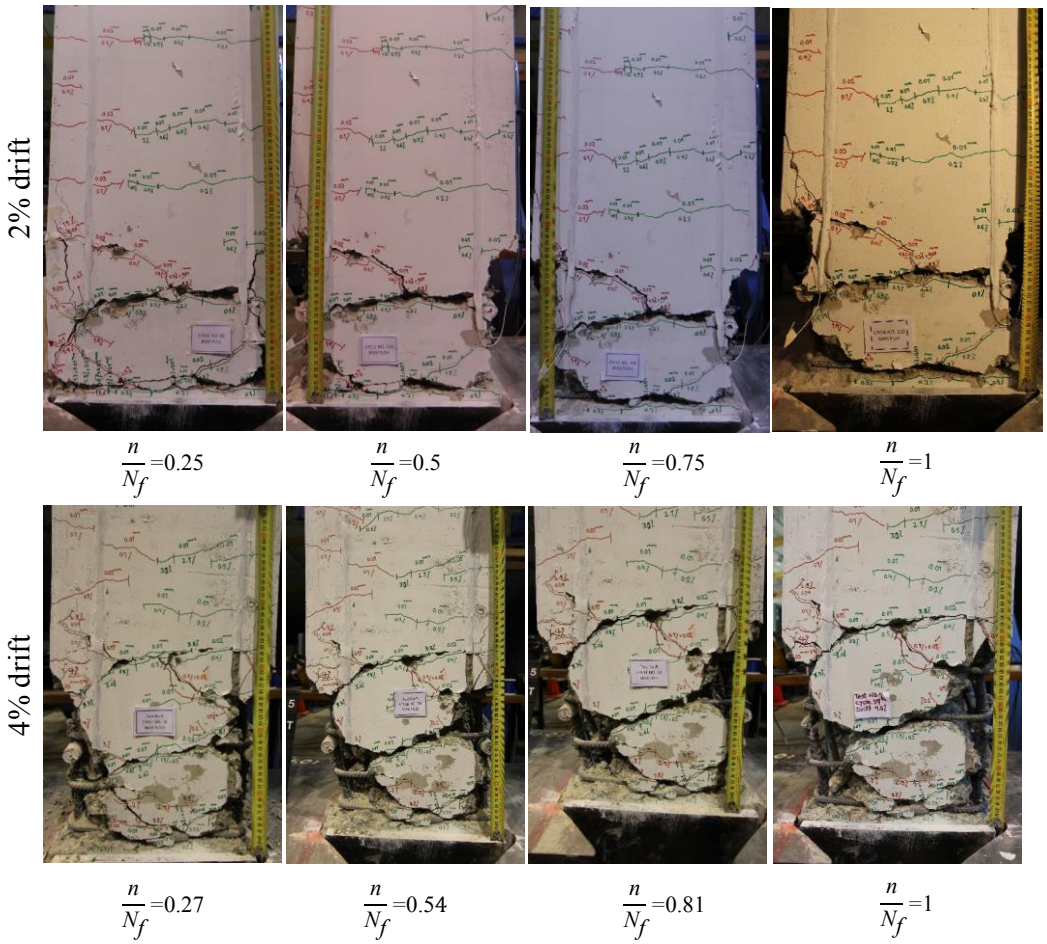

Figure 6-6 Damage progress at different fatigue life ratios, n/N_f

Figure 6-7 shows the typical failure mode of test beams mainly due to low-cycle fatigue fracture of longitudinal bar. In the case of 4% drift, however, this was followed

by buckling of the longitudinal reinforcement as well. In all the experiments, longitudinal bars snapped on the side first subjected to tension.

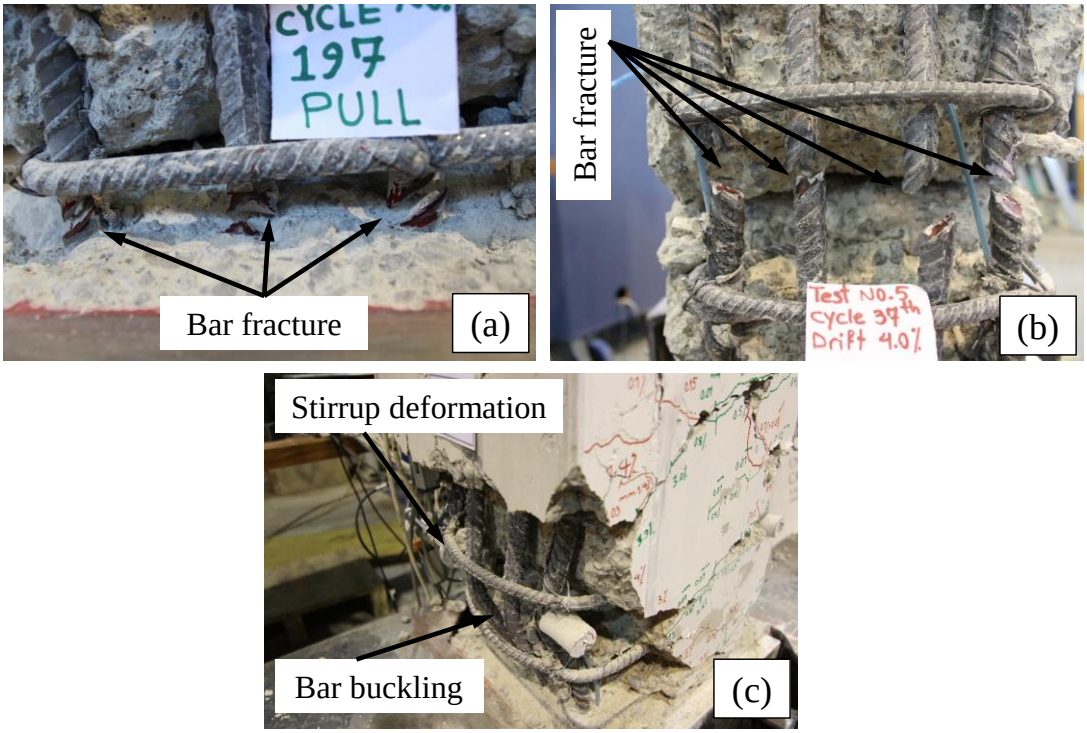

Figure 6-7 Typical failure modes: (a) bar fracture at 2%; (b) bar fracture at 4%; (c) bar buckling and stirrup deformation at 4%

6.3.4 Fatigue test- development of strain, cracking and beam elongation

Figure 6-8 shows the development of steel strain, measured using strain gauges attached to the longitudinal reinforcing bar experienced tension in the first cycle, located at 120 mm above steel footing at 2 and 4% drift.

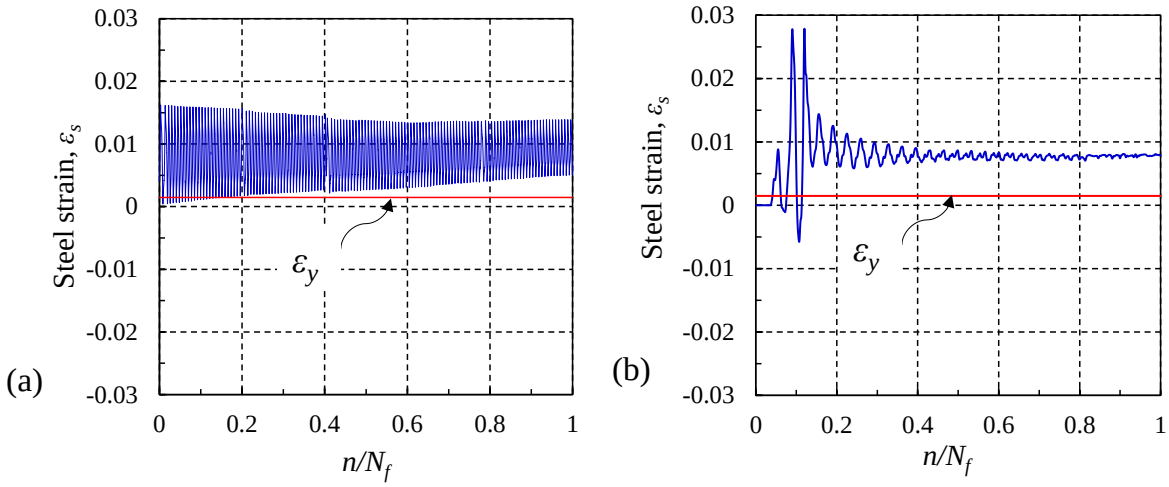

Figure 6-8 Development of steel strain in reinforcing bar over fatigue life: (a) 2% drift; (b) 4% drift

To quantify observable damage in terms of cracking in the highly damaged region of the tested beam (i.e., 300 mm above steel footing), crack widths were measured every 30 and 10 cycles of displacement loading protocol at 2% and 4% drift, respectively. The measurement was made for the maximum crack width (w_{cr}) associated with concrete which had been cracked between tension and compression longitudinal reinforcement. That is because the spalling of cover concrete did not allowed for measuring width of crack propagated to cover concrete. Figure 6-9 shows development of the maximum crack width over fatigue life of RC beams.

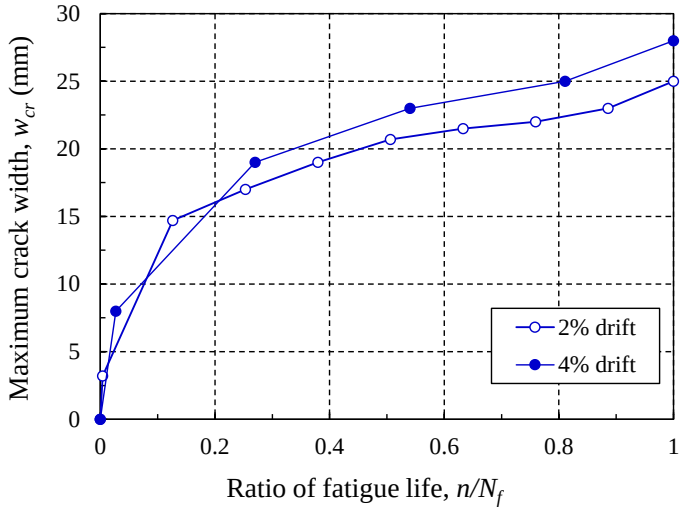

Figure 6-9 Development of maximum crack width over fatigue life of RC beams at 2% and 4% drift

In the cyclic specimen, flexural cracks did not fully close upon loading reversal due to lack of axial load to help yield reinforcement in compression. This led to increased crack widths with each cycle and cracks extending through the depth of the beam, reducing the shear friction capacity in the plastic hinge zone and forcing shear to be transferred through dowel action of the longitudinal bars. This caused bending of the bars, which led to buckling of reinforcement on subsequent cycles. Figure 6-10 shows the development of beam elongation measured during testing. The maximum beam elongations measured during cyclic loading at ±2% and ±4% drift were 9.2 mm and 26.3 mm, respectively. Emergence of wide cracks in the beams denote the elongation of the beam, and can be used to estimate beam elongation by adding the residual crack widths. However, it should be noted that since the measurement of crack width in this study has been made using crack gauge on the face of the beam, the width of cracks reported are comparatively larger than crack width if it was possible to measure crack width in the core section. Thus, in this experiment adding crack width will result in overestimation of beam elongation compared to actual measured value.

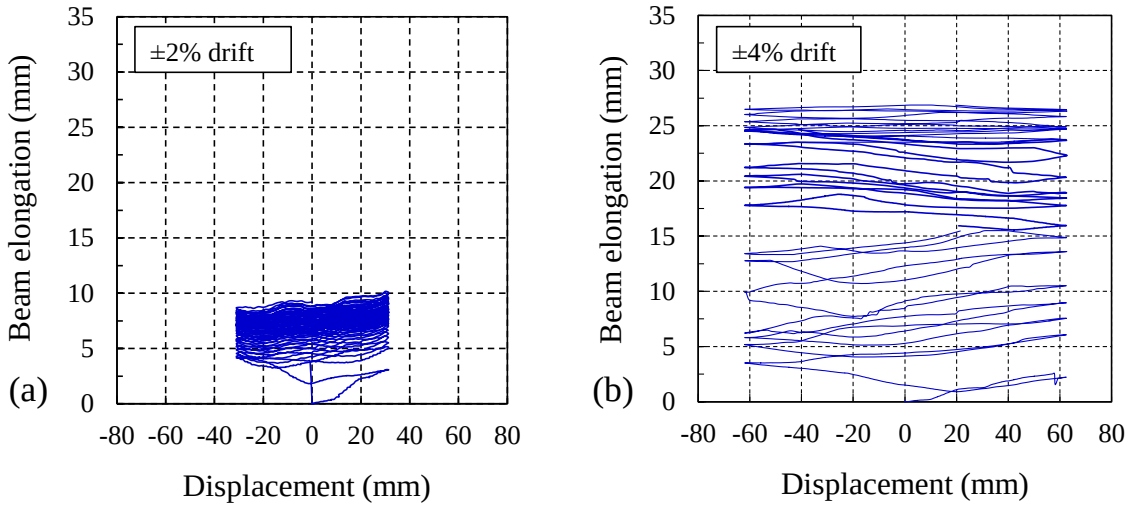

Figure 6-10 Development of beam elongation over fatigue life: (a) 2% drift; (b) 4% drift

6.3.5 Fatigue test- degradation in stiffness, strength and energy dissipation capacity

Figure 6-11 provides spectra by which the degradation in mechanical properties can be evaluated over the entire fatigue life in terms of the reductions in strength,

stiffness, energy dissipation capacity, and damping at each drift level. The spectra did not show the classic S-shaped trend as in the case of low-cycle fatigue loading; however, three different regions can still be identified. Figure 6-11(a) shows the ratio of the maximum lateral force achieved in each consecutive cycle (F_{max}) to the maximum lateral force achieved in the first cycle ($F_{max,0}$). As can be seen, the initial phase starts with a decrease up to about 10% of fatigue life, followed by a gradual descending trend during the second stage up to 0.81, 0.69 and 0.85 of fatigue life, where the first bar fracture occurs for 1%, 2% and 4% drift, respectively. The third stage, consisting of the last 20–30% of fatigue life includes significant drops due to fracture of longitudinal reinforcement. Results show that the higher level of drift incurs a higher rate of decay, and also causes the deterioration spectrum to become smoother with no evident drops, showing a more stretched, classic S-shaped response to low-cycle fatigue loading. Although the reduction in strength capacity of damaged beams with respect to applied drift level at 70% fatigue life is not identical, it is a limit beyond which bar fracture occurred in all the experiments. This implies that this fraction of fatigue life may be considered as a threshold beyond which the failure of the test specimen is inevitable.

The fatigue loading resulted in progressive damage with a marked degradation in stiffness of the RC beams. Such damage can be represented by introducing characteristic parameters of secant modulus, calculated as the ratio of maximum force to corresponding displacement (Gao and Hsu 1998). Figure 6-11(b) shows the ratio between the secant modulus of the test beam (K_s) in each cycle and its secant modulus in the first cycle (K_{s0}). As can be seen, the behaviour of the test beams is similar to that shown in the strength deterioration spectrums. In the case of 1% drift, stiffness showed slight degradation over a wide range of fatigue life and retained its resilience over hundreds of cycles. For the spectrum associated with 4% drift, in spite of bar fracture at 91% of fatigue life, no distinct drop was observed, possibly due to significant decay that had already occurred.

During low-cycle fatigue, energy inputted to an RC specimen is dissipated through damping mechanisms along with plastic deformation, resulting in structural damage. In fact, fatigue damage is the consequence of plastic energy, which is dissipated during consecutive cycles. Figure 6-11(c) shows the process of dissipation of energy,

represented as a form of dimensionless ratio of dissipated energy in each cycle (E_D) to dissipated energy in the first cycle (E_{D0}), against the fatigue life of the RC beam. The dissipated energy was calculated from numerical integration of the area enclosed under the hysteresis loops (Equation (7.2)). As shown, there is a significant loss, specifically after the first cycle, which indicates that the area formed during the first reversal is considerably higher than in the following cycles. It is clear that the specimens subjected to 1% and 2% drift levels dissipate more energy before 13% of fatigue life, while beyond that, the application of 4% drift leads to more degradation in the energy dissipation capacity. Irrespective of applied drift level, the rate of deterioration in the dissipation energy spectrum is higher than in the strength or stiffness spectrums. Overall, the ability of damaged RC beams to dissipate the input energy at 20% of fatigue life diminishes to about 40% of its dissipation capacity during the first cycle.

$$E_D = \sum \frac{(F_i + F_{i+1})(\Delta_{i+1} - \Delta_i)}{2} \tag{6.2}$$

where E_D = dissipated energy per cycle (N·mm); F_i = load at each increment (N); and Δ_i = displacement at each step (mm).

Figure 6-11(d) shows the change of equivalent viscous damping over the fatigue life of the test beam. Equivalent viscous damping (ξ_{eq}) is a key parameter, influencing not only the seismic response of an RC member, but also affecting the capacity of energy dissipation due to nonlinear behaviour. Having determined the dissipated energy, the corresponding equivalent viscous damping was calculated using the concept of dissipated and stored energy (E_{sto}) (Jacobsen 1930). The value of the equivalent viscous damping can be calculated by equating the energy dissipated through a viscous damper with the energy dissipated from nonlinear behaviour, as expressed in Equation (3)–(4). As shown, equivalent viscous damping shows a significant decrease during cycles from zero to 10% of fatigue life. That is because, in the very first cycles, the area enclosed by the hysteresis loop is huge, leading to large numerator. In the range of 10–70% of the fatigue life, in spite of subjecting the test beams to different drift levels, the equivalent viscous damping is approximately constant and equal to 30%. This level of damping is mostly contributed by the steel material, as the concrete in the plastic hinge zone has gone. In the case of 2% and 4%

drift, equivalent viscous damping shows increasing jumps, which is due to reduction in the capacity to dissipate energy once bar fracture happens.

$$\xi_{eq} = \frac{1}{4\pi}\frac{E_D}{E_{sto}} \tag{6.3}$$

$$E_{sto} = \frac{F_{max}\Delta_{max}}{2} \tag{6.4}$$

where ξ_{eq} = equivalent viscous damping; E_{sto} = equivalent elastic stored energy per cycle (N·mm); F_{max} = maximum load at each cycle (N); and Δ_{max} = maximum displacement at each cycle (mm).

For a member/structure, it is of great interest to define appropriate limit states to distinguish undesirable structural behaviour (e.g., structural collapse or instability). Based on the damage observations made during testing following four limit states were considered: (i) yielding of reinforcing bars, (ii) onset of spalling of the concrete cover, (iii) fracture of the longitudinal reinforcing bars, and (iv) pinching in hysteresis loops. Figure 6-11 shows the limit states considered in this study. It should be noted that evolution of the fatigue damage at each drift level has its own limit states; however, the limit states illustrated are corresponding to the minimum ratio of fatigue life (n/N_f) required to incur associated limit state. The limit state associated with yielding of reinforcement has not displayed as yielding of bars occurs during the first half cycle, resulting in approximately n/N_f equal to zero.

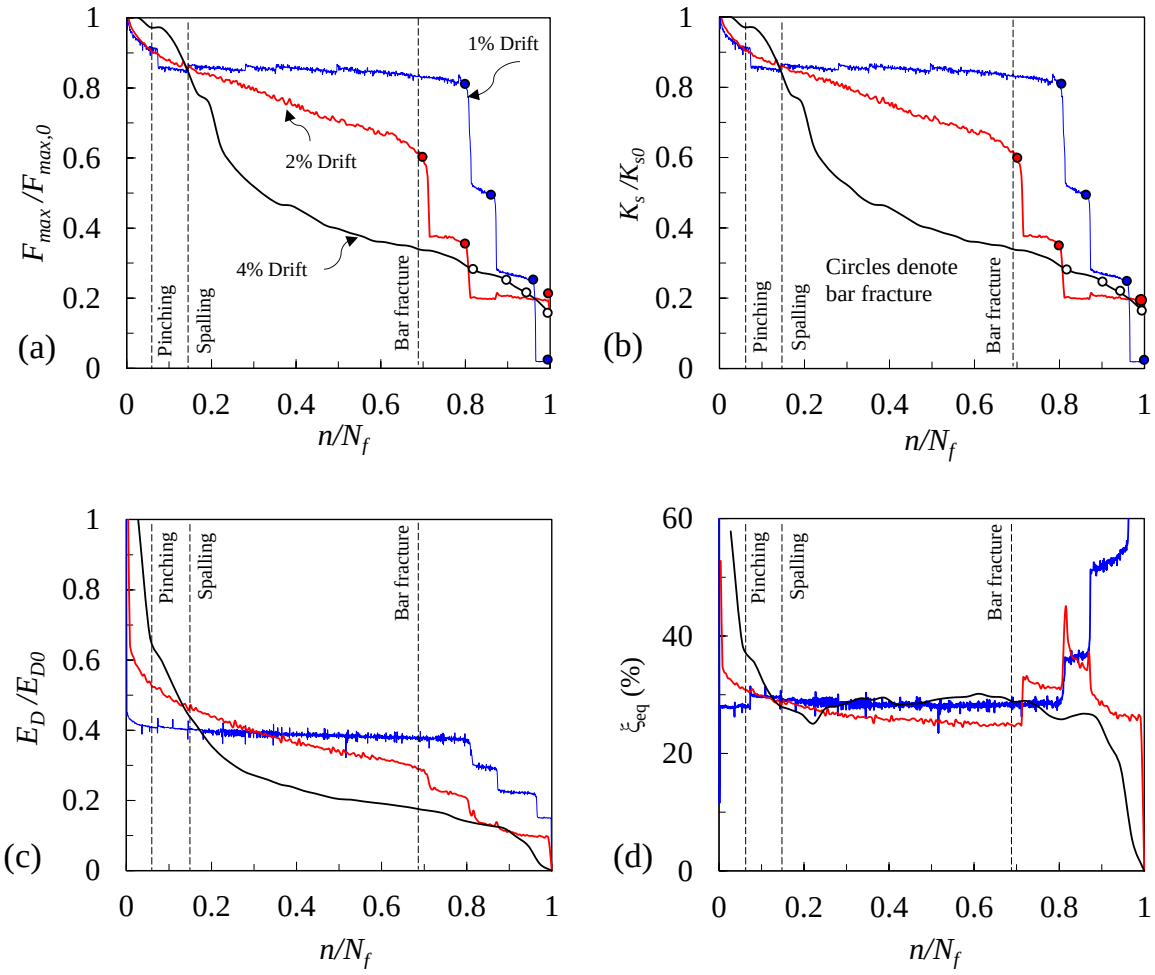

Figure 6-11 Fatigue damage evolution: (a) degradation of strength; (b) degradation of secant modulus; (c) degradation of energy dissipation capacity; (d) change in equivalent viscous damping

6.3.6 Residual lateral load-carrying capacity

To determine the residual lateral load-displacement capacity of RC beams in this study, a two-phase experimental program was carried out. In the first phase, four intact RC beams were subjected to two prescribed fractions of fatigue life at two different drift levels. In the second phase, the previously damaged RC beams were recentered and subjected to monotonic lateral loading test. The experiments were tagged using a 3-component ID according to their variables (e.g., R-0.7-2%). The first part, R, denotes the test program (Residual capacity testing), the second is the fraction of fatigue life at

which the fatigue loading stopped (70% or 90%), and the last component represents the drift level at which fatigue loading was conducted (2% or 4%).

Figure 6-12 shows the residual force–displacement relationships of damaged specimens monotonically reloaded after fatigue loading. The force–displacement of the intact specimen subjected only to monotonic loading is also shown for comparison purposes. It is evident that the minimum level of damage in terms of reduction in strength and deformation capacity is related to the response of the damaged beam that was subjected to 70% of its fatigue life at 2% drift (R-0.7-2%). The behaviour of the experiment named R-0.9-2%, is initially similar to its companion specimen, up to 7.3% drift where a marked drop happened because of bar fracture. The specimen still retained its strength up to 12.5% drift, beyond which no strength was shown. In the case of experiments R-0.7-4% and R-0.9-4%, results showed a soft inclined behaviour, which is attributed to a significant loss in stiffness. As expected, the experiment with the lower level of induced damage exhibited higher strength and deformation capacity. Both R-0.7-2% and R-0.7-4% showed similar capacity of deformation; however, in terms of strength capacity, the latter is considerably weaker. Generally, the application of 70% of the fatigue life degrades strength and stiffness capacities in the subsequent monotonic behaviour of the specimen, but there is no degradation in deformation capacity.

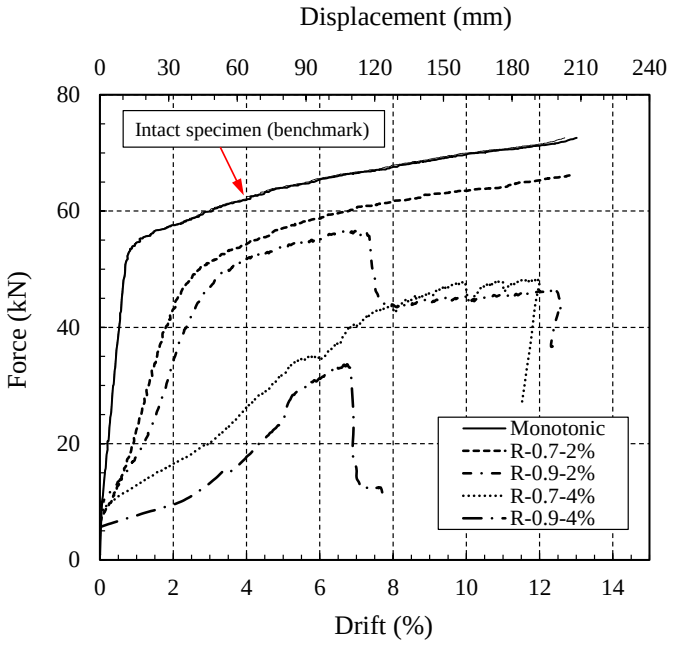

Figure 6-12 Residual force–displacement capacity of pre-damaged beams

Figure 6-13 provides spectrums by which the residual capacities have been assessed for pre-damaged specimens against monotonic reloading. As seen, the residual capacities for all drift levels reduce gradually, from zero up to 70% of fatigue life, beyond which a significant descending concave behaviour is observed. Results show

that loss of mechanical properties in pre-damaged test specimens are no more than 30%, for a fatigue life of 60% and below.

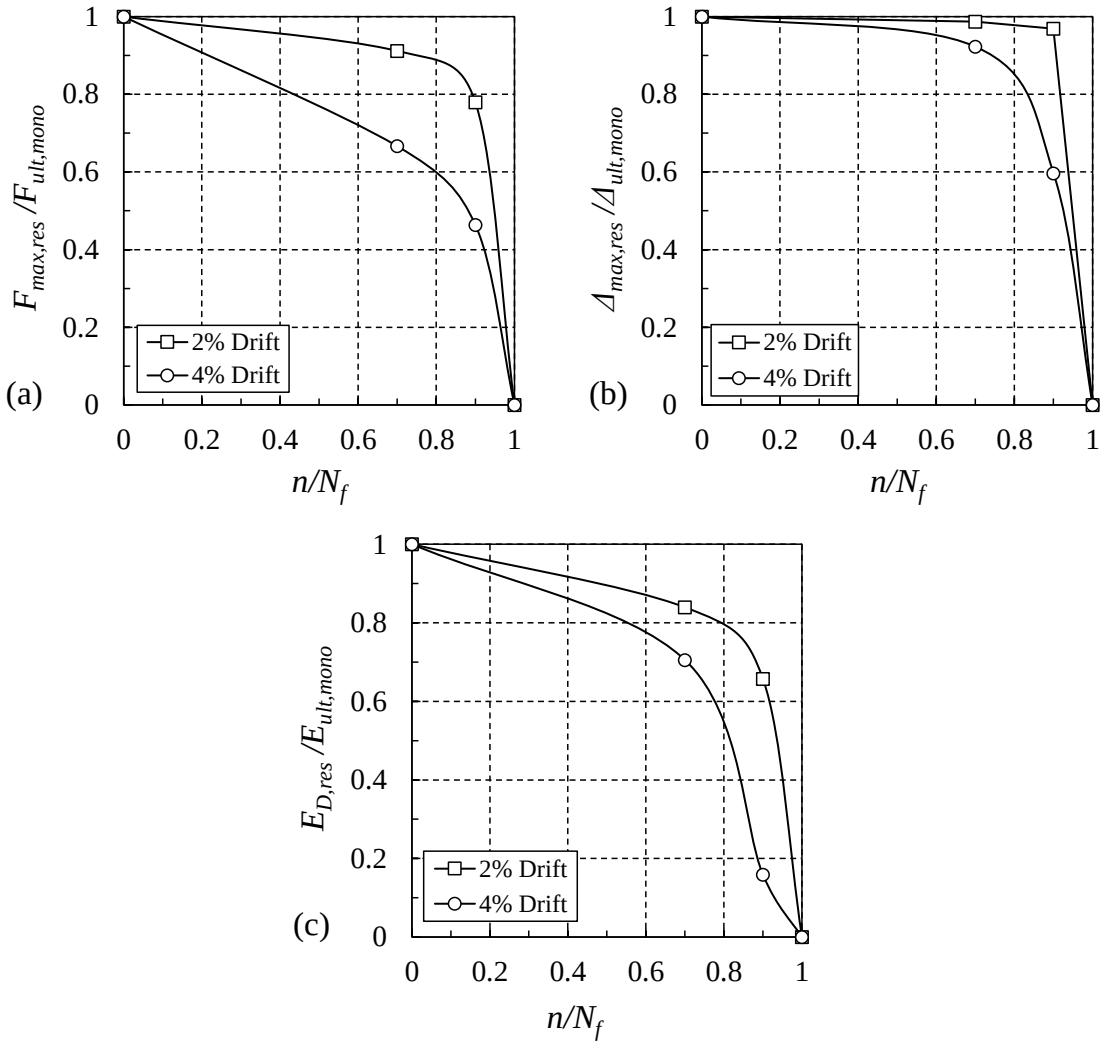

Figure 6-13 Residual capacities spectrums over fatigue life: (a) residual capacity of strength;(b) residual capacity of deformability; (c) residual capacity for dissipating energy

6.4 Limitations/Relevance

The residual lateral load-displacement capacity of previously damaged RC beams in this research, was also assessed by monotonically re-loading damaged specimens and comparing their load-bearing capacity with monotonic behaviour of the specimens if the beams were tested intact. This comparison can be made against any other loading protocol such as conventionally used incremental cyclic loading protocol provided by

ACI 374-1 . In this study, residual capacity was considered in a form of residual monotonic load-carrying capacity. That is because for moment-curvature and subsequent force-displacement analysis of RC member which is of great interest from engineering point of view for seismic assessment (NZSEE/MBIE 2017), a monotonic lateral push loading is applied on cantilever scheme. Thus, determination of residual monotonic capacity provides a basis to understand to what extent the upper (i.e., intact) and lower (i.e., application of 90% of the number of cycles failure) bounds of lateral force-displacement capacity of an existing RC beam can differ.

6.5 Conclusions

This chapter presented the results of an extensive investigation into the development of damage, material degradation, residual mechanical capacity and damage assessment of RC beams subjected to fatigue loading. The following conclusions can be drawn, based on the results of this chapter:

1. The fatigue life (S–N curve) was drawn and the relationship that best predicts it was established. The relationship was found to have a form of power function, allowing an estimation of the total number of cycles that the specimen can take at each desired drift level. The spectrums did not show the classic S-shaped trend as in the case of low-cycle fatigue loading, but three different regions can still be identified. Initial degradation occurs up to about 10% of fatigue life, followed by a gradual decay up to about 70–80% of fatigue life, and the third stage, consisting of significant drops due to fracture of longitudinal reinforcement. The rate of deterioration increases as the drift level increases: at the same fraction of fatigue life, the specimen subjected to higher drift level degrades more. With respect to type of response, the most severe rate of deterioration occurred in energy dissipation capacity, such that the ability of damaged RC beams to dissipate the input energy at 20% of fatigue life decreased to about 40% of its dissipation capacity during the first cycle. In the case of equivalent viscous damping, in a wide range of the fatigue life (10–70%), irrespective of drift levels, it is approximately constant and equal to 30%.
2. Having monotonically reloaded damaged specimens, previously subjected to different ratios of fatigue under two different drift levels, the residual force–

displacement relationships were established. Observations showed a significant decay in strength, stiffness, energy dissipation and deformation capacity. Residual capacities showed a gradual deterioration up to 70% of fatigue life, beyond which a significant descending behaviour was observed. It was also found that as the drift level increases, the post-event residual load-deformation bearing capacity of the specimen degrades more. 70% of fatigue life was identified as the fraction of fatigue life that may be considered as the threshold beyond which the failure of the test specimen is inevitable. Although the study presented herein was conducted at member level, the concept can serve for the system level and subsequent decision-making.

6.5 References

ACI 374-1 (2005). "Acceptance criteria for moment frames based on structural testing and commentary." ACI.

Chai, Y., and Romstad, K. (1997). "Correlation between strain-based low-cycle fatigue and energy-based linear damage models." *Earthquake spectra*, 13(2), 191-209.

Chung, Y.-S., Park, C. K., and Meyer, C. (2008). "Residual seismic performance of reinforced concrete bridge piers after moderate earthquakes." *ACI structural journal*, 105(1), 87.

Coffin, J., and Fo, L. (1954). "A study of the effects of cyclic thermal stresses on a ductile metal." *trans. ASME*, 76, 931-950.

Cuevas, A., Pampanin, S., Carr, A., and Ozbolt, J. (2015). "Seismic residual capacity of reinforced concrete frames: Part I: General Framework. ." *Research Report UC 2015-4, Part I, Department of Civil and Natural Resources Engineering, University of Canterbury, Christchurch, New Zealand*.

El-Bahy, A., Kunnath, S. K., Stone, W. C., and Taylor, A. W. (1999). "Cumulative seismic damage of circular bridge columns: Benchmark and low-cycle fatigue tests." *ACI Structural Journal*, 96, 633-641.

Elwood, K., Marder, K., Pampanin, S., Ramirez, A. C., Kral, M., Smith, P., Cattanach, A., and Stannard, M. (2016). "Draft framework for assessing residual capacity of earthquake-damaged concrete buildings." *NZSEE*Christchurch, New Zealand.

Erberik, A., and Sucuoğlu, H. (2004). "Seismic energy dissipation in deteriorating systems through low-cycle fatigue." *Earthquake engineering & structural dynamics*, 33(1), 49-67.

Gao, L., and Hsu, C.-T. T. (1998). "Fatigue of concrete under uniaxial compression cyclic loading." *Materials Journal*, 95(5), 575-581.

Graf, O., and Brenner, E. (1934). "Experiments for investigating the resistance of concrete under often repeated compression loads." *Bulletin*(76).

Jacobsen, L. S. (1930). "Steady forced vibrations as influenced by damping." *Transactions*, 52(15), 169-181.

JBDPA (2001). "The Japan Building Disaster Prevention Association, Guideline for Post-earthquake Damage Evaluation and Rehabilitation."Japan.

Krawinkler, H. "Loading histories for cyclic tests in support of performance assessment of structural components." *Proc., The 3rd international conference on advances in experimental structural engineering, San Francisco*, Citeseer.

Krawinkler, H., and Zohrei, M. (1983). "Cumulative damage in steel structures subjected to earthquake ground motions." *Computers & Structures*, 16(1), 531-541.

Kunnath, S. K., El-Bahy, A., Taylor, A., and Stone, W. (1997). "Cumulative seismic damage of reinforced concrete bridge piers." National Center for Earthquake Engineering Research.

Mackie, K. "Degradation of reinforced concrete column axial strength." *Proc., The 5th International Symposium in Civil Engineering*.

Maeda, M., and Kang, D. E. (2009). "Post-earthquake damage evaluation of reinforced concrete buildings." *Journal of Advanced Concrete Technology*, 7(3), 327-335.

Maeda, M., Nakano, Y., and Lee, K. S. "Post-earthquake damage evaluation for R/C buildings based on residual seismic capacity." *Proc., Proceedings of the 13th World Conference on Earthquake Engineering*.

Manson, S. S. (1953). "Behavior of materials under conditions of thermal stress." National Advisory Committee for Aeronautics.

Marquis, F., Kim, J. J., Elwood, K. J., and Chang, S. E. (2017). "Understanding post-earthquake decisions on multi-storey concrete buildings in Christchurch, New Zealand." *Bulletin of Earthquake Engineering*, 15(2), 731-758.

McCabe, S., and Hall, W. (1989). "Assessment of seismic structural damage." *Journal of Structural Engineering*, 115(9), 2166-2183.

Miner, M. (1945). "Cumulative fatigue damage." *Journal of applied mechanics*, 12(3), A159-A164.

Naeim, F. (1989). *The seismic design handbook*, Springer Science & Business Media.

NZSEE/MBIE (2017). "The Seismic Assessment of Existing Buildings." *Technical Guidelines for Engineering Assessment*, NZSEE/MBIE.

Suidan, M. T., and Eubanks, R. A. (1973). "Cumulative Fatigue Damage in Seismic Structures." *Journal of the Structural Division*, 99(5), 923-943.

Tasai, A. "Residual axial capacity and restorability of reinforced concrete columns damaged due to earthquake." *Proc., US-Japan Workshop on Performance-Based Earthquake Engineering Methodology for Reinforced Concrete Building Structures*, 191-202.

Terzic, V., Mackie, K., and Stojadinovic, B. "Experimental evaluation of the residual axial load capacity of circular bridge columns." *Proc., 14th World Conference on Earthquake Engineering, Beijing, China*, 1-8.

Wood, A., Noy, I., and Parker, M. (2016). "The Canterbury rebuild five years on from the Christchurch earthquake." *Reserve Bank of New Zealand Bulletin*, 79, 1-16.

Chapter 7 *Finite element modelling of RC beams subjected to low-cycle fatigue*

7.1 Introduction

To simulate the cyclic nonlinear inelastic behaviour of a RC member, several techniques have been proposed in literature. The implementation of appropriate technique depends on how much detail information is required which results in the levels of discretisation and complexities. To capture global behaviours, relatively simple macroscopic models can be used. Using macroscopic models reduces the computational effort, however to reproduce the observed behaviour of RC elements, phenomenological idealizations are often utilised.

If more detailed information is required regarding the damage state in the individual elements, more complex analysis methods such as finite element methods (FEM) are generally utilised. Finite element analysis (FEA) is the practical application of the finite element method (FEM) to model the structural members in a virtual environment. This provides a basis through which the real behaviour of a structure can be mathematically simulated and numerically solved. Modelling can reveal any potential/existing structural defects as well as performance issues.

The geometry is substituted by a set of elements, consisting of nodes with a certain degrees of freedom. The finite elements are connected to these nodes which form a grid called the mesh. Material properties are then assigned to the elements placed in model defining the structural response to a specified loading protocol. The refinement of the mesh might change throughout the model, depending on the variation of stress in different regions. The finite element method can be defined as a general method of structural analysis in which a continuous solid is replaced by a finite number of elements interconnected at a finite number of nodal points. The most robust method in terms of the highest level discretisation and complexity, amongst the existing finite element modelling techniques, is the 3D continuum FE modelling. This technique

results in a more refined analysis, accurate results and information of the inner mechanics of the analysed structural member.

Reviewing literature shows the first study to develop a finite element model to numerically simulate the behaviour of reinforced concrete members were conducted by Ngo and Scordelis (1967). The FE model proposed by Ngo and Scordelis was used to analyse the response of singly reinforced concrete beams on simple supports with different idealized cracking patterns. However, no general conclusions regarding the behaviour of the RC beams under load were attempted in that investigation. This model which included a cracking was called the *discrete crack model*. Results provided a complete picture of stress distribution in the entire beam. Figure 7-1 shows the FE idealization proposed by Ngo and Scordelis.

Following this approach, Rashid (1968) introduced another approach (i.e., smeared crack model) for the analysis of RC members. While the discrete crack model intends to capture initiation and propagation of dominant cracks, the smeared crack model is based on the idea that in concrete, due to its heterogeneity and the presence of reinforcement, many small cracks nucleate which only in a later stage of the loading process link up to form one or more dominant cracks (Borst et al. 2004). As a result, relative displacements of crack surfaces are represented by crack strains and the constitutive behaviour of cracked concrete can be modelled in terms of stress-strain relations (Rots et al. 1985).

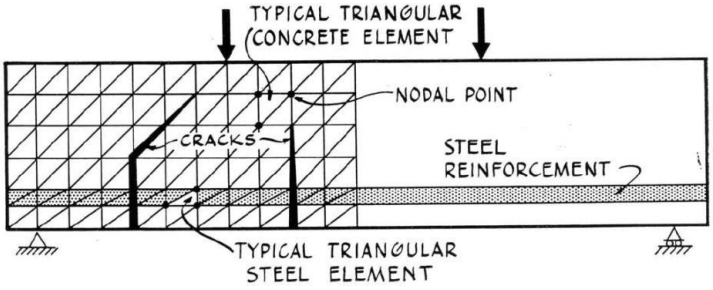

Figure 7-1 FE idealization in RC beam proposed by Ngo and Scordelis

From these early pioneering studies onwards, the analysis of RC members using FEM has received great interest. However limited FE analysis has been carried out on cyclic response of a RC beam subjected to constant amplitude fatigue loading. As a contribution to fill this gap in knowledge and to provide a basis for future studies, in

this chapter numerical modelling have been carried out to develop three-dimensional FE models. The primary aim of this chapter is to develop a complete FE model that can provide accurate simulation of behaviour of a RC beam subjected to low-cycle fatigue loading. The model, therefore, is to be capable of simulating the full cyclic performance of the specimens including strength degradation, failure mode, propagation of cracking, crushing of concrete and tension stiffening.

The outcomes of the finite element analyses were compared with and validated against the experimental findings in terms of global load-displacement behaviour and damage propagation. To this end, a general purpose finite element program, ABAQUS, was used. ABAQUS is a software suite for finite element analysis and computer-aided engineering, originally released in 1978. ABAQUS has an extensive range of material and elements libraries which make it capable for FEA investigations.

7.2 Development of the FE model

To model the RC beams tested in this study, three-dimensional, 8-node, reduced integration with hourglass control, C3D8R, linear brick solid elements were used in FE package *ABAQUS*. For the case of longitudinal reinforcing bar, a 2-node linear beam element with six degrees of freedom (DOF), B31, was employed for modelling. That is because the beam element has the merit of being capable of transferring both transverse shear and flexural moment. In the case of stirrups, 2-node linear displacement truss elements in 3D space (T3D2) were used. Figure 7-2 shows the realistic display of the longitudinal and transverse reinforcement assembly in the FE model.

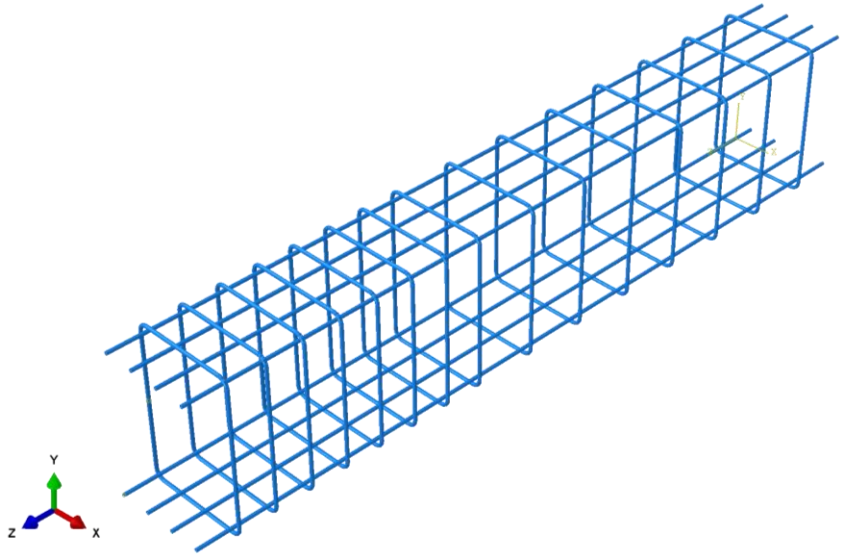

Figure 7-2 reinforcement modelling

An embedded elements technique was adopted, in which beam elements were hosted by solid brick elements. The use of this technique will allow for rotational DOF of the embedded nodes. However, the response of host elements will be used to constrain the translational DOF of the nodes of embedded elements. When a node of an embedded element is positioned within a host element, the translational DOF at the node is eliminated and the node becomes an embedded node. In fact, the translational DOF of the embedded node is constrained to the interpolated values of the corresponding DOF of the host element. For this purpose, a geometric tolerance is defined to determine how far an embedded node can lie outside the regions of the host elements (*ABAQUS 2015*). Although the tolerance can be adjusted, *ABAQUS* requires embedded nodes to be located within a distance of 5% of the average size of all non-embedded elements in the model.

The geometric tolerance can be defined as a fraction of the average size of all non-embedded elements in the model. Alternatively, it is possible to define the geometric tolerance as an absolute distance in the length units chosen for the model. If both exterior tolerances are specified, *ABAQUS* uses the tighter tolerance of the two. The average size of all the non-embedded elements is calculated and multiplied by the fractional exterior, which is then compared to the absolute exterior tolerance to determine the tighter tolerance of the two. The exterior tolerance for embedded elements in host elements is indicated by the shaded region in Figure 7-3.

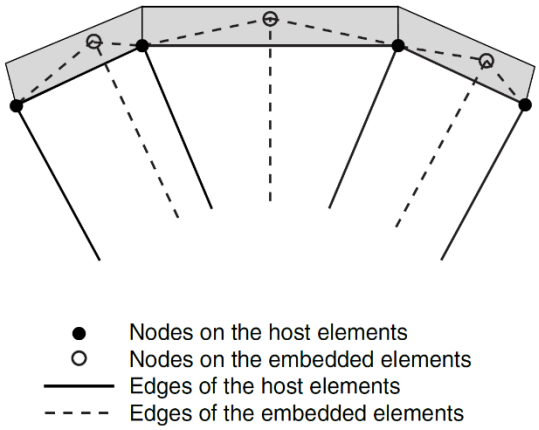

Figure 7-3 The exterior tolerance for embedded elements (ABAQUS)

In finite element analysis (FEA), the size of the mesh is a significant parameter as it affects the failure force and displacement results. In this work, mesh convergence studies were conducted with respect to experimental results in an attempt to determine an accurate and optimum mesh size that provided almost the same force–displacement curves. The mesh size of D/25 (D = width of the section) was found to be the optimum size, whereas finer or coarser sizes resulted in error and divergence. Figure 7-4 shows the mesh discretization of the FE model of the RC beams. As seen, in the unloaded part of the RC beam (support), mesh density was intentionally refined because of the substantial concentration of damage. While for the noncritical part of the beam (the loaded part), a coarser size of mesh was used.

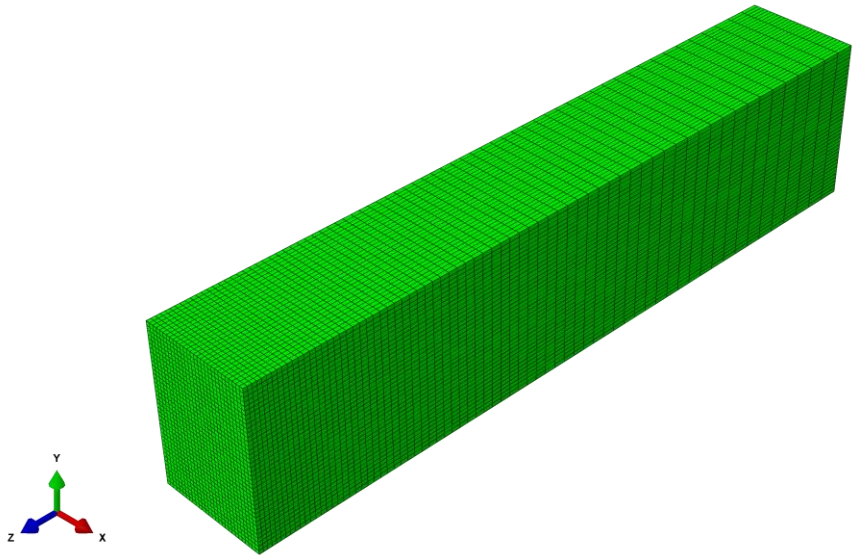

Figure 7-4 Mesh discretization of the beam model

In this study, the *ABAQUS/Explicit* was employed, as it accounts for both material and geometrical nonlinearities and also determines the solution without iteration by explicitly advancing the kinematic state from the previous increment, which is of great merit from a computational cost standpoint. That is because implicit method will encounter some difficulties when a complicated three dimensional model is considered. The reasons are as follows: (i) as the reduction of the time increment continues, the computational cost in the tangent stiffness matrix is dramatically increased and even causes divergence; (ii) local instabilities cause force equilibrium to be difficult to achieve (Sun et al. 2000).

7.3 Modelling of concrete

To simulate the behaviour of concrete material in *ABAQUS*, three models are provided: concrete smeared cracking, brittle cracking model, and concrete damaged plasticity (CDP). The CDP model is employed in this study because of its great potential and capability to accurately represent complete cyclic compressive and tensile behaviour of concrete in the inelastic region by considering damage characteristics. The CDP model was first proposed by Lubliner et al. (1989) and further developed by Lee and Fenves (1998a) for concrete structures subjected to cyclic loading. The model

is a continuum, plasticity-based, damage model for concrete, and is based on the assumption of scalar damage. The model suits applications in which the concrete is subjected to arbitrary loading conditions (i.e., cyclic loading). The model takes into consideration the degradation of the elastic stiffness induced by plastic straining both in tension and compression, and also accounts for stiffness recovery under cyclic loading. In this model, the main two failure mechanisms are tensile cracking and compressive crushing of the concrete material (*ABAQUS 2015*). In addition, the evolution of the yield (or failure) surface is controlled by two hardening variables: compressive and tensile equivalent plastic strains ($\tilde{\varepsilon}_c^{pl}$ and $\tilde{\varepsilon}_t^{pl}$) that are linked to failure mechanisms under tension and compression loading respectively.

7.3.1 Compressive and tensile behaviour

Under tension, the stress–strain response in the CDP model follows a linear elastic trend until tensile strength f_t is reached. The failure stress corresponds to the onset of microcracking in the concrete material. Beyond the failure stress, the formation of microcracks is represented macroscopically by a softening stress–strain response, which induces strain localization in the concrete structure. Under compression, the response shows a linear trend until initial yield, σ_{c0}, whereupon nonlinear behaviour is observed up to concrete compressive strength, f'_c. Beyond that, and in the plastic regime, the response is typically characterized by strain softening.

The definition of compressive behaviour of concrete by virtue of the CDP model in *ABAQUS* is elaborated in Figure 7-5. When the concrete specimen is unloaded from any point on the strain-softening branch of the stress–strain curves, the unloading response is weakened and a degradation in elastic stiffness of the material occurs. The degradation of the elastic stiffness is characterized by two damage parameters, d_c and d_t. These damage variables can take values from zero, representing the undamaged material, to one, which represents total loss of strength. The stress–strain relationships of concrete based on the CDP model under compression and tension is expressed as follows:

$$\sigma_c = (1- d_c) E_0 (\varepsilon_c - \tilde{\varepsilon}_c^{pl}) \tag{7.1}$$

$$\sigma_t = (1- d_t) E_0 (\varepsilon_t - \tilde{\varepsilon}_t^{pl}) \tag{7.2}$$

where σ_c = compressive stress of concrete; σ_t = tensile stress of concrete; d_c = compressive damage parameter; d_t = tensile damage parameter; E_0 = initial elastic stiffness of the undamaged concrete; ε_c = compressive strain; ε_t = tensile strain; $\tilde{\varepsilon}_c^{pl}$ = compressive equivalent plastic strain; and $\tilde{\varepsilon}_t^{pl}$ = tensile equivalent plastic strain.

Calculations of damage associated with the post-peak response of concrete in both tension and compression was based on the damage model proposed by Lubliner et al. (1989). The model is substantially based on classical theory of plasticity and specified more for frictional material (e.g., concrete) using yield criteria of Mohr - Coulomb and Drucker and Prager . In this model, stiffness is proportional to the cohesion of the concrete and degradation occurs only in the softening region as expressed by Equation 7.3.

$$d = \frac{c}{c_{max}} \tag{7.3}$$

where c = cohesion in the yield; and c_{max} = maximum cohesion in the yield. Following this approach, the tensile and compressive damages in this study were introduced as follows:

$$d_c = \frac{\sigma_c}{f'_{cc}} \tag{7.4}$$

$$d_t = \frac{\sigma_t}{f_t} \tag{7.5}$$

To establish the compressive stress–strain behaviour of the concrete outside the elastic range (strain–softening regime), *ABAQUS* requires the stress values to be provided as a function of inelastic strain, $\tilde{\varepsilon}_c^{in}$, not plastic strain, $\tilde{\varepsilon}_c^{pl}$. The inelastic strain is defined as the total compressive strain (ε_c) minus the elastic strain corresponding to the undamaged material (ε_{0c}^{el}). This model assumes that ε_{0c}^{el}, is constant after peak stress is reached. *ABAQUS* will then automatically convert the inelastic strain values to plastic strain values using following expression:

$$\tilde{\varepsilon}_c^{pl} = \tilde{\varepsilon}_c^{in} - \frac{d_c}{(1-d_c)}\frac{\sigma_c}{E_0} \tag{7.6}$$

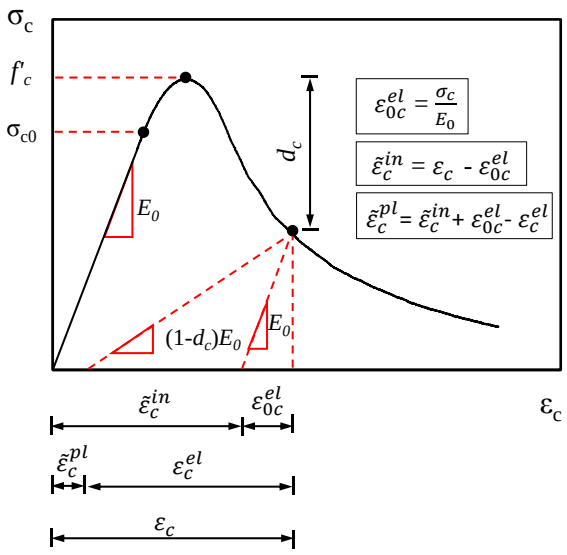

Figure 7-5 Illustration of the compressive behaviour, characteristics and compression hardening data of CDP model in ABAQUS

Figure 7-6 illustrates the definition of tensile stress–strain behaviour in *ABAQUS*. As seen, the stress values need to be introduced as a function of cracking strain, $\tilde{\varepsilon}_t^{ck}$. That is because the CDP model requires the definition of tension stiffening in order to accurately simulate tensile behaviour after failure. The cracking strain is, in fact, the difference between total tensile strain and the elastic strain in the undamaged condition, as illustrated in Figure 7-6. The plastic strain values will then be automatically calculated by the software using following expression:

$$\tilde{\varepsilon}_t^{pl} = \tilde{\varepsilon}_t^{ck} - \frac{d_t}{(1-d_t)}\frac{\sigma_t}{E_0} \tag{7.7}$$

Once inelastic strain or cracking strain have been calculated, it is essential to translate them to a new coordinate system. That is because *ABAQUS* requires inelastic strain or cracking strain data to be introduced in a pure coordinate system, starting from the origin. It should be noted that compressive stress–strain data, ranging from zero up to 40% of the ultimate strength, were ignored in establishing the inelastic strain, because concrete behaves elastically within this customary working stress (ASTM C469/C469M). Similarly, in the case of tensile stress–strain, data less than the ultimate tensile strength were not considered in the establishment of the tensile stress–cracking strain curve.

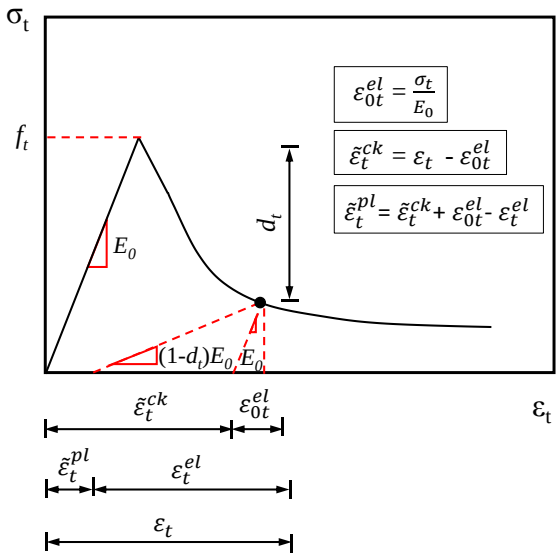

Figure 7-6 Illustration of the tensile behaviour, characteristics and tension stiffening data of CDP model in ABAQUS

The prerequisite for establishing a precise set of data for CDP model is a proper definition of the tensile and compressive behaviour of concrete. In this study, the compressive behaviour of core concrete (the area embraced by the stirrups) was assigned based on the confined concrete model proposed by Mander et al. (1988). This model can accurately account for the effect of confinement provided by transverse reinforcement. For cover concrete, in which the beneficial effects of confinement are not present, the compressive behaviour was defined using the stress–strain relationships obtained from the average of three experimental tests on concrete cylinders (200 mm × 100 mm), tested on the same date as the experiment. In the case of the tensile behaviour of concrete, the stress–strain data were calculated using the analytical expression proposed by Belarbi and Hsu (1994). Figure 7-7 shows the compressive and tensile relationships of concrete material obtained from the above-mentioned analytical models. Regarding confined compressive behaviour, the ultimate compression strain, ε_{cu}, was calculated using the conservative expression given by Priestley et al. (1996), and increased by 50% because the section is subject to bending. Once the compressive strain in concrete reaches this threshold, the stress drops to 20% of the compressive

strength of confined concrete, f'_{cc}, which corresponds to the maximum damage status expected for concrete in compression.

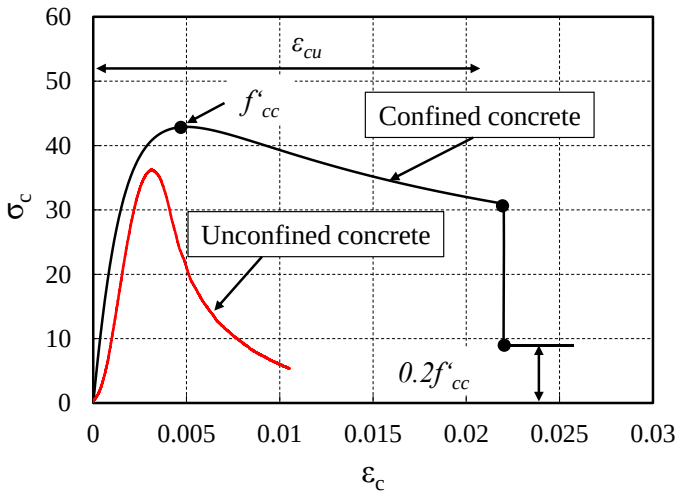

Figure 7-7 Behaviour of concrete in compression adopted from Mander et al. (1988)

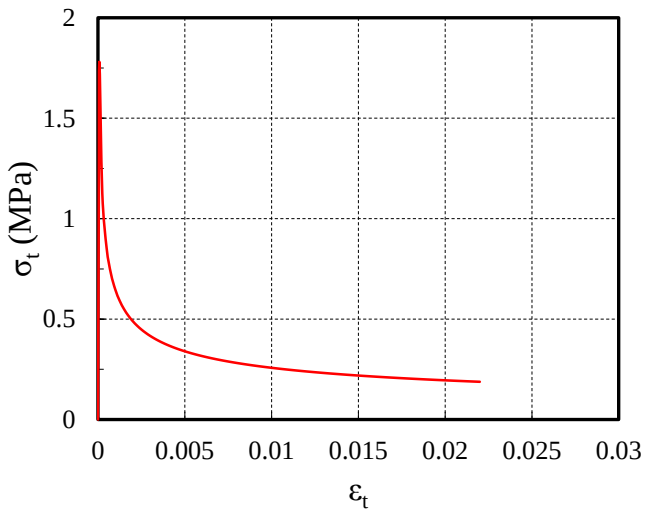

Figure 7-8 Behaviour of concrete in tension adopted from Belarbi and Hsu (1994)

Appendix D provides detailed information and the sequence of data calculation, used to introduce the compressive and tensile behaviour of concrete to *ABAQUS*. It should be noted that although the tensile strain capacity of concrete is considerably less than its compressive capacity, the tensile stress–strain relationship of concrete was inputted in the same range of compressive strain. That is because the behaviour of a material beyond the limit of definition is considered as a constant value by *ABAQUS*.

Thus, if the definition of tensile stress–strain relationship was terminated earlier, a higher constant value of stress was expected. Following the calculation of required data as described above, the tensile behaviour, compressive behaviour, tensile damage parameter and compressive damage parameter, were inputted to the software, as shown in Figure 7-9.

During cyclic loading, the degradation mechanisms involve the opening and closing of previously formed microcracks, and their interactions. Studies in the past showed that there is some recovery of the elastic stiffness as the load changes sign during a uniaxial cyclic test (Fenwick 1983). The effect is further highlighted by changing load direction from tension to compression, causing tensile cracks to close, which results in the recovery of the compressive stiffness. The CDP model allows for incorporating the recovery of the tensile and compressive stiffness upon load reversal by introducing tension and compression recovery factors (w_t and w_c respectively). The default values for tension recovery stiffness ($w_t=0$) and compression recovery ($w_c=1$) were assumed in the present study. This allows for (and results in) full recovery of compressive stiffness upon crack closure as the load changes from tension to compression, and no recovery of tension stiffness as the load changes from compression to tension, once crushing of the concrete is initiated.

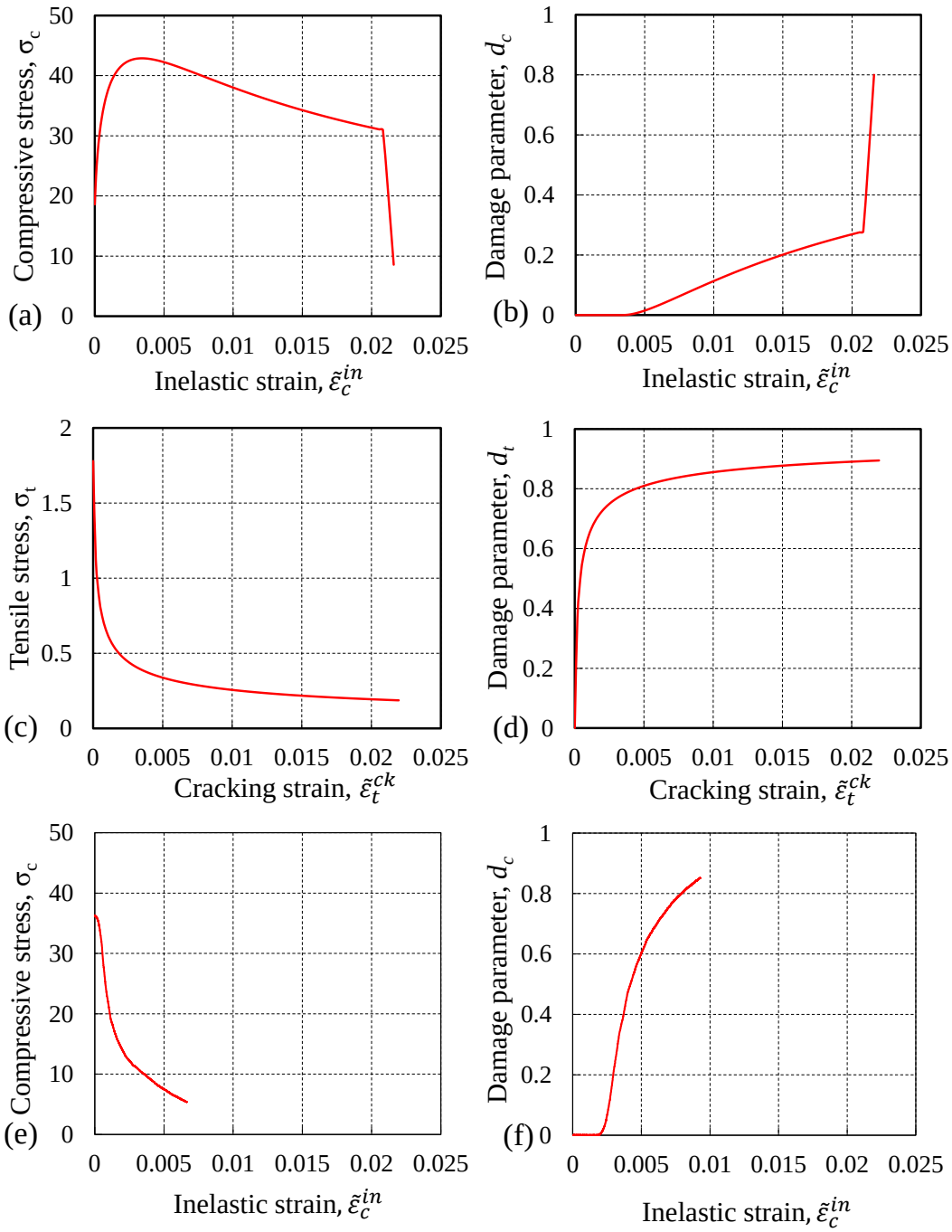

Figure 7-9 Definition of uniaxial behaviour of concrete in ABAQUS: (a), (b) confined compressive behaviour; (c), (d) tensile behaviour; (e), (f) unconfined compressive behaviour

7.3.2 Plasticity characteristics of concrete

The CDP model is an isotropic plasticity model, based on the assumption of non-associated potential plastic flow based on the Drucker-Prager hyperbolic function:

$$G = \sqrt{(\epsilon \sigma_{t0} tan\, \psi)^2 + \bar{q}^2} - \bar{p}\, tan\, \psi \tag{7.8}$$

where G = flow potential function; ψ = dilation angle; ϵ = eccentricity that controls the curvature to the flow potential; σ_{t0} = uniaxial tensile stress at failure (shown by f_t in this study); $\bar{q}$ = Mises equivalent effective stress; and $\bar{p}$ = effective hydrostatic pressure stress.

The dilation angle, the angle between failure surface and hydrostatic axis, is a parameter that specifies the behaviour of concrete under a combination of stresses. This angle was introduced by Hansen (1958) and represents the ratio of plastic volumetric strain to plastic shear strain. The dilation angle after intense shearing vanishes gradually, and further subsequent shearing causes no more change in the volume. Dilation angle physically denotes the internal friction angle in concrete, and is determined in the p–q plane (meridional plane) at high confining pressure. However, Vermeer and De Borst (1984) showed the dilation angle is at least 20° less than the friction angle. That is why it is essential to use a non-associated flow rule which is associated with a potential function (yield function), but based on dilation angle instead of a friction angle.

The dilation angle is affected by the confining stress and plastic strain of concrete, and influences the ductility performance of the concrete (Karabinis and Kiousis 1996; Yu et al. 2010). It is worth mentioning that an increase in ψ accounts for confining and biaxial stress states, as Lee and Fenves (1998a) used dilation angles of 31° and 20° for concrete under uniaxial and biaxial stress states respectively. It was found that the value of the dilation angle that is assigned to the confined concrete is considerably lower than for unconfined concrete. This is in line with a study conducted by Tao et al. (2013) which reported that increasing the confinement leads to a decrease in the dilation angle of concrete.

The eccentricity determines the rate at which the flow potential hyperbola function approaches its asymptote. The default value for eccentricity is 0.1, which causes the dilation angle of concrete to remain constant, over a wide range of confining pressure stress values. As seen in Figure 7-10, the flow potential in the meridional plane becomes a straight line (asymptote) when the eccentricity tends to zero (i.e., classic Drucker and Prager model). Increase in the eccentricity leads to more curvature to the

flow potential, implying that the dilation angle increases more rapidly as the confining pressure decreases.

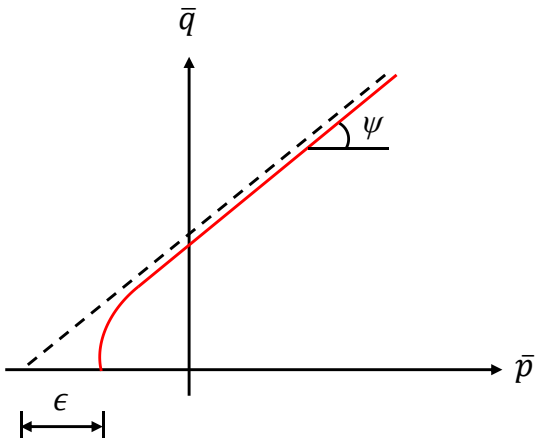

Figure 7-10 Illustration of hyperbolic flow potentials in the meridional stress plane

The evolution of the yield surface is determined by the tensile and compressive equivalent plastic strains. The yield function, F, in terms of effective stresses, is expressed as follows:

$$F = \frac{1}{1-\alpha}(\bar{q} - 3\alpha\bar{p} + \beta(\tilde{\varepsilon}^{pl})\langle\hat{\bar{\sigma}}_{max}\rangle - \gamma\langle-\hat{\bar{\sigma}}_{max}\rangle) - \bar{\sigma}_c(\tilde{\varepsilon}_c^{pl}) = 0 \qquad (7.9)$$

in which the parameters of α, β and γ are defined as follows:

$$\alpha = \frac{(\sigma_{b0}/\sigma_{c0})-1}{2(\sigma_{b0}/\sigma_{c0})-1} \qquad 0 \leq \alpha \leq 0.5$$

$$\beta = \frac{\bar{\sigma}_c(\tilde{\varepsilon}_c^{pl})}{\bar{\sigma}_t(\tilde{\varepsilon}_t^{pl})}(1-\alpha) - (1+\alpha)$$

$$\gamma = \frac{3(1-K_c)}{2K_c-1}$$

and where $\hat{\bar{\sigma}}_{max}$ = maximum principal effective stress; σ_{b0}/σ_{c0} = ratio of initial equibiaxial compressive yield stress to initial uniaxial compressive yield stress; K_c = ratio of the second stress invariant on the tensile meridian to that on the compressive meridian; $\bar{\sigma}_c(\tilde{\varepsilon}_c^{pl})$ = effective compressive cohesion stress; and $\bar{\sigma}_t(\tilde{\varepsilon}_t^{pl})$ = effective tensile cohesion stress.

Figure 7-11 shows the typical yield surfaces for the CDP model used in this study. The value of K_c, in fact, determines the shape of the yield surface and its definition is

based on the full triaxial tests of concrete. It takes the minimum value of 0.5, and, at most, reaches 1.0; however, the default value is 2/3, similar to the convexity of the ellipsoidal triaxial failure surfaces formulated by Willam and Warnke (1975). The ratio of σ_{b0}/σ_{c0}, denotes a point at which the concrete undergoes failure under equal compressive stresses in two principal directions. The default ratio is 1.16, which is based on the experimental biaxial test results reported by Kupfer et al. (1969).

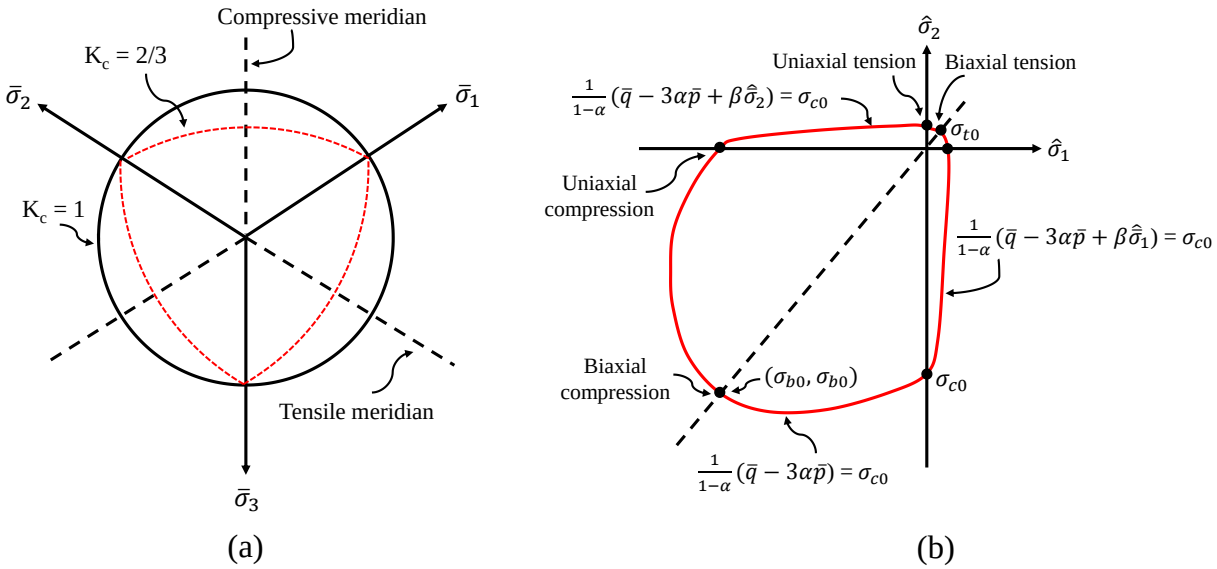

Figure 7-11 Typical yield surfaces of the CDP model: (a) yield surfaces in the deviatoric plane; (b) yield surface in plane stress conditions

The use of a concrete model consisting of both softening behaviour and stiffness degradation often leads to severe numerical convergence problems in *ABAQUS*. That is why viscoplastic regularization of the constitutive equations is generally employed to overcome some of these convergence issues. The technique is based on a generalization of the Duvaut-Lions regularization approach (Duvant and Lions 2012) that causes the consistent tangent stiffness of the softening material to become positive for sufficiently small time increments. In fact, introducing the viscosity parameter, μ, in the CDP model represents a relaxation time of the viscoplastic system, allowing stresses to be outside the yield surface (*ABAQUS 2015*). The incorporation of μ results in the establishment of a viscoplastic strain rate tensor, $\dot{\varepsilon}_v^{pl}$, as follows:

$$\dot{\varepsilon}_v^{pl} = \frac{1}{\mu}(\varepsilon^{pl} - \varepsilon_v^{pl}) \tag{7.10}$$

Similarly, a viscous stiffness degradation variable, $\dot{d}_v$, for the viscoplastic system is expressed as

$$\dot{d}_v = \frac{1}{\mu}(d - d_v) \tag{7.11}$$

where d is the degradation variable determined in the inviscid backbone model. Finally, the stress–strain relationship of the viscoplastic model in the incremental sense, by taking into account two admissible stress rate fields, can be expressed as

$$\boldsymbol{\sigma} = (1 - d_v)\boldsymbol{D}_0^{el} : (\varepsilon - \varepsilon_v^{pl}) \tag{7.12}$$

Note that the colon operator in the above equation denotes the double dot product. Also, in the case of a nonzero value for μ, the output results of the plastic strain and stiffness degradation refer to the viscoplastic values, ε_v^{pl} and d_v, respectively. The time increment step is the parameter that specifies the value of the viscosity parameter. Although considering μ avoids numerical instability, its value should be chosen appropriately. The higher the value of μ, the less running time is needed. Lee and Fenves (1998b) considered 0.15 of the time step as viscosity parameter and stated that, at this condition, the element size can be used directly as the characteristic length. Table 7-1 shows the plasticity parameters of the CDP model used in this study.

Table 7-1 The plasticity parameters of CDP model

ψ	ϵ	σ_{b0}/σ_{c0}	K_c	μ
27	0.1	1.16	0.52	0.0008

7.4 Modelling of steel

7.4.1 Uniaxial tension behaviour

Figure 7-12 shows the stress–strain relationships for the reinforcing bar. *ABAQUS* requires the user to define the behaviour of reinforcement as true stress versus true strain. For this, the engineering (nominal) stress–strain results, obtained from a tensile test on 16 mm Grade 300E reinforcement using a universal machine, were converted to true stress versus true strain, as follows:

$$\sigma_{true} = \sigma_{nom}\,(1+\varepsilon_{nom}) \tag{7.13}$$

$$\varepsilon_{true} = ln\,(1+\varepsilon_{nom}) \tag{7.14}$$

Just as for concrete material, it is also essential to separately define the elastic and inelastic behaviour of reinforcing steel. Elastic behaviour is characterized by introducing the elastic modulus (E_0) and Poisson's ratio (ν), while to define plastic behaviour, the yield stresses and plastic strain values are needed. The average values of modulus of elasticity, yield stress and Poisson's ratio from three tensile tests were found to be 212.76 GPa, 297.14 MPa and 0.29, respectively. The plastic strain of steel (ε_s^{pl}), is the difference between true strain and elastic strain ($\varepsilon_s^{pl} = \varepsilon_{true} - \sigma_{true}/E_0$). It is worth mentioning that, since the plastic strain value should represent the onset of plasticity, it starts from zero when inputted to *ABAQUS*.

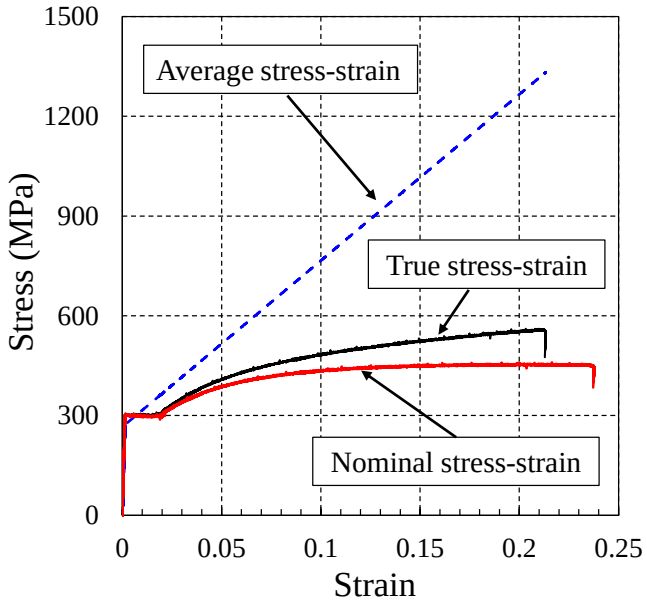

Figure 7-12 Illustration of average, true and nominal stress–strain relationships

Once the true stress versus true strain data were achieved, the analytical model proposed by Belarbi and Hsu (1994) was used to construct the average stress–strain curve of embedded steel bar. That is because available studies confirm that the behaviour of steel bar while it is embedded in concrete is distinct from its behaviour when it is tested bare. In fact, while the stress–strain curve of a steel bar tested in a bare condition shows a significant yield plateau, in the case of the average stress–strain curve of steel bar embedded in concrete, no yield plateau is observed. Furthermore, the yield stress shifts down compared with the yield stress of a bare bar (Shima et al. 1987; Belarbi and Hsu 1994; Maekawa et al. 2003). Note that although the use of the average

stress–strain curve results in a significant difference in steel stress at high levels of inelastic deformation (up to 2.5 times), in the normal range of strain to which an RC member is subjected (before the onset of strain hardening), the difference in stress values acquired from the two curves is limited.

7.4.2 Cyclic inelastic behaviour

To accurately model the cyclic inelastic behaviour of steel material, a nonlinear combined (isotropic/kinematic) hardening model was used. The evolution law of this model consists of two components: a nonlinear kinematic hardening component, and an isotropic hardening component (Chaboche 1986). The former describes the translation of the yield surface in stress space through the back stress (α) when the size of the yield surface is retained, while the latter determines the change of the equivalent stress which leads to the size of the yield surface (σ^0) (Figure 7-13). The incorporation of kinematic hardening was essential, since the isotropic hardening does not account for the Bauschinger effect. This effect is characterized by a reduced yield stress upon load reversal after plastic deformation has occurred during the initial loading. Although the linear kinematic hardening component takes this effect into consideration, the nonlinear component improves the shape of the cycles. Moreover, the model allows for superposition of multiple kinematic hardening components (back stresses), which results in further improvement of the shape of the cycle (ABAQUS 2015).

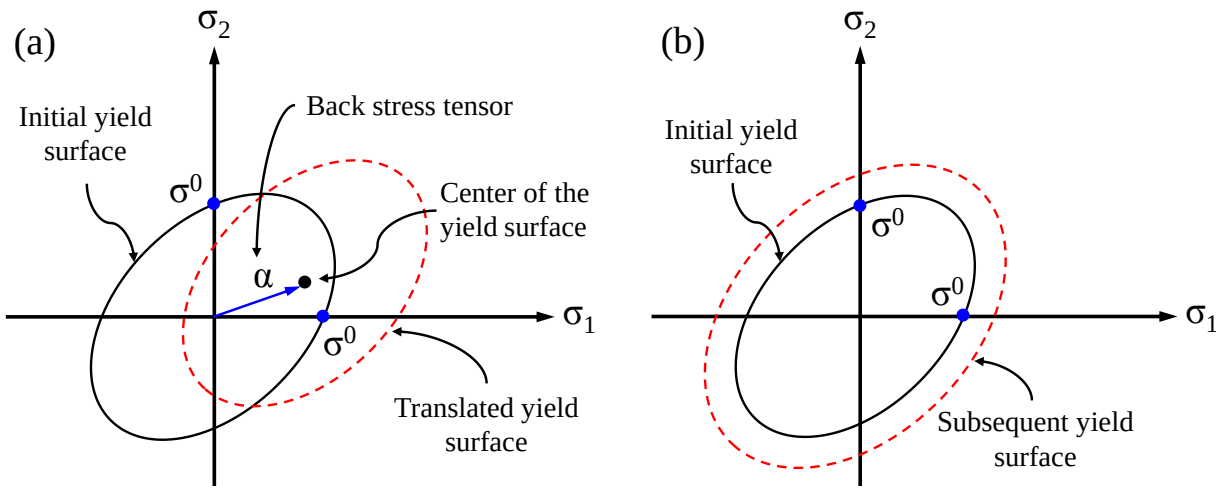

Figure 7-13 Evolution of the yield surface in the biaxial stress plane: (a) kinematic hardening, (b) isotropic hardening

For the case of kinematic hardening, the magnitude of back stresses at large plastic strains is expressed as:

$$\alpha^s = \sum_{k=1}^{N} \frac{C_k}{\gamma_k} \tag{7.15}$$

where α^s = the magnitude of α; N = number of back stresses; C_k and γ_k = material parameters that must be calibrated from cyclic test data. C_k is the initial kinematic hardening moduli, and γ_k determines the rate at which the kinematic hardening moduli decrease with increasing plastic deformation.

The parameters C_k and γ_k were specified using a stabilized cycle method. This method requires stress–strain data, obtained from the stabilized cycle of a steel specimen which had been subjected to symmetric strain cycles. Once data were provided, the kinematic hardening parameters can be determined by the software. Figure 7-14 shows the result of a low-cycle fatigue test on a reinforcing bar using the MTS 810 machine. Apart from the first cycle that shows a slight rise to the stress, for the rest of cycles the cyclic softening occurs, which is in line with experiments conducted by Mander et al. (1994). This is attributed to the "saturation hardening" effect that happens in the early stage of the fatigue life of steel, as illustrated by Manson (1965). Regarding the beneficial effect of the number of back stresses in simulations when the combined hardening model is employed, nine back stresses were considered in the analysis.

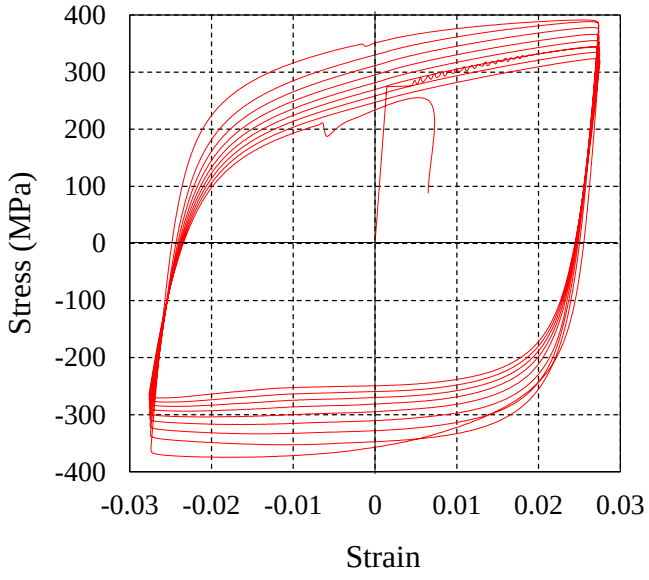

Figure 7-14 Cyclic stress–strain behaviour of reinforcing bar

Isotropic hardening was introduced in the model using a simple exponential law, a function of the equivalent plastic strain ($\bar{\varepsilon}^{pl}$) as expressed below:

$$\sigma^0 = \sigma|_0 + Q_\infty(1 - e^{-b\,\bar{\varepsilon}^{pl}}) \tag{7.16}$$

where $\sigma|_0$ = the yield stress at zero plastic strain; Q_∞ = maximum change in the size of the yield surface; and b = material parameters that define the rate at which the size of the yield surface changes as plastic straining develops.

To obtain the isotropic hardening parameters (Q_∞ and b), a set of data pairs of σ^0, as a tabular function of $\bar{\varepsilon}^{pl}$, is needed. For this, data obtained from the symmetric strain-controlled cyclic test (Figure 7-14) were used. The size of the yield surface at corresponding equivalent plastic strain for each cycle can be obtained from Equation 7.17.

$$\sigma_i^0 = \sigma_i^t - \alpha_i \tag{7.17}$$

where $\alpha_i = (\sigma_i^t + \sigma_i^c)/2$; σ_i^t = peak tensile stress at cycle *i*; and σ_i^c = peak compressive stress at cycle *i*.

Also, the equivalent plastic strain corresponding to σ_i^0 is determined as follows:

$$\bar{\varepsilon}_i^{pl} = \frac{1}{2}(4i - 3)\Delta\varepsilon^{pl} \tag{7.18}$$

where i = cycle number; $\Delta\varepsilon^{pl}$ = plastic strain range ($\Delta\varepsilon^{pl} \approx \Delta\varepsilon - 2\sigma_1^t)/E$), in which σ_1^t is the peak tensile stress in the first cycle.

Figure 7-15 shows the data pairs ($\sigma_i^0, \bar{\varepsilon}_i^{pl}$) along with the best nonlinear exponential fit of Equation 20 on the test data to obtain the isotropic hardening parameters. The values of Q_∞ and b were found to be −2927.7 MPa and −0.022, respectively. The negative value for Q_∞ denotes the strain softening behaviour that confirms the experimental observations, and is in line with previous studies by You and Miskiewicz (2008), and Roufegarinejad and Tremblay (2012).

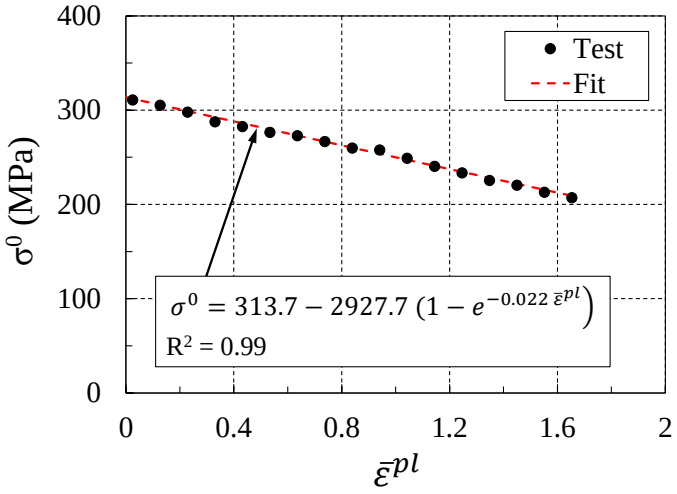

Figure 7-15 Curve fitting for isotropic hardening parameters

It is worth mentioning that the application of a nonlinear isotropic/kinematic hardening model allows for the expansion or contraction of yield surface range due to the isotropic component. This is a key feature by which low-cycle fatigue failure as well as inelastic deformation of reinforcing bars can be modelled.

7.5 Finite element analysis results

7.5.1 Pushover behaviour

Figure 7-16 shows the monotonic force–displacement results of the numerical study and test. As seen finite element analysis (FEA) shows a slightly stiffer response (i.e., higher initial stiffness) compared with the experiment that might have originated from the initial microcracking of the beam prior to testing. For drift levels beyond 4%, FEA shows lower post-yield stiffness. This possibly refers to the definition of the average stress–strain behaviour of reinforcement embedded in concrete. Figure 7-17 shows the damage status in terms of crack propagation in the specimen. As seen, the formation of main cracks and their pattern has been acceptably captured by the model.

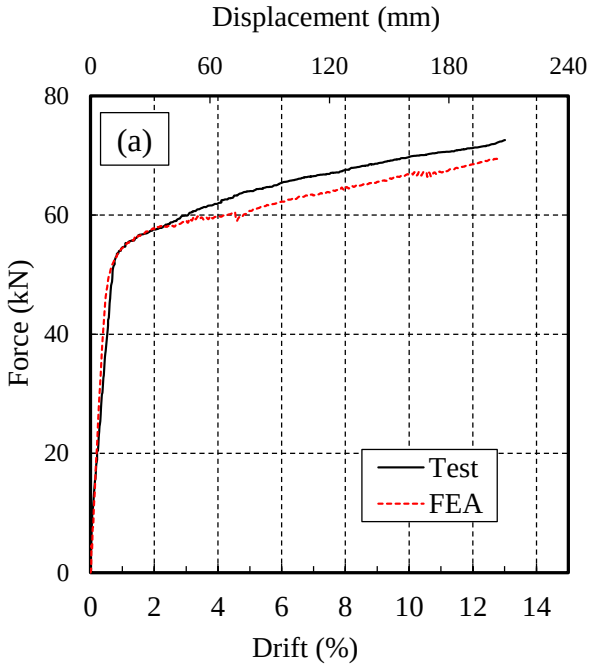

Figure 7-16 Monotonic load-displacement response of RC beam

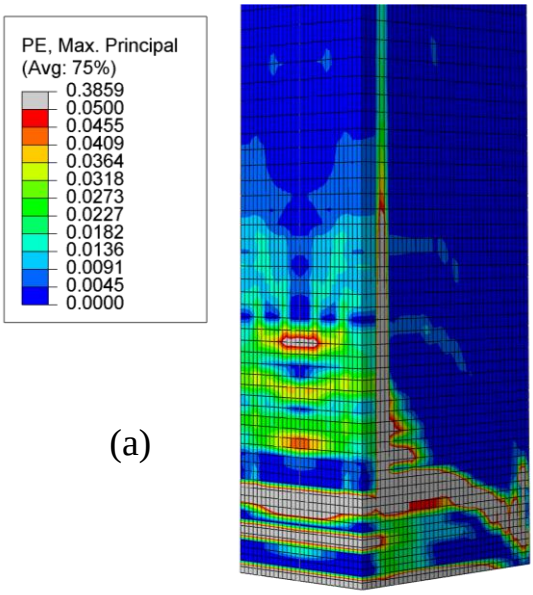

Figure 7-17 Cracking pattern at the end of pushover analysis

7.5.2 Fatigue behaviour

The hysteresis behaviours of the specimens subjected to 2% and 4% drift cyclic loading from experiment and FEA were plotted in Figure 7-18(a)–(b). As it can be seen

the FEA results show good agreement with experiments. However, the maximum force (strength) archives in each cycle in numerical results are less than experiments. Also, FEA results in lesser number of cycle that specimen can take up to failure (i.e., fatigue life). That is because the data used for simulation of low-cycle fatigue behaviour of bars is related to nude bar tested in lab, not a bar embedded in concrete. It should be noted that the FE graphs of cyclic loading is considerably smoother compared to monotonic graph smooth. That is because in FEA associated with monotonic loading, the lateral displacement was applied in a very small increments over 2030 steps. In other word, in each increment, 0.01 mm of the total displacement (i.e., 203 mm) was applied. While in the case of cyclic loading constantly at 2% drift (i.e., 31.2 mm), the loading protocol was applied in faster manner to reduce the computational time required by the *ABAQUS*. Thus, increments equal to 0.1 mm was considered which resulted in 249600 steps of loading for about 200 cycles (4×312×200).

The model took about 69 hours to complete. Although increasing the increments may seem to reduce the computational time, there is a limit beyond that increasing the increments causes significant irregularities in results. Figure 7-19 shows the cracking pattern and damage in terms of plastic strain (PE). It shows that the FE model can satisfactorily simulate damage distribution of the test specimens. Severity of the cracks had increased as the drift cycles got bigger.

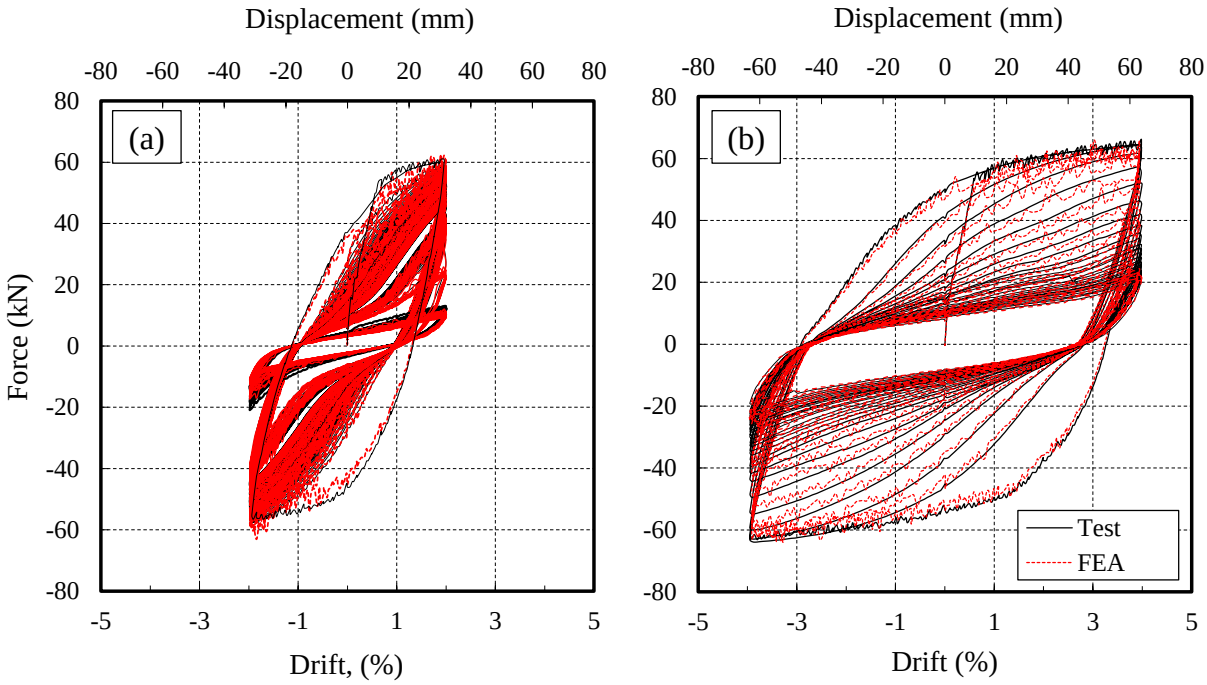

Figure 7-18 Load-displacement response of RC beams subjected to constant-amplitude cyclic loading: (a) at 2% drift; (b) at 4% drift

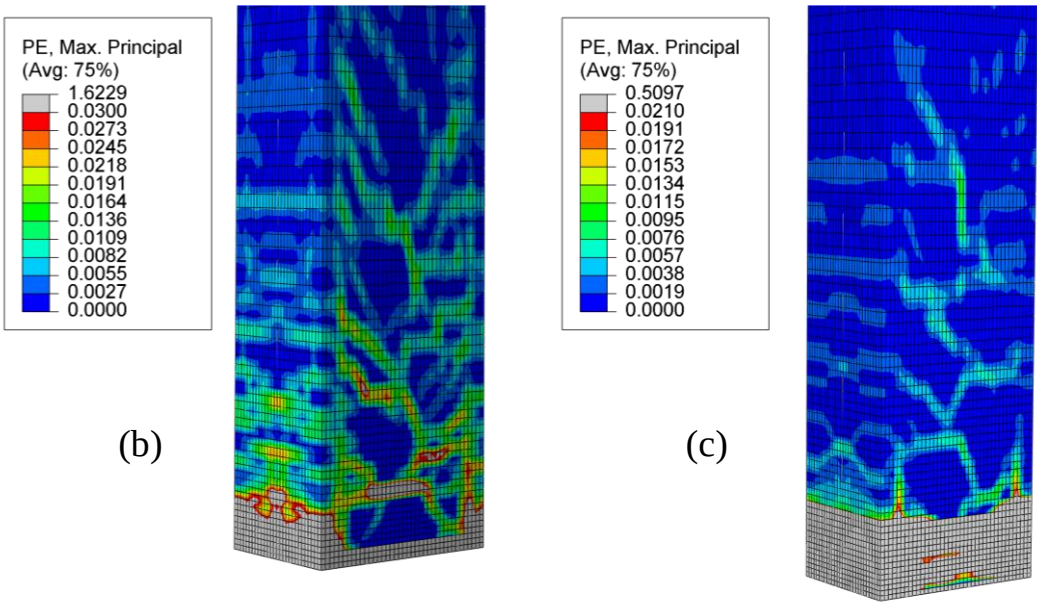

Figure 7-19 Cracking pattern at the ultimate fatigue life: (a) cyclic at 2% drift; (b) cyclic at 4% drift

7.6 Conclusions

Overall, the FE predictions performed using nonlinear analysis with ABAQUS, showed a reasonable agreement with the actual experimental test results. This also shows that the selected finite element based software with its implemented material models and element library was capable of dealing with the complexities involved in modelling and analysing fatigue behaviour of RC beams. On the basis of FEA, following conclusions were deduced:

1. Pushover analysis was conducted first to examine the capability of the developed model of further cyclic analysis. That is because pushover analysis is comparatively simple, stable, results in better convergence and requires lesser time. The appropriateness of the finite element model, mesh sensitivity were checked, fine tuning of the model and suitability of the material models were investigated at this stage.
2. The good agreement between numerical and experimental results confirmed the capability of the FE model developed in this study to predict the behaviour of beams under fatigue loading. The formation and propagation of cracking as well as force–displacement responses were accurately captured. The CDP model was adopted to represent the nonlinear behaviour of concrete using tensile and compressive damage parameters. For steel, the nonlinear combined (isotropic/kinematic) hardening model was adopted and calibrated using low-cycle fatigue tests on similar reinforcement to accurately capture its behaviour. The presented FEA showed promise for conducting a future parametric study on different aspects affecting the fatigue behaviour of tested beams.

7.7 References

ABAQUS (2015). "Analysis user's manual 2016." *Dassault System Simulia Corp.*

ASTM C469/C469M (2014). "Standard test method for static modulus of elasticity and Poisson’s ratio of concrete in compression." ASTM International, West Conshohocken, PA.

Belarbi, A., and Hsu, T. T. (1994). "Constitutive laws of concrete in tension and reinforcing bars stiffened by concrete." *Structural Journal*, 91(4), 465-474.

Borst, R. d., Remmers, J. J., Needleman, A., and Abellan, M. A. (2004). "Discrete vs smeared crack models for concrete fracture: bridging the gap." *International*

Journal for Numerical and Analytical Methods in Geomechanics, 28(7-8), 583-607.

Chaboche, J.-L. (1986). "Time-independent constitutive theories for cyclic plasticity." *International Journal of plasticity*, 2(2), 149-188.

Coulomb, C. A. (1773). "Essai sur une application des règles de maximis et minimis à quelques problèmes de statique relatifs à l'architecture." *Mem. Div. Sav. Acad.*, 7.

Drucker, D. C., and Prager, W. (1952). "Soil mechanics and plastic analysis or limit design." *Quarterly of applied mathematics*, 10(2), 157-165.

Duvant, G., and Lions, J. L. (2012). *Inequalities in mechanics and physics*, Springer Science & Business Media.

Fenwick, R. (1983). "Strength degradation of concrete beams under cyclic loading." *Bulletin of NZ Society for Earthquake Engineering*, 16(1), 25-38.

Hansen, B. "Line ruptures regarded as narrow rupture zones. Basic equations based on kinematic considerations." *Proc., Proc. Conf. Earth Pressure Problems, Brussels*, 39-48.

Karabinis, A., and Kiousis, P. (1996). "Strength and ductility of rectangular concrete columns: a plasticity approach." *Journal of Structural Engineering*, 122(3), 267-274.

Kupfer, H., Hilsdorf, H. K., and Rusch, H. "Behavior of concrete under biaxial stresses." *Proc., Journal Proceedings*, 656-666.

Lee, J., and Fenves, G. L. (1998a). "Plastic-damage model for cyclic loading of concrete structures." *Journal of engineering mechanics*, 124(8), 892-900.

Lee, J., and Fenves, G. L. (1998b). "A plastic-damage concrete model for earthquake analysis of dams." *Earthquake engineering & structural dynamics*, 27(9), 937-956.

Lubliner, J., Oliver, J., Oller, S., and Onate, E. (1989). "A plastic-damage model for concrete." *International Journal of solids and structures*, 25(3), 299-326.

Maekawa, K., Okamura, H., and Pimanmas, A. (2003). *Non-linear mechanics of reinforced concrete*, CRC Press.

Mander, J., Panthaki, F., and Kasalanati, A. (1994). "Low-cycle fatigue behavior of reinforcing steel." *Journal of Materials in Civil Engineering*, 6(4), 453-468.

Mander, J. B., Priestley, M. J., and Park, R. (1988). "Theoretical stress-strain model for confined concrete." *Journal of structural engineering*, 114(8), 1804-1826.

Manson, S. (1965). "Fatigue: a complex subject—some simple approximations." *Experimental mechanics*, 5(7), 193-226.

Mohr, O. (1906). *Abhandlungen aus dem gebiete der technischen mechanik*.

Ngo, D., and Scordelis, A. "Finite element analysis of reinforced concrete beams." *Proc., Journal Proceedings*, 152-163.

Priestley, M. N., Seible, F., and Calvi, G. M. (1996). *Seismic design and retrofit of bridges*, John Wiley & Sons.

Rashid, Y. (1968). "Ultimate strength analysis of prestressed concrete pressure vessels." *Nuclear engineering and design*, 7(4), 334-344.

Rots, J., Nauta, P., Kuster, G., and Blaauwendraad, J. (1985). "Smeared crack approach and fracture localization in concrete." *HERON, 30 (1), 1985*.

Roufegarinejad, A., and Tremblay, R. (2012). "Finite element modeling of the inelastic cyclic response and fracture life of square tubular steel bracing members subjected to seismic inelastic loading." *Behaviour of Steel Structures in Seismic Areas*, 97-103.

Shima, H., Chou, L.-L., and Okamura, H. (1987). "Micro and macro models for bond in reinforced concrete." *Journal of the Faculty of Engineering*, 39(2), 133-194.

Sun, J., Lee, K., and Lee, H. (2000). "Comparison of implicit and explicit finite element methods for dynamic problems." *Journal of Materials Processing Technology*, 105(1), 110-118.

Tao, Z., Wang, Z.-B., and Yu, Q. (2013). "Finite element modelling of concrete-filled steel stub columns under axial compression." *Journal of Constructional Steel Research*, 89, 121-131.

Vermeer, P. A., and De Borst, R. (1984). "Non-associated plasticity for soils, concrete and rock."

Willam, K. J., and Warnke, E. P. (1975). "Constitutive model for the triaxial behavior of concrete." *International association for bridge and structural engineering proceedings*, 19, 1-30.

You, J.-H., and Miskiewicz, M. (2008). "Material parameters of copper and CuCrZr alloy for cyclic plasticity at elevated temperatures." *Journal of Nuclear Materials*, 373(1), 269-274.

Yu, T., Teng, J., Wong, Y., and Dong, S. (2010). "Finite element modeling of confined concrete-II: Plastic-damage model." *Engineering Structures*, 32(3), 680-691.

Chapter 8 *Damage assessment of RC beams subjected to low-cycle fatigue at high rate of loading*

8.1 Introduction

In the event of an earthquake, RC buildings located in seismically active areas are likely to experience seismic loading at a high rate. Since the mechanical properties of steel (Norris 1959; Cowell 1969), concrete (Cowell 1966), and steel-to-concrete bond (Robert and Atis 1962) are all rate-dependent, the response of the RC members (i.e., strength, stiffness, deformability and failure mode) is also likely to be dependent on the load rate and may differ substantially from the response under low rate static loading. The importance of the effect of loading rate on the seismic performance of RC buildings has been highlighted in the recent earthquake (Canterbury Earthquakes Royal Commission 2012). The current practice, which is used to design RC members, does not adequately account for the effect of the rate of loading.

The core knowledge of the structural behaviour of RC members and subassemblies under cyclic loading has generally been obtained based on experimental results of specimens tested under pseudo-static conditions. The limited availability of high-speed actuators, the need for special equipment and complexities in conducting high-speed experiments resulted in limited data regarding the effect of rate of loading in the literature. This chapter intends to experimentally determine the effect of high rate of loading on the behaviour of seismically designed cantilever RC beams, subjected to constant-amplitude cyclic fatigue loading at two varied loading rates.

8.1.1 Effect of rate of loading on concrete/steel

The effect of rate of loading on RC buildings can be investigated at four levels: constituent materials (i.e., concrete or steel), members, subassemblies, and system level. At the material level, it is well-accepted in the literature that an increase in the rate of loading results in an increase in both the compressive and tensile strength of plain concrete (Rostasy et al. 1984; Bischoff and Perry 1991; Malvar and Ross 1998). Similarly, a study conducted by Fu et al. (1991) showed that for confined concrete, the

compressive strength, tensile strength and slope of the stress–strain relationship in the post-peak region also increases. With regard to reinforcing steel, an increase in the rate of loading causes the yield stress, ultimate strength and the strains corresponding to these stresses to increase (Soroushian and Choi 1987; Malvar 1998; Cadoni et al. 2015). However, for both materials, the literature shows that as the strength of the material increases its sensitivity to the rate of loading decreases (Fu et al. 1991). Figure 8-1 shows a typical comparison of the static and dynamic behaviour of steel reinforcing bar and concrete.

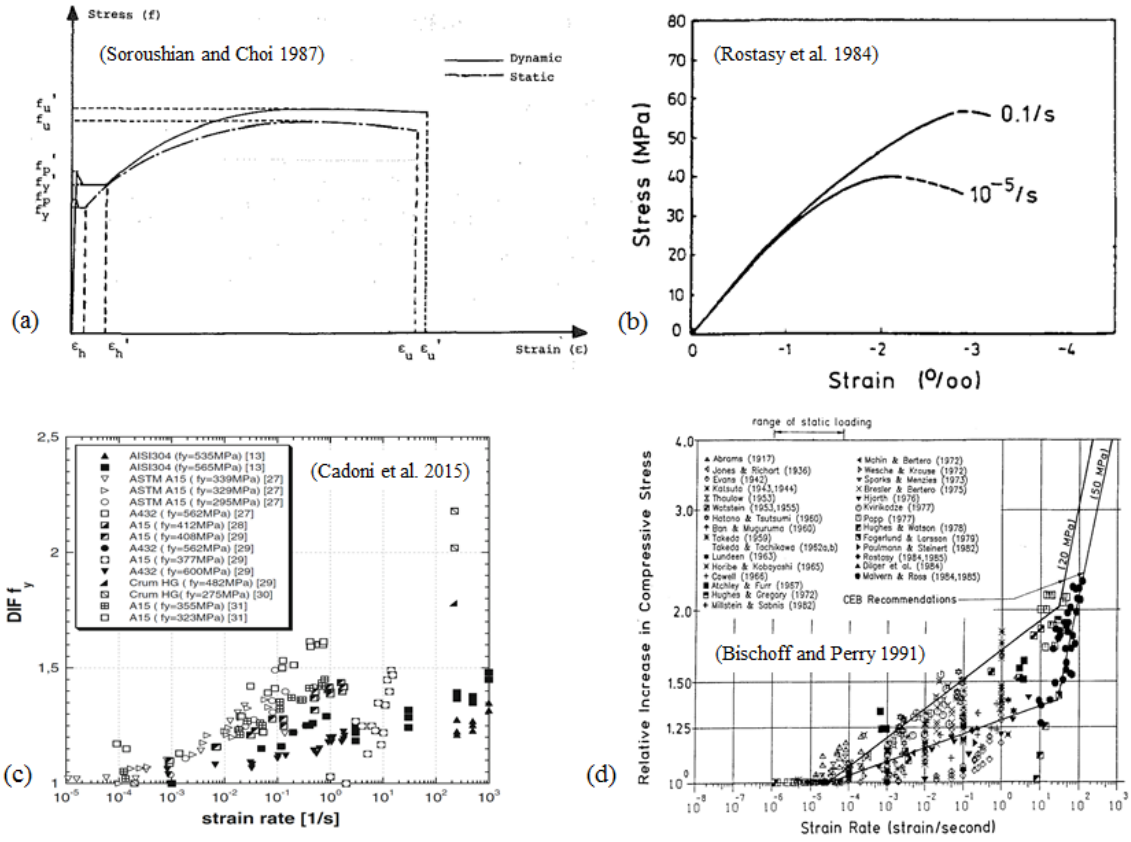

Figure 8-1 Illustration of strain rate effect on mechanical properties of steel and concrete: (a) stress–strain response for reinforcing bar in tension at low and high strain rates: (b) stress–strain response for concrete in compression at low and high strain rates; (c) dynamic increase factor (DIF) for yield stress of steel bar versus strain rate; (d) relative increase in the compressive strength of concrete

8.1.2 Effect of rate of loading on RC beam-column joints/system

At the subassemblies level, Shah et al. (1987) investigated the effect of rate of loading on the beam-column joints through application of cyclic loading at 2.5×10^{-3} and 1 Hz. Results showed that at a faster rate of loading: (a) the maximum load carrying capacity of the specimen is higher; (b) the damage that occurred was reported to be more significant than that at the slower rate; and (c) fewer and more-localized cracks were observed on the specimen. Chung and Shah (1989) also found that beam-column joints, subjected to cyclic loading at a rate of 2 Hz, failed at a lower ductility ratio compared to specimen tested at a lower rate of loading. Furthermore, the study showed that at a faster rates of loading, fewer and wider cracks were formed near the column face, while more widely distributed cracks emerged in the beam part. Dhakal and Pan (2003) also investigated the effects of high rates of loading on the performance of a beam-column joint. The loading protocol followed an incremental trend, starting at a frequency of 20 Hz associated with ±0.25% drift angle, and ending at a frequency of 3 Hz at ±2.5% drift angle. The study highlighted more the technical aspects of performing a high-speed test: the influence of inertia force, filtering and the quality of instruments for successful data acquisition. It also showed the shear capacity of the tested joints under high-speed cyclic loading was higher than that computed with the empirical equation in seismic codes.

At a system level, the effect of rate of loading on RC buildings/frames, has been observed through many shaking table tests (Inoue et al. 2000; Stavridis et al. 2012; Ghannoum and Moehle 2012; Nagae et al. 2015). However, because of the substantial expensive associated with conducting such tests, the difficulty of direct assessment of the effect of rates of loading on the response of components, and also the difficulty of performing a parametric study, it is of great interest to study this effect at member/subassemblies level individually.

8.1.3 Effect of rate of loading on RC beams

Regarding the effect of rate of loading on the behaviour of structural RC elements, Penzien and Hansen (1954) reported the very first study on the elastic behaviour of simple and continuous RC beams under impulse loading. The results showed that the maximum strain recorded under dynamic loading is comparatively higher than the

strain measurements in static loading, even though both were applied with the same amplitude. In the study conducted by Takeda and Tachikawa (1972), Takeda et al. (1977) and Takeda (1984), it was observed that increasing the rate of loading, the fracture of the specimen occurred earlier compared to a companion specimen tested statically. This was attributed to some loss in shear strength because of the rapid propagation of shear cracks near the loaded areas. Mahin et al. (1972) conducted a landmark study on the responses of RC beams tested under a 4 point load condition with quasi-static (2.5 mm/s) and dynamic (25 mm/s) loading. The key findings were reported as follows: (a) the yield strength may increase significantly at a higher rate of loading; however, by increasing the post-yield deformation, the difference between maximum dynamic strength and quasi-static strength decreases; (b) there was a very small increase in the initial elastic stiffness at a high rate of loading; and (c) at a high rate of loading, during the first cycle, a slight increase in energy dissipation was observed.

A study conducted by Bertero et al. (1973) also showed that high rates of loading cause an increase in the yield strength on the first loading excursion. Wakabayashi et al. (1980) also found that the monotonic load carrying capacity of the RC beam during a 4 point load test increased with an increase in curvature rate. The results of the study reported by Mutsuyoshi and Machida (1984b) also showed a marked increase in the monotonic load carrying capacity response of singly reinforced tested beams at high rates of loading. The results of the study conducted by Kulkarni and Shah (1998) on singly reinforced RC beams tested monotonically using a four-point load configuration, also indicated an increase in the rate of loading, peak load and energy absorption capacity. It was also found that at high rates of loading, the total number of cracks decreased considerably.

Moreover, at high rates of loading, the failure mode shifted from shear failure to flexural failure. Although, the occurrence of such a failure mode was tentatively ascribed to the sensitivity of different steel used in this study, it is in contradiction with the generally accepted transition of flexural failure at static loading to shear failure at dynamic loading (Bertero et al. 1973; Mutsuyoshi and Machida 1984b; Fu et al. 1991). In a study performed by Otani et al. (2003), an increase of 7-20% in the flexural strength of the tested cantilever RC beams was reported. However, companion specimens

showed similar crack patterns under both static and dynamic tests. Investigation by Li and Li (2012) on the effect of the rate of loading on cyclic behaviour of RC beams under the 4 point load test, showed by increasing the rate of loading, the load bearing capacity and the equivalent damping increase. However, the ductility and stiffness decreased, and most importantly no change in the failure mode of beams was reported. The results of a study by Somraj et al. (2013) indicated with an increase in the rate of loading, the maximum strength of the RC beams tested monotonically under a 3 point load increases. Besides, it was reported that the influence of the loading rate on the maximum strength is more significant for the specimens which failed in shear rather than those which failed in flexure. More recently, studies conducted by Adhikary et al. (2012) and Adhikary et al. (2014) on the effect of high rates of loading on the monotonic behaviour of RC beams under a 3 point load configuration, also showed an increase in the ultimate load, cracking stiffness and energy absorption.

8.1.4 Effect of rate of loading on RC columns

With respect to the effect of rate of loading on axial response of RC members, Reinschmidt et al. (1964) carried out a series of static and dynamic tests on RC columns of varying length by applying axial loads with and without eccentricity. Columns under dynamic loading showed 30-40% more strength compared to companion columns loaded pseudo-statically. In terms of the response of columns subjected to lateral cyclic loading, results reported by Arakawa and Arai (1984) showed yield strength, load carrying capacity and failure mode of the tested RC columns were not affected by increasing the rate of cyclic loading from 0.05 Hz to 1 Hz. In contrast, a study conducted by Mutsuyoshi and Machida (1984a) on the responses of RC piers under lateral monotonic loading showed an increase not only in yield strength, but also in the initial stiffness and maximum strength under dynamic test. However, the effect of an increase in the rate of loading in the behaviour of the specimen under cyclic loading was reported as insignificant. This study also reported the total energy dissipation capacity of the RC piers at dynamic condition (1000 mm/s) compared to that under static (1 mm/s) were not recognizable and the hysteresis loops were almost the same.

In respect of the failure of RC columns at high rates of loading, a study carried out by Ichihashi and Wada (1987) reported instant fracture of RC columns at high rates

of loading compared to gradual fracturing. Nevertheless, a study by Ghannoum et al. (2012) showed that despite a 33% increase in the lateral load capacity of RC columns tested under symmetric double curvature bending conditions, the failure mode did not change. More recently, a study by Witarto et al. (2014) on the shear behaviour of RC columns, under lateral cyclic loading at a rate of 5 Hz, showed no difference with the paired specimen's response tested at 0.05 Hz.

A review of the literature shows some inconsistencies in the findings as well as a lack of information on the state of the art on the effect of high rates of loading on the seismic performance of RC elements. With the aim of providing further information, this chapter reports the results of experimental investigations on the performance of RC beams subjected to constant-amplitude fatigue loading at two loading rates of 0.5 mm/s and 500 mm/s, to address the following objectives: (1) to determine the effect of the rate of loading on the cyclic behaviour of the specimens; (2) to assess the effect of the rate of loading on the fatigue life of the specimens; (3) to assess the effects of the rate of loading on the degradation of strength and energy dissipation over the fatigue life of the specimens; and (4) to examine the effects of rate of loading on the failure mode and the cracking pattern of the specimens.

8.2 Experimental program

8.2.1 Test specimen and test set-up

Four RC beams, two low rate and two at high rate of loading were subjected to constant amplitude cyclic loading at 2% and 4% drift (i.e., chord rotation). The test specimens used in the high speed testing were identical to those used in the previous tests, the details of which can be found in section 7.2.1 and 7.2.2 . In the case of high speed testing, an actuator with a capacity of 150 kN at a rate as high as 1000 mm/s and similar stroke to the 400 kN actuator was used. The high-speed actuator was equipped with a servo valve capable of supplying oil at a rate of 400 L/min. The applied load was measured using the load cell positioned at the head of actuator.

8.2.2 Instrumentation and data acquisition

For measuring global lateral displacement of the specimen, in the case of low rate of loading, a string potentiometer was connected to a hook welded to clamping plates

on the top of the specimen at the same level at which the load was applied. However, to measure the same displacement, at high rate of loading a special displacement transducer, which was insensitive to shock and vibration (Balluff Micropulse P BTL5) with a resolution of 0.001 mm, was used. With this type of transducer, the measurement section is protected inside an extruded aluminum profile, and a passive encoder with no power supply marks the measuring point on the measuring path. To measure the acceleration during high rate of loading tests, an accelerometer was mounted on the clamping plate, which had been designed to connect the head of the actuator to the specimen. Readings from the load cell and displacement transducer associated with global force-displacement behaviour of the test specimen were automatically recorded using specific test control software which offered high-speed communication (RMCTools)

In order to gather detailed information on the behaviour of the specimen, particularly in the plastic hinge region at different rates, two specimens tested at low rate of loading were well instrumented with strain gauges and linear variable displacement transducers (LVDTs). However, in the case of high speed experiments, the motion-tracking technique was used. That is because conventional measuring tools (i.e., LVDTs and potentiometers), data logger and connecting cables were not able to record data, send data and communicate with the specific high-speed data acquisition system. Besides this, since there was no possibility of stopping the test at some fraction of the fatigue life in order to map cracking and measure crack widths, an alternative measuring method was employed.

The motion-tracking technique requires acquisition and provision of high-quality video/images of the objects of interest during the test to track their movements. For this, a special high speed and low noise camera (IDS uEye) with a frame rate of 166 fps and a 2.3 MP sensor (Sony IMX174) was used. To track the motion of each point of interest, some marks were prepared and screwed to the beam specimens through a M6 coupler previously welded to the longitudinal bar. Welding of couplers to the longitudinal bar allowed the measurement of movement in reinforcement and also avoided any detaching of marks during the test due to spalling of the cover concrete. Once the marks were screwed to the specimen, each mark was assigned a tag ID in the motion-tracking software (IDS uEye Cockpit) and the coordinates of the center of each

mark was determined with respect to an arbitrary origin. To identify the center of each mark as accurately as possible, a checkered motif type label was glued to each mark. When the test started, the camera captured the images of the deformed test specimen sequentially at a rate of 100 Hz (i.e, 100 readings with intervals of 10 ms in 1s). Using motion tracking software, the new coordinates of each displaced mark (i.e., the movement along the X and Y axes) were tracked and analyzed. To provide better contrast, two sets of metal halide linear projectors were placed close to the test specimen.

A 10-bit number counter was used to provide a way of re-synchronizing the video data with the other recorded data (i.e., load, displacement and acceleration readings) in the event that frames were dropped during the video recording. The 10-bit number used to drive the LED bar graph display was recorded along with the other data and was incremented every time the camera captured a frame. Thus, if a frame had been dropped, it was possible to step through the video and locate the missing frame(s), then correct the timestamp for the following frames, and thus ensure that the video based data remained in sync with the other recorded data. It was fortunate that this did not happen during the high speed tests. The configuration of the motion-tracking system is shown Figure 8-2.

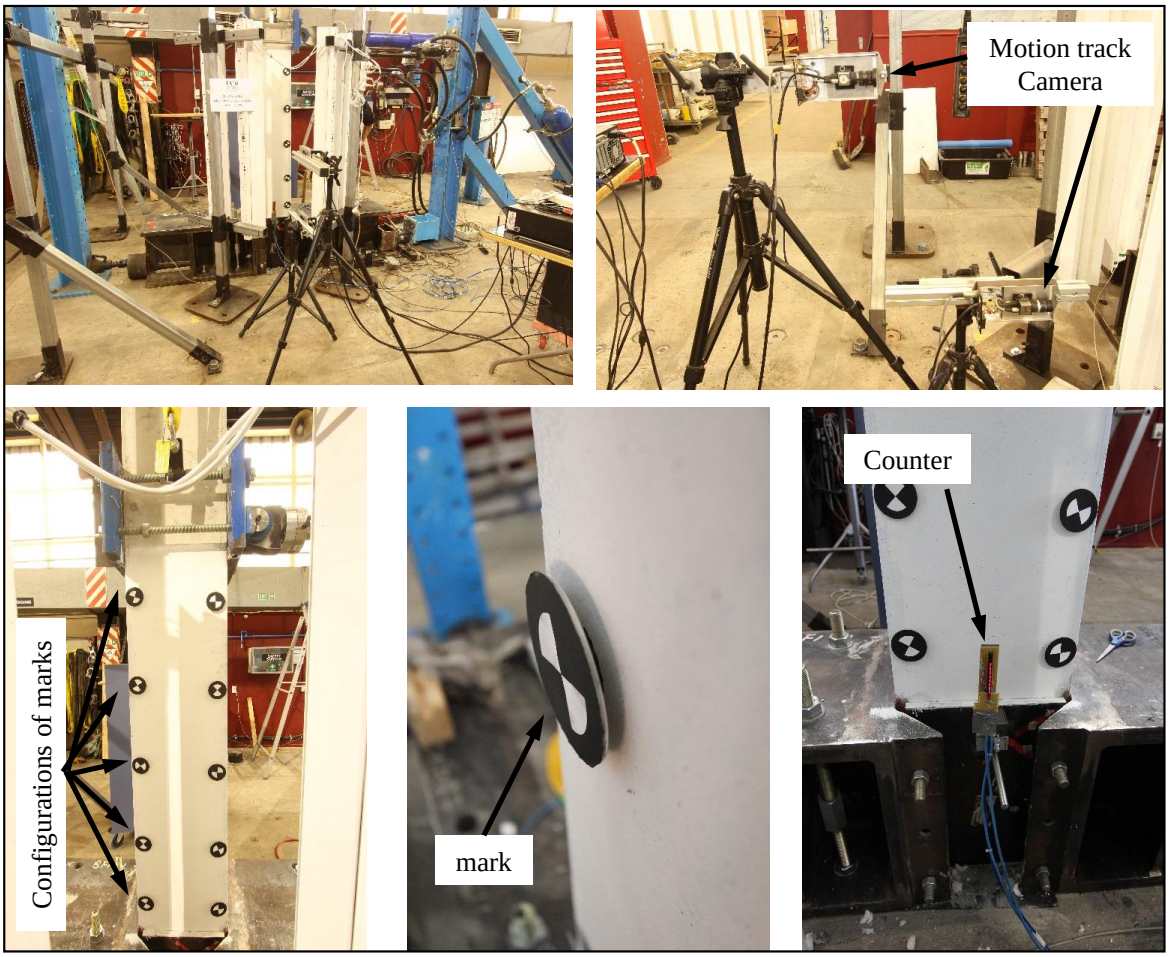

Figure 8-2 Configuration of the motion-tracking system

8.3 Results and discussion

8.3.1 Effect of inertia

When the specimen is subjected to high rate of cyclic loading, the inertia force is produced at a point of loading on top of the specimen. The inertia force is the product of the acceleration measured in the direction of loading and the participating mass of the test specimen, as well as the mass of the attached equipment (i.e., clamping plates and rods). It should be noted that, if the effect of the inertia force is not considered in the post-processing of data, the reaction force recorded at a high rate of loading will be an overestimation of the resisting force of the specimen. That is why, to obtain the true

resisting force of the test specimen under the high rate of loading condition, the inertia force was deducted using Equation 9.1.

$$F_R(t) = F_L(t) - (M_b + M_a) \times \ddot{x}(t) \quad (8.1)$$

where $F_R(t)$ = true resisting force of the RC beam in the absence of an inertial force at time t; $F_L(t)$ = the measured force by load cell at time t; M_b = participation mass of RC beam (i.e., calculated to be 520 Kg); M_a = mass of the attachments (i.e., calculated to be 115 Kg); and $\ddot{x}(t)$ = acceleration recorded at the level of applied force by the accelerometer at time t.

8.3.2 Filtering

Due to unwanted vibrations of the test frame, data has been filtered to remove spurious high frequency components. The average frequencies of the test beams at 2% and 4% drift, were 2.55 Hz and 1.27 Hz, respectively. Thus, a Butterworth filter with order 20 and cutoff frequency of 10Hz was used to reject the portion of the loads and displacements that have been induced by the vibration of the test frame, while preserving the fundamental loads and displacement responses associated with the test specimen.

8.3.3 Load carrying capacity

Figure 8-3 shows the cyclic force-displacement relationships of the RC beams tested at constant push-pull regime at 2% and 4% drifts, at low and high rate of loading. As seen, the behaviour of specimens are not symmetric in the push and pull directions since the damage that occurred during the first half-cycle affected the sequence of the hysteresis loops. The behaviour of the specimen at high rate of loading is similar to that at low rate of loading; however, the maximum load carrying capacity (strength) of the specimens increases as the rate of loading increases. In the case of specimens subjected to cyclic loading at 2% drift, the maximum resisting lateral force produced in the specimen increased from 60.8 kN at a low rate of loading to 67.5 kN, which shows about 11% growth. For specimens subjected to cyclic loading at 4% drift, the maximum resisting lateral force at a high rate of loading was 69.2 kN which indicates a 4.5% increase, compared to 66.2 kN, reached at a low rate of loading. Interestingly, the rate of increase in the maximum load carrying capacity of the specimen at 2% drift is more

than 4%. That is because the rate of load reversals (excursions) at 2% drift (i.e., 2.55 Hz), is twice the rate of load reversals at 4% drift. As described earlier, both steel and concrete are rate-dependent; thus, in the absence of inertia effects, the increase in the maximum load carrying capacity may be attributed to the rate-dependency of the constituent materials.

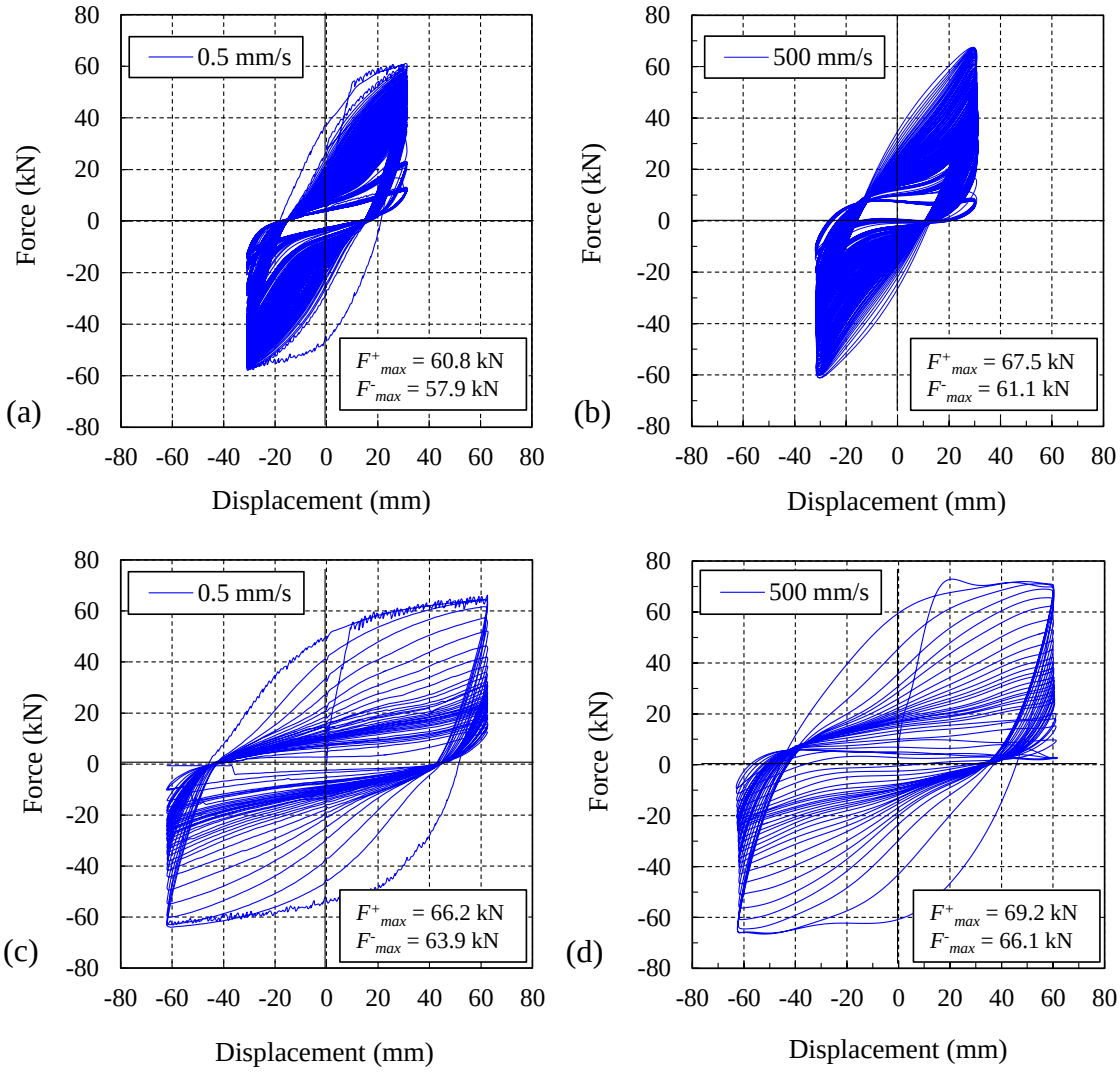

Figure 8-3 Force-displacement behaviours (a), (b) at 2% drift; (c), (d) at 4% drift

8.3.4 Stiffness

Considering the secant stiffness of the specimens during the first excursion, calculated as the ratio of maximum force to corresponding displacement, 11% and

4.7% increases in secant stiffness of the specimens tested at 2% and 4% drift, were observed. Such increases in stiffness result in about 5% and 2% decreases in the elastic period of the specimens. Decreases in the elastic period, implicitly denote increases in shear demand. Thus, there might be a potential risk of an increase in shear demand on structures in the case of applying a load at a significant high rate of loading.

8.3.5 Fatigue life

The total number of cycles that the test specimen endured to failure (N_f) is referred to as fatigue life (Graf and Brenner 1934). In this study, N_f for each experiment was counted, corresponding to the failure status at which the force–displacement of the RC beams (hysteresis loop) were flattened as a result of fracturing the longitudinal bars. The values of N_f for specimens tested cyclically at 2% drift, were found to be 239 and 217, for low and high speed tests, respectively. For specimens tested cyclically at 4% drift, the number of cycles that were required to failure of the specimens were 37 and 25, for low and high speed tests, respectively.

The relationship between the fatigue life of the test specimen and the drift level is conventionally displayed in logarithmic scale graphs and referred to as *S-N* curves (or Wöhler curve), as illustrated in Figure 8-4a. The representation of S-N curve in non-logarithmic scale has also shown in Figure 8-4b to illustrate how change in the drift level (demand) can increase the rate of decay in fatigue life of the RC beam. It can be seen that the effect of the drift level on the fatigue life of RC beams is quite significant: the fatigue life decreases with increasing drift level. In addition, the results showed that the fatigue life is inversely proportional to the rate of loading: the higher rate of loading, the less fatigue life. This implies that, given identical loading amplitude, the rate of decay in capacity of specimens subjected to higher rate of loading is higher.

Equations 8.2a and 8.2b express the best prediction models for the fatigue life following the curve-fitting exercise, as follows:

$$\theta\,(\%) = -1.07 \ln (N_f) + 7.8 \tag{8.2a}$$

$$\theta\,(\%) = 11.2\,(N_f)^{-0.32} \tag{8.2b}$$

where θ = drift (chord rotation); and N_f =total number of cycles required to failure.

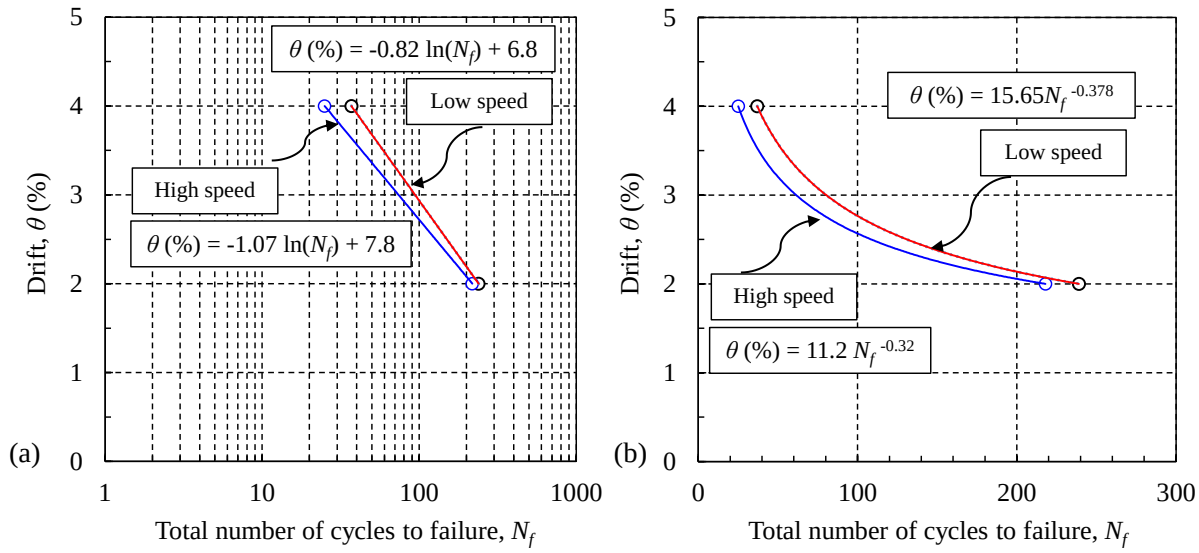

Figure 8-4 Fatigue life relationship: (a) logarithmic scale; (b) non-logarithmic scale

8.3.6 Strength degradation over fatigue life

During cyclic loading, the strength (i.e., maximum force) of the specimen reached at each cycle degrades. That is mainly due to the evolution of damage over the fatigue life of the specimen, which results in the deterioration of the mechanical properties of the RC beam under reversals of loading. Figure 8-5 shows the change in the ratio of the maximum lateral force achieved in each consecutive cycle (F_{max}) to the maximum lateral force achieved in the first cycle ($F_{max,0}$), over the entire fatigue life of the specimens. As can be seen in Figure 8-5a, in the case of specimens subjected to cyclic loading at 2% drift, the initial phase starts with a gradual decrease in strength up to 0.57 and 0.69 of fatigue life (i.e., n/N_f = 0.57 and 0.69), at which the strength reached 62% and 51% of its original strength, for specimens loaded at high and low rate, respectively. These fractions of fatigue life were where the first bar fracture occurs for high and low rate of loading. As seen, the rate of degradation in strength for a specimen tested at a high rate of loading is more than that tested at a low rate of loading. That is because, the drop in load for each successive cycle was greater for the specimen tested at the faster rate. However, after $0.7N_f$, the difference between the rate of degradation in strength reduced, and both experiments show a similar pattern.

For specimens tested cyclically at 4% drift (Figure 8-5b), the degradation in strength started at a very early ratio of fatigue life such that at $0.75N_f$, irrespective of

the rate of loading of the specimens, only 30% of the original strength remained in both specimens. The results show that a higher level of drift incurs a higher rate of decay, and also causes the deterioration trend to become smoother without an abrupt drop. It may be concluded that by increasing the loading demand (i.e., drift), the response of the specimen is less affected by the rate of loading.

Generally, at a given ratio of remaining strength to the original strength (F_{max} / $F_{max,0}$), the low rate of loading results in a higher fraction of fatigue life. The current study showed that the rate of deterioration in mechanical properties of the specimens accelerates once the rate of loading increases. This is in line with lower values of fatigue life (N_f) found for beams tested at a higher rate of loading.

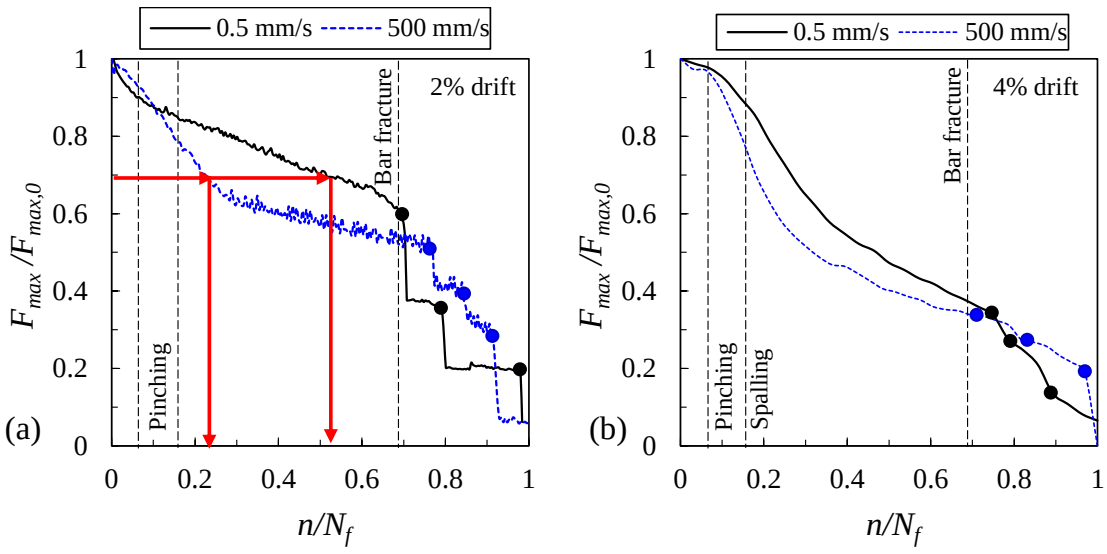

Figure 8-5 Strength degradation over fatigue life (a) 2% drift (b) 4% drift

8.3.7 Energy dissipation over fatigue life

Figure 8-6 shows the degradation of energy dissipation capacity, represented as a dimensionless ratio of dissipated energy in each cycle (E_D) to dissipated energy in the first cycle (E_{D0}), against the fatigue life of the RC beams. The dissipated energy was calculated from numerical integration of the area enclosed under the hysteresis loops (Equation 8.3). The results show that there is a significant loss, specifically after the first cycle, which indicates that the area formed during the first reversal is considerably higher than the following cycles.

$$E_D = \sum \frac{(F_i + F_{i+1})(\Delta_{i+1} - \Delta_i)}{2} \tag{8.3}$$

where E_D = dissipated energy per cycle (N·mm); F_i = load at each increment (N); and Δ_i = displacement at each step (mm).

Similar to the strength degradation spectrum, it can be seen that the rate of decay in the energy dissipation capacity of the specimens is exacerbated at a higher rate of loading. However, by increasing the drift level, the effect of the rate of loading on degradation in energy dissipation capacity becomes less. Furthermore, by comparing the absolute value of the energy dissipated in each cycle, it was found that at a lower rate, a higher amount of energy is dissipated. This implicitly denotes that there is a higher level of damage in the specimens subjected to a lower rate of loading. The current study showed that the rate of deterioration in the dissipation energy spectrum is higher than in the strength spectrums.

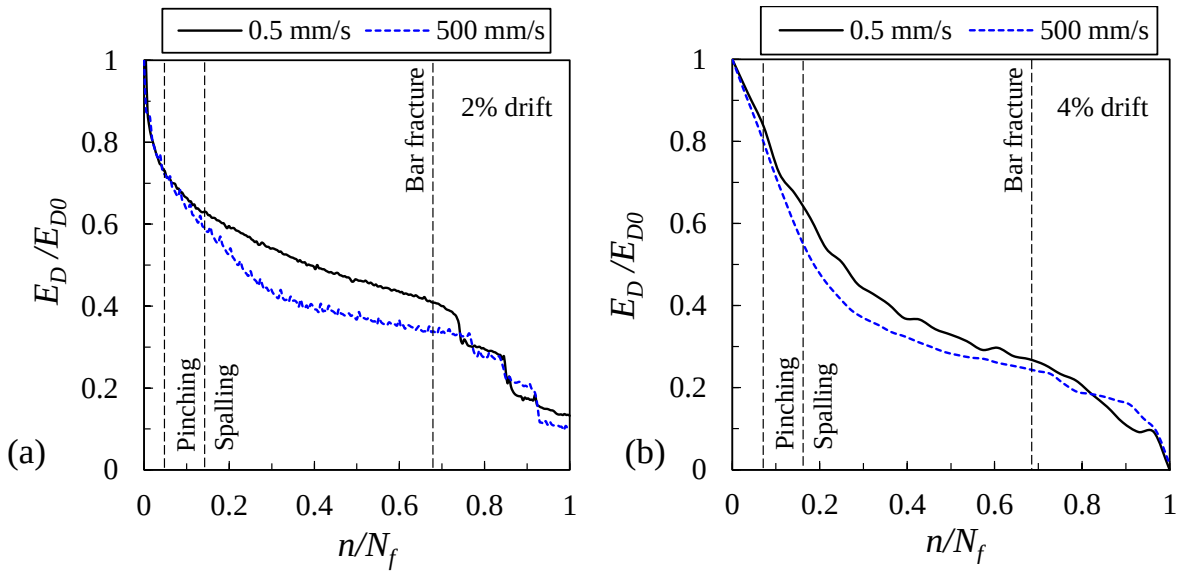

Figure 8-6 Degradation of energy dissipation capacity (a) 2% drift (b) 4% drift

8.3.8 Failure mode and cracking pattern

Figure 8-7 shows failure modes and cracking patterns of the damaged RC beams at failure. In the case of the beam subjected to 2% drift at a low rate of loading, the first cycle was sufficient to incur cracks along the length of the specimen. The maximum measured crack widths on either side were between 2.6 and 2.7 mm. For the case of

beam tests at 4% drift under a low rate of loading, significant damage (i.e., spalling, crushing, deformation of hoops and buckling of longitudinal bars) was observed on the very first cycle. The maximum crack width was measured as 4.5 mm. In the case of high-speed tests, no direct measurement was conducted. However, post-processing of images taken during tests through motion-tracking software revealed that the maximum crack width reached at 2% and 4% drift levels were 3.3 mm and 5.7 mm, respectively. It is worth mentioning that, in all the experiments, the fracturing of the longitudinal bars occurred on the side first subjected to tension.

Comparing crack patterns shows that flexural cracks were well-dispersed for the specimens tested at the low rate, while for the high-speed tests, there were fewer, wider and more localized cracks. This indicates that the transfer of forces between reinforcing bars and concrete (i.e., bond stress) at a low rate of loading is more efficient. Because of the more efficient load-transfer occurring at the slow rate, additional cracking progressively developed in the plastic hinge region of the specimens. On the other hand, specimens subjected to a high rate of loading benefit from an increase in tensile strength of the concrete and enhanced bond strength, leading to fewer cracks and more localized strain in the steel (Fu et al. 1991). Such strain concentrations could lead to premature fracture of the reinforcing bars for specimens tested at high rate of loading, which is consistent with the lower value of fatigue life obtained for specimens tested at high rate of loading.

With respect to the plastic hinge regions, beams tested at high rate of loading showed the region associated with severe damage (Figure 8-7) has got a length of 350 mm for both loading conditions (i.e., constant amplitude cyclic loading at 2% and 4% drift). Plastic hinge length in the case of beams tested at low rate of loading was measured to 270 mm and 330 mm for cyclic loading at 2% and 4% drift, respectively. Although the study showed the length of plastic hinge has not been significantly affected by increase in the rate of loading, the cracking pattern over plastic hinge showed significant different failure. It was seen that rather than a large number of hairline cracking evenly distributed and forming in the beams, only a small number of widely spaced large cracks formed. This is in line with the type of damage occurred during Christchurch earthquake (Clifton et al. 2015). In fact, these large cracks put an

increased strain demand on the steel that runs across the crack, reducing the post-earthquake capacity of the structure for a given plastic hinge rotation.

The current study showed the mode of failure shifted from a ductile flexural failure to a brittle shear failure with less hysteretic energy absorption. Such a change in the failure mode possibly affects the redistribution of forces within the specimen which subsequently may alter the redistribution of forces in the structural system. As a result, it may be concluded that a high rate of loading may hinder formation of expected plastic hinges and affect its length in the specimens, resulting in overloading of some other elements of the structure.

To find out the effect of rate of loading on the temperature of the longitudinal bars, the temperature of the longitudinal bars at the end of the test were measured using an infrared thermometer and compared with the ambient temperature. The results showed that during the high-speed tests, there is a considerable increase in the temperature of the longitudinal bar in the plastic hinge region. In the case of the beam tested at 2% drift, the temperature increased from 15.1ºC, at ambient temperature prior to the start of the test, to 58.5ºC at the end of the test, showing a 43.4°C increase. For the beam tested at 4% drift, the temperature rose from 17.2°C at room temperature prior to the start of the test to 47.5°C, which represents a 30.5°C increase. The study shows that as the rate of loading increases, the temperature generated in the longitudinal bar increases; however, the rate of increase shows more dependency on the total number of cycles that the specimen experienced.

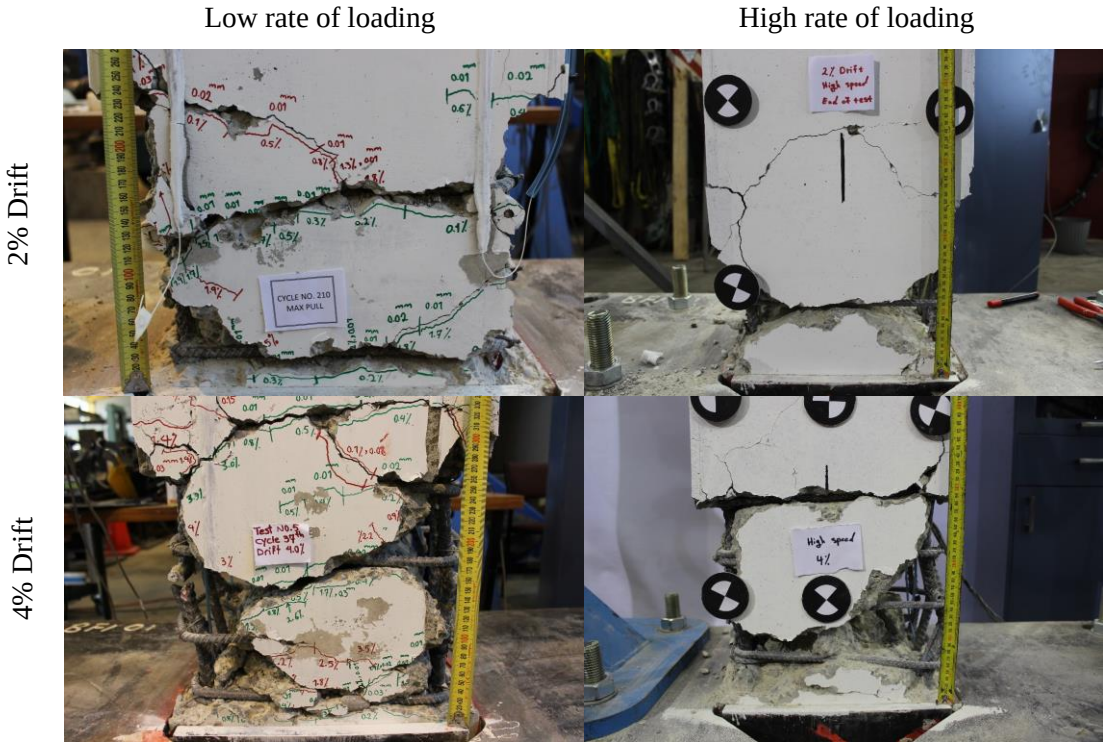

Figure 8-7 Failure modes and cracking pattern of specimens at failure

8.3.9 Beam elongation

Figure 8-8 shows the axial elongation of the beams tested at low and high rate of loading. As seen, the beam elongation is permanent and cumulative. Maximum elongation in the beams tested at low rate of loading for 2% and 4% drift was 9.2 mm and 26.3 mm, respectively. However, for beams subjected to high rate of loading, the maximum elongation was 4.6 mm and 13.2 mm, for similar drift levels, respectively. The maximum elongation measured for the low speed test was equal to 0.6% and 1.75% of the cantilever length (i.e., 1500 mm), while in the case of the high speed test, elongation corresponded to 0.3% and 0.8% of the beam length. Comparing the results of elongation for the low and high-speed tests, the beams elongated about 50% less under high rate of loading. This shows that an increase in the rate of loading hinders beams to be axially lengthened. The reduction in beam elongation at high rate of loading is consistent with the limited distribution of damage and shorter plastic hinge length observed in the case of high speed tests. Although, the elongation reported herein provides a better understanding of the behaviour of a tested cantilever beam, the results

are not fully representative of beam elongation occurring in an earthquake. That is because the test set-up employed in this study allowed for free beam elongation without any restraint action at the loaded end, which is not analogous to the case of real RC buildings.

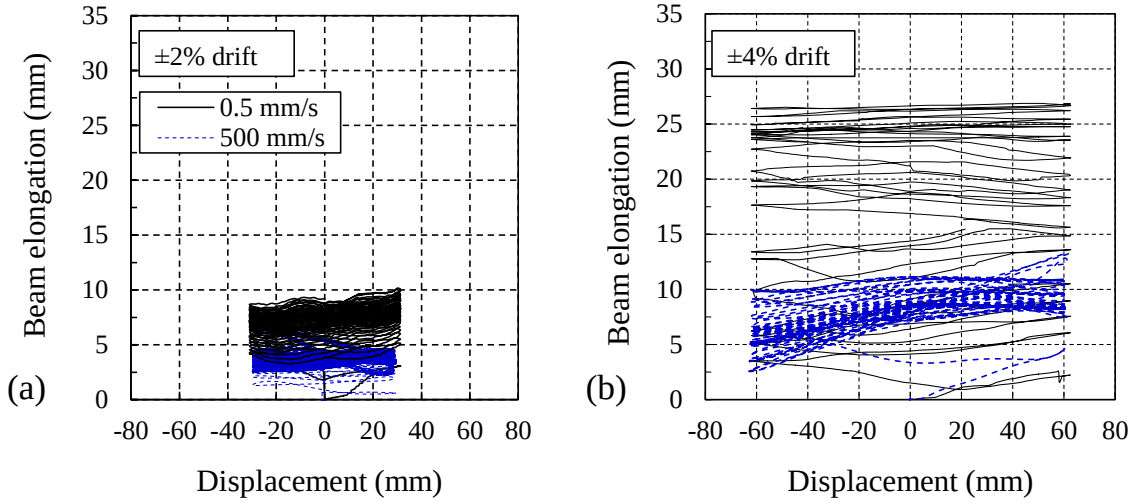

Figure 8-8 Beam elongation (a) 2% drift (b) 4% drift

8.3.10 Bar fracture

Figure 8-9 shows the fracture surfaces of the longitudinal bar for the low and high speed tests. As seen, an increase in the rate of loading resulted in the bars being fractured with a rough and uneven surface compared to a smooth surface created at the end of the low-speed test. This denotes a more brittle failure (fracture) for the high-speed test rather than the ductile failure (fracture) for the low-speed test, as described earlier.

Figure 8-9 fracture surface

8.4 Conclusions

This chapter aimed to shed some light on the effect of high rate of loading on cyclic behaviour of RC beams subjected to low-cycle fatigue loading. Based on the current test results, the following conclusions can be drawn:

1. Results showed the application of high rate of loading causes an increase in the strength and cracking secant stiffness of the specimen, while the energy dissipation capacity and elongation of beam decrease. The increase in the maximum load carrying capacity (strength) in the absence of inertia effects may be attributed to the rate-dependency of the constituent materials (i.e., steel and concrete). Enhancement of the stiffness results in a reduction in the elastic period, leading to an increase in shear demand. Thus, there might be a potential risk for an increase in the shear demand of the structure in the case of applying a load at a significantly high rate of loading. Since the rates at which the specimens are cyclically tested are substantially lower than those that would be expected in an earthquake, it is of vital importance to fully understand the

influence of rate-dependent effects on the behaviour of a RC member in relation to the analysis and design of structures in both building codes and practice.

Moreover, with respect to elongation, beams showed 50% less elongation at high rate of loading. Also, the surface of the fractured bars showed that with an increase in the rate of loading, the surface fractures form a rougher and more uneven surface compared to the smooth surface created at the end of low-speed test. Increase in the rate of loading also caused a significant increase in the temperature of the longitudinal bars.

2. The results showed that the fatigue life is inversely proportional to the rate of loading: the higher the rate of loading, the lower the fatigue life. This implies that, given identical loading amplitude, the rate of decay in the specimen subjected to higher rate of loading is higher.
3. The rate of deterioration in the strength and energy dissipation capacity of the specimens over cycles, is exacerbated by higher rate of loading. However, as the drift level (i.e., demand) increases, the response of the specimen is less affected by the rate of loading. Results show that higher level of drift incurs a higher rate of decay, and also causes the deterioration trend to become smoother with no evident sign of bar fracture (i.e., drop in spectrums).
4. This study showed a shift in the failure mode from a ductile flexural failure at low rate of loading to a brittle shear failure once the specimens were subjected to high rate of loading. Changes in the failure mode possibly affect the redistribution of forces within the specimen which subsequently may alter the redistribution of forces in the structural system. As a result, it may be concluded that high rate of loading may hinder formation of expected plastic hinges and affect its length in the specimens, resulting in overloading some other elements of the structure. Comparing crack patterns showed that flexural cracks were well-dispersed for the specimens tested at the low rate, while for the high-speed tests, the damage was mainly fewer, wider and more localized cracks. This may be ascribed to a more efficient transfer of forces between the reinforcing bars and the concrete (i.e., bond stress) at the low rate of loading.

8.5 References

Adhikary, S. D., Li, B., and Fujikake, K. (2012). "Dynamic behavior of reinforced concrete beams under varying rates of concentrated loading." *International Journal of Impact Engineering*, 47, 24-38.

Adhikary, S. D., Li, B., and Fujikake, K. (2014). "Effects of high loading rate on reinforced concrete beams." *ACI Structural Journal*, 111(3), 651-660.

Arakawa, T., and Arai, Y. "Effects of the rate of cyclic loading on the inelastic behavior of R/C columns." *Proc., Eighth world conference on earthquake engineering*, 521-528.

Bertero, V. V., Rea, D., Mahin, S. A., and Atalay, M. B. "Rate of loading effects on uncracked and repaired reinforced concrete members." *Proc., Fifth World conference on earthqauke engineering*, 1461-1470.

Bischoff, P., and Perry, S. (1991). "Compressive behaviour of concrete at high strain rates." *Materials and structures*, 24(6), 425-450.

Cadoni, E., Dotta, M., Forni, D., and Tesio, N. (2015). "High strain rate behaviour in tension of steel B500A reinforcing bar." *Materials and Structures*, 48(6), 1803-1813.

Canterbury Earthquakes Royal Commission (2012). "Final report: Volume 2: The performance of Christchurch CBD buildings." *Wellington, New Zealand*.

Chung, L., and Shah, S. P. (1989). "Effect of loading rate on anchorage bond and beam-column joints." *Structural Journal*, 86(2), 132-142.

Clifton, G., van Bysterveldt, A., Clifton, G., and Ferguson, G. "The cracking behaviour of reinforced concrete beams under static and dynamic loading." *Proc., New Zealand Society for Earthquake Engineering 2015 Annual Conference*.

Cowell, W. (1969). "Dynamic tests on selected structural steels." *Technical Report R-642*, U. S. NAVAL Civil Engieering Laboratory, Port Hueneme, California.

Cowell, W. L. (1966). "Dynamic properties of plain Portland cement concrete." *Technical Report* U. S. NAVAL Civil Engieering Laboratory, Port Hueneme, California.

Dhakal, R., and Pan, T.-C. (2003). "Characteristics of High-Speed Cyclic Test of Beam-Column Joints." *ACI Structural Journal*, 100(2), 188-196.

Fu, H., Erki, M., and Seckin, M. (1991). "Review of effects of loading rate on reinforced concrete." *Journal of structural engineering*, 117(12), 3660-3679.

Ghannoum, W., Saouma, V., Haussmann, G., Polkinghorne, K., Eck, M., and Kang, D.-H. (2012). "Experimental investigations of loading rate effects in reinforced concrete columns." *Journal of Structural Engineering*, 138(8), 1032-1041.

Ghannoum, W. M., and Moehle, J. P. (2012). "Shake-table tests of a concrete frame sustaining column axial failures." *ACI Structural Journal*, 109(3), 393.

Graf, O., and Brenner, E. (1934). "Experiments for investigating the resistance of concrete under often repeated compression loads." *Bulletin*(76).

Ichihashi, S., and Wada, A. (1987). "High-speed Loading Analysis of Reinforced Concrete Columns." *Numerical Techniques for Engineering Analysis and Design*, Springer, 419-426.

Inoue, N., Inai, E., Wada, A., Kuramoto, H., Fujimoto, I., and Iiba, M. "A Shaking table test of reinforced concrete frames designed under old seismic regulations in Japan." *Proc., Twelfth World Conference on Earthquake Engineering*, Chapter 1783.

Kulkarni, S. M., and Shah, S. P. (1998). "Response of reinforced concrete beams at high strain rates." *ACI Structural Journal*, 95(6), 705-715.

Li, M., and Li, H. "Effects of loading rate on reinforced concrete beams." *Proc., Fifteenth World Conference on Earthquake Engineering*, 24-28.

Mahin, S., Bertero, V., Atalay, M. B., and Rea, D. (1972). "Rate of Loading Effects on Uncracked and Repaired Reinforced Concrete Members." *Report No. EERC 72-9*Earthquake Engineering Research Center, Univ. of California at Berkeley.

Malvar, L. J. (1998). "Review of static and dynamic properties of steel reinforcing bars." *ACI Materials Journal*, 95(5), 609-616.

Malvar, L. J., and Ross, C. A. (1998). "Review of strain rate effects for concrete in tension." *ACI Materials Journal*, 95(6), 735-739.

Mutsuyoshi, H., and Machida, A. "Dynamic properties of reinforced concrete piers." *Proc., Eighth World Conference on Earthquake Engineering*, 913-920.

Mutsuyoshi, H., and Machida, A. (1984b). "Properties and failure of reinforced concrete members subjected to dynamic loading." *Transactions of the Japan Concrete Institute*, 6, 521-528.

Nagae, T., Ghannoum, W., Kwon, J., Tahara, K., Fukuyama, K., Matsumori, T., Shiohara, H., Kabeyasawa, T., Kono, S., and Nishiyama, M. (2015). "Design implications of large-scale shake-table test on four-story reinforced concrete building." *ACI Structural Journal*, 112(2), 135.

Norris, G. H., Hansen, R. J., Holley, M. J., Biggs, J. M., Namyet, S., and Minami, J. K. (1959). *Structural design for dynamic loads*, McGraw Hill Book Co., New York, N.Y.

Otani, S., Kaneko, T., and Shiohara, H. (2003). "Strain rate effect on performance of reinforced concrete members." *Kajima Technical Research Institute, Kajima Corporation, Japan*.

Penzien, J., and Hansen, R. J. "Static and dynamic elastic behavior of reinforced concrete beams." *Proc., Journal Proceedings*, 545-567.

Reinschmidt, K. F., Hansen, R. J., and Yang, C. Y. "Dynamic tests of reinforced concrete columns." *Proc., Journal Proceedings*, 317-334.

Robert, J. H., and Atis, A. L. (1962). "Behavior of bond Under Dynamic Loading." *ACI Journal Proceedings*, 59(4), 563-584.

Rostasy, F., Scheuermann, J., and Sprenger, K. (1984). "Mechanical behaviour of some construction materials subjected to rapid loading and low temperature." *Betonwerk+ Fertigteil-Technik*, 50(6), 393-401.

Shah, S. P., Wang, M.-L., and Chung, L. (1987). "Model concrete beam-column joints subjected to cyclic loading at two rates." *Materials and Structures*, 20(2), 85-95.

Somraj, A., Fujikake, K., and Li, B. (2013). "Influence of loading rate on shear capacity of reinforced concrete beams." *International Journal of Protective Structures*, 4(4), 521-543.

Soroushian, P., and Choi, K.-B. (1987). "Steel mechanical properties at different strain rates." *Journal of Structural Engineering*, 113(4), 663-672.

Stavridis, A., Koutromanos, I., and Shing, P. B. (2012). "Shake-table tests of a three-story reinforced concrete frame with masonry infill walls." *Earthquake Engineering & Structural Dynamics*, 41(6), 1089-1108.

Takeda, J. "Dynamic fracture of concrete structures due to severe earthquakes and some consideration on countermeasures." *Proc., Eighth world conference on earthquake engineering*, 299-306.

Takeda, J., and Tachikawa, H. "Deformation and fracture of concrete subjected to dynamic load." *Proc., Proceedings of the Conference on Mechanical Behavior of Materials*, 267-277.

Takeda, J., Tachikawa, H., and Fujimoto, K. "Effects of straining rate on deformation and fracture of reinforced concrete members." *Proc., Proc. of Sixth World Conference on Earthquake Engineering*, 3256.

Wakabayashi, M., Nakamura, T., Yoshida, N., Iwai, S., and Watanabe, Y. "Dynamic loading effects on the structural performance of concrete and steel materials and beams." *Proc., Seventh world conference on earthquake engineering*, 271-278.

Witarto, W., Lu, L., Roberts, R. H., Mo, Y., and Lu, X. (2014). "Shear-critical reinforced concrete columns under various loading rates." *Frontiers of Structural and Civil Engineering*, 8(4), 362-372.

Chapter 9 *Permeability-based damage assessment and residual capacity of concrete material in damaged RC members*

9.1 Introduction

After an RC building goes through an earthquake, depending on the level of damage, a decision is required regarding occupancy as is, repairing or demolishing it. If the building is safe enough to withstand further seismic demands whilst maintaining the designed level of performance under service load (i.e., deflection, vibration and cracking), the approval for occupancy in the existing circumstances might be justified. Various level of repair and retrofit, however, can be considered as a possible strategy in case the damage is severe enough to compromise the immediate or longer term functionality of the damaged building but its overall performance is expected to be retained by utilizing some cost-effective repair options. Demolition is adopted when the building is highly damaged and repair options are found technically/financially inapplicable to restore the expected performance for the purposes of a resilient community. But to take an appropriate course of action, it is of vital importance to determine what the level of damage is and how much capacity remains in the damaged building.

Residual load-bearing capacity can be investigated at four levels: material, components, subassemblies, and, finally, system level. However, post-event stress–strain relationships associated with degraded material, particularly concrete, is the prerequisite for the subsequent damage assessment. That is because, to conduct any analytical or numerical structural analysis, the properties of material are the first inputs that should be introduced to the program. The idea of determining residual capacity at the structure or member level has drawn considerable attention from researchers (Cuevas and Pampanin (2014); Tasai (1999); Chung et al. (2008); Maeda and Kang (2009); Bao and Li (2010) ; Baghaei et al. (2011); Li et al. (2012)); however, it has not

yet been broadly studied from the concrete material point of view. There is also a strong need for an indicator of damage, as the decision is based on damage measured. Damage in the reinforced concrete (RC) members denotes the damage associated with reinforcements or concrete. Under severe loading demands, concrete-associated damage in an RC component emerges with visual signs (i.e., spalling, cracking and crushing); however, in minor cases microcracking in the microstructural system of concrete material can occur without significant visual signs. This is also affected by the confinement, and the location in the member. Amongst structural members, columns should be prioritized in the damage evaluation process, since the lack of sufficient capacity to sustain loading demand may cause a sudden and/or progressive collapse of the structure.

Of the methods implemented to date to evaluate damage in concrete material, including visual inspection Perenchio 1989, ultrasonic tomography Bishko et al. 2008, acoustic emission Schofield 1963, radiography Mullins and Pearson 1949, and permeability Grube et al. 1984, permeability testing seems to be promising for further study, as it is highly sensitive to microcracking damage. That is because structural cracks in the concrete material induced by external loading are not only indicative of damage, but also allow for rapid fluid transport, resulting in a more permeable material. The topic of permeability assessment of cracked concrete has been extensively studied for small-scale plain concrete in the past (Wang et al. (1997); Hearn and Lok (1998); Kermani (1991); Tegguer et al. (2013)). However, there are limited studies in the literature addressing permeability-based damage evaluation at reinforced concrete member level (Girrens and Farrar (1991); Hutchinson and Soppe 2011; Soppe and Hutchinson (2011); Nganga et al. 2013). Although each technique examines damage in terms of change in the specific characteristic of the concrete, none of them provide relationships to determine loss in strain/strength capacity of the material. Thus, to make a correlation between material degradation (deterioration in mechanical properties) and damage occurred in the microstructural system of concrete (change in durability feature of the material) seems necessary.

9.1.1 Scope of work/motivation

From the previous discussion, it may seem that for robust post-earthquake decisions to be made, a practical method to assess post-event material characteristics of the damaged concrete member is of vital importance. This chapter summarizes the experimental work from permeability testing conducted on three types of RC specimens: columns, beams and a beam-column joint taken from a real structure subject to loading during the Christchurch earthquakes of 2010 and 2011. This chapter aims to provide answers to some of needs delineated earlier:

1- Does the performance of preloaded concrete in a RC member differ from that of unloaded concrete in the cylinder compressive test?

2- How does permeability relate to change in concrete properties?

3- What is the extent of concrete damage along the length of test specimen?

4- Can an assessment procedure be developed to acquire post-event properties and the determine residual capacity of damaged concrete?

9.2 Permeability-based damage assessment of RC columns

First type of specimens consists of three large-scale RC columns with three levels of confinement – low, medium and high – and similar to the specimens studied by Mander et al. (1988) which were subjected to the compression test to capture force-displacement (global behaviour) at member level. Subsequently, two types of small-scale testing, namely compression tests on cored cylinders and permeability testing on concrete disks sawn from cored cylinders, were then conducted to obtain both residual mechanical properties and also to get some information on damage that had occurred in the microstructural system of the concrete. Finally, a correlation between damage in the microstructure of concrete, represented by change in the permeability feature, and degradation in material properties, represented by change in strain capacity, was made.

9.2.1 Columns specimen

Three circular RC columns, all 1500 mm in height and 500 mm in diameter, were constructed. Columns were caged using 12 deformed bars, all 16 mm in size for longitudinal bars with a 12 mm plain bar as a transverse reinforcement. Three different

transverse reinforcement configurations were fabricated to represent three confinement conditions: low, medium and high. All three columns were poured with the same concrete batch, provided by a local ready-mix supplier with specified target strength of 40 MPa at 28 days, and a slump of 80 mm. General purpose (GP) cement was used and the aggregate was semi-crushed with a maximum size of 19 mm. To simulate the three different confinement levels, transverse reinforcements with spiral spacing of 40 mm, 70 mm and 105 mm were placed over 1 m at the mid-height of the columns. The transverse reinforcements were placed closer (70% of the corresponding pitch) in the upper and lower quarters of the columns to transfer damage to the middle part of each column. The volumetric ratios of confinement reinforcement ($\rho_{s,h} = 4A_{sh} / d_s\ s$) were 0.025, 0.015 and 0.01 for high, medium and low confined columns, respectively.

Both ends of the longitudinal bars were cut straight without any hook. The transverse reinforcements were formed of helical hoops without any splicing along the height of the columns, and terminated through a 135° anchorage. Modular column formwork (Geotub) was used for casting, due to the ease of assembling the mould by locking a handle onto each pair of segments. Each formwork was mounted vertically on horizontal plywood bases. Concrete was poured in three lifts, and mechanically vibrated every 500 mm of pouring. The details of column specimens and transverse reinforcement are illustrated in Figure 9-1.

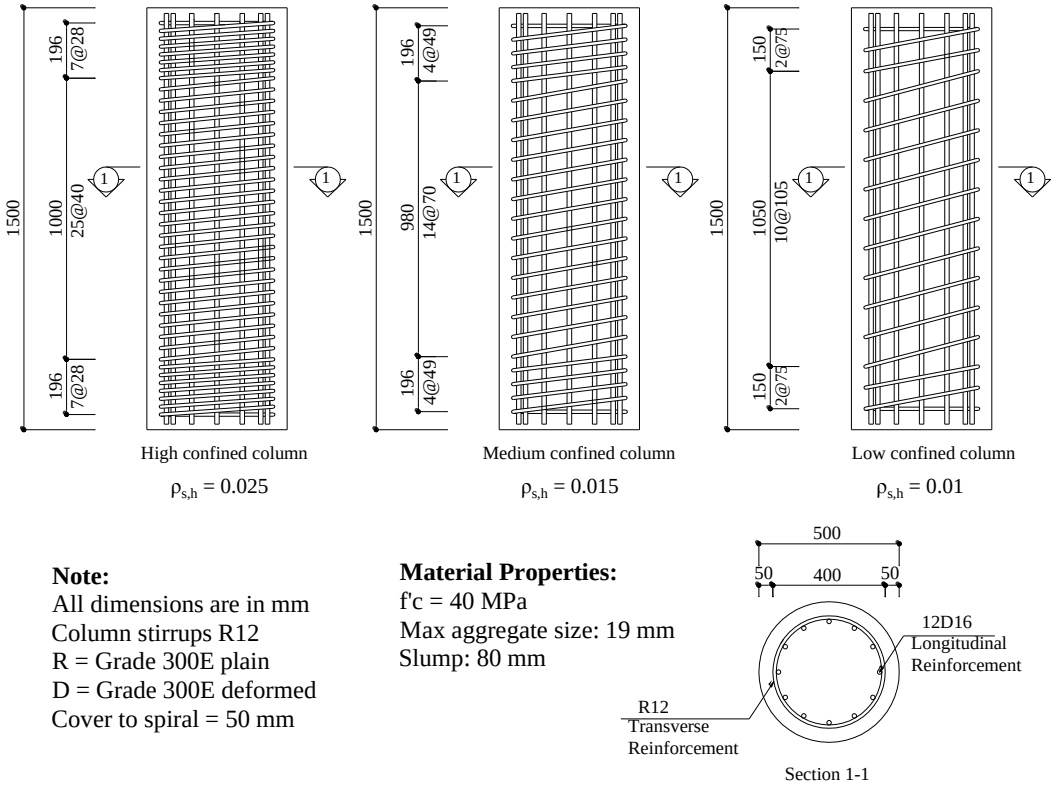

Figure 9-1 Details of the column assemblies

9.2.2 Testing protocol

The RC columns were loaded axially using the 10,000 kN Dartec universal testing machine (Figure 9-2a). The machine has a fixed reaction plate at the base extending from floor level, and a movable reaction head at the top, allowing load to be evenly distributed on the test specimen. The experiment was conducted as a monotonic axial compression with a displacement rate of 0.1mm/s until failure. Both applied load and overall displacement that occurred in the specimens were measured during testing through a load cell installed on the machine. The axial deformation on each column was also recorded via eight linear variable displacement transducers (LVDT), over a central 450 mm gauge length. To capture strain in concrete material, two orthogonal plain rebar were placed in the cross section of columns before casting. Four LVDTs were placed between the ends of plus-shape bars at every 90°. In addition, to measure strain in steel, four strain gauges were mounted between two ends of a piece of rebar welded perpendicularly to longitudinal bars (Figure 9-2b).

(a) (b)

Figure 9-2 test set-up (a) experimental test apparatus (b) status of column at zero loading

9.2.3 Overall damage observations of RC columns

The appearance of vertical cracks in the cover concrete was the first damage observation as the loading applied to the specimen proceeded. Local crushing and subsequent spalling of the cover concrete stimulated quick propagation of these cracks. Despite spalling of the cover concrete, which made it malfunction, the presence of spiral reinforcement increased both ductility and strength properties of the remaining concrete core.

For both high and medium confined columns, vertical cracks formed in the central part of the columns just after the peak load. The concrete cover of the damaged area was spalled after the peak load, and hoop fracture occurred as a consequence of hoop expansion in the central part of the column. All longitudinal bars buckled, and concrete located in the core of column was seriously crushed. Figure 9-3 shows the status of the columns at different level of damage: before starting test, just following peak load, and at the end of the test for high, medium and low confined columns.

The typical longitudinal bar buckling and hoop fracture is also shown in Figure 9-4. In the case of the low-confined column, the first hoop fracture triggered shear diagonal sliding, and led to the formation of a diagonal failure plane. The propagated cracks in the low-confined column were mainly formed from one-third of the height to the top of the column. Therefore, the concrete cover of approximately one-third of the height of the column remained almost undamaged. The concrete cover of the damaged area was spalled after the peak load, and all longitudinal bars were buckled.

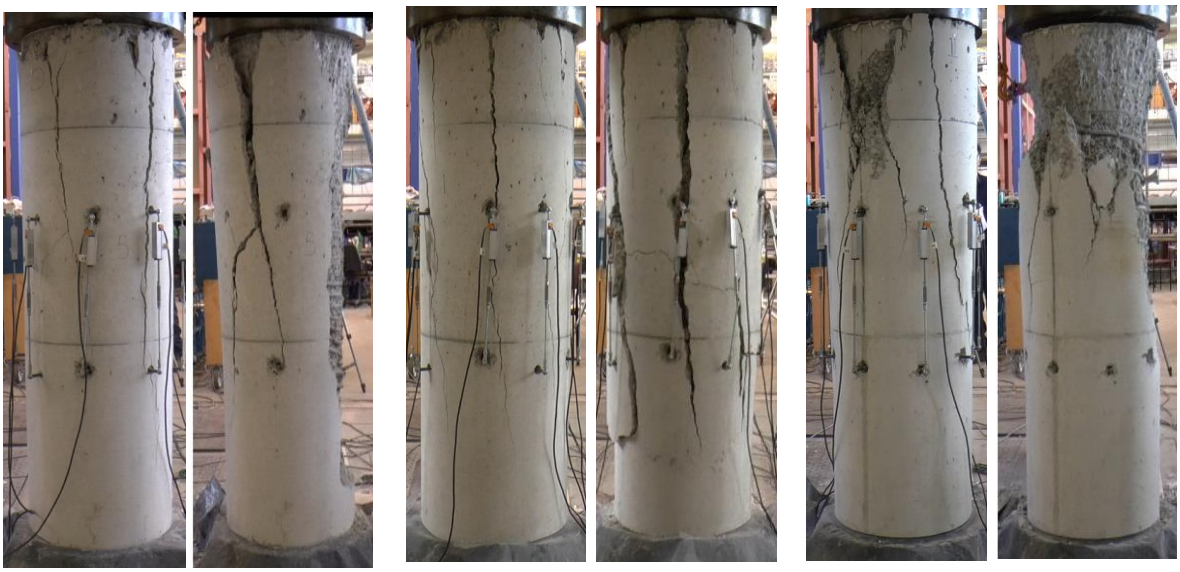

Figure 9-3 Damage status of column at peak load and the end of the test (a) high-confined column (b) medium-confined column (c) low-confined column

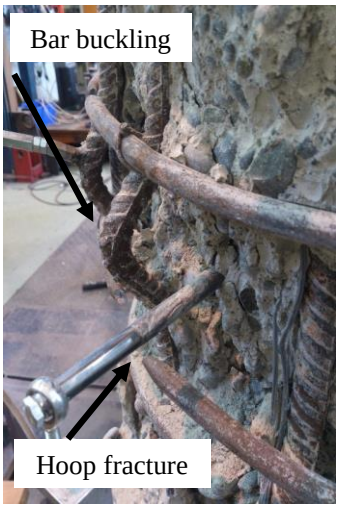

Figure 9-4 Typical failure mode

Figure 9-5 presents both the force-displacement, as well as stress–strain results, for all three types of column. As the load increased, the axial capacity increased to the peak. This was followed by a strength degradation caused by bar buckling and yielding of the spiral reinforcement. At the end, a sudden drop occurred, which is attributed to the significant dilatancy in the section, whereby strain demand generated in the spiral exceeded its capacity and steel fracture occurred. Note that the results associated with strain herein are the average values obtained from stroke of the Dartec machine over the entire height of the columns (global behaviour). The average strain has the advantage of representing the whole damaged areas, not specifically the highly damaged central area. In spite of the efforts to capture strain in both steel and concrete material using LVDTs, there was no chance to record reliable data after significant damage. In the case of concrete, due to the deformation of orthogonal bars passing across the cross section of columns, recorded data were found imprecise. For steel, the buckling of bars did not allow precise measurements. Thus, the average strain was determined as the measured displacement divided by total height of the column. This approach is in line with the measuring procedure recommended by Mander et al. (1988) and recently implemented by Welt et al. (2016).

Moreover, in the range of loading before peak load, the stress values calculated by dividing total force by total cross-sectional area of columns; however, after that point, the stress is determined by dividing total force to area of concrete core encapsulated by perimeter hoop, because of spalling of the cover concrete. Even though the arrangement of transverse reinforcing for low- and medium-confined columns was different, the force–displacement behaviours did not show a remarkable difference. Compared to low- and medium-confined specimens, the high-confined column indicated a remarkably higher capability of energy dissipation; nevertheless, this configuration showed just 12% higher strength. The load-deformation and failure pattern of all three types of columns are in line with results reported by Mander et al. (1988).

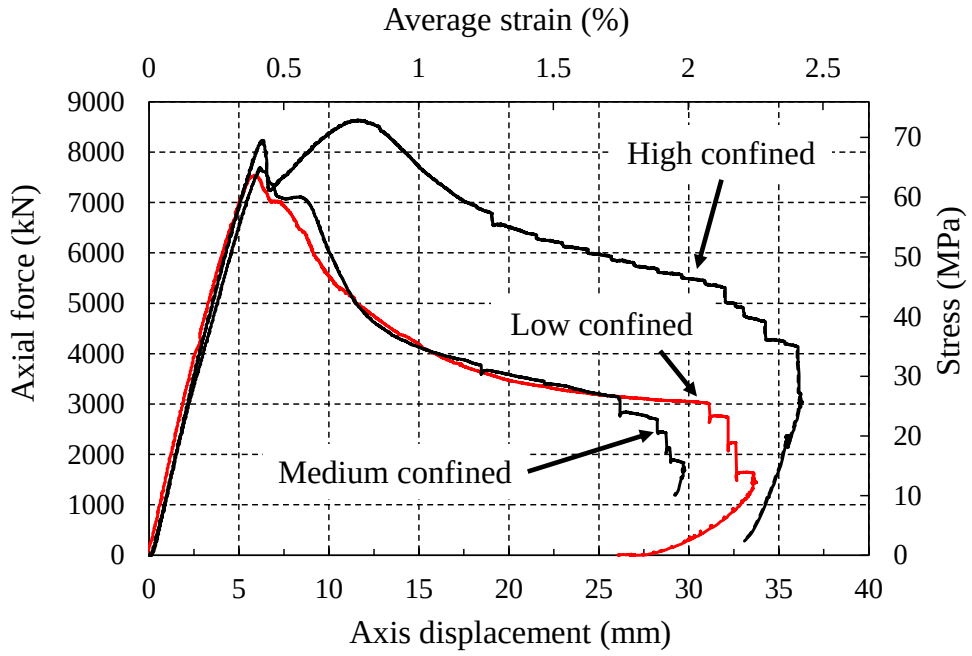

Figure 9-5 Force-displacement and stress-strain response of RC columns

9.2.4 Damage assessment

To evaluate the level of damage incurred by axial loading on concrete material in a column subjected to monotonic loading until collapse, two approaches were used. The first followed the idea of establishing an oxygen permeability coefficient profile over the height of a damaged RC column, while the second attempted to capture the remaining stress–strain capacity of the concrete material. To achieve these goals, concrete cores were needed from areas of interest in collapsed columns.

The coring procedure was planned to be conducted vertically to avoid cutting any reinforcement, getting cores in the direction that material has been previously loaded and also take sequential cores as much as possible to come up with the continuous profile. Therefore, damaged RC columns were all laid down and cut into three pieces to enable coring from the central part of sections. Cutting was conducted in two phases; pre-cut and final cut. At first, the Cut-off saw with a central saw arm (Stihl-TS 800) was used to cut the whole perimeter of the column up to 150 mm in depth for the pre-cut stage. Then, an end roller saw (Husqvarna K970) was implemented to accommodate for deeper cut up to 280 mm (Figure 9-6). For safety requirements, the

cover concrete was cleanly removed and sawing started carefully, perpendicular to the longitudinal axis of the column. Figure 9-7 shows the final cut pieces obtained from the top, medium and bottom parts of each damaged column.

(a) (b)

Figure 9-6 Concrete cutter machines (a) Cut-off saw (b) all-around cutter

(a) (b)

(c)

Figure 9-7 Columns cut pieces

A diamond core bit with working length of 430 mm and nominal diameter of 93 mm was then used along with the core drill machine (Hilti DD150-U) to take desired cores from the damaged pieces. In the next step, the machine was attached to the drilling stand (DD-ST 150-U CTL) to facilitate the coring process. Figure 9-8 shows the process followed to take cored cylinders from damaged columns. The assembly was then mounted on the forks of a forklift to give more flexibility in taking a core from points of interest. Each piece was flipped over and two cores were taken perpendicular to the cross section of the core concrete in the direction of previous compression loading. The location of the cores within the section was selected in a way that avoided any facing with embedded reinforcement. Two companion cores were taken from each piece to provide enough material for both permeability and supplementary compression tests. One core was used to supply concrete disks distributed over the height of the column; however, no disks could be obtained in the highly central damaged area of the high-confined column. The second core was secured for a compression test to capture the stress–strain relationship in the damaged concrete core. The MK brick-saw was then used to cut the uneven end of each core. The cores were washed, cleaned with a clean towel, and transferred by gloved hand to the concrete laboratory.

Figure 9-8 Coring process

9.2.5 Sample preparation for oxygen permeability test

To conduct the permeability test, 25 mm-thick disks were first extracted and appropriately prepared from damaged concrete cores obtained from bottom, mid and top parts of low, medium and high confined columns (Fig. 5). Slicing began precisely from one end of the core, once the uneven portion had been removed and continued until the whole core was used. Each disk's thickness was measured with an accuracy of 0.1 mm and tagged sequentially. The disks were oven dried at 50°C until the disks reached a steady state moisture content where the difference between their mass measured between two consecutive days in the oven was less than 0.1%. Any potential additional damage to the microstructure of concrete that might have originated from the above-mentioned steps was ignored in this study. The oxygen permeability test was conducted on concrete disks sawn from core cylinders as described in section 2.2.5.

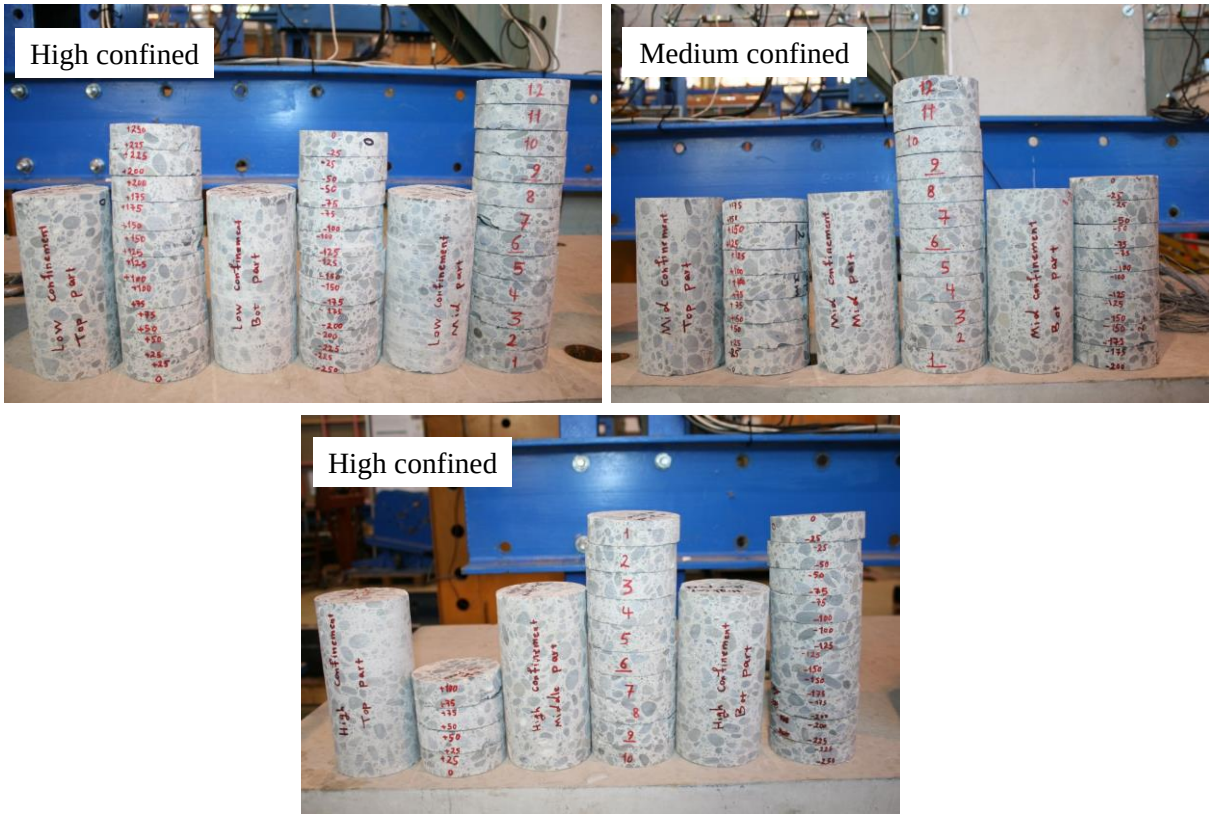

Figure 9-9 . Prepared cored cylinders and companion disks prepared for compression and permeability test

9.2.6 Quantitative permeability-based damage assessment

Having calculated the coefficient of permeability of all disks taken continuously over the height of the damaged column, the distribution of k can be established. Figure 9-10a indicates the variation of coefficient of permeability over the height of the damaged column. This profile provides a basis to spot the location of local damage and also determine how far the damage has spread out with regard to the increase in permeability. These profiles reveal how far it is necessary to move away from the visibly damaged area to assure concrete is essentially undamaged.

The value of k increased by a factor of 32 from an average value of 22×10^{-11} m/s over the upper and bottom thirds of the column to 700×10^{-11}m/s as the peak value over the central area for the low-confined column. The value of k of the medium-confined column also surged from an average of 35×10^{-11} m/s in the

relatively lower damaged area in the vicinity of both ends of the column, to 734×10^{-11} m/s at the extremely damaged zone in the middle part of the column. The value of k associated with the low and medium-confined columns, achieved approximately similar values, which shows that in the areas in which the disks can be taken, confinement did not significantly affect the permeability. This is also in agreement with the force-displacement results obtained for these two columns. In the case of the high-confined column, there was no chance to plot a continuous diagram because of the severe damage which did not allow extraction of concrete disks from the extremely damaged zone. The average value of k in the relatively undamaged area of the high-confined column is 62×10^{-11} m/s, which is twice as large as the OPI value related to the same zones in the low- and medium-confined columns. If it were possible to measure k, it would offer no resistance to flow, resulting in a considerably large, off-scale value.

The k values calculated for all disks, taken over the height of the columns, can also serve to introduce a damage parameter, addressing the material deterioration through the change that happens in permeability. Permeability damage index, DI_P, can be estimated as a relative change in permeability, as follows:

$$DI_P = \frac{k-k_0}{k_{peak}} \tag{9.1}$$

where k = coefficient of permeability of the concrete disk at any location; k_{peak} = the coefficient of permeability of the concrete disk taken from the highly damaged area, and k_0 = the coefficient of permeability of the concrete disk taken from the relatively undamaged area. In practice, it is impossible to get a disk from a highly damaged area, especially in the high-confined column, as the concrete is completely crushed to loose and unintegrated aggregates. Although it is numerically difficult to derive $DI_P = 1$, it is plausible to assign 100% damage to an area where there is extreme damage visible. The minimum of damage ($DI_P = 0$) happens in the areas which are acceptably undamaged. The damage parameter is intentionally defined as a relative quantity because k_0 is obtained from the cores taken from the most intact areas of the specimen, not from the concrete cylinder prepared during casting. That is because in practice access to these cylinders is very unlikely, so considering

concrete disk samples extracted from relatively undamaged areas instead makes good sense.

Figure 9-10b shows the distribution of the damage parameter over the height of the column as a function of permeability. The damage parameter achieves the highest values of 0.99 and 0.98 for low- and medium-confined columns, respectively, over the central zone. It decreases drastically once it reaches both top and bottom ends, which matches with observations during the test. For the case of the highly confined column, the graph cannot continuously plot over the central zone due to the impossibility of preparing disks from this area. The extent of the damaged area associated with the high-confined column is greater for than the others. This is substantially attributed to the higher level of stresses generated during the test. The extent of damage for the low-confined column ($l_{d,l}$), from where the damage index surged from an average value of 0.03 to the peak of 0.98 (737mm–1,087mm) and again dropped to the same level of damage, was 350 mm, which is 25% of the column height.

In the case of the medium-confined column the extent of damage ($l_{d,m}$) occurred from the height of about 712 mm to 1,112 mm, which is 400 mm. The larger damage length was observed for the high-confined column ($l_{d,h}$ = 550 mm), from the level of about 687 mm to 1,237 mm, which is 40% of the height.

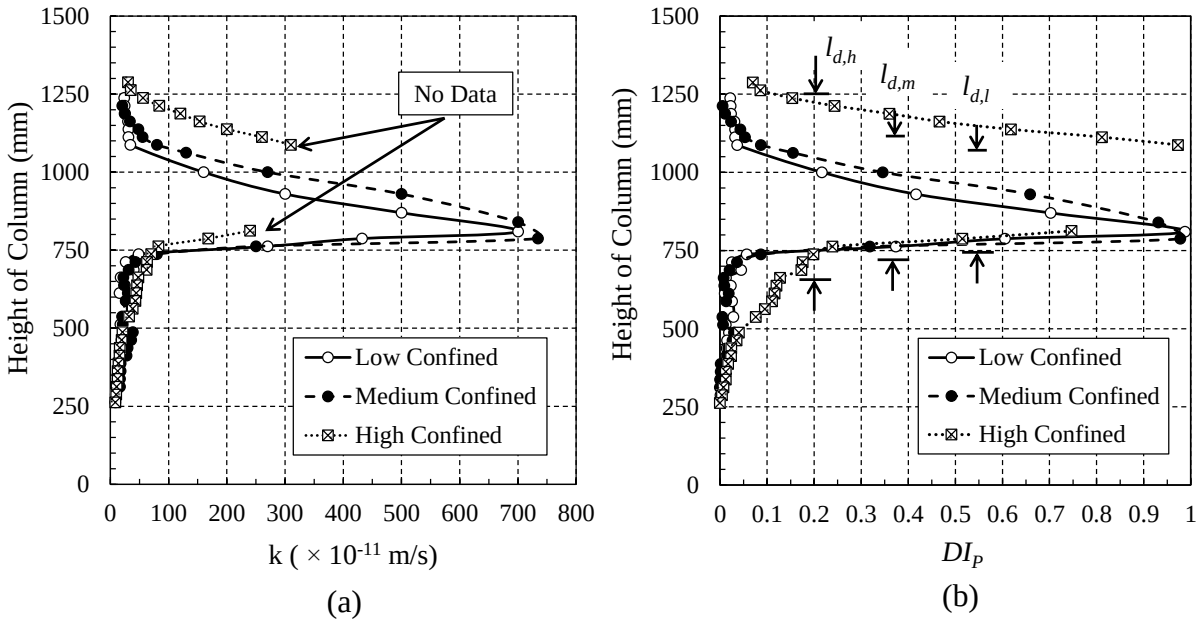

Figure 9-10 Distribution of coefficient of permeability over the height (b) illustration of damage parameter and damage length over the height

9.2.7 Sample preparation for compression test

Once the stress–strain behaviour is established, it is possible to characterize how the material behaves during loading, where it is supposed to fail (ultimate strength), and how much strain it can sustain up to failure, suggesting the ultimate ductility. To find out how much capacity has remained in a damaged concrete material, there is a need to determine how much reduction in the ultimate strength and strain (material degradation) has occurred in the specimen with respect to applied damage. For this purpose, concrete cores were cut to a length of approximately 186 mm, to maintain a height/diameter ratio of 2, and also to be consistent with the results of intact cylinders. The area at which strain gauges were to be glued were ground using 120-grit sand chapter, and cleaned with acetone to remove any dirt and the residue of dust. Two-component, PS polyester adhesive was then used as a pre-coating substance as a part of the surface preparation process. This secured a base layer on which the strain gauges were bonded.

From supplementary tests in this study, not reported herein, it was found that gluing strain gauges on the surface of ordinary concrete cylinders without any

preparation leads to imprecise results. Furthermore, the coating provides alkali resistance, and effectively blocks the entrance of moisture and gas from the inside of the concrete. Part A was poured into a mixing bowl, weighed on the scale and then part B was proportionally dropped on top of that (part B = 3% by weight of part A) and mixed to come up with the homogenous mixture. A thin layer of the mixture was then applied with a brush, and on top of that a piece of transparent film (binder) was placed and secured using masking tape. The gel hardened in about 6 hours and a smooth surface was revealed as the film was removed. Two PL-60-11 strain gauges (TML) with a gauge length of 60 mm were axially attached to the prepared surface using cyanoacrylate CN-E adhesive on each core cylinder to measure the axial strain.

It is worth mentioning that strain gauges with a short gauge length are not good candidates to capture global strain of the concrete surface since they measure localized strain. Strain gauges with a long length are capable of recording average strains over a larger distance. For a heterogeneous material like concrete, a gauge length is required that can average out the irregular stresses in the material. Thus, the gauge length used in this research met the criterion highly recommended by the manufacturer, which requires the sensing length to be at least three times the diameter of the largest aggregate size. This ensures the readings are an average evaluation of the strain in the concrete surface. To account for any asymmetric axial strain inconsistency, strain gauges were mounted at 180° intervals. The circumferential strains were also measured using the same type of strain gauges laid on the mid-height of both sides of each specimen.

Figure 9-11a shows the configuration of both strain gauges. The samples were then loaded at the rate equal to 400με/min using a servo-hydraulic compression machine of 3000 KN capacity up to failure to determine residual stress–strain capacity of the cylinders (Figure 9-11b).

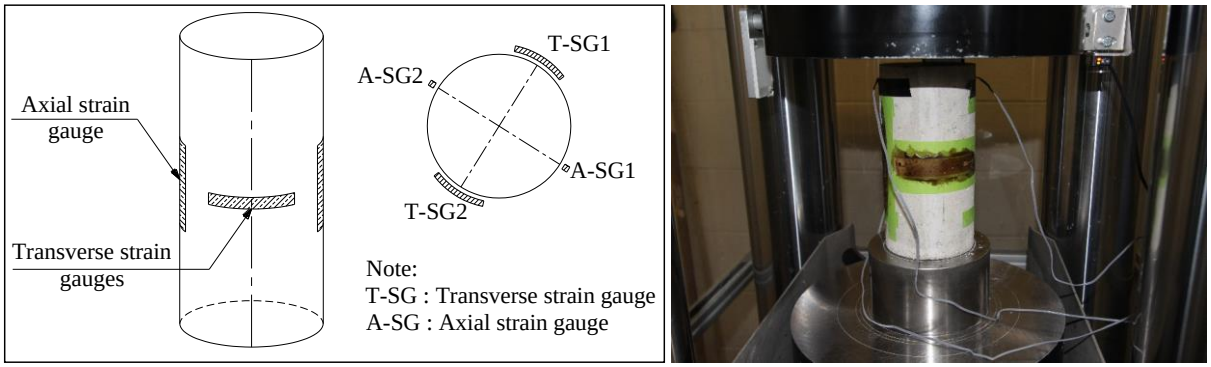

Figure 9-11 (a) Configuration of axial and lateral strain gauges (b) compression test apparatus

9.2.8 Residual capacity and deterioration in mechanical properties

A compression test was conducted on the instrumented cores taken from the bottom, mid and top parts of each damaged column. As illustrated in Figure 9-12, typical failure mode of cores, after being subjected to a compression test, are mostly bursting type. This behaviour is noticeably different from the common failure rupture mode associated with undamaged concrete cylinders, which tend to be fractured at 45° shear plane (cone failure) under similar testing conditions. It was observed that the concrete cores lost their integrity such that aggregates could be segregated easily from the cement paste, unlike intact cylinders. While cement paste in the intact cylinders retained the solidarity of the sample in a way that aggregates were broken during the compression test, no sign of breakage in gravel was found in the damaged concrete cores. These cores were more brittle, which seems to be caused by existing cracks in the sample, leading to less ductile response.

Figure 9-12 Typical failure mode of cored cylinder in compression test

Figure 9-13 displays residual stress–strain capacity obtained from the compression test on core samples. It should be noted that both axial and transverse strain values presented herein are the average readings of two pairs of strain gauges for each sample. The stress–strain curve displayed is associated with the average of three pristine, unconfined concrete cylinders cured in the fog room, and tested at the age of 180 days. The average strain and strength capacity of these intact cylinders was 2764 με and 38.9 MPa, respectively. The strength and strain of three cores taken from the top, mid and bottom parts of the low-confined column presented an average value of 26 MPa and 1440 με, respectively. In the low-confined column, the weakest core was taken from the mid part, which acquired 1007 με and 24 MPa (Figure 9-13a). The average of the strength in the cores procured from the top, mid and bottom parts the column with the medium confinement was 29 MPa, while its strain acquired 1540 με (Figure 9-13b). The least strain value in this case was related to the core from the middle part, which showed 1320 με as its strain capacity. In the case of cores taken from the high-confined column, the average of the strain and strength measured from all three cores was 1360 με and 25 MPa. Similarly to the medium-confined column, the minimum of

strength and strain values were still associated with the middle part, which showed only a strength of 12 MPa, and a strain equal to 612 με (Figure 9-13c).

Having compared the average ultimate strain capacity of intact concrete cylinders with damaged cores in all parts of all three specimens, about 1050 με reduction in the ultimate strain of damaged concrete was observed, which represents 42% loss of axial strain capacity. The largest reduction in mechanical properties of damaged concrete is attributed to the lateral strain capacity, as it showed an average of 68% degradation in its capacity. It was also found that the strain capacity of cores taken from the bottom part of all three types of column is higher than the other segments. With respect to strength capacity, the average of strengths obtained from all cores showed a 33% drop in comparison with undamaged cylinders. This study also showed that cores extracted from the middle part of columns showed less strain and strength compared to the cores from the top and bottom parts, which implies the middle area has been more affected by the damage.

The elastic modulus of damaged concrete is also relatively lower than undamaged concrete. Results show more deviation from the elastic modules of undamaged cylinders, once stress increases. The average of the elastic modulus of the three undamaged concrete cylinders, calculated from the axial branch, is 31.3 GPa, while the average of E-modulus between all damaged cores is 21.8 GPa. This is an indication of 30% degradation in stiffness. These values were calculated at a stress level corresponding to 40% compressive stress, as has been recommended by ASTM C469/C469M .

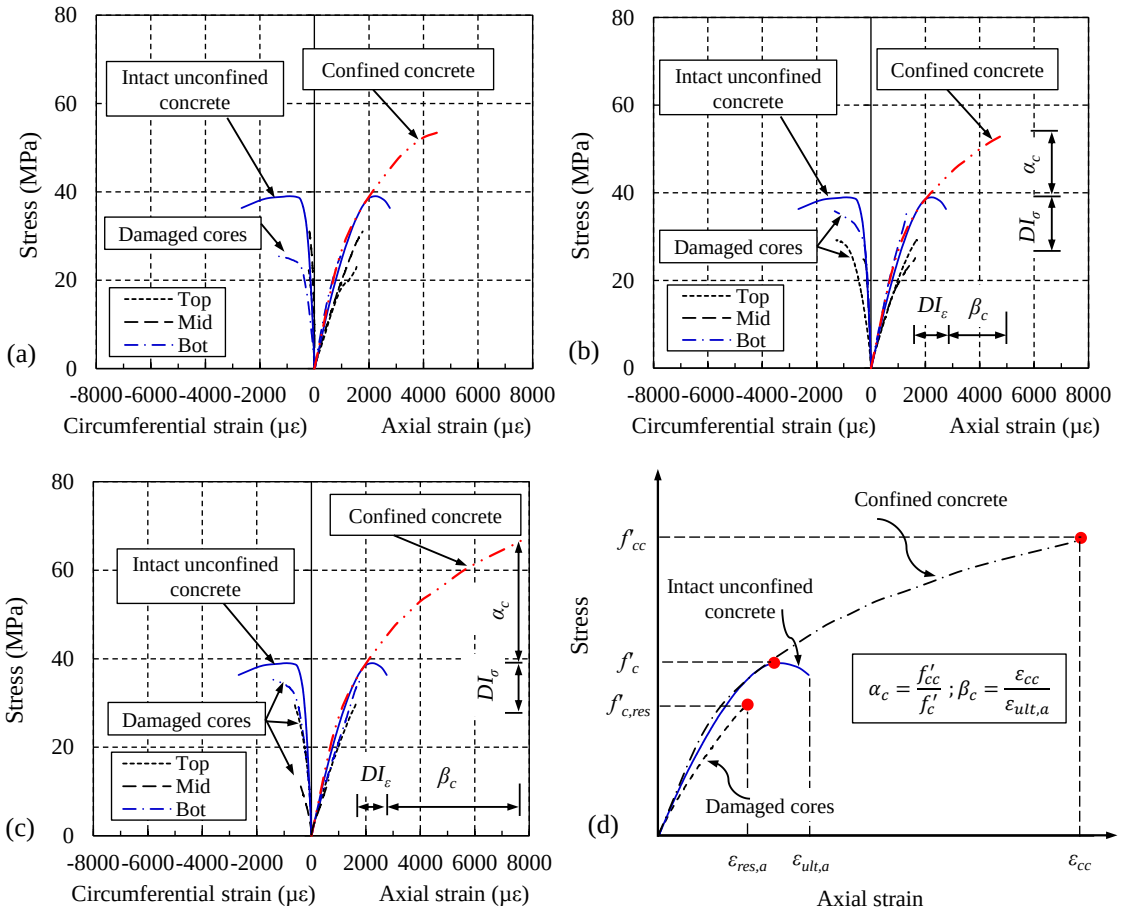

Figure 9-13 Residual stress–strain capacity of damaged core

To quantitatively represent damage that occurred in the concrete material with respect to degradation in strain and strength, damage indices were introduced through Equations of 9.2-9.4. These equations estimate damage using strain and strength values associated with damaged cores as follows:

$$\boldsymbol{DI}_{\varepsilon,a} = 1 - \frac{\varepsilon_{res,a}}{\varepsilon_{ult,a}} \tag{9.2}$$

$$\boldsymbol{DI}_{\varepsilon,c} = 1 - \frac{\varepsilon_{res,c}}{\varepsilon_{ult,c}} \tag{9.3}$$

$$\boldsymbol{DI}_{\sigma} = 1 - \frac{\sigma_{res}}{f'_c} \tag{9.4}$$

where $\boldsymbol{DI}_{\varepsilon,a}$, $\boldsymbol{DI}_{\varepsilon,c}$ and $\boldsymbol{DI}_{\sigma}$ = damage indices of loss in axial strain, circumferential strain and strength capacity; $\varepsilon_{res,a}$ = residual axial strain of damaged

core; $\varepsilon_{ult,a}$ = ultimate axial strain of concrete cylinder; $\varepsilon_{res,c}$ = residual circumferential strain of damaged core; $\varepsilon_{ult,c}$ = ultimate circumferential strain of concrete cylinder; σ_{res} = residual strength of damaged core; f'_c = strength of undamaged concrete.

Figure 9-14a shows the distributions of damage indices associated with cored cylinders taken from top, mid and bottom part of the low, medium and high-confined columns in terms of degradation in axial strain. Figure 9-14b also shows distribution of damage indices with respect to degradation in circumferential strain of cored cylinders. Deterioration in load bearing capacity of cored cylinders showed comparatively lower level of damage as illustrate in Figure 9-14c.

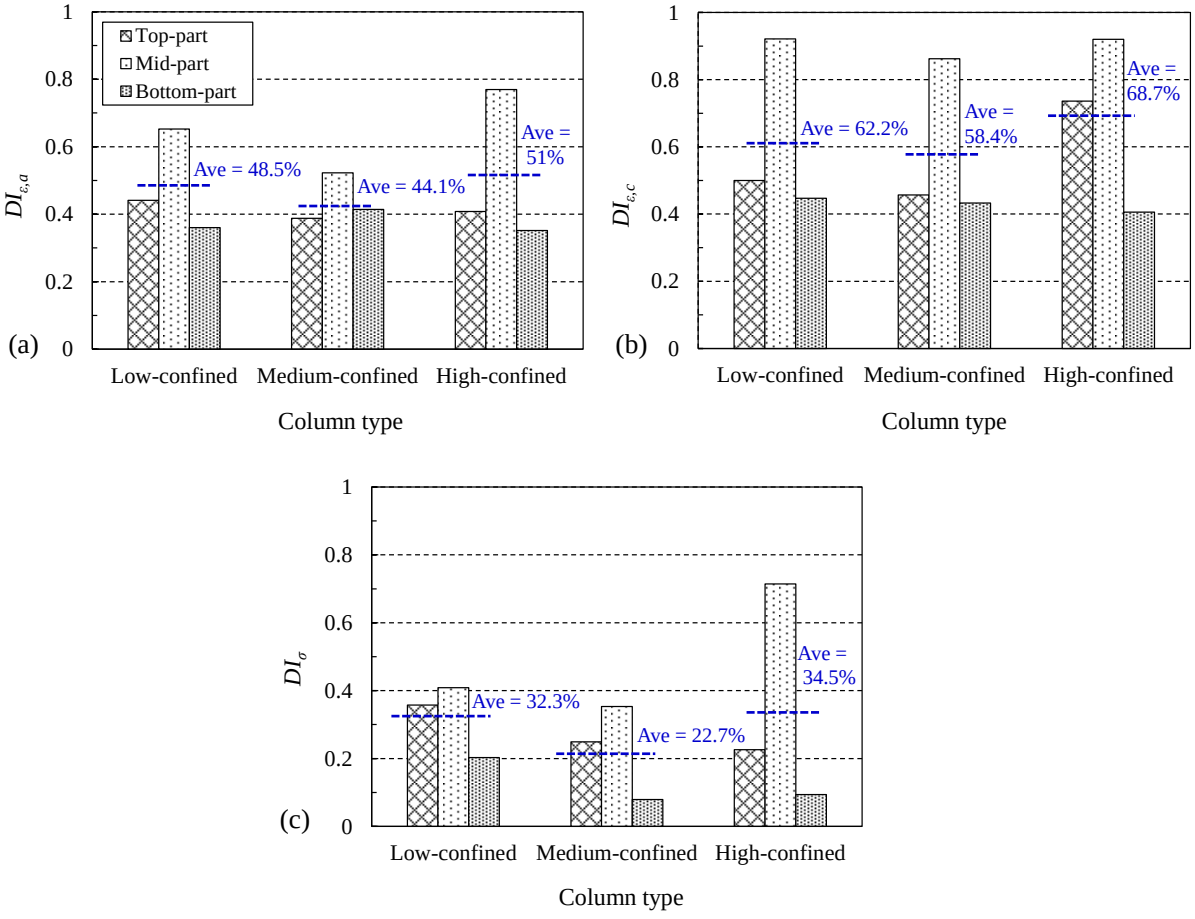

Figure 9-14 Damage indices distribution in terms of axial strain

9.2.9 Effect of Confinement on Concrete Material Capacity

As was shown in Figure 9-13, the stress–strain capacity of concrete material while it is within the large-scale RC columns is significantly higher than stress–strain behaviour associated with intact concrete tested under unconfined condition. This is because at high levels of compressive loading, confinement provided by the lateral reinforcement is activated, which allows the concrete to continue to perform functionally while it experiences stress–strain values that are substantially beyond its unconfined capacity. The factor of α_c represents the ratio of ultimate calculated compressive strength of concrete while it was provided with three levels of confinement ($f'_{c,c}$) inside the RC column to the strength of a pristine concrete cylinder tested under unconfined conditions (f'_c). This factor quantifies the loss that occurs in the strength when confinement is no longer provided. Similarly, the coefficient βc, which is the ratio of calculated strain reached in the presence of confinement (ε_{cc}) to the maximum axial strain attained during testing of intact concrete cylinder ($\varepsilon_{ult,a}$), was introduced to measure the degradation that happens in the strain capacity of concrete material in the absence of confinement.

These factors account for the microcracking damage that occurred in the concrete material under confined conditions while it was within the large-scale RC columns. As expected, the high-confined column takes the most advantage of the confinement effect as its strain and strength capacity substantially increased by factors of 2.79 and 1.71 compared to the unconfined intact concrete cylinder. However, the strain and strength associated with the concrete material related to low- and medium-confined columns showed significantly lower values of loss in capacity when confinement was not provided. The strength, strain at peak stress, confinement and damage-related loss factors are given in Table 9-1.

Obviously, the cored cylinders would have shown higher strain and strength capacity if they had been subjected to compression tests under confined conditions. Thus, the loss in strain and strength capacity of damaged concrete observed in this study is the upper bound of loss and can be considered as a conservative estimation of material degradation in an RC column. In other words, in reality the degradation in the

stress–strain capacity of damaged confined concrete in an RC member is less than that presented herein.

Table 9-1 Experimental results: strength, strain at peak stress, confinement and damage loss factors

Confinement level	Pristine-concrete cylinder[c]		RC column confined concrete		Damaged cored cylinder		α_c	β_c	DI_σ (%)	DI_a (%)
	Strength f'_c (MPa)	Strain $\varepsilon_{ult,a}$ (με)	Calculated strength $f'_{c,c}$ (MPa)	Calculated strain ε_{cc}	Strength $f'_{c,res}$ (MPa)	Ultimate axial strain $\varepsilon_{res,a}$				
Low[a]			53.4	4504	26.3	1425	1.37	1.63	32.3	48.5
Medium[a]	38.9	2764	53.7	5036	30	1544	1.38	1.82	22.7	44.1
High[b]			66.7	7726	25.5	1356	1.71	2.80	34.5	51.0

[a]Average of top, mid and bottom core samples.
[b]The mid core sample was taken from the height between 525 mm to 820 mm.
[c]Average of three concrete cylinders at the age of 180 days.

9.2.10 Correlation between the Degradation in Material and Permeability

Figure 9-15 indicates a correlation between damage that occurred in the axial and circumferential strain, and the strength of cored cylinders with respect to their permeability damage index. Both axial and circumferential strains damage indices show a consistent degradation by an increase in the permeability damage index; however, in the case of transverse strain, the rate of deterioration is more predominant. Considering the lower bound limit for the deterioration of mechanical properties in terms of the changes that occur in the permeability of concrete, it might be interpreted that a 46% increase in the permeability damage index of concrete material may result in a minimum of 33% damage index of loss in axial strain capacity ($DI_{\varepsilon,a}$) of the damaged concrete. However, in the case of transverse strain, a minimum of 38% damage index of loss in circumferential strain ($DI_{\varepsilon,c}$) was observed once the permeability damage index exceeded 22%.The higher value of $DI_{\varepsilon,a}$ compared to $DI_{\varepsilon,c}$, indicates that at the same level of damage, incurred by external loading and represented indirectly through permeability damage index, circumferential strain of concrete becomes more degraded. This shows axial strain is less affected by the absence of lateral confinement during compression testing of cored cylinders. Also, the damage

index of loss in strength capacity (DI_σ) reached 17% when the permeability damage index of concrete reached 48%.

The relationship between damage indices have been shown at three points, representing top, mid and bottom part of each column. In fact, the damage indices associated with the permeability of concrete disks at each part have been averaged and then correlated to companion concrete cores which were subjected to compression tests.

Despite the limited data in this study, implementation of the permeability technique on sliced concrete disks shows promise for damage assessment. Whether the concrete disks were taken parallel to the axial direction of the column, as in the current investigation, or perpendicular, as would typically be the case for coring into a damaged member, there should still be a relative increase in measured permeability due to microstructural damage caused by the applied loads. The relative comparison of damaged versus undamaged concrete provides the basis for the damage index described in this chapter. In the cases where it is not possible to take cores or where extracting cored samples may affect the structural performance of the member, the surface permeability tester (Torrent 1992) may be used for on-site damage assessment of concrete. There are, however some challenges associated with on-site measurements as variations in surface moisture content can significantly affect the observed permeability of the concrete.

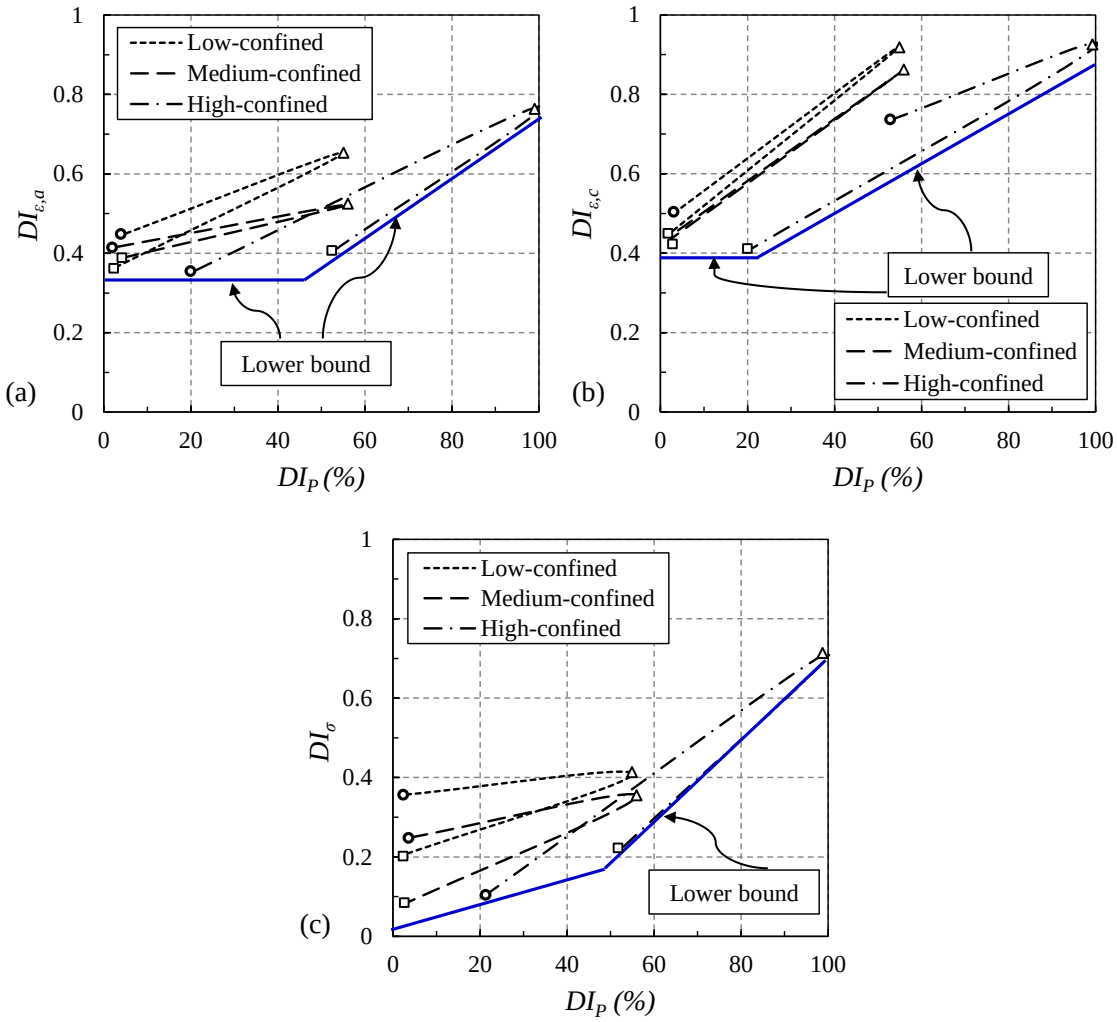

Figure 9-15 Permeability-based damage versus damage in load bearing capacity (strength)

9.3 Permeability-based damage assessment of RC beams

In an attempt to examine the applicability of permeability testing technique to assess damage in actual RC members, in this section the implementation of permeability test on three RC beam is presented. Of all RC beams tested in this PhD research, three beams which were subjected to monotonic loading up to 13% drift, cyclic loading at constant amplitude of 2% drift and cyclic loading at constant amplitude of 4% drift were chosen for permeability-based damage assessment. The full description of the behaviour and fatigue performance of these large scale beam specimens was presented in chapter 6. In this section, the supplementary permeability

testing are explained. Figure 9-16 shows typical test set-up and damage status of the beam specimen at 2% drift.

Figure 9-16 Test setup

9.3.1 Damage assessment

As described in section 9.2.6, to conduct permeability test there is need to extract cored cylinders from damaged RC beams. For this purpose, the damaged beam were cut into four pieces at pre-defined sections and two companion cores were taken from each block. Cutting process followed at two stages; pre-cut and final cut. At first, the Cut-off saw with a central saw arm was and then an end roller saw was implemented to accommodate for deeper cut using HYCON hydraulic cut-off saws. The process of cutting RC beams is shown in Figure 9-17.

Figure 9-18 shows the distribution of the coefficient of permeability (k) over the height of the three beams tested under monotonic, cyclic loading at 2% and cyclic loading at 4% drift, respectively. The distribution of permeability damage index, DI_P, defined as a relative change in permeability (Equation 9.1) was also provided. As it is described earlier in section 9.2.6, in the context of permeability-based damage assessment, the extent of damage (l_d) is defined as a length over which the coefficient of permeability is comparatively higher than the coefficient of permeability associated with intact part of the RC beam. In the case of specimen subjected to monotonic lateral loading, the permeability surged from an average value

of 250 × 10-11 m/s at the height of 575 mm to the maximum value of 4320 × 10-11 m/s at the height of 150 mm, resulting in a damage length (l_d) of 425 mm. For the beam tested cyclically at 2% drift, the extent of damage ($l_{d,c2\%}$) occurred from the height of about 125 mm to 700 mm, in which the coefficient of permeability showed a significant increase from about 260 × 10-11 m/s to 5170 × 10-11 m/s. For the beam tested at 4% drift, the damage length ($l_{d,c4\%}$) was associated with increase of permeability from 270 × 10-11 m/s at the height of 750 mm to 6200 × 10-11 m/s at the height of 150 mm.

Figure 9-17 Cutting process of RC beams

As seen, the graph cannot be continuously plot over highly damaged area of plastic hinge region due to the difficaulty of preparing disks from this area. Regarding the fact that no concrete disks were taken from the first 150 mm along the height of the beam, the total length of damage for specimens tested under monotonic, cyclic loading at 2% and cyclic loading at 4% drift are 1025 mm, 1075 mm and 1125 mm, respectively. The extent of the damage associated with the beam tested cyclically at 4% drift is greater for than the others. This is substantially attributed to the higher level of stresses generated during the test.

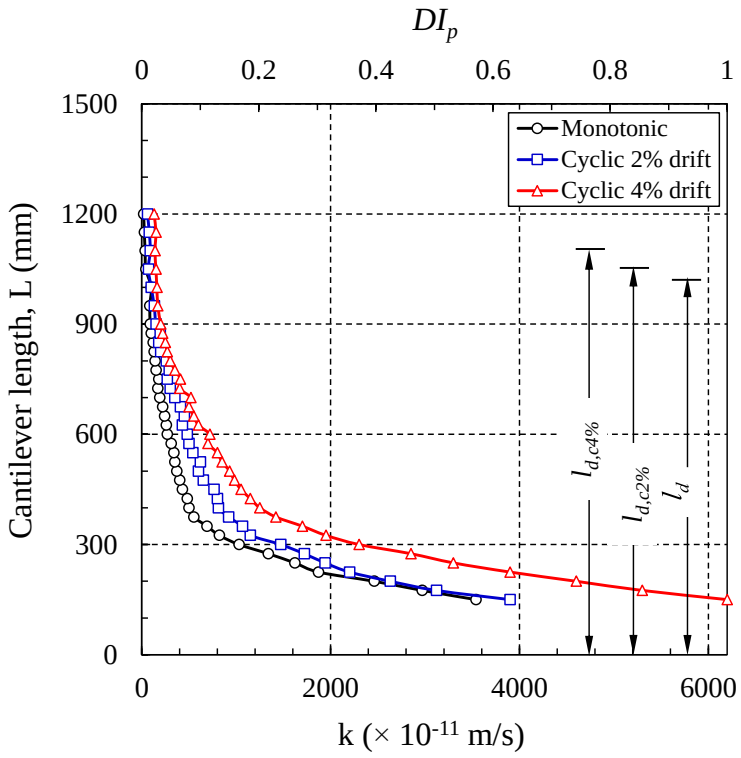

Figure 9-18 Distribution of coefficient of permeability over the height

9.3.2 Correlation between the permeability-based and mechanical properties-based damage assessment

As it was seen in Figure 5 11, the yield length (l_y): the length over which strain exceeds yield strain (ε_y), during pushover of the beam at 1%, 2%, 3% and 4% drift were measured to 580 mm, 730 mm, 790 mm and 960 mm, respectively. The yield length from mechanical properties point of view, is in fact a length over which actual plasticity spreads, and affects the extent of damage along the length of the specimen. Section

9.3.1 illustrated a methodology to investigate the extent of damage in RC beams from permeability perspective. The damage length was assessed in terms of increase in the permeability of concrete disks, prepared from cored concrete taken from core section of beams with reference to intact concrete. This provided a basis by which the length of damage for beams subjected to monotonic, cyclic loading at 2% and cyclic loading at 4% drift were determined to 1025 mm, 1075 mm and 1125 mm, respectively. In the case of monotonic test, damaged length form permeability-based and mechanical properties-based standpoints are in good agreement. However, it should be noted that the extent of damage using permeability technique was determined after application of 13% drift (1025 mm) while the maximum length of damage in terms of yield length is associated with application of 4% drift (i.e., 960 mm). In the case of beams tested cyclically at ±2% and ±4% drift, no comparison was made as the yield length was not provided.

9.4 Permeability-based damage assessment of RC beam-column joints

In a further attempt to examine the applicability of permeability testing technique to assess damage in actual RC members, in this section the implementation of permeability test on a pre-damaged RC beam-column joint is presented. The specimen was originally tested to determine post-seismic capacity of damaged plastic hinges extracted from an existing RC buildings (Cuevas and Pampanin 2017).

9.4.1 Specimen detail and testing protocol

The “H frames” extracted during the deconstruction process of the PwC building located on Armagh Street in the Christchurch’s Central Business (CBD) area. It was a 22-storey structure which was designed in the 1980s following capacity design principles. The “H frames” were cut in two “T-shape” specimens due to the laboratory crane capacity limitations. The beam length (measured from the column face to the point of load application), width and height were 2550 mm, 575 mm and 1100 mm, respectively. The (main) longitudinal reinforcement consists of top and bottom 4 D-28 straight bars and 2 additional D28 hooked bars (within the plastic hinge relocation detail); the transverse reinforcement consists of 2 R-12 stirrups (one interior, one

exterior) spaced at 150 mm. There is also secondary reinforcement detailed such that it provides vertical support to the flooring system. The columns are 2700 mm long, and 1100 mm square at the section. The nominal steel yield strength, fy, and concrete compressive strengths, f'_c as specified in the drawings, are 300 MPa and 30 MPa, respectively.

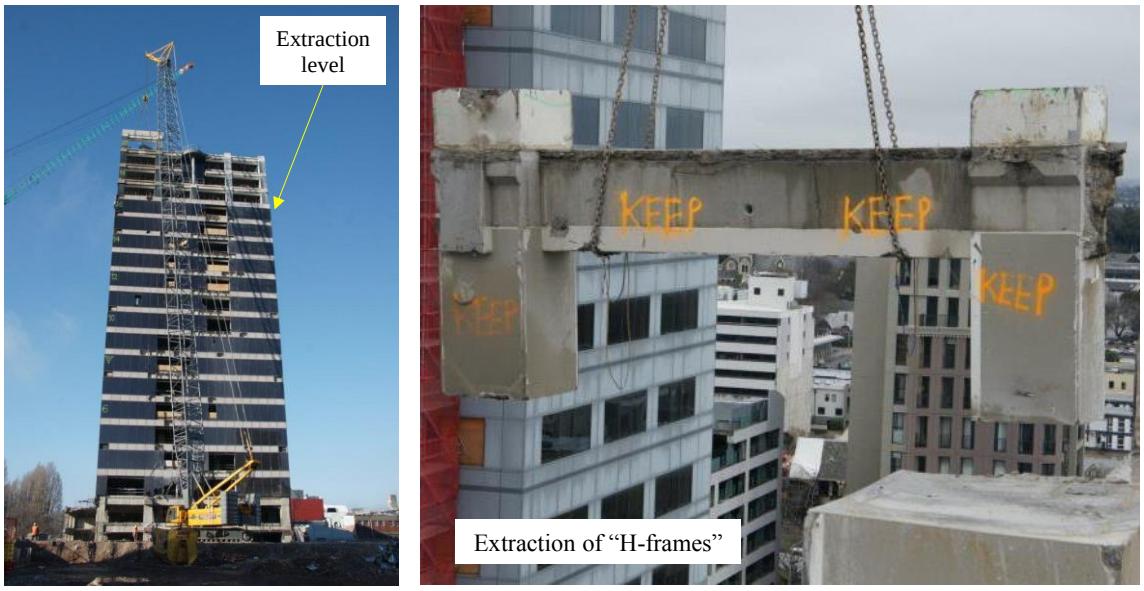

Figure 9-19 Elevation of the PWC building during the deconstruction process (Cuevas and Pampanin 2017)

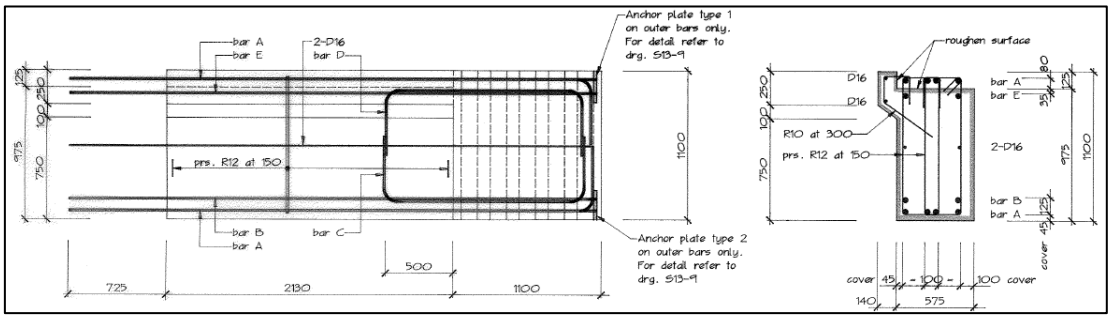

Figure 9-20 specimen details (Holmes Consulting Group, 1988)

The specimen was subjected to a standard quasi-static reverse cyclic testing loading protocol up to a maximum "total" rotation of 2.5%. The actuator was located approximately at the theoretical inflection point at mid-span of the beam. A quasi-static displacement-controlled cycling loading protocol was applied at the beam-end with

increasing "total" beam rotations of ±0.1%, ±0.2%, ±0.5%, ±0.75%, ±1.0%, ±1.5%, ±2.0%, ±2.5%, ±3.5%, and ±4.5%. The loading protocol was applied according to "acceptance criteria for moment frames based on structural testing and commentary" (ACI 374-1).

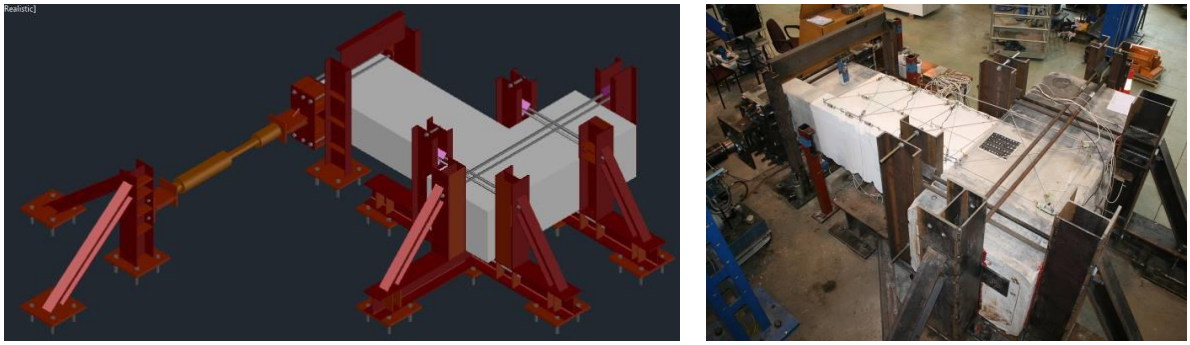

(a) (b)

Figure 9-21 (a) 3D CAD view of the reaction frame (b) specimen during the test (image courtesy of Alberto Cuevas)

9.4.2 Damage assessment

As described in section 9.2, to conduct permeability test there is need to extract cored cylinders from damaged beam-column joint. In this case, the cores were taken at pre-defined locations along the length of the beam in parallel to the width direction as shown in Figure 9-22. The process of coring from RC beam-column joint is shown in Figure 9-23. While the cores taken from beams and columns (section 9.2 and 9.3) were parallel to longitudinal axis of the member, in the case of beam-column joint, cores were taken perpendicular to longitudinal axis. Thus, the coefficient of permeability presented are possibly less than values if the cores were taken in parallel. It is worth mentioning that in the case of beam-column joint though permeability testing was conducted on highly damaged plastic hinge region, it was possible to extract cores.

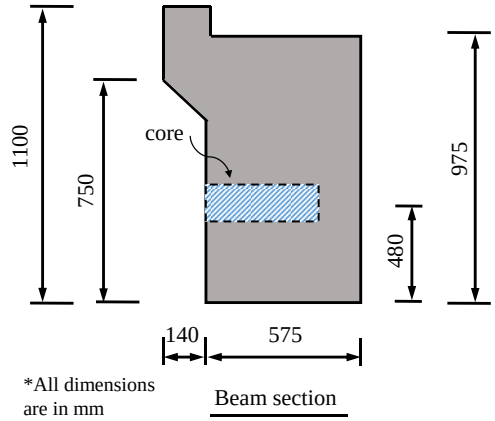

Figure 9-22 Coring direction

Figure 9-23 coring process from damaged beam-column joint

Figure 9-24 shows the distribution of the coefficient of permeability (k) along the length of beam in a beam-column joint. As seen, study shows permeability test is capable to reveal the extent of damage in terms of increase in permeability in reference to its value in minimum damaged area (i.e., S_4). From permeability-based perspective, the length of damage (l_d), was found to be 1370 mm.

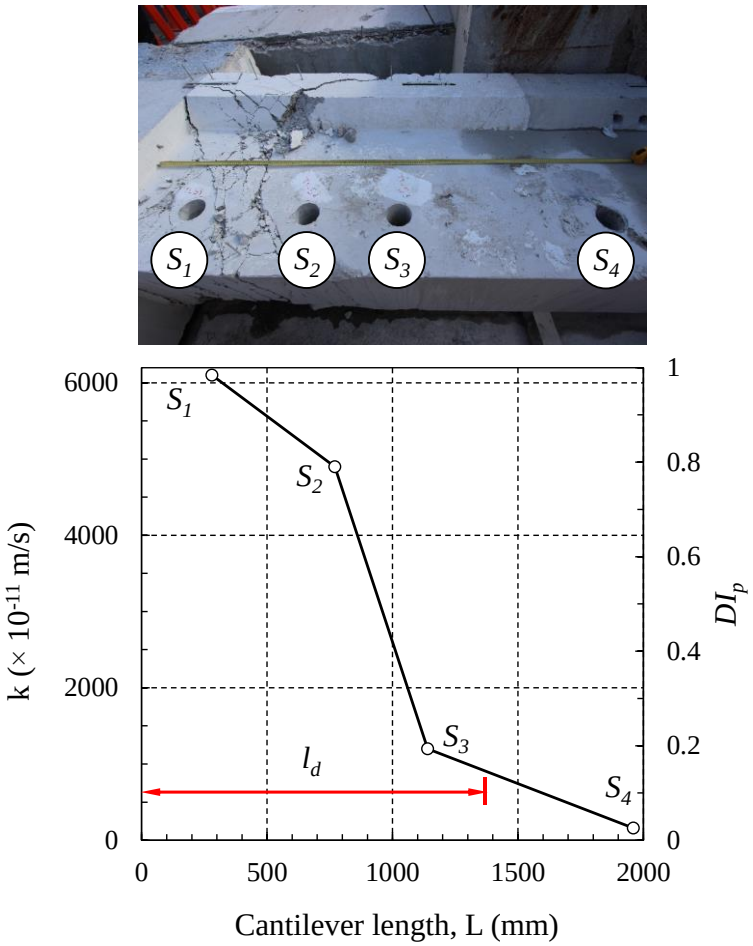

Figure 9 24 Distribution of coefficient of permeability along the length of beam

9.5 Application of methodology to earthquake damaged buildings

The need to develop low invasive techniques to evaluate damage to RC member and concrete material after Christchurch earthquakes in order to quantify the level and extent of damage has been perceived. In this chapter, the proposed damage assessment methodology based on change in the permeability of damaged concrete seems to reasonably answer these questions. The experimental testing campaign presented in this chapter was carried out to verify the feasibility and potential of the permeability testing technique. Although the results are associated with permeability test on concrete disks prepared from cores taken form damaged RC member, the relative comparison of damaged versus undamaged concrete provides the basis for the damage index described in this chapter. In the cases where it is not possible to take cores or where

extracting cored samples may affect the structural performance of the member, the surface permeability tester (Torrent 1992) may be used for on-site damage assessment of concrete. While the South African durability index approach used in this study is performance-based method for assessing durability properties of concrete, the Torrent method (The Swiss approach) is a performance-based method that makes use of an in situ air-permeability test method. Most recently, Starck et al. (2017) suggested an integrated approach based on incorporating in situ and laboratory-based permeability test methods for improving the lab-based permeability measurements by supplementary use of the Torrent method. Variations in the moisture content of the surface concrete however may affect the accuracy of on-site measurements. The application of the methodology developed in this work is line with durability index performance-based approaches recently developed for the assessment of large-scale RC structures (Beushausen and Luco 2015).

The study showed the method can be effectively implemented to assess damage in RC members (i.e., beam, column and beam-column joint). For this, there is a need to determine the coefficient of permeability for concrete sample extracted form the most undamaged area (k_0), highly damaged area (k_{peak}) and in-between areas (k). This will allow the calculation of a permeability damage index (DI_p) along the length of damage RC member. The damage length (l_d): the length over which coefficient of permeability increase is almost an order of 10-100 (based values achieved in this study), can be identified. Figure 9-24 illustrates the overall procedures need to be taken to assess damage. The information on the level of damage in the concrete component of the various members can be combined with hardness data from the reinforcing steel (Loporcaro et al. 2017) to produce an overall assessment of the likely remaining capacity of the structure.

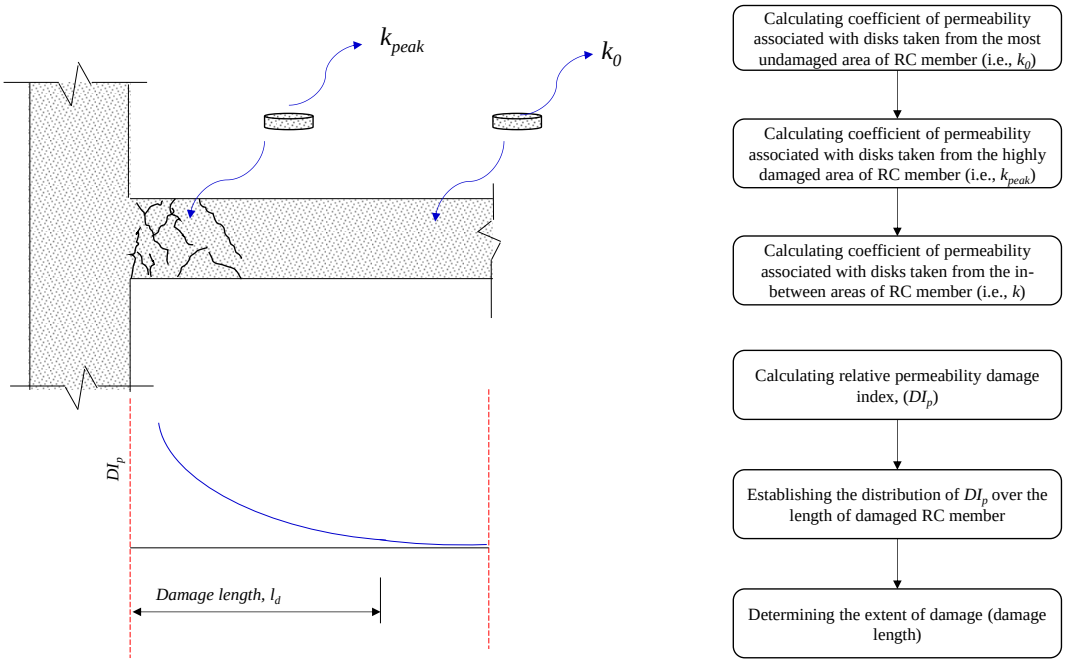

Figure 9-24 Flowchart of the permeability-based damage assessment methodology

9.6 Conclusions

The purpose of this chapter was to demonstrate the application of permeability-based damage assessment in the concrete material obtained from damaged RC members–columns, beams and beam-column joints– in an attempt to correlate material degradation with level of structural damage. In fact, when the material characterization of an existing concrete building is required, recognition of the mechanical properties of the concrete is the first priority in the evaluation process. The outcomes and accomplishments of this chapter are summarized below:

1. The structural performance of the damaged concrete (represented by post-event stress–strain behaviour of cored cylinders) differs considerably from the compressive behaviour associated with pristine concrete cylinders. Mechanical properties of the damaged concrete (i.e., axial strain, lateral strain, strength and E-modulus,) were all affected by the strain/stress level applied during testing. Lateral strain showed 38% loss as an average, while axial strain lost an average of 26% of its capacity, resulting in less deformable material. An average of

degradation in the ultimate strength capacity was also found to be 18%, which is lower than for strain. Stiffness of the damaged concrete (E-modulus) deteriorated by about 30% compared to intact concrete. This could imply that damage (e.g., crushing) would occur earlier if the damaged member were subject to the next loading demand (i.e., earthquake/aftershock). In other words, to determine the residual capacity of a damaged RC member, stress–strain diagrams related to intact concrete are no longer valid and a revised relationship, showing the damaged stress–strain relationship, should be used. Adopting undamaged stress–strain behaviours of concrete material for the purpose of assessment in a damaged RC structure leads to overestimations of the capacity.

2. Permeability is a measure of the transport property of the concrete and can be related to the microstructural damage experienced by the concrete under various loading conditions. Once the coalescence of microcracking occurs there is an increase in the permeability of the concrete. The formation and emergence of such microcracks consequently causes the mechanical properties of the concrete to deteriorate. It was found that a 33%, 38% and 17% degradation in the axial strain capacity, transverse strain capacity and compressive strength respectively of damaged concrete resulted in a 46% increase in the permeability of the concrete.
3. Using the profile of permeability over the height of the damaged RC column, the extent of damage was identified, and was in excellent agreement with measured laboratory observations. The extent of damage with respect to the length in which the propagation of cracking caused a marked increase in the permeability of concrete was determined. In the case of the low-confined column, this length was measured as 350 mm, which is 25% of column height. For medium- and high-confined columns, the extent of damage was 400 mm and 600 mm, respectively, which are 27% and 40% of the height of the column.
4. The permeability-based damage assessment showed a great potential to reveal the extent of damage in damaged RC beams. The total length of damage form in the context of permeability-based damage assessment for beam specimens tested under monotonic, cyclic loading at 2% and cyclic loading at 4% drift

were found 1025 mm, 1075 mm and 1125 mm, respectively. In the case of beam-column joint extracted from PwC building, permeability-based damage assessment resulted in revealing the length of damage equal to 1370 mm.

5. To obtain post-event properties of damaged concrete, two issues should be addressed: applying a robust and reliable technique to assess both the level and the extent of damage that has occurred in the specimen and, secondly, understanding the amount of loss in strength and strain capacity (material degradation). Permeability testing was found to be reliable enough to correlate observed damage with material degradation. In addition, the supplementary investigation conducted to capture stress–strain behaviour also led to an estimation of the residual axial capacity of the damaged concrete material.

9.6 References

ACI 374-1 (2005). "Acceptance criteria for moment frames based on structural testing and commentary." ACI.

ASTM C469/C469M (2014). "Standard test method for static modulus of elasticity and Poisson's ratio of concrete in compression." ASTM International, West Conshohocken, PA.

Baghaei, R., Feng, M. Q., and Torbol, M. "Residual capacity estimation of bridges using structural health monitoring data." *Proc., SPIE Smart Structures and Materials+ Nondestructive Evaluation and Health Monitoring*, International Society for Optics and Photonics, 79833I-79833I-79812.

Bao, X., and Li, B. (2010). "Residual strength of blast damaged reinforced concrete columns." *International journal of impact engineering*, 37(3), 295-308.

Bishko, A., Samokrutov, A. A., and Shevaldykin, V. G. "Ultrasonic echo-pulse tomography of concrete using shear waves low-frequency phased antenna arrays." *Proc., Proceedings of the 17th World Conference on Nondestructive Testing*.

Chung, Y.-S., Park, C. K., and Meyer, C. (2008). "Residual seismic performance of reinforced concrete bridge piers after moderate earthquakes." *ACI structural journal*, 105(1), 87.

Cuevas, A., and Pampanin, S. "Accounting for residual capacity of reinforced concrete plastic hinges: current practice and proposed framework." *Proc., 2014 New Zealand Society of Earthquake Engineering Conference, Auckland, New Zealand*.

Cuevas, A., and Pampanin, S. (2017). "Post-Seismic Capacity of Damaged and Repaired Reinforced Concrete Plastic Hinges Extracted from a Real Building." *Seventeenth world conference on earthquake engineering* Santiago, Chile.

Girrens, S. P., and Farrar, C. R. (1991). *Experimental assessment of air permeability in a concrete shear wall subjected to simulated seismic loading*, Los Alamos National Laboratory.

Grube, H., Lawrence, C., Cement, and Association, C. (1984). *Permeability of concrete to oxygen*, Cement and Concrete Association.

Hearn, N., and Lok, G. (1998). "Measurement of permeability under uniaxial compression: a test method." *Materials Journal*, 95(6), 691-694.

Hutchinson, T. C., and Soppe, T. E. (2011). "Experimentally measured permeability of uncracked and cracked concrete components." *Journal of Materials in Civil Engineering*, 24(5), 548-559.

Kermani, A. (1991). "Permeability of stressed concrete: Steady-state method of measuring permeability of hardened concrete studies in relation to the change in structure of concrete under various short-term stress levels." *Building research and information*, 19(6), 360-366.

Li, B., Nair, A., and Kai, Q. (2012). "Residual axial capacity of reinforced concrete columns with simulated blast damage." *Journal of Performance of Constructed Facilities*, 26(3), 287-299.

Maeda, M., and Kang, D. E. (2009). "Post-earthquake damage evaluation of reinforced concrete buildings." *Journal of Advanced Concrete Technology*, 7(3), 327-335.

Mander, J., Priestley, M., and Park, R. (1988). "Observed stress-strain behavior of confined concrete." *Journal of structural engineering*, 114(8), 1827-1849.

Mullins, L., and Pearson, H. (1949). "The X-Ray Examination of Concrete." *Civil Engineering and Public Works Review*, 44(515), 256-258.

Perenchio, W. F. (1989). "The condition survey." *Concrete International*, 11(1), 59-62.

Schofield, B. (1963). "Acoustic emission under applied stress." DTIC Document.

Soppe, T. E., and Hutchinson, T. C. (2011). "Assessment of gas leakage rates through damaged reinforced-concrete walls." *Journal of Materials in Civil Engineering*, 24(5), 560-567.

Tasai, A. "Residual axial capacity and restorability of reinforced concrete columns damaged due to earthquake." *Proc., US-Japan Workshop on Performance-Based Earthquake Engineering Methodology for Reinforced Concrete Building Structures*, 191-202.

Tegguer, A. D., Bonnet, S., Khelidj, A., and Baroghel-Bouny, V. (2013). "Effect of uniaxial compressive loading on gas permeability and chloride diffusion coefficient of concrete and their relationship." *Cement and concrete research*, 52, 131-139.

Torrent, R. J. (1992). "A two-chamber vacuum cell for measuring the coefficient of permeability to air of the concrete cover on site." *Materials and Structures*, 25(6), 358-365.

Wang, K., Jansen, D. C., Shah, S. P., and Karr, A. F. (1997). "Permeability study of cracked concrete." *Cement and Concrete Research*, 27(3), 381-393.

Welt, T. S., Massone, L. M., LaFave, J. M., Lehman, D. E., McCabe, S. L., and Polanco, P. (2016). "Confinement Behavior of Rectangular Reinforced Concrete Prisms Simulating Wall Boundary Elements." *Journal of Structural Engineering*, 04016204.

Chapter 10 *Conclusions and recommendations*

Assessing the level of damage and estimating the residual load-carrying capacity of concrete and RC members after an earthquake is an imperative task. The outcomes provide sound information about the condition of the structure which allows an appropriate course of action: re-occupancy, repair (to the same level or even to the higher standard), or demolition, to be taken. This thesis focused on several issues in assessing damage which are not adequately addressed in the existing literature. The study focused on the following three main objectives as set out earlier in Chapter 1: (i) damage assessment and residual capacity at material level (i.e., concrete); (ii) damage assessment of bond between deformed bar and concrete; and (iii) damage assessment and residual capacity at member level (i.e., RC beam). The main findings and limitations of this research are presented in this chapter and possible areas for future research are also identified.

10.1 Key findings

10.1.1 Damage assessment and Residual capacity and at material level

Three durability testing techniques—oxygen permeability, electrical resistivity, and porosity—were used to assess the damage that occurred in concrete. In this context, change in the durability properties was considered as representative of damage in the microstructural system of concrete material induced by external axial compression. This investigation highlighted the robustness and sensitivity of the permeability test to identify the level of damage with respect to applied stress. Neither the resistivity nor the volume of permeable voids tests were found capable of revealing the varying degrees of damage in the concrete microstructure.

The critical stress (i.e., the point at which oxygen permeability coefficient dramatically increased for small increase in stress) was found to be exceeded when the concrete cylinders were loaded to stress levels between $0.7f'_c$ and $0.95f'_c$. Critical stress is a threshold: when the applied load exceeds it, interconnected channels already formed in the damaged concrete do not completely close after unloading. Results

showed the effect of these irreversible cracks can be efficiently identified using the permeability test. This was line with the critical stress value ($0.88f'_c$) obtained from the volumetric strain diagram.

The experimental results showed that pre-loading concrete specimens causes concrete to lose its strain capacity with little or no accompanying degradation in the strength. An average reduction of about 24% in strain capacity associated with preloaded samples up to 0.7-0.95f'_c was observed. A permeability-based damage index (PDI) was proposed to estimate the residual strain in uniaxial damaged concrete.

The study showed that the application of a fluorescent microscopy technique along with supplementary image analysis on petrographic thin sections can be used effectively to quantify damage in terms of microcracking occurring in the microstructural system of concrete. The applied impregnation method was successful in creating images with excellent contrast, which facilitated the quantitative analysis procedure. Observation of the thin petrographic sections in ultraviolet light using a stereomicroscope at a magnification of 4 times was sufficient to detect the microcracks.

It was found that most of the pre-existing cracks in the concrete prior to the application of load, attributed to the environmental conditions and possible shrinkage of the cement paste, had crack widths of less than 0.005 mm. At $0.5f'_c$, while bond cracks were clearly observed, no noticeable sign of mortar cracks were present. At $0.7f'_c$ the first mortar cracks were measured, indicating that mortar cracks develop in the range from $0.5f'_c$ to $0.7f'_c$. The study showed that at $0.9f'_c$, bond cracking increased considerably and the coalescence of the microcrack network resulted in the formation of continuous cracks by bridging action between adjacent bond cracks.

The experiment showed that even though the failure of concrete is attributed to the development of a network of microcracks, due to the increase in the level of damage, the formation of continuous cracks does not by itself lead to loss in the bearing capacity of concrete. Concrete can still sustain considerable strain capacity beyond $0.9f'_c$ and retain its short-term stability, prior to reaching the fracture point where the concrete cannot support further loading demand. Furthermore, the distribution of microcrack width showed that at $0.9f'_c$, microcrack width generally did not exceed 0.05 mm, which is still hard to identify without the aid of microscope.

The investigation revealed a good correlation between the damage represented as geometrical characteristics (i.e., length, area and the width) of microcracks and the applied compressive stress. Quantitative microcrack analysis was found to be a powerful tool to evaluate damage in concrete. Results showed that the area of cracks, which implicitly accounts for length and width, is highly sensitive to stress-induced damage and could be used as an indicative parameter to assess the degree of damage in concrete material.

A comprehensive set of experimental tests were conducted to address this objective. The study showed that while post-peak behaviour of unconfined concrete under axial compression loading follows a descending trend (i.e., softening), confined concrete exhibits an ascending branch (i.e., hardening). The slope of the hardening branch for tested specimens was found to be 7.1% of the tangent modulus of confined concrete in the first branch. The presence of GFRP-wrap confinement increased the strength and strain capacity by 65% and 74%, respectively.

Fatigue life curves (*S*–*N* curves) were established for both confined and unconfined concrete. It was found that the number of cycles to failure (N_f) was almost identical for both the confined and unconfined concrete at the same applied stress/strength ratio (σ/f'_c or σ/f'_{cc}). It should be noted that while the ratio was the same, the magnitude of the applied stress was much higher for the confined concrete.

Damage to the mechanical properties of unconfined concrete in terms of degradation in secant modulus, total and plastic strain, followed the commonly observed three-component S-shape spectrum. In the case of confined concrete, the initial damage accumulation was much higher, resulting in only two stages of the damage spectrum: a significant initial drop followed by a gradual decrease with a minimal dependency on stress levels.

During fatigue loading, part of the kinetic energy was converted to heat, measured by a rise in temperature at the surface of specimens. Results showed that as the level of stress increased, the rate of increase in surface temperature decreases. This indicates that the amount of heat generated is mainly dependent on the number of cycles and rate of loading, rather than stress levels. Moreover, the experiments showed the amount of heat generated in confined concrete is considerably higher than unconfined concrete.

This is mainly due to the severe dislocation of aggregates at stress levels far beyond the strength of unconfined concrete.

The ultimate strength of confined and unconfined concrete was not significantly affected by preloading the specimens, even up to $0.95f'_c$ or $0.95f'_{cc}$. However, the residual strain capacity of preloaded specimens was shown to decrease markedly compared with intact specimens. Results indicated that to determine the residual capacity of a damaged RC member, stress–strain diagrams related to intact concrete are no longer valid and a revised relationship should be used.

The oxygen permeability of concrete disks, taken from loaded specimens, showed a good correlation with the degree of mechanical damage experienced by confined and unconfined concrete. The permeability damage index was an effective indicator of the remaining strain capacity of concrete subject to fatigue loading and can provide a useful tool for the post-event damage assessment of reinforced concrete structures.

Using the profile of permeability over the height/length of the damaged RC member, the extent of damage was identified, and was in excellent agreement with measured laboratory observations. The extent of damage with respect to the length in which the propagation of cracking caused a marked increase in the permeability of concrete was determined. In the case of the low-confined column, this length was measured as 350 mm, which is 25% of column height. For medium- and high-confined columns, the extent of damage was 400 mm and 600 mm, respectively, which are 27% and 40% of the height of the column. The permeability-based damage assessment showed a great potential to reveal the extent of damage in damaged RC beams. For beam specimens tested under monotonic, cyclic loading at 2% and cyclic loading at 4%, drift values were found 1025 mm, 1075 mm and 1125 mm, respectively. In the case of a beam-column joint, permeability-based damage assessment revealed the length of damage was 1370 mm.

In the case of RC columns, it was found that the formation and emergence of microcracks causes the mechanical properties of the concrete to deteriorate. The study showed that a 33%, 38% and 17% degradation in the axial strain capacity, transverse strain capacity and compressive strength respectively of the damaged concrete resulted in a 46% increase in the permeability of the concrete.

It was found that the structural performance of the damaged concrete (represented by post-event stress–strain behaviour of cored cylinders) differs considerably from the compressive behaviour associated with pristine concrete cylinders. Mechanical properties of the damaged concrete (i.e., axial strain, lateral strain, strength and E-modulus,) were all affected by the strain/stress level applied during testing. In the case of damaged RC columns, lateral strain showed 38% loss as an average, while axial strain lost an average of 26% of its capacity, resulting in less deformable material. An average of degradation in the ultimate strength capacity was also found to be 18%, which is lower than for strain. Stiffness of the damaged concrete (E-modulus) deteriorated by about 30% compared to intact concrete. This could imply that damage (e.g., crushing) would occur earlier if the damaged member were subject to the next loading demand (i.e., earthquake/aftershock). In other words, to determine the residual capacity of a damaged RC member, stress–strain diagrams related to intact concrete are no longer valid and a revised relationship, showing the damaged stress–strain relationship, should be used. Adopting undamaged stress–strain behaviours of concrete material for the purpose of assessment in a damaged RC structure leads to overestimations of the capacity.

To obtain the post-event properties of damaged concrete, two issues should be addressed: applying a robust and reliable technique to assess both the level and the extent of damage that has occurred in the specimen and, secondly, understanding the amount of loss in strength and strain capacity (material degradation). Permeability testing was found to be reliable enough to correlate observed damage with material degradation. In addition, the supplementary investigation conducted to capture stress–strain behaviour also led to an estimation of the residual axial capacity of the damaged concrete material.

10.1.2 Damage assessment of bond between deformed bar and concrete in the post-yield region

A thorough investigation was performed on bond performance of reinforcing steel with a focus on post-yield bond properties and also the damage assessment of RC beams in the post-yield range of steel reinforcement using a state-of-the-art distributed fibre optic strain sensing system (DFOSSS). The technology allowed for continuous

strain measurements along the length of the specimen using sensor spacing of 2.6 mm along its length. The technology reduced the error associated with instrumentation of the specimen as the size and the installation method of the fibres imposed little damage to the reinforcing bars, compared with the measuring techniques used in the past.

Once the strain profile was established, a bilinear average stress–strain curve was used to obtain the axial stress values corresponding to the strain at any location. In this way, the bond stress distribution along the reinforcement was determined using the slope of the axial steel stress profile. Mechanical properties of the reinforcement were found to have a significant influence on the bond behaviour particularly in the post-yield range.

The bond deterioration length was found to vary from $36d_b$ at 1% drift to $45d_b$, $49d_b$ and $60d_b$, for 2%, 3% and 4% drift, respectively. The bond deterioration length increases as the applied drift levels increase.

The review of bond deterioration models indicated that the available models either overestimate or underestimate the deterioration of the bond after yielding and cannot accurately represent the rate of decay for a member under flexure. Thus, a new strain-based model was proposed to accurately predict the behaviour of bond in the pre- and post-yield range of steel strain in a RC beam subjected to flexure. The proposed model showed good agreement with experimental results. It was found that once yielding occurs, irrespective of drift level, almost 80% degradation in bond capacity can be expected. The study also showed that for an RC cantilever beam subjected to flexure, the maximum bond stress in the elastic range can be considered to be $0.6 f'_c{}^{1/2}$, which is lower than the proposed values in the literature.

The mean bond stress was found to be $0.47 f'_c{}^{1/2}$ and $0.21 f'_c{}^{1/2}$, for pre- and post-yield range, respectively. These values were obtained on the basis of the interfacial fracture energy concept and can be used to simplify the evaluation of bond stress in both pre- and post-yield regions.

10.1.3 Damage assessment and residual capacity at member level

An extensive experimental campaign was carried out to investigate the development of fatigue damage, resulting in degradation of mechanical properties of RC beams.

The fatigue life (*S*–*N* curve) was drawn and the relationship that best predicts it was established. The relationship was found to have a form of power function, allowing an estimation of the total number of cycles that the specimen can take at each desired drift level. The spectrums did not show the classic S-shaped trend as in the case of low-cycle fatigue loading, but three different regions can still be identified. Initial degradation occurs up to about 10% of fatigue life, followed by a gradual decay up to about 70–80% of fatigue life, and the third stage, consisting of significant drops due to fracture of longitudinal reinforcement. The rate of deterioration increases as the drift level increases: at the same fraction of fatigue life, the specimen subjected to higher drift level degrades more. With respect to type of response, the most severe rate of deterioration occurred in the energy dissipation capacity, such that the ability of damaged RC beams to dissipate the input energy at 20% of fatigue life decreased to about 40% of its dissipation capacity during the first cycle. In the case of equivalent viscous damping, in a wide range of the fatigue life (10–70%), irrespective of drift levels, it is approximately constant and equal to 30%.

Having monotonically reloaded damaged specimens, previously subjected to different ratios of fatigue under two different drift levels, the residual force–displacement relationships were established. Observations showed a significant decay in strength, stiffness, energy dissipation and deformation capacity. Residual capacities showed a gradual deterioration up to 70% of fatigue life, beyond which a significant descending behaviour was observed. It was also found that as the drift level increases, the post-event residual load-deformation bearing capacity of the specimen degrades more. 70% of fatigue life was identified as the fraction of fatigue life that may be considered as the threshold beyond which the failure of the test specimen is inevitable. Although the study presented herein was conducted at member level, the concept can serve for the system level and subsequent decision-making.

Finite element analysis (FEA) was conducted using ABAQUS. Results showed a reasonable agreement with the actual experimental test results. This also shows that the selected finite element-based software with its implemented material models and element library was capable of dealing with the complexities involved in modelling and analysing fatigue behaviour of RC beams.

Pushover analysis was conducted first to examine the capability of the developed model of further cyclic analysis. That is because pushover analysis is comparatively simple, is stable, results in better convergence and requires less time. The appropriateness of the finite element model and mesh sensitivity were checked, and fine tuning of the model and suitability of the material models were investigated at this stage.

The good agreement between numerical and experimental results confirmed the capability of the FE model developed in this study to predict the behaviour of beams under fatigue loading. The formation and propagation of cracking as well as force–displacement responses were accurately captured. The concrete damage plasticity (CDP) model was adopted to represent the nonlinear behaviour of concrete using tensile and compressive damage parameters. For steel, the nonlinear combined (isotropic/kinematic) hardening model was adopted and calibrated using low-cycle fatigue tests on similar reinforcement to accurately capture its behaviour. The presented FEA showed promise for conducting a future parametric study on different aspects affecting the fatigue behaviour of tested beams.

Experimental tests using a high-speed actuator allowed the application of cyclic loading as high as 500 mm/sec. The study showed that the application of a high rate of loading causes an increase in the strength and cracking secant stiffness of the specimen, while the energy dissipation capacity and elongation of beam decrease. The increase in the maximum load-carrying capacity (strength) in the absence of inertia effects may be attributed to the rate-dependency of the constituent materials (i.e., steel and concrete). Enhancement of the stiffness results in a reduction in the elastic period, leading to an increase in shear demand. Thus, there might be a potential risk for an increase in the shear demand of the structure in the case of applying a load at a significantly high rate of loading. Since the rates at which the specimens are cyclically tested are substantially lower than those that would be expected in an earthquake, it is of vital importance to

fully understand the influence of rate-dependent effects on the behaviour of an RC member in relation to the analysis and design of structures in both building codes and practice. Moreover, with respect to elongation, beams showed 50% less elongation at high rate of loading. Also, the surface of the fractured bars showed that with an increase in the rate of loading, the surface fractures form a rougher and more uneven surface compared with the smooth surface created at the end of the low-speed test. Increase in the rate of loading also caused a significant increase in the temperature of the longitudinal bars.

The results showed that the fatigue life is inversely proportional to the rate of loading: the higher the rate of loading, the lower the fatigue life. This implies that, given identical loading amplitude, the rate of decay in the specimen subjected to a higher rate of loading is higher.

The rate of deterioration in the strength and energy dissipation capacity of the specimens over cycles, is exacerbated by a higher rate of loading. However, as the drift level (i.e., demand) increases, the response of the specimen is less affected by the rate of loading. Results show that a higher level of drift incurs a higher rate of decay, and also causes the deterioration trend to become smoother with no evident sign of bar fracture (i.e., drop in spectrums).

The study showed a shift in the failure mode from a ductile flexural failure at a low rate of loading to a brittle shear failure once the specimens were subjected to high rate of loading. Changes in the failure mode possibly affect the redistribution of forces within the specimen, which subsequently may alter the redistribution of forces in the structural system. As a result, it may be concluded that high rate of loading may hinder formation of the expected plastic hinges and affect its length in the specimens, resulting in overloading some other elements of the structure. Comparing crack patterns showed that flexural cracks were well-dispersed for the specimens tested at the low rate, while for the high-speed tests, the damage was mainly less, and wider with more localized cracks. This may be ascribed to a more efficient transfer of forces between the reinforcing bars and the concrete (i.e., bond stress) at the low rate of loading.

The study showed that the proposed damage assessment methodology based on the change in the permeability of concrete can be effectively implemented to assess

mechanical damage both at the material level and also to determine the extent of damage at a member's level (i.e., beam, column and beam-column joint). To assess damage, the coefficient of permeability for concrete sample extracted from the most undamaged area (k_0), highly damaged area (k_{peak}) and in-between areas (k), are determined. This will allow permeability damage index (DI_p) along the length of damage RC member to be calculated. In the next step, compression testing is conducted to establish the residual stress−strain capacity of damaged concrete. The corresponding coefficient of permeability of the damaged concrete is related to degradation in the mechanical properties through the permeability-based damage index which can be used as a tool to estimate residual capacity of concrete material. In the cases where it is not possible to take cores or where extracting cored samples may affect the structural performance of the member, the surface permeability tester (Torrent 1992) may be considered for on-site damage assessment of concrete. However, variations in the moisture content of the surface concrete may affect the accuracy of on-site measurements. The implementation of this method also allows the extent of damage (l_d), the length over which the coefficient of permeability exceeds its intact undamaged value, to be identified.

The application of the methodology developed in this work provides information on the level of damage in the concrete component of the various members, based on the permeability data, to produce an overall assessment of the likely remaining capacity of the concrete material.

10.2 Recommendations for future research

Considering the limitations of this dissertation and the existing literature, the following recommendations are made for future work.

10.2.1 Residual capacity and damage assessment at material level

A thorough investigation was performed to assess the level of damage and residual mechanical properties of previously damaged concrete; however, more investigation is required on the following issues to provide a complete picture.

- One of the key aspects affecting the residual capacity of concrete material is aging. Aging can affect the deformability (i.e., strain capacity) of the material, and taking this into account can result in a more realistic assessment of damage.
- The permeability investigations in this study were conducted on disks taken from either fabricated or cored concrete cylinders, which is quite invasive. Thus, the application of site in situ permeability testing technique (i.e., a non-invasive technique) is of great interest for future studies. Also, a study of the correlation between the two types of testing technique is recommended.
- Assessment of damage on the mechanical properties of concrete requires capturing of the complete stress–strain relationship of the material. Since the capability of strain gauges to measure deformations are limited to a certain level, it is highly recommended that special instruments (e.g. laser distance sensor) be used to obtain the complete post-peak behaviour of concrete. In other words, the use of strain gauges does not allow of fully capturing strain in the post-peak region (i.e., descending branch of stress–strain curve).
- In this study, fatigue loading on unconfined and GFRP-wrapped confined concrete cylinders was conducted at a certain rate of loading. In view of the fact that the rate of loading influences the fatigue response of the cyclically tested confined and unconfined specimens, the effect of higher rate of loading on deterioration of mechanical properties and residual capacity of the test specimens needs to be more closely studied.
- It is recommended that in future research the permeability on the disk be correlated with coefficient of permeability obtained by measuring permeability

on surface (e.g. Proceq permeability tester) in an attempt to obviate the need for invasive sampling. This will prevent incurring extra damage to member by coring.

10.2.2 Damage assessment of bond between deformed bar and concerte in the post-yield region

- The conventional moment–curvature (M–φ) analysis for the purpose of seismic assessment of damaged RC members is made on the assumption that the bond between reinforcement and surrounding concrete is perfect. However, it was observed that in the plastic region of the steel bond deterioration can occur by up to 80% its capacity in elastic region. Ignoring this in the current practice results in overestimation of member capacity. Thus, further analytical research is required, incorporating post-yield bond deterioration to develop a more realistic generation of moment–curvature curves.
- Since the application of DOFSSS allowed for continuous measurement of the strain profile in reinforcement, a more accurate analytical model to determine the plastic hinge length may be achieved by further investigations.
- Due to the breakage of fibre optics attached to the steel reinforcement, during cyclic testing at ±2% and ±4% drift, the strain of reinforcing bar was not measured during the entire experiment. Development of more resilient fibre in the future will allow the determination of cyclic bond deterioration, which is of great interest in the literature.
- Since the main focus of this part of the research was to develop a new approach to assess the behaviour of bond stress in the post-yield range of steel strain, no variables such as bar size, or concrete strength were studied.

10.2.3 Residual capacity and damage assessment at member level

- The ultimate goal of this research area is to achieve a platform to systematically assess the residual capacity of seismically damaged RC members, in the context of low cycle fatigue. Thus as a complementary part, it would be a great research topic to employ an appropriate method (e.g., rain flow cycle counting, range pair counting, peak counting, level crossing counting and range counting

methods (Dowling 1971) to decompose an earthquake record to a number of complete constant amplitude reversals. Since the total number of cycles to failure have already been estimated, this will allow an estimate of the degradation that had already occurred in the mechanical properties of damaged RC member using fatigue-based damage assessment. Then, the remaining fatigue life can be evaluated using spectra similar to those provided in Chapter 6.

- The residual capacity of RC beams in this study was determined by pushover of previously cyclically damaged beams at certain fractions of fatigue life. It would be of great interest to assess residual capacity while specimens were subjected to a conventional incremental loading protocol.
- The available commercial FE packages of ABAQUS cannot accurately account for cyclic bond-slip relationship. Therefore, an improvement to the cyclic deterioration of the bond in FE package could be an attractive research topic.
- Because of a limitation in the number of experiments intended to experience a high rate of loading, the residual monotonic load-carrying capacity of damaged RC beams previously tested at high rate of loading was not investigated.
- The residual capacity of previously damaged RC beams were determined against monotonic loading. Other loading protocols could be considered; however, due to the monotonic push-loading scheme considered for moment–curvature and subsequent force–displacement analysis, monotonic loading was considered.
- The effect of rate of loading in this study was examined in terms of the speed at which the specimen is loaded. However, it is recommended for future study that the effect of rate of loading be investigated in terms of the frequency at which the specimen is loaded.
- Since the main focus of this part of research was to develop a new approach to assess the behaviour of bond stress in the context of low-cycle fatigue, a prototype beam was prepared to represent the behaviour of an actual RC beam representative of 1980s NZ standard, thus variables including bar size and concrete strength were not studied.

10.3 References

Dowling, N. E. (1971). "Fatigue failure predictions for complicated stress-strain histories." ILLINOIS UNIV AT URBANA DEPT OF THEORETICAL AND APPLIED MECHANICS.

Appendix A Assessment of bond

A.1 Assessment/Measurement of bond

Several different types of experimental test methods have been used by researchers for bond evaluation. The majority of bond tests could be classified in five major categories; single bar pullout specimens, beam specimens, beam-end specimens, lap splice tensile specimens and lap splice beam specimens. Though several experimental studies may be said to use the same category of specimen, the particular details of specimens used in different studies may vary. No bond test method can be considered to be universally valid for all practical applications. Confining reinforcement may or may not be placed around the embedded bar. Bar force can be measured directly as well as slip at the loaded and free ends of the bar Noakowski 1978. For this reason it is important that the setup is defined precisely to allow comparability and reproducibility. The normalisation of the bond strength with reference to the actual concrete strength is discussed by Harajli et al. 2002. Two standardised test setups, beam test and the pullout test, specified in RILEM/CEB/FIP are used to determine the bond behaviour of concrete reinforcement. In the following major tests set ups are presented.

A.1.1 Pull-out tests

A.1.1.1 Pull-out test by Abrams

Pullout test is the most and oldest technique used by a huge number of researchers because of its simplicity. Almost one century ago, Abrams (1913) was the first researcher who implemented this test (Figure A. 1).

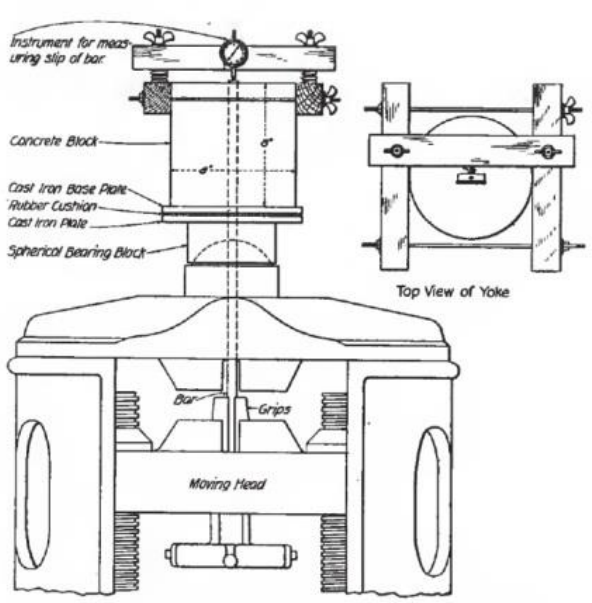

Figure A. 1 Pull-out test setup (Abrams, 1913)

A.1.1.2 Pull-out test by Rehm

Rehm (1961) conducted pull-out tests on a very short bar embedded length, equal to the rib spacing for deformed bars and the bar diameter for plain bars. The relationship between the local bond stress and the slip, were directly measured (Figure A. 2)

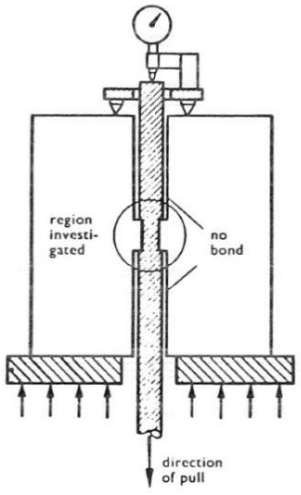

Figure A. 2 Pull-out test setup Rehm (1961)

The friction between the specimen and the bearing plate, as well as deflection of the bearing plate in the central region during loading, were considered disadvantages of the method.

A.1.1.3 Pull-out test by RILEM/CEB/FIP

In the RILEM/CEB/FIP recommendation a 10d × 10d × 10d concrete cube (where d is the bar diameter) including a rebar in its axis is subjected to a pull-out test. To reduce the influence of the disturbed area that forms close to the bearing plate, the bonded length is just half of the cube. As a result, the disadvantages presented in the Rehm method are overcome. Figure A. 3 and Figure A. 4 show the illustration of test specimen nd test set up proposed by RILEM.

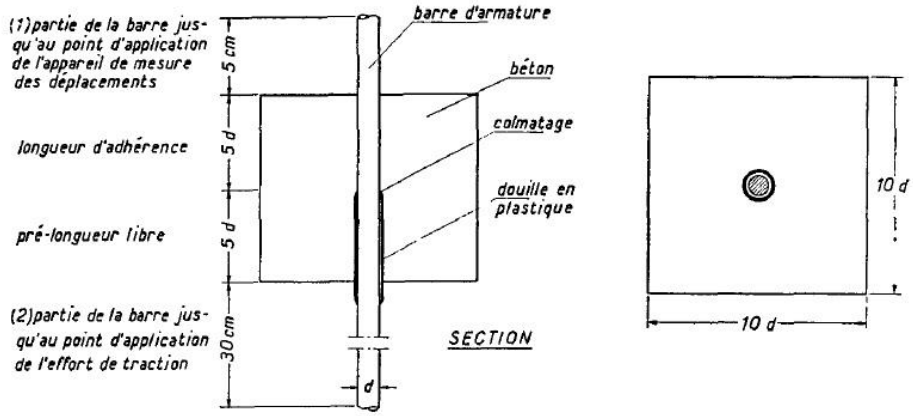

Figure A. 3 RILEM/CEB/FIB Pull-out test specimen (1973)

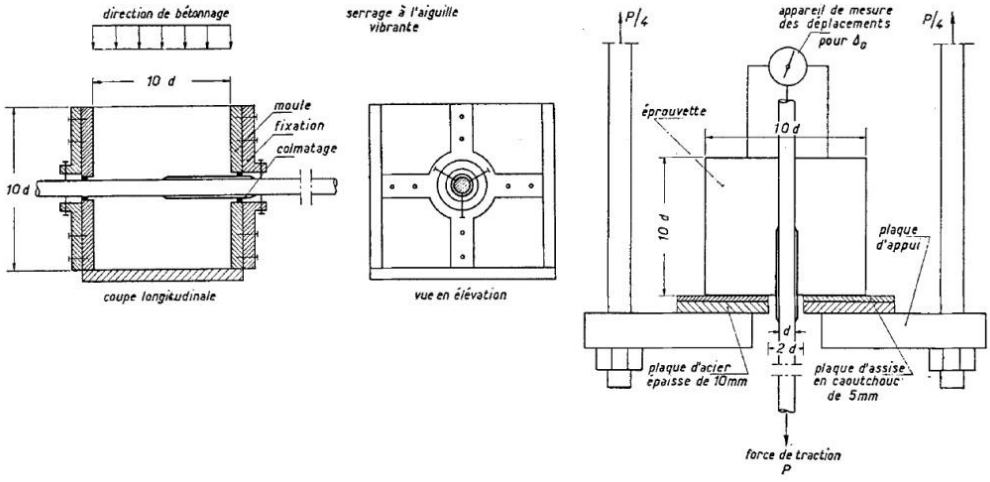

Figure A. 4 RILEM/CEB/FIB Pull-out test apparatus (1973)

A.1.1.4 Pull-out test by Hungspreug

Hungspreug (1981) tested 54 standard concrete cylinder pull-out tests as shown in Figure A. 5 with short embedment bar to investigate the impact of parameters, such as confinement,

bar geometry, load history, internal and surface cracking. The test results show that confining pressure increases the peak bond strength, but not initial stiffness. The bond slip and deterioration propagates from ribs near the load end to the free end. The first rib near the load end experiences largest slip and carries most of the load. An ink injection hole was devised in order to track cracks inside specimen. Test specimens include bar with one rib, two ribs and three ribs. Two and three ribs bar have similar behaviour, both exhibit higher bond strength in comparison with one rib bar.

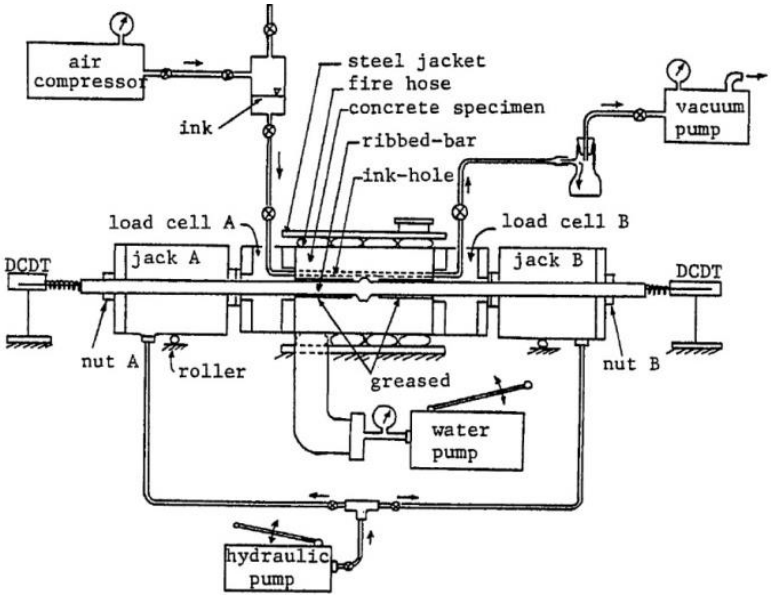

Figure A. 5 Pull-out test setup by Hungspreug (1981)

A.1.1.5 Pull-out test by Eligehausen

Eligehausen et al. (1983) conducted comprehensive pull-out tests on 125 reinforced concrete specimens to simulate the confined region of beam-column joint. The bars in these specimens were bonded for a short length (five times the bar diameter) in the middle of concrete blocks containing various amounts of transverse reinforcement. The parameters studied include loading history, confining reinforcement, bar diameter, concrete compressive strength, bar spacing, active transverse pressure and loading rate. Tests results showed more brittle splitting failure when transverse reinforcement is not enough. It has been observed that once the passive confinement reach the minimum value that prevents the specimen from splitting failure, more restraining reinforcement did not improve the bond behaviour (Figure A. 6).

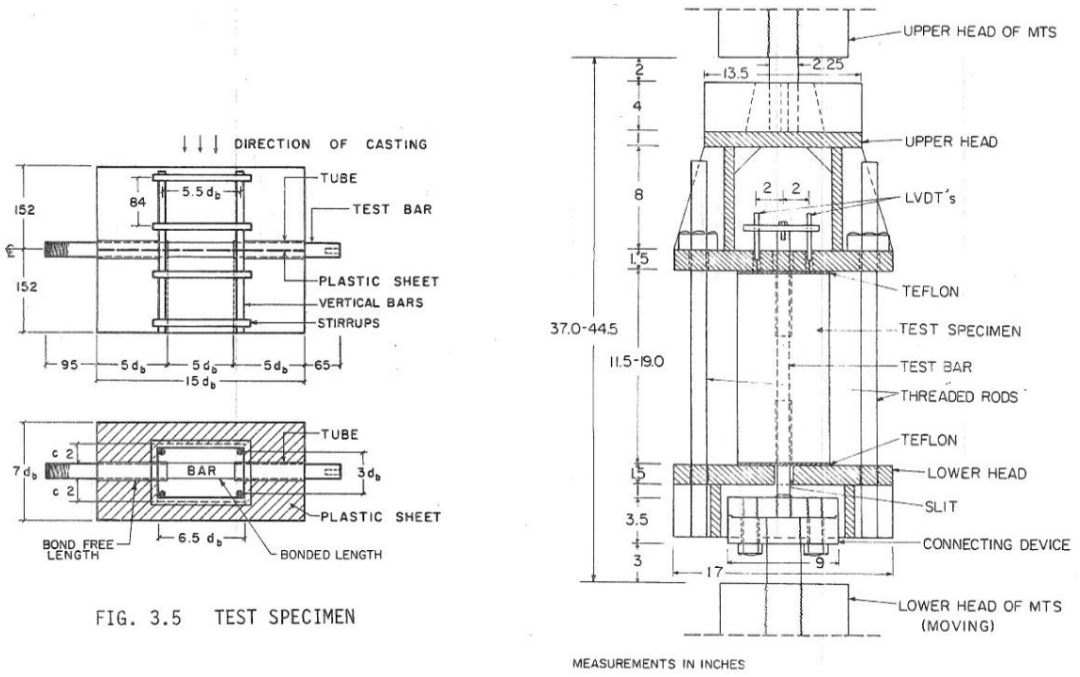

Figure A. 6 Pull-out test setup by Eligehausen et al. (1983)

A.1.1.6 Pull-out test by Shima

Shima et al. (1987) conducted pull-out tests on short and long bar embedment to study the stress strain distribution along the bar and the bond behaviour after the bar yields. The pull-out concrete cylinder had large diameter of 50cm with a 19mm diameter bar in the centre. After bar yielded, the bond stress had sudden decrease and slip was increased. Results showed that the bond stress-strain relation after bar yielded depends on the properties of steel. If the free end slip exists, Bond-slip relationship varies with the location along a bar. Results showed that bond-slip relationship in specimen with short length depends on locations along a bar and it becomes larger at the location closer to the free end. However, if the embedment length is long enough, Bond-slip relationship at different locations along a bar are the same (Figure A. 7).

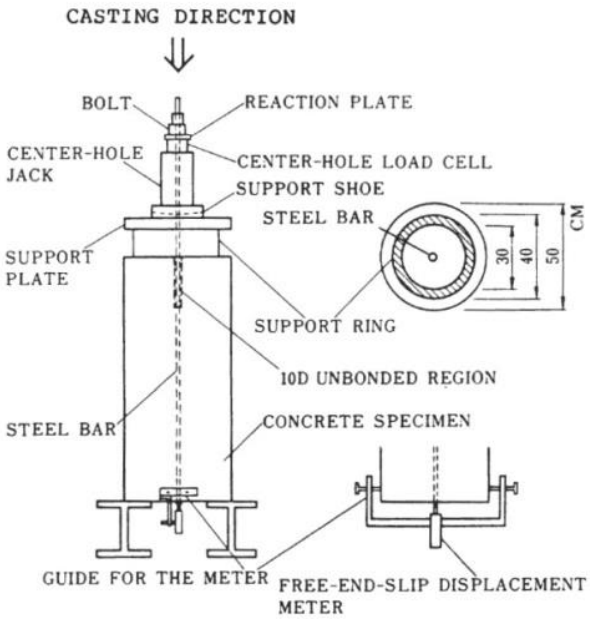

Figure A. 7 Pull-out test setup by Shima (1987)

A.1.1.7 Pull-out test by Rehm

In this type of test, a small load causes a slip and develops a high bond stress near the loaded end, but let the unloaded end be unstressed Ferguson et al. 1988. In reinforced concrete beams or slabs, the concrete surrounding the tensile reinforcement is in tension, whereas the concrete in this test is in compression, which not only eliminates tension cracks in the specimen but also increases the bond strength. In this type of test set-up the specimen is not subjected to external shear or bending moments, which are present in the actual structures. For these reasons, the failure patterns such as splitting or slipping in the pullout specimens are not realistic (Figure A. 8).

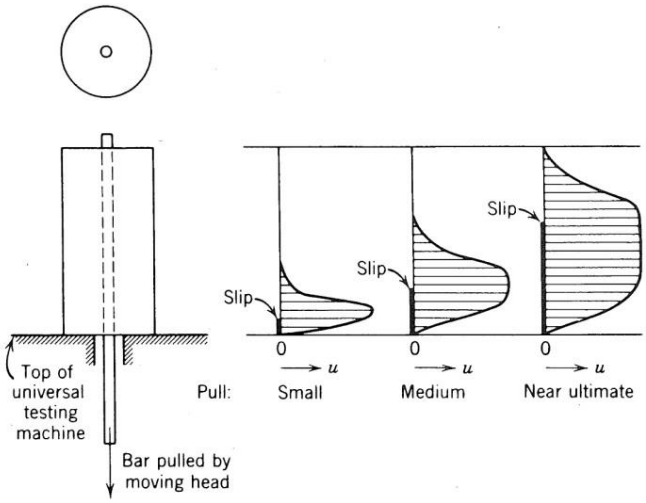

Figure A. 8 Bond pullout test and bond stress distribution (Ferguson 1988)

A.1.1.8 Pull-out test by Malvar

Malvar (1992) also carried out tests on short bonded lengths reinforced concrete specimens with special attention to the role of radial stress and deformation in the bond stress-slip behaviour. He applied different levels of active confinement to examine its effect on the pre- and post-peak bond stress behaviours. Figure A. 9 shows a schematic of Malvar's test set-up.

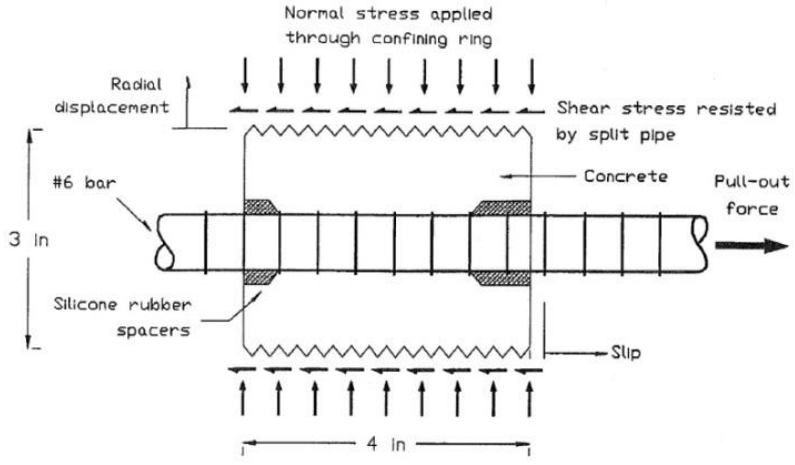

Figure A. 9 Malvar's Bond Test Set-Up (1992)

A.1.1.9 Pull-out test by Mo

Mo and Chan (1996) conducted pull-out tests following the procedure similar to ASTM C234 as it is shown in Figure A. 10. In this kind of apparatus, the bar which is pulled out of the concrete cylinder reacts against a 13 mm thick steel plate with a 25 mm

hole in centre. The steel plate is supported against the moving plate such that the bar passed through the hole is anchored in the fixed jaw (Figure A. 10).

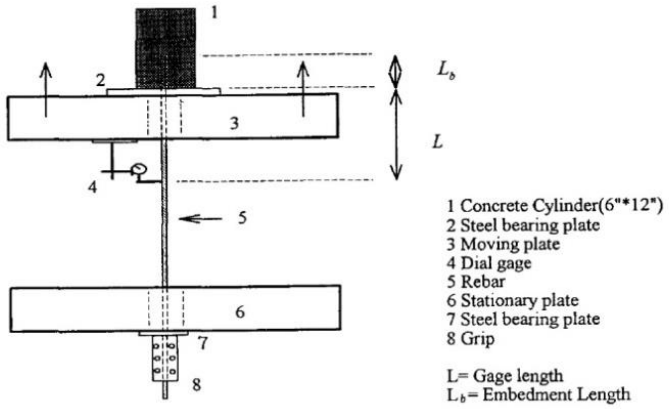

Figure A. 10 Pull-out test setup by Mo and Chan (1996)

A.1.1.10 Pull-out test by Kankam

Kankam 2003; 1997 conducted tests on a prismatic double pull-out specimen (100 ×100 × 200 mm) acquiring transverse anchor bar at the centre of the reinforcement to assure the point of zero slip halfway between two cracks. This configuration was just designed to simulate the actual loading of reinforcement between cracks in a structural concrete member. The load was applied incrementally to each free end of the bar followed by measurement of the overall elongation of the bar relative to the surrounding concrete. Dial gauges were used to measure the extension of the small length of free bar between the concrete face and the reference point in the bar. As a result, the deformation of the bar could be determined (Figure A. 11).

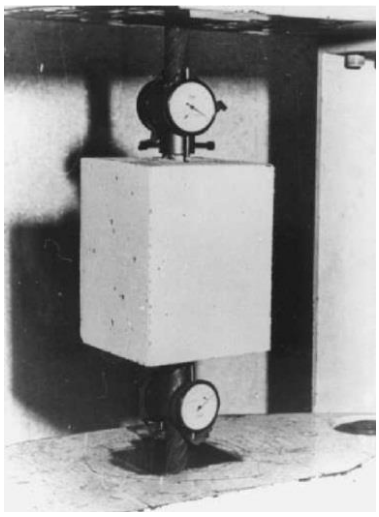

Figure A. 11 Pull-out test set-up by Kankam (1997, 2003)

A.1.1.11 Pull-out test by Soleymani

Soleymani Ashtiani et al. (2013b) conducted 30 force control pull-out test on specimens were casted perpendicular to the direction of the loading. Study showed that confinement ratio of at least 12 is essential in order to prevent splitting tensile cracks in high strength concrete when no other means of confinement are used. It was found that due to the contraction of the steel bar at and beyond yielding, the outward component of the pressure may decrease, resulting in a reduced contribution of macro-friction. Results showed at a given loading level, the average-strain outside the bond-length is far greater than the local-strain inside the concrete. They concluded that once pull-out (including free-end slip) starts, the relationship between slip and strain is no longer unique (Figure A. 12).

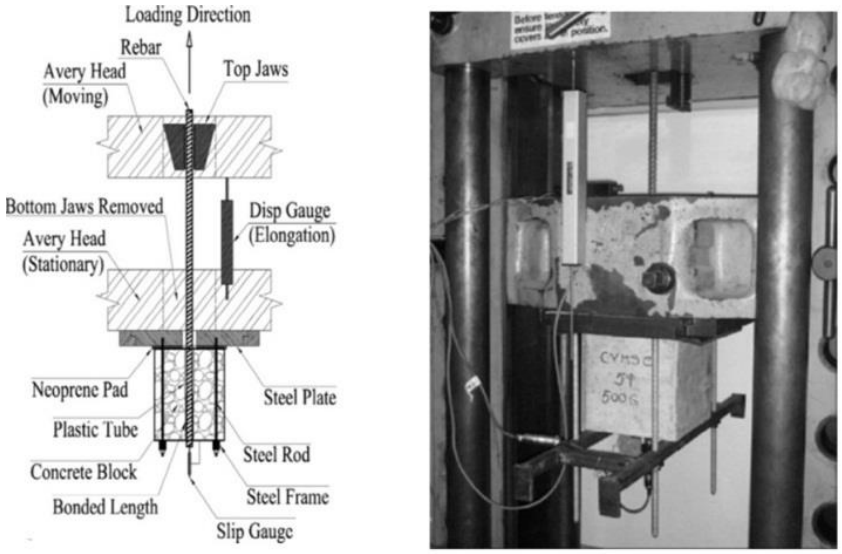

Figure A. 12 Pullout test setup by Soleymani et al. (2013)

A.1.2 Tension/Splitting Tests

Modification to concentric pull out test to eliminate compression on the concrete specimen is called the tension pullout test. However, the interaction between spaced splices and crack pattern introduces problems in this test (Ferguson, 1988). Tension tests are intended to simulate bond-zone conditions within the tension zone of a flexural element. In this case, reinforcing steel carries maximum stress at both ends of a reinforced concrete element and lower stress within the element. If steel stress demands are large enough and bond strength is adequate, tension transferred to the concrete will cause the concrete element to crack. In tension testing, the focus is on the cracking damage patterns on the specimen.

A.1.2.1 Tension test by Broms

Broms (1965) tested a series of long and short tension specimens with different cross sections to investigate the crack spacing and width. A small hole formed by small neoprene hose was designed close the bar and along bar axis. During test, air pressure was applied to the reservoir as shown in Figure A. 13 forcing resin into the very tiny internal cracks. After around 8 hours to let resin get hardened the specimen cut by high-speed diamond saw to study internal tensile cracks by means of a microscope. Study showed the internal crack pattern of reinforced concrete members is frequently different from that observed on the surface of members. To put into details, the crack width measured at the surface of flexural members may be two to three times the crack width close to the reinforcement. He also concluded internal secondary and longitudinal cracks often develop at relatively high loads levels.

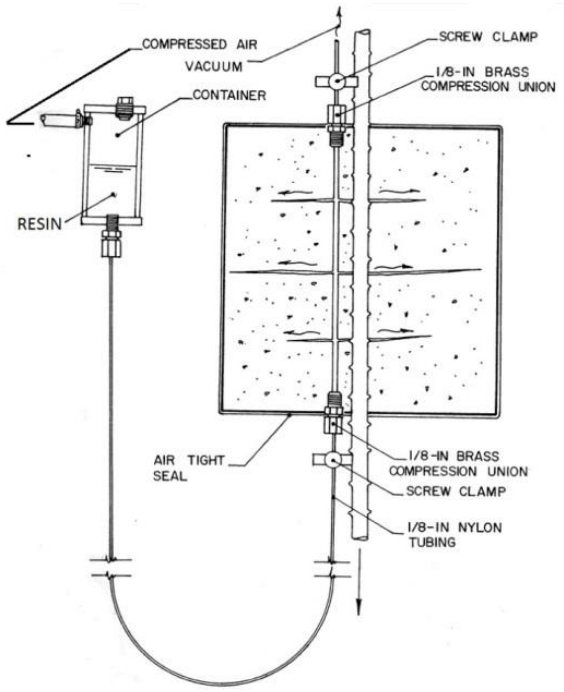

Figure A. 13 Tension test setup by Broms (1965)

A.1.2.2 Tension test by Goto

Goto (1971) designed square cross-section specimens with different ribs configuration to investigate the internal cracking pattern. During test, ink was injected into 4 holes improvised parallel to bars at four corners of the cross-section (Figure A. 14). After test the specimen was cut off and similar findings to Broms observed. Results show regular secondary cracking pattern which is inclined about 60 degree to the reinforcing bar axis.

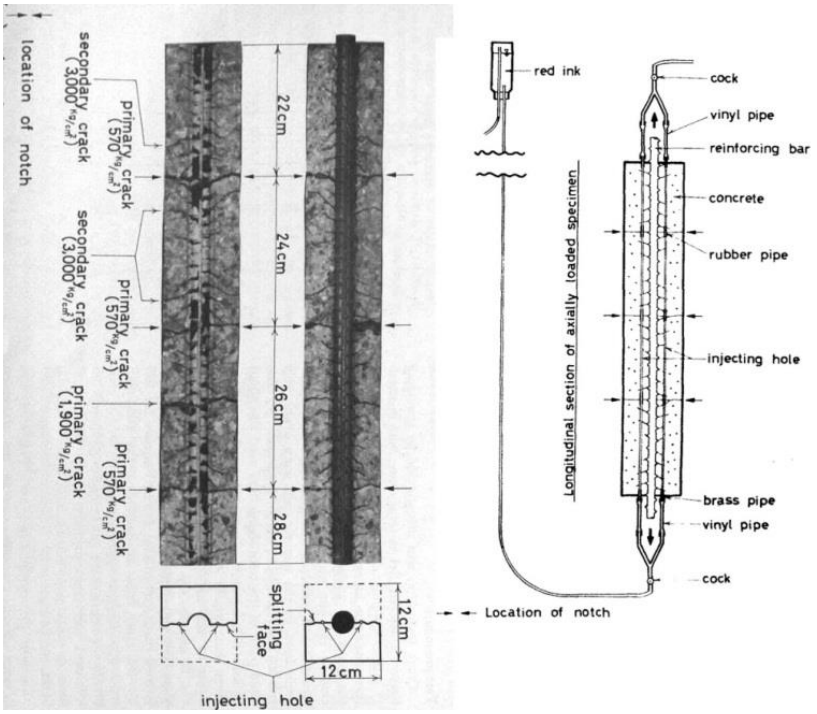

Figure A. 14 Tension test setup by Goto (1971)

A.1.2.3 Tension test by Nilson

Nilson (1972) found that since bond stress and slip for any loading level vary with distance along the bar, establishing a continuous function in terms of distance would be desirable. He stated that bond stress at any location and loading level, is proportional to the slope of steel strain at that point (Figure A. 15). To this end, he designed a novel method to determine bond stress-slip relationship. In this method longitudinal rebar was halved and strain gages were mounted in a trench devised at each half section (Figure A. 16). The method had two key merits. First, no interference with the normal distribution of stresses at interfacial layer was considered. Furthermore, in contrast to other techniques which just measured slip at discrete points, this method captured the slip along the entire interface.

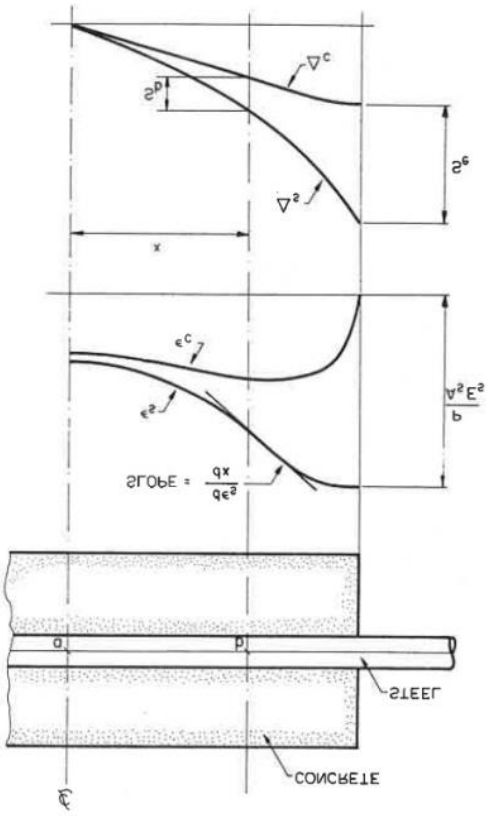

Figure A. 15 Determination of slip from strain distribution (Nilson, 1972)

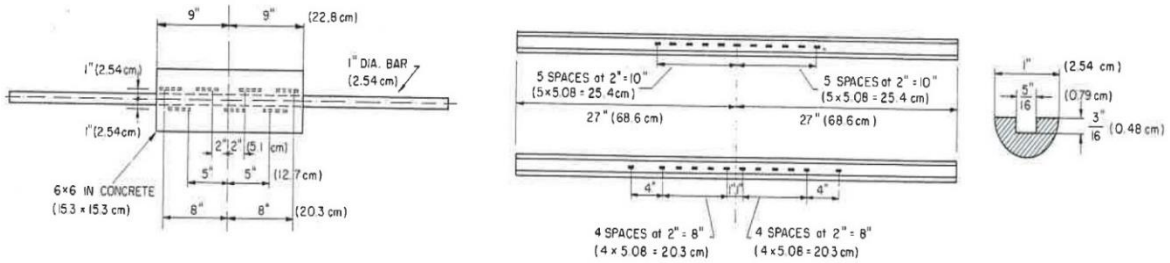

Figure A. 16 Details of tensile test specimen (Nilson, 1972)

A.1.2.4 Tension test by Tepfers

Tepfers (1979) carried out pull-out tests to determine the state of stress in the concrete due to bond forces from deformed bars. Figure A. 17 shows the concrete ring model developed for determination of the cracking resistance of the concrete cover. The specimens had a short bond length and the bond stress was assumed to be evenly distributed.

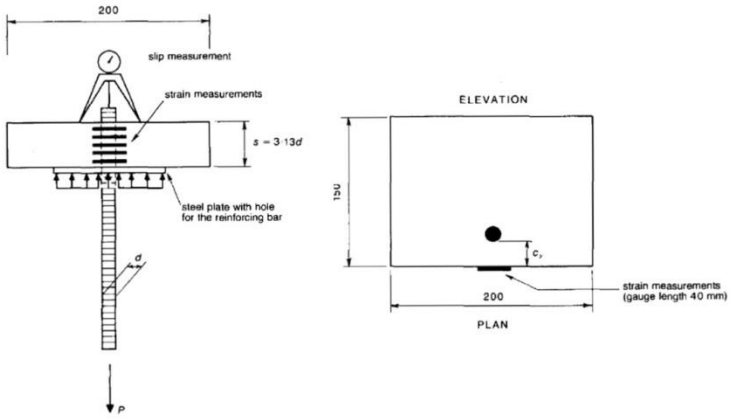

Figure A. 17 Tension test setup by Tepfers (1979)

A.1.2.5 Tension test by Morimoto et al.

In order to investigate the mechanism of the splitting bond failure along column bars during seismic events Morimoto (1984) carried out a total of six column specimens. Specimens had 20 cm^2 cross-section and 80 cm height. Specimens sustained constant axial load of 20 ton as well as lateral load applied by a hydraulic jack simultaneously. Local bond stress-slip relationships measured directly in this study show a great dependency on surrounding concrete and geometrical condition (Figure A. 18).

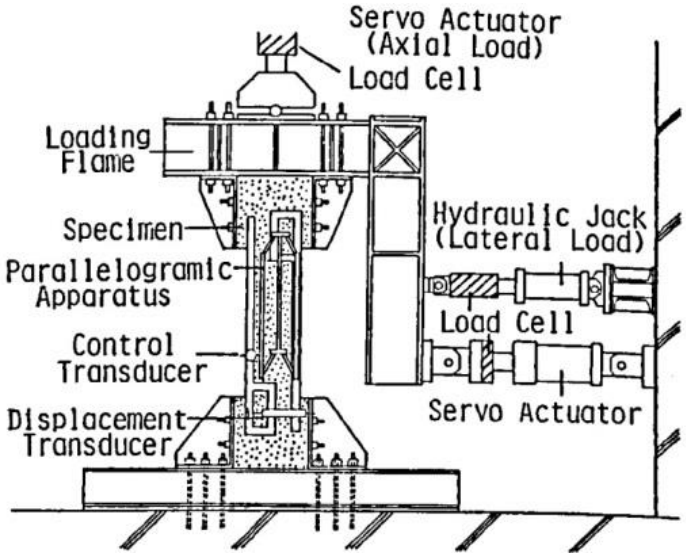

Figure A. 18 Test setup by Morimoto et al. (1984)

A.1.2.6 Tension test by Chana

Chana (1990) implemented a test method to determine the bond strength of reinforcement. The test was designed in a way that 4 parallel rebars were placed close to each

corner of a rectangular concrete prism as shown in Figure A. 19. This type of specimen allowed the bond strength to be directly compared for both a top cast and bottom cast condition. The test set up is shown in Figure A. 20.

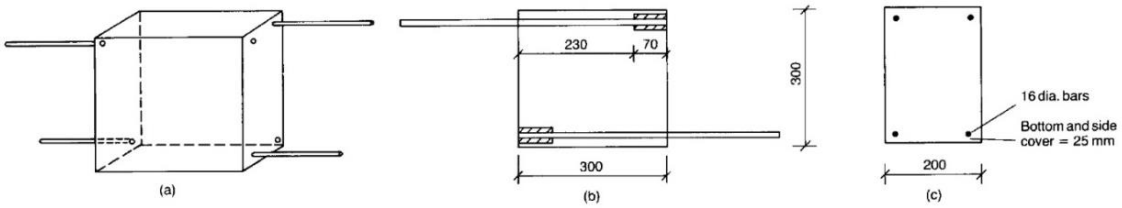

Figure A. 19 Chana Four Corners Specimen (1990)

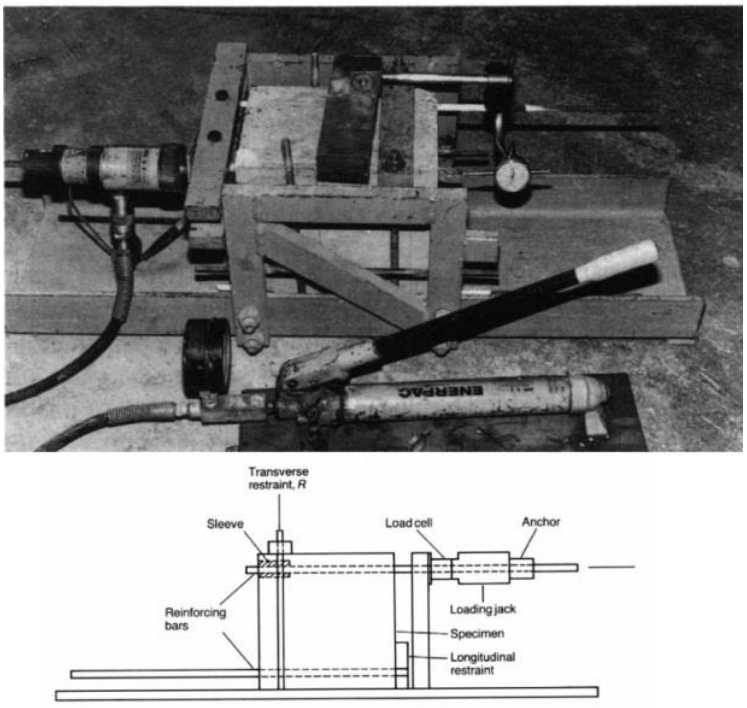

Figure A. 20 Test arrangement (Chana, 1990)

A.1.2.7 Tension test by Gambarova and Rosati

To evaluate the influential parameters affecting splitting in addition to the load, Gambarova and Rosati (1996) conducted bond tests using a pre-split specimen shown in Figure A. 21. The specimens had a predefined "splitting" crack provided by placing some dividers alongside the bar in the formwork. The bond tests were carried out by forcing the crack opening to remain constant throughout the whole loading process. The mechanical machine test and confinement cell is illustrated in Figure A. 22.

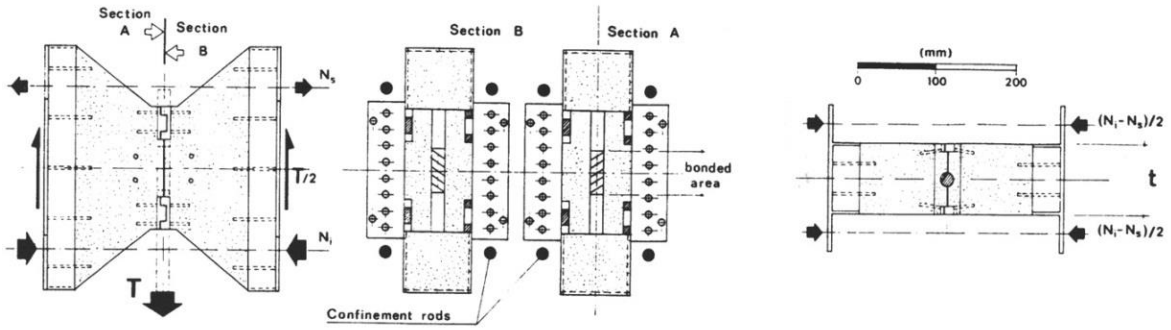

Figure A. 21 Presplit Specimen Used by Gambarova and Rosati (1996)

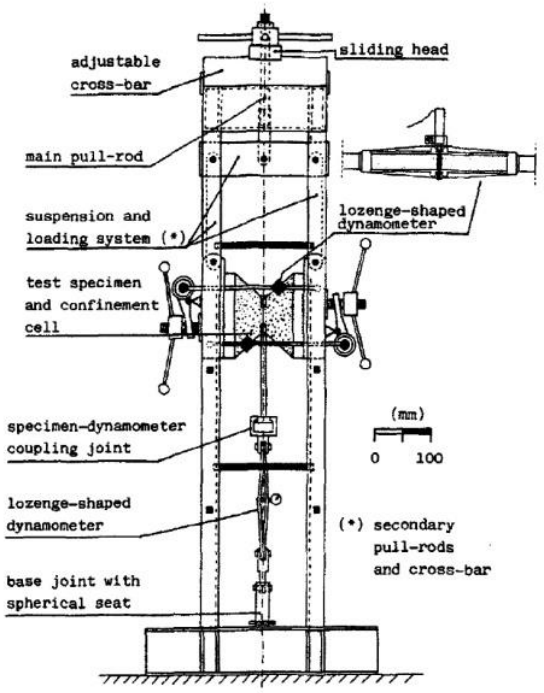

Figure A. 22 Mechanical machine test and confinement cell by Gambarova and Rosati (1996)

A.1.3 Beam Tests

This category of bond test comprises specimens which represent the structural situation as closely as possible since the concrete surrounding the anchorage can carry tension and shear.

A.1.3.1 Beam tests by Snowdon

Snowdon (1970) studied the standard American beam test which is illustrated in Figure A. 23. The specimen presents crack propagation under the load point, and the results of the test were obtain in terms of bond stress-slip curves.

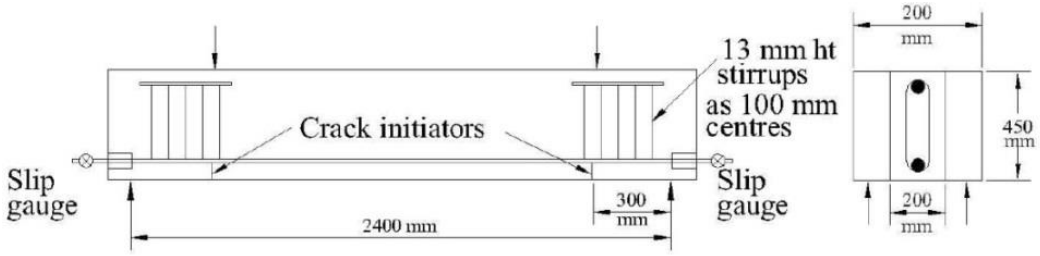

Figure A. 23 The Standard American beam test tested by Snowdon (1970)

A.1.3.2 Beam tests by RILEM

This test employs a beam specimen consisting of two parallel RC blocks, interconnected to each other through a rebar passing from one segment to another at bottom and steel hinge at top. Specimen is subjected to two equal concentrated forces at mid span to sustain simple flexure. During loading up to failure, the slip of the two ends of the rebar is measured (Figure A. 24).

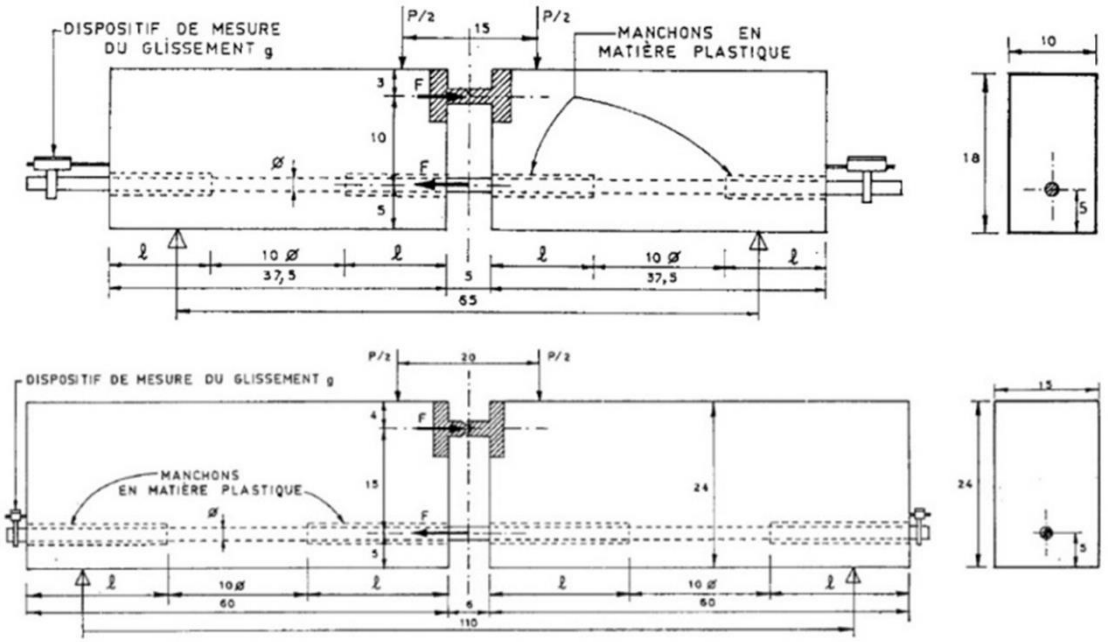

Figure A. 24 Beam test setup proposed by RILEM (a) for bar size less than 16mm (b) for bar size greater than 16mm

A.1.3.3 Beam tests by Roberts

A modified beam test, based on ACI Committee ACI , was proposed by Roberts (1973) and it is shown in Figure A. 25. The supports of the beam were adapted to avoid problems of shear.

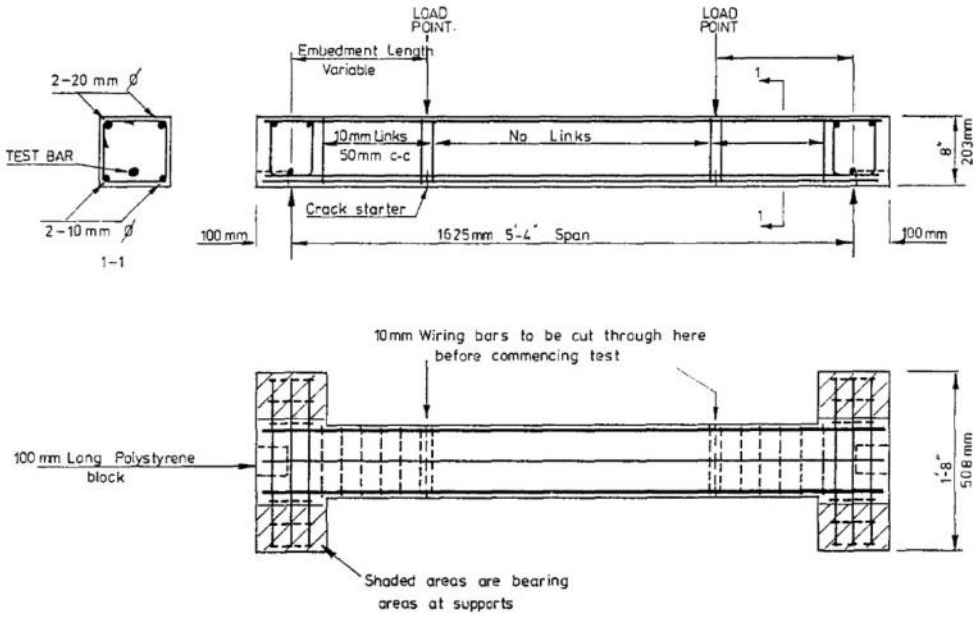

Figure A. 25 Modification of American type of bond test beam (Roberts, 1973)

A.1.3.4 Beam tests by Ferguson

The results of this type of test are considered more reliable because the tests truly represent the actual bond stress conditions encountered in the flexural members. However, the major concern in the bond beam test is the reaction restraint that might increase the confining of the concrete over the bar at the supports by increasing the splitting resistance Ferguson et al. 1988 (Figure A. 26).

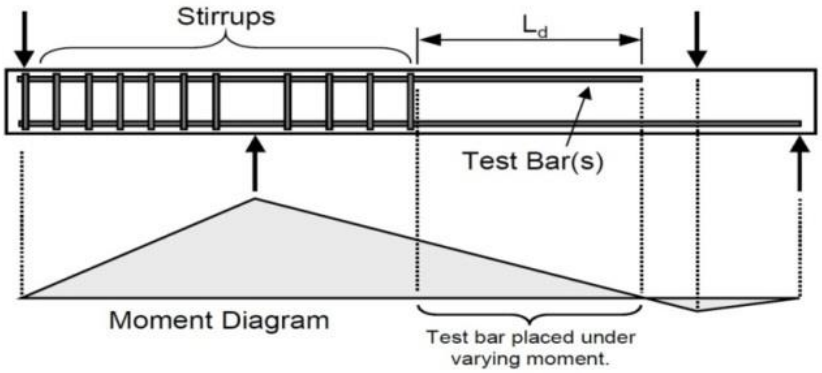

Figure A. 26 Bond beam test- University of Texas redraw by (Thompson et al. 2002) from (Ferguson, 1988)

A.1.3.5 Beam tests by Kemp

This test was developed by Kemp 1979; 1968 to overcome some of the disadvantages in the pullout test. This test produces bond stress situations similar to those existing along tensile reinforcing bars in flexural members. As opposed to the traditional pullout test, concrete and steel experience similar tensile strains and, in addition, cantilever test bond stresses are more representative of actual bond stresses in beams because both external shear and bending moment are present in the test specimen (Figure A. 27).

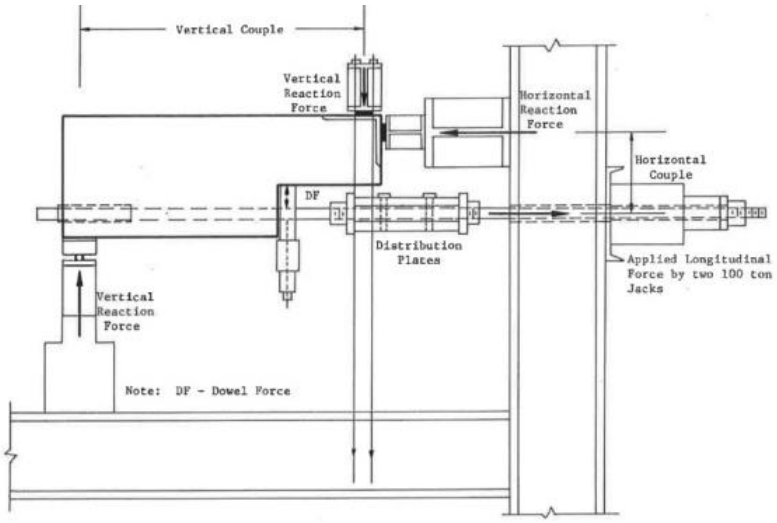

Figure A. 27 Schematic bond test (Kemp, 1979)

A.1.4 Semi-beam Tests

A compromise specimen between a pullout test and a beam test is the stub-beam or beam-end specimen. Figure A. 28 shows a typical beam-end specimen. Only the end region of the beam is fabricated for such a test. Less material is necessary than for a full beam test and the exposure of the bar for loading simplifies the readings of the bar force. Direct compression of the concrete near the loaded end of the bar is avoided by separating the load ram from the surface of the specimen. Access to the bar's free and loaded ends is available for slip measurements. The beam-end specimen was recently standardized in ASTM A944 . The main disadvantage of the beam-end test is the complexity of load arrangement.

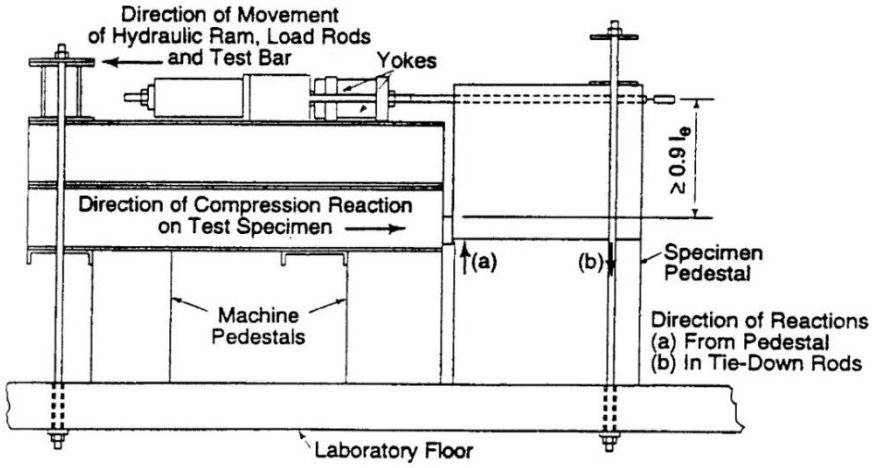

Figure A. 28 Typical beam-end test (ASTM A944-2010)

A.1.5 Cyclic Tests

As pullout tests are handicapped to monitor cyclic behaviour of bond stress-slip. Eligehausen et al. (1983) described cyclic bond behaviour comprehensively. For the loading cycle OA , the response is similar to monotonic curve. After unloading (AF), a gap remains with a width equal to the slip at point F as only the small portion of the slip caused by elastic concrete deformation is expected to be recovered. Once further slip in the reverse direction is applied, frictional strength is motivated. At H the lug is again in contact with concrete, however a gap has opened at the right side of the lug. A significant rise in stiffness of hysteretic curve (HI) is expected due to the concrete blocking. With increase in loading, the old cracks close, letting the transfer of compressive stresses across the crack. Inclined cracks will open when the negative bond stress keep rising, leading to joining of old and new cracks. Figure A. 36 illustrates this process.

A.1.5.1 Cyclic Tests by Ismail & Jirsa

Ismail and Jirsa (1972) investigated the behaviour of twenty cantilever beam specimens under cyclic and repeated cycles to failure. Steel rebar were anchored into the enlarged end stub supported on a concrete pedestal sustaining constant normal pressure to simulate beam-column joints conditions. Load cycles were considered in a range of 5 to 10 times the end deflection at yield. Results showed that under repeated loads, stresses and bar elongations increased gradually; however under reversed cyclic loads elongations increased drastically.

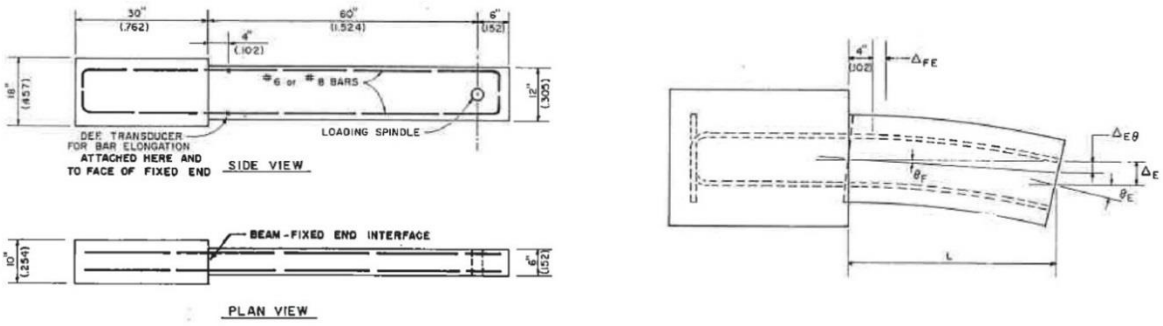

Figure A. 29 Cyclic test on cantilever beam (Ismail and Jirsa, 1972)

Study exhibited that stress distribution did not change remarkably under reversed loading. It was found that in the case of specimens in which shear or large flexural deformation cause beam to be softened, bar elongation decreases with the number of cycles. Under reversed loads elongation of the anchored bars contributed up to 60% of the end deflection of the beam, while for monotonic loading the elongation of the anchored bars contributed between 30 to 45 percent of the total end deflection of the beam. Although the stress distribution and depth of yield penetration did not exhibits large changes with increasing number of cycles, the bar elongation varied considerably. It was observed that when cyclic protocol is being continued to a specified end deflection, the softening of tensile steel or compression zone of the beam occurs, affecting structural response.

A.1.5.2 Cyclic Tests by Morita and Kaku

Morita and Kaku (1973) studied the role of bond in the behaviour of RC structures under load reversals. The test consists of five rebar embedded in short RC beam in a vertical position. The bond zone was located at mid-height of the beam to avoid the influence of the flexural stress of the beam (Figure A. 30). It was found that the deterioration of the local bond stress depends on the magnetite of the previous maximum local slip such that the larger the previous slip, the greater reduction in the bond stress at lower slip levels.

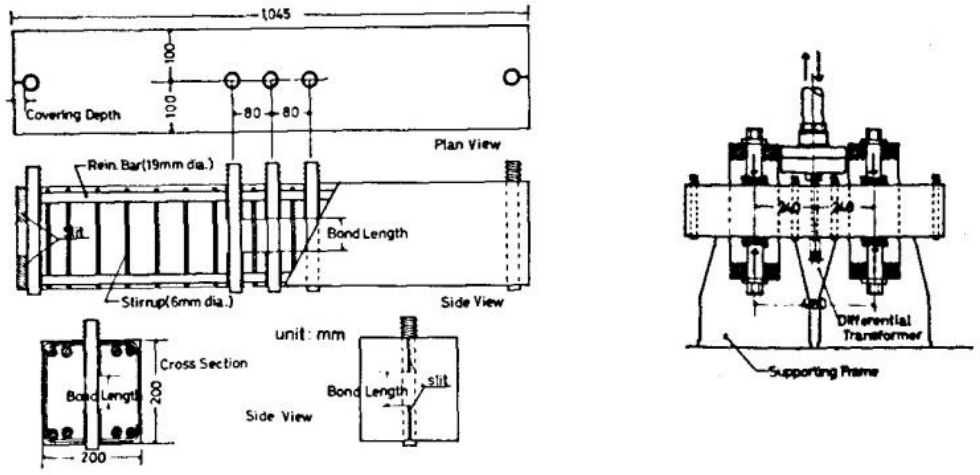

Figure A. 30 Test specimen and loading arrangement (Morita and Kaku, 1973)

A.1.5.3 Cyclic Tests by Balazs

Balazs (1989) studied the bond behaviour 60 pullout specimens subjected to cyclic loading. Tensile forces were alternatively applied at 2 opposite end sections. During first cycle the response is the same as for monotonic loading. It was observed that, the first negative half cycle shows a 7% softening of the bond stress at loaded end and 10% softening at unloaded end. In slip control the max bond stress decrease asymptotically. In other words, bond softening is characterized by a decrease in max bond stress.

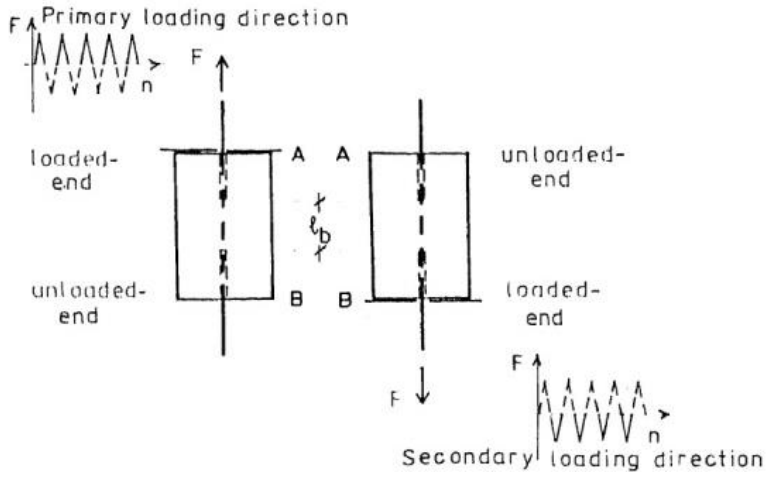

Figure A. 31 Test specimen and loading protocol (Balazs,1989)

A.1.5.4 Cyclic Tests by Balazs and Koch

Balazs and Koch (1995) investigated the bond behaviour under reversed loading tests within three conditions. The results of the constant stress loading, presented in Wohler diagram showed that fatigue strength could be achieved in lower values for the reversed cyclic

conditions in comparison with repeated loadings. Study indicated that bond action experiences the most deterioration under reversed cyclic loadings. This mainly is attributed to the peak slip in each direction reached in previous excursion. Number of load cycles and the amplitude of cycles also affect bond degradation rate. Pull-out of the reinforcing bar or 2×10^6 full cycles are considered as the technical limits during test. Results showed no sign of degradation during force control protocol, while for displacement control a significant decline could be found (see Fig. 11-36)

A.1.5.5 Cyclic Tests by Raynor et al.

Raynor et al. (2002) studied cyclic bond behaviour of reinforcing bars grouted in ducts to put forth deeper insight into seismic response of precast concrete joints. Tests were run in a MTS machine through applying 10 cycles of designated displacement and then the specimen was pulled out monotinically to failure. Results showed that the characteristics of the cyclic displacement histories, and the pre-yielding condition have significant influence on bond-slip. The envelope of the cyclic response is similar to the monotonic curve but, for a given slip, the cyclic bond stress is smaller than the monotonic one. (10 % for slips below u_{peak} but up to 70 % for slips greater than u_{peak}). No cracking was found in the body of the grout cylinder, but the grout surronding the bar suffered significant crushing. That crushing caused voids around the bar. This behaviour is in contrast with Goto (1971) as he observed extensive pattern of radial bond cracks emanating from bar lugs.

A.1.5.6 Cyclic Tests by Li et al.

Li et al. (2007) experimentally investigated the bond behaviour in high performance concrete (HPC) under cyclic loads. The effective bond lengths of these specimens were 4d (d is the diameter of the bar. To obtain the descending branch of the bond stress–slip relation curves, two stirrups with tensile yield strength 235 MPa and diameter 6 mm were laid in the specimens with a space of 30 mm in the molds to avoid splitting abruptly. The specimens used in this program had a prismatic shape with dimensions 154×154×166 (or 188) mm^3, as shown in Figure A. 32.

Figure A. 32 Test setup and instrumentation (Li et al., 2007)

A.1.5.7 Cyclic Tests by Verderame et al.

Verderame et al. (2009) investigated the cyclic behaviour of bond in plain bars. To assess the bond slip relationship, five cycles for each intended slip value of 0.5, 2.0, 4.0 and 8.0mm were applied to the specimen in a pullout test apparatus (Figure A. 33). The displacement rate of the test was equal to 0.01 mm/s. It was found that due to poor bond performance and reduced embedment length, the maximum value of the tension experienced during the tests, both in tension and in compression, is less than third of the yielding stress. In other words, results are just applicable for the bond mechanisms of plain bars that develop in the elastic field.

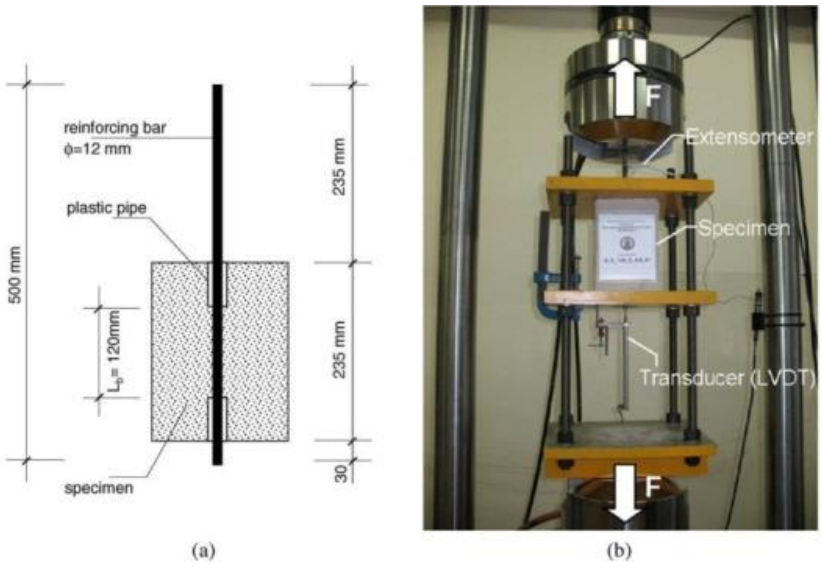

Figure A. 33 Geometry of the pullout test (a) and test setup (b) (Verderame et al., 2009)

A.1.5.8 Cyclic Tests by Murcia-Delsoet et al.

Murcia-Delso et al. (2013) studied the bond strength and cyclic bond deterioration of large diameter reinforcing bars embedded in well-confined concrete. Two types of cyclic reversals were considered; full cycles with the same slip amplitudes in both directions for each cycle, and half cycles with slips mainly in one direction and slightly passing the origin in the other.

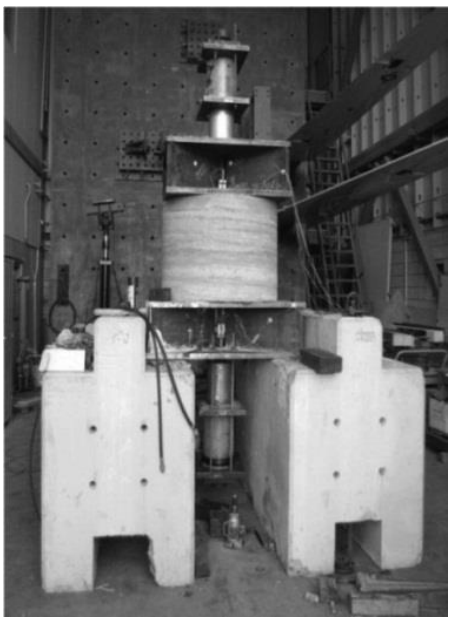

Figure A. 34 Test setup (Murcia-Delsoet et al., 2013)

A.1.5.9 Cyclic Tests by Soleymani et al.

Soleymani Ashtiani et al. (2013a) designed a beam specimen originally proposed by RILEM for assessing of bond properties under monotonic flexural loading. Test set up arranged such that apparatus could stand for displacement reversals without premature buckling of the bar. The incremental displacement loading protocol was applied through an actuator located in the mid span of experiment (see Fig. 11-47). Each cycle was repeated three times in order to account for the effects of loading reversals on bond strength.

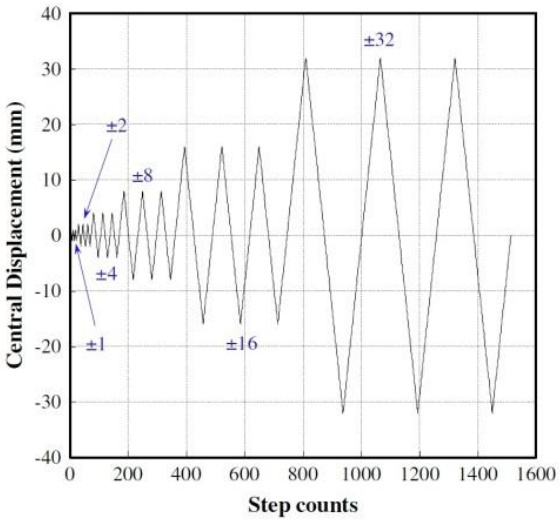

Figure 0-1 Displacement protocol applied to the centre of the beam specimen (Soleymani, 2013)

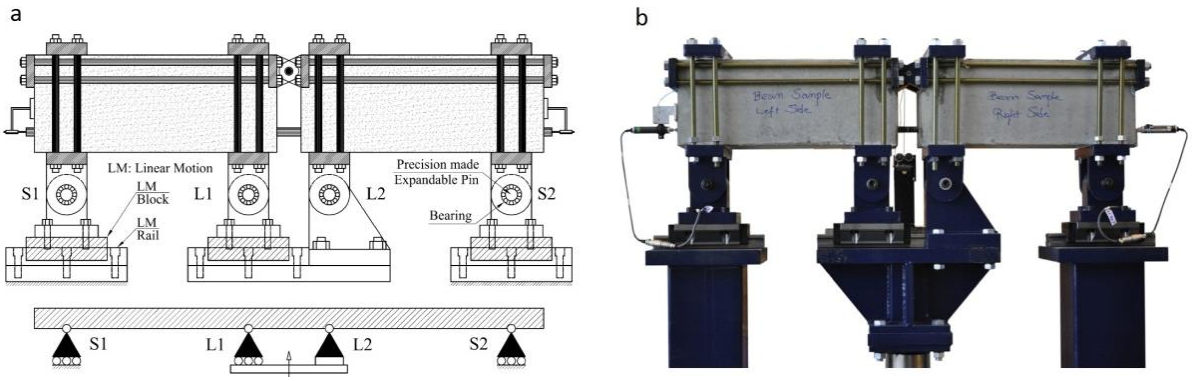

Figure A. 35 Details of the modified RILEM cyclic test beam (a) schematic (b) lab experiment (Soleymani, 2013)

A.1.6 Repeated tests

In this kind of tests the sign of loading does not change meaning that amplitude increases from zero to peak value and again comes to zero. Bond strength decreases strength with increasing number of cycles. If no fatigue failure of bond occurs during repeated loading and

load increased afterwards, the monotonic envelope is reached again and followed thereafter Rehm and Eligehausen 1977.

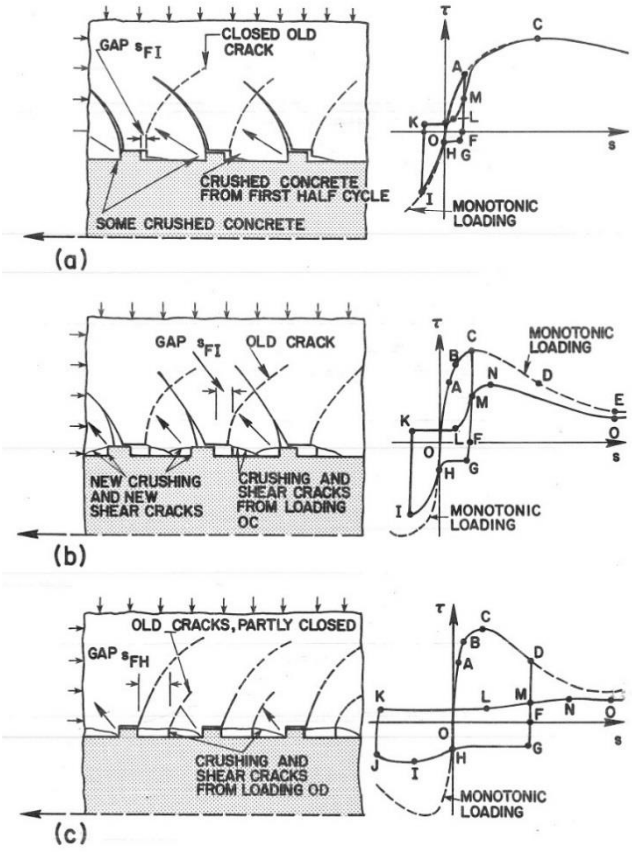

Figure A. 36 Mechanism of cyclic bond behaviour Eligehausen et al. 1983

A.1.6.1 Repeated tests by Perry & Jundi

Perry and Jundi (1969) studied the effect of the repeated loadings on the distribution of bond stress in eccentric pullout specimens. Around 500-1000 sinusoidal loadings cycles with amplitude equal to 56% of ultimate load applied with a frequency of 5 cycles per min for both static and dynamic rates. The repeated loading was increased to nearly 80% of ultimate load in case of no significant change in the force distribution. If no change in distribution of forces was monitored, the load was surged until failure happened (Figure A. 37).

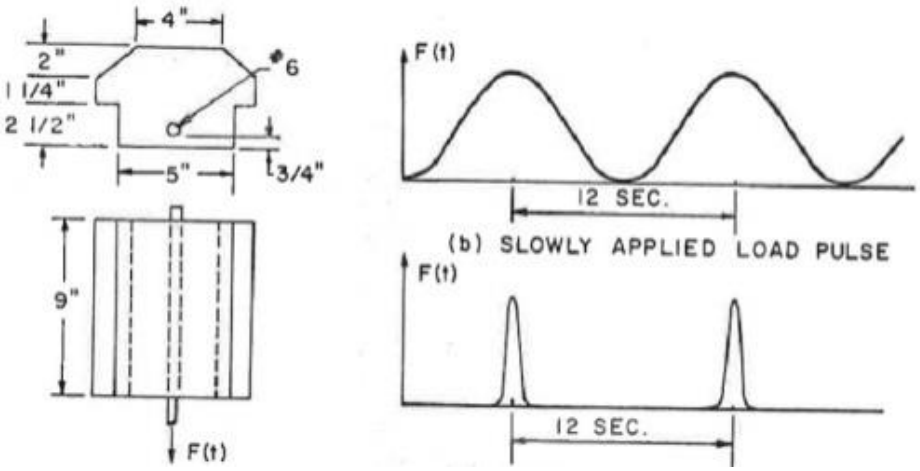

Figure A. 37 Specimen geometry and loading protocol (Perry & Jundi, 1969)

A.1.6.2 Repeated tests by Edwards & Yannopoulos

Edwards and Yannopoulos 1978; 1979 conducted some repeated loading test in which nine load cycles of constant amplitude, followed by monotonic loading to failure were imposed to 38 mm embedment length pull-out specimens (Figure A. 38). Three different loading regimes corresponding to bond stress of 2.0, 3.9 and 5.6 N/mm2 were considered to investigate degradation of bond under repeated loadings. To obtain more general results, each test was repeated for four times.

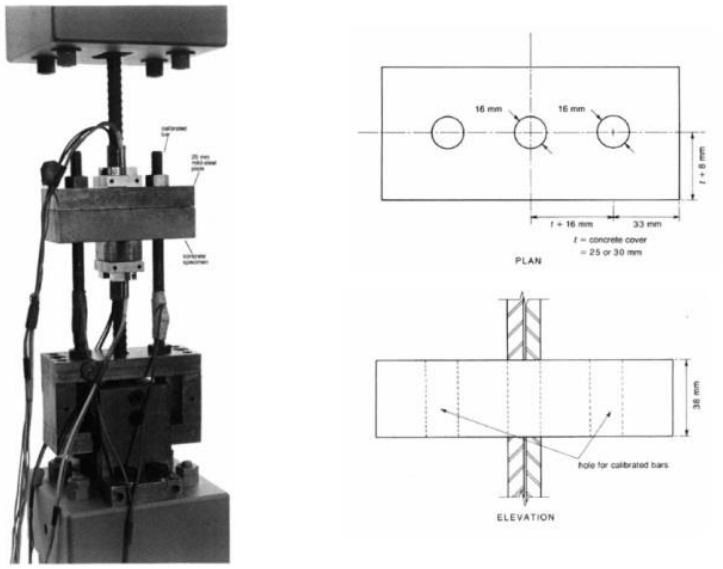

Figure A. 38 Test set up apparatus by (Edwards & Yannopoulos, 1978)

A.1.6.3 Repeated tests by Rehm & Eligehausen

Rehm and Eligehausen (1979) conducted experimental tests on 308 specimens to understand how many load cycles as a function of the maximum and minimum load are possible before fatigue failure of bond. If after 10^6 load reversals no failure ocurred, the specimens were loaded similar to static way to failure. Figure A. 39 shows specimens specifications.

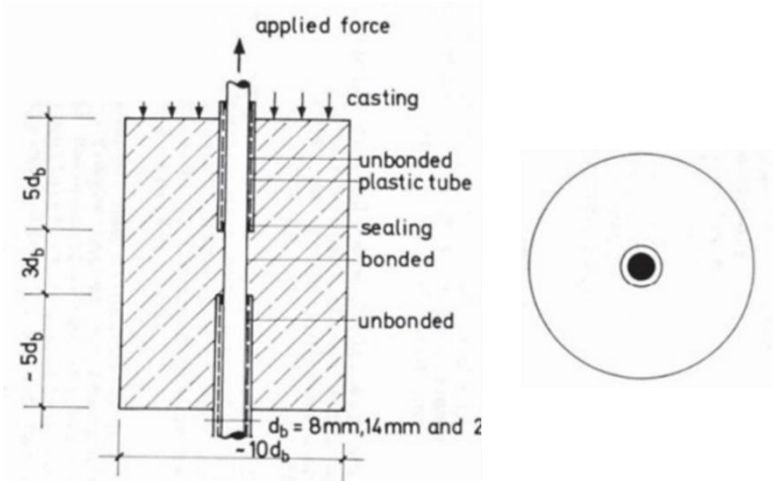

Figure A. 39 Test specimen (Rehm & Eligehausen, 1979)

A.1.6.4 Repeated tests by Balazs and Koch

Balázs (1986) studied the effect of repeated loading on bond behaviour. Study showed although the effect of repeated load on bond is only one of the factors, it has a great importance because a pullout failure can occur due to repeated load without applying the ultimate load. Slip increment also depends on the bond length and the parameters of repeated loads. The specimen configuration and test set up are shown in Figure A. 40 and Figure A. 41, repectively.

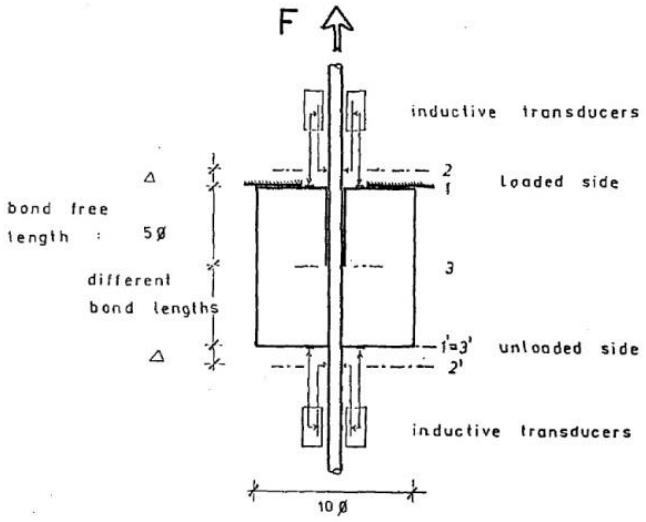

Figure A. 40 specimen with slip measuring system (Balazs, 1986)

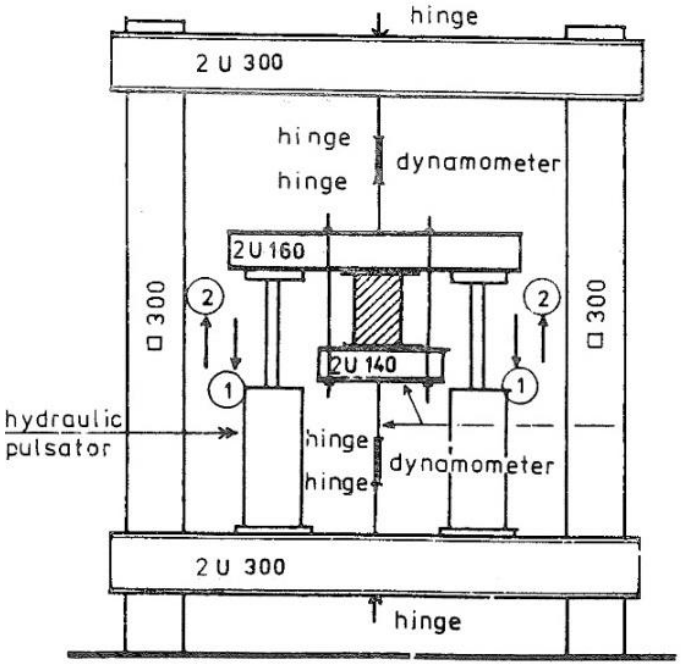

Figure A. 41 Scheme of test setup (Balazs, 1986)

A.1.6.5 Repeated tests by Oh and Kim

Oh and Kim (2007) conducted several fatigue test series to investigate real behaviour of local bond stress-slip of reinforced concrete under repeated loading. The specimens were subjected to pull-out tests after sustaining repeated loading. This serves sufficient data to propose the models on local bond stress-slip relationship under repeated loading. The minimum fatigue load level of 0.107 MPa and maximum fatigue load levels of 0.45, 0.60,

and 0.75 of static pull-out failure loads were imposed through sinusoidal pulsating load with the loading rate of 2 Hz, as shown in Figure A. 42.

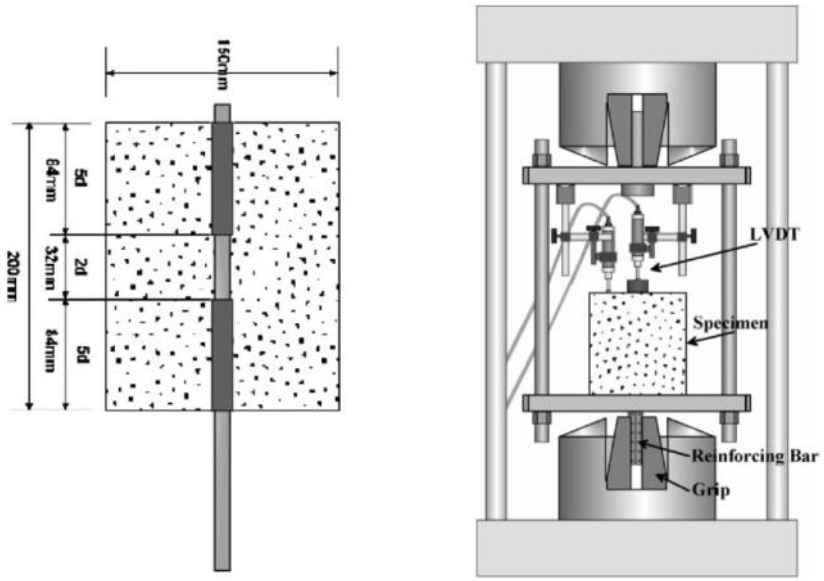

Figure A. 42 Test setup (Oh and Kim, 2007)

A.1.6.6 Repeated tests by Lindorf

Lindorf et al. (2009) experimentally evaluated the bond behaviour under transverse tension and repeated loading. The influence of repeated loads on bond is characterized by increasing slip value depending on increasing number of load cycles. The transverse tensile load required for the longitudinal crack width was introduced by four reinforcing steel bars. He considered the condition described in Model Code 90, saying that one cyclic pull-out test included one million load cycles with an overall duration of 56 h. load spectrum for the bond area was applied in terms of steel stresses σ_s instead of bond stresses. In some cases steel fatigue occurred before bond failure could develop, especially in tests without transverse tension (Figure A. 43).

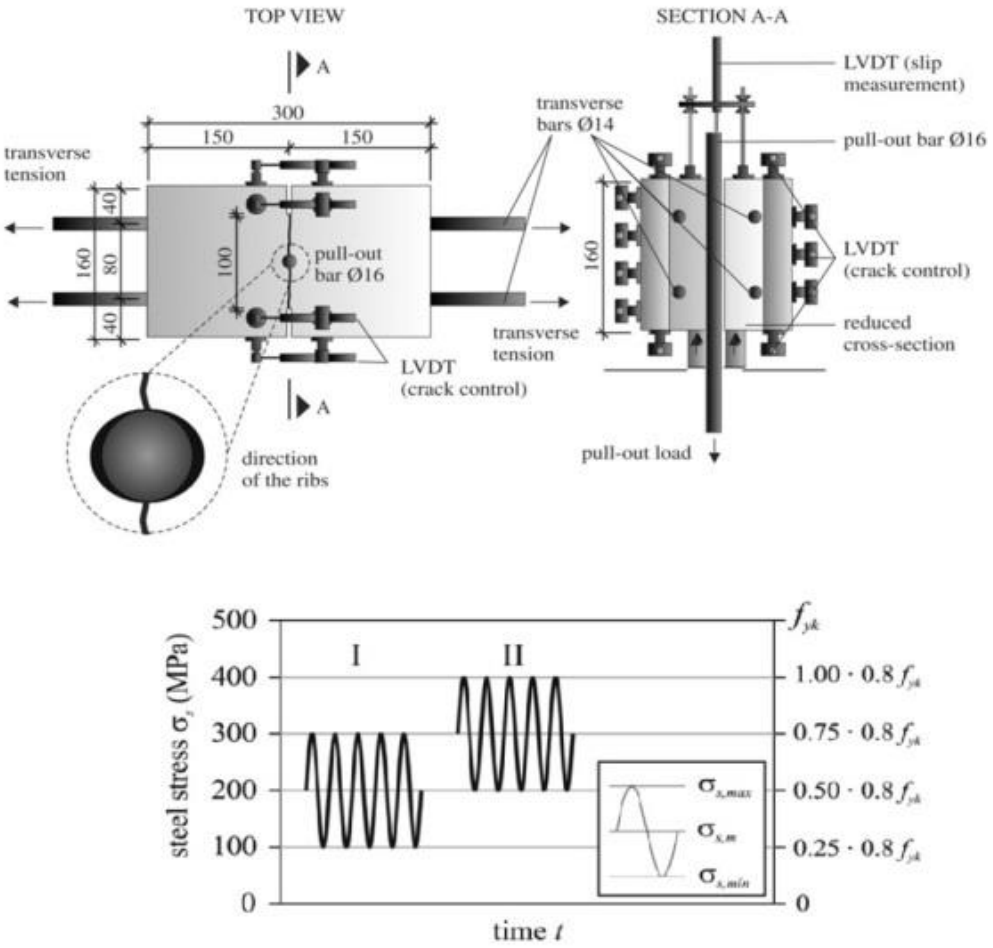

Figure A. 43 Load levels for experimental program and test setup (Lindorf et al., 2009)

A.1.6.5 Repeated tests by Rteil et al.

Rteil et al. (2011) studied the bond behaviour of nine anchorage-beam specimens (250 ×150×2000 mm) under different repeated loading levels (Figure A. 44). The minimum load was kept constant for all fatigue tests at 10% of the specimen's static load capacity while the maximum load was varied to give the desired range of fatigue lives (between 1000 and 1,000,000 cycles). Tests were stopped either when the specimen failed or at 10^6 cycles.

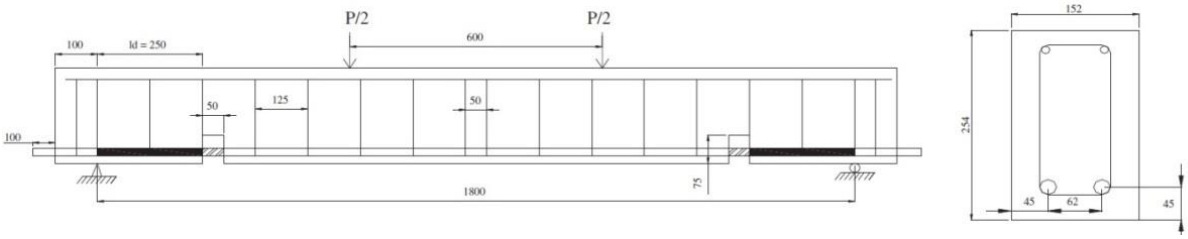

Figure A. 44 Longitudinal and cross-sectional details of the beam-anchorage Rteil et al. (2011)

A.2 Non-destructive methods for bond degradation monitoring

A.2.1 Acoustic Emission

Acoustic Emission is commonly defined as the transient sound elastic waves produced within a material, caused by the release of localized stress energy due to an external force. It is used in monitoring structures or components for flaws. This is done by mechanically loading the item under test either physically or by applying internal pressure to a specimen which forces the flaw to release energy. The released energy is in the form of stress waves that are detected by the AE sensors mounted on the item under test.

Balázs et al. (1993) investigated the implementation of Acoustic Emissions technique in detection of damage in the interface of steel bar and concrete. Results showed that the slip and AE registrations follow similar trends, such that the highest AE amplitudes within a short time interval were recorded in the region of the highest bond stresses. The damage accumulation, defined as the cumulated AE amplitudes against time, has a point of inflexion at about the point where bond strength is reached.

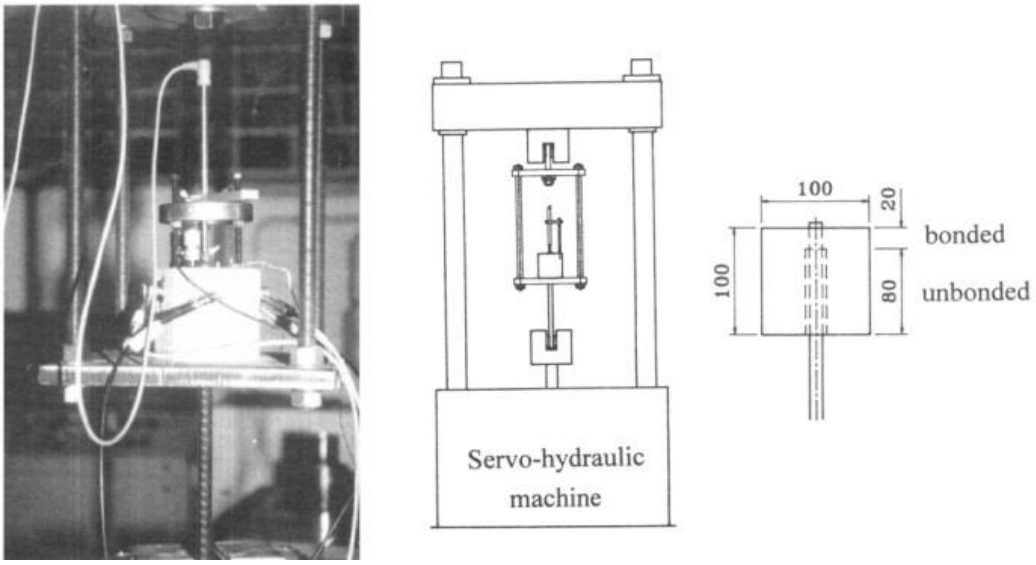

Figure A. 45 (a) Acoustic emission sensors and LVDT (b) test set-up (Balazs et al. 1993)

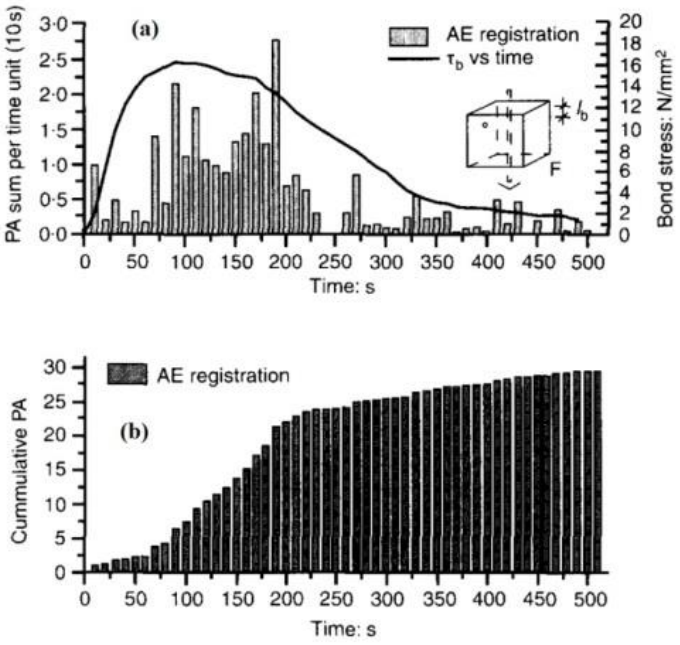

Figure A. 46 monotonic pull-out test with detection of acoustic emission signals (a) Peak Amplitude sums and bond stress against time relationship; (b) cumulative AE amplitudes against time diagram (Balazs et al. 1993)

Figure A. 47 indicates test results under repeated loading of 4 S^{-1} frequency on one load level. Study showed that most of AE signals were recorded during application of the initial monotonic load up to the mean value of the cyclic load and immediately preceding the pull-out failure.

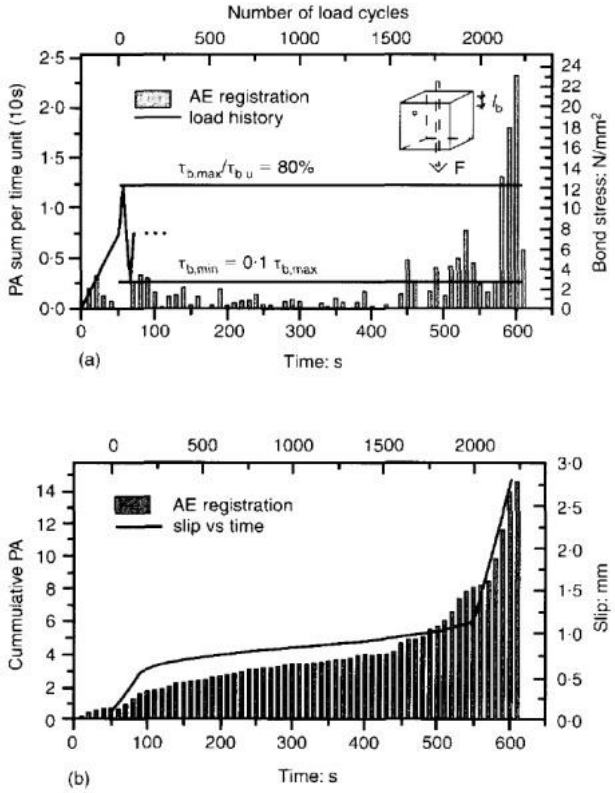

Figure A. 47 cyclic pull-out test with one level of constant amplitude loading (a) PA and bond stress against time relationship (b)cumulative PA against time and slip against time relationship (Balazs et al. 1993)

Test results from Long-tern loading are illustrated in Figure A. 48. Likewise cyclic tests, AE signals were observed not only on reaching the load level but also under the constant load. The damage accumulation also indicates a similar tendency to slip increase.

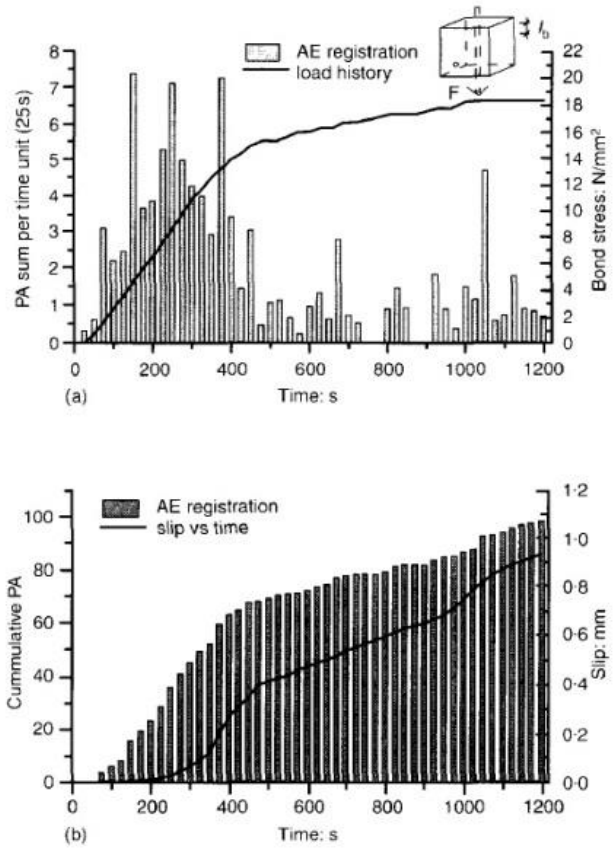

Figure A. 48 long-term pull-out test (a) PA sums and bond stress against time relationship (b)cumulative PA and slip against time relationship (Balazs et al. 1993)

Chiang et al. (2000) utilized a combination of acoustic through-transmission and pull-out tests to evaluate the bond strength between the reinforcement and concrete after fire damage. Results show that bond strength and pulse velocity decreased substantially as the temperature or the heating time increased. They concluded that the decrease in acoustic wave velocity certainly provides some indication of significant loss in bond strength after exposure to elevated temperature.

A.2.2 Piezoelectric Elements

Piezoelectric ceramics have specific electrical-mechanical properties such that they can convert electrical energy to mechanical energy and vice versa. Wu and Chang 2006a; 2006b carried out some experimental tests to find out if piezoelectric elements can be implemented to reveal debonded zone between reinforcement and concrete. Experiments instrumented with piezoelectric disks as actuators and sensors. Actuators and sensors were placed on the bar and the bar was cast into a concrete beam. A five-peak burst ultrasonic wave with a peak value of 200V was applied to the actuators. Five pair beam specimens were constructed with un-

bonded length as well as the zero length as benchmark. As it is illustrated in Figure A. 49 the signals increased with the rise in debonded zone. Test results demonstrated that debonding damage of RC members can be detected using embedded piezoelectric actuators and sensors placed in the RC structures.

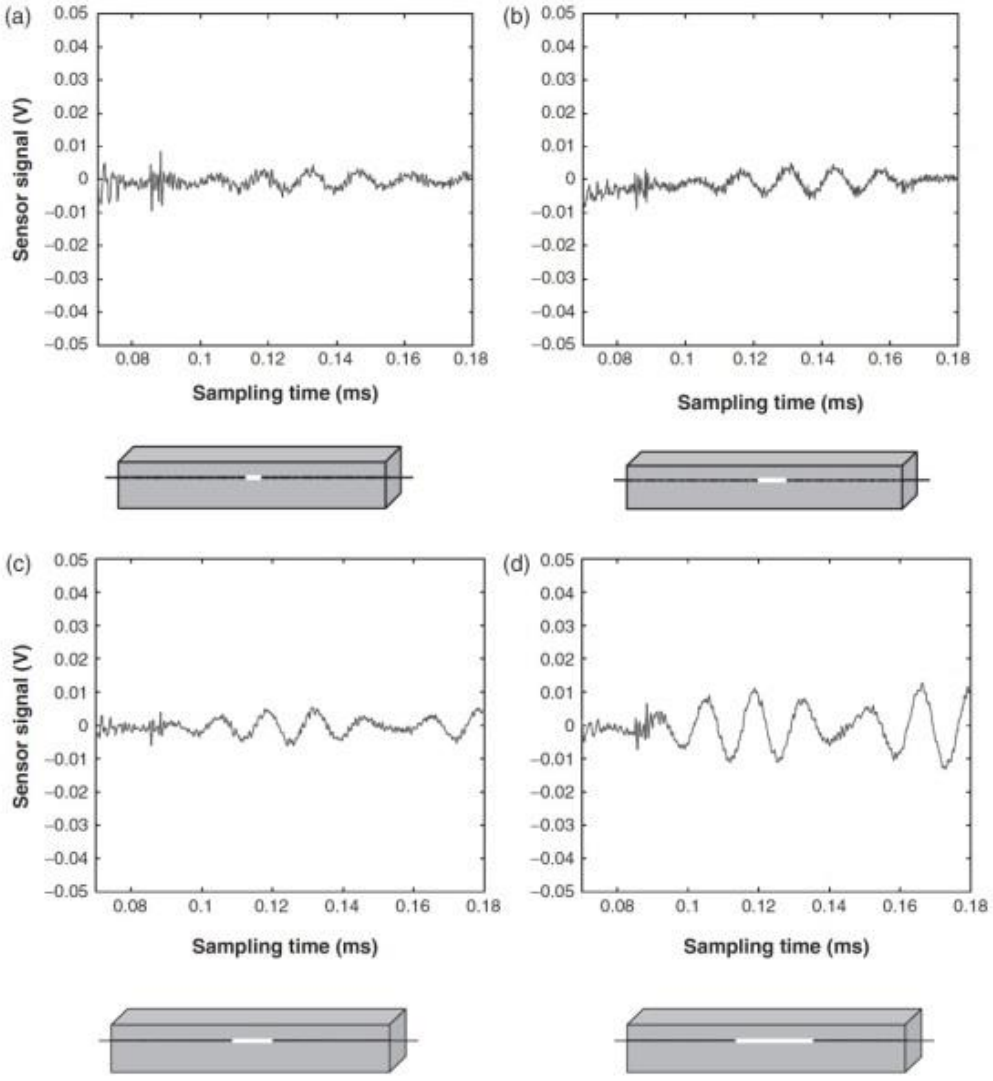

Figure A. 49 Sensors output for different debonded length: (a) 1in; (b) 2in; (c) 3in; 4in; and (d) 8in (Wu and Chang, 2006)

A.2.3 Contact electrical resistance measurement

Fu and Chung (1995) found that the bond strength and contact electrical resistivity are linearly related. The volume electrical resistivity of the concrete at 28 days was obtained by the four-probe method. Each of one current contact and one voltage contact was

circumferentially on the rebar. The other voltage and current contacts were on the concrete embedding the rebar. The total measured resistance between the two voltage probes was the summation of three components; rebar volume resistance, the steel-concrete contact resistance and concrete volume resistance. The volume resistance of the rebar was ignored and the steel-concrete contact resistance was calculated by subtracting the concrete volume resistance (Figure A. 50).

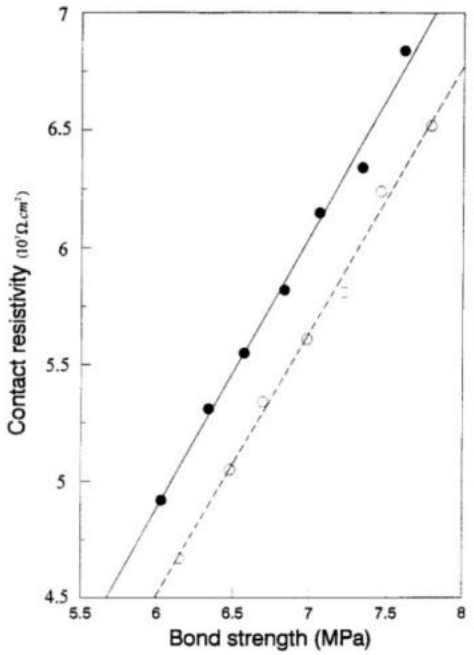

Figure A. 50 Variation of contact electrical resistivity with bond strength (Fu and Chung, 1995)

Cao and Chung (2001) measured the degradation of the bond between steel reinforcing bar and surrounding concrete under cyclic shear loading using the contact electrical resistance of the joint. Degradation, which caused a decrease in bond strength but no visual damage, was indicated by a sudden increase in the resistance at a small fraction of the fatigue life. Shear stress was imposed by applying a downward load on the top surface of A, while the bottom flat surface of B was supported by a steel ring C with a central hole slightly larger than the cross section of A (Figure A. 51). C was electrically insulated from A and B. The four-probe method was used. The outer two contacts (a and d) were considered for passing current while the inner two contacts (b and c) were expected to measure voltage. Shear stress and contact electrical resistance were simultaneously measured during cyclic loading at different shear stress amplitudes. The apparatus served a non-destructive technique to track no visually observable loss of bond strength, through indicating significant increase in the

electrical resistance. This provides a real time monitoring of bond strength condition in a RC elements.

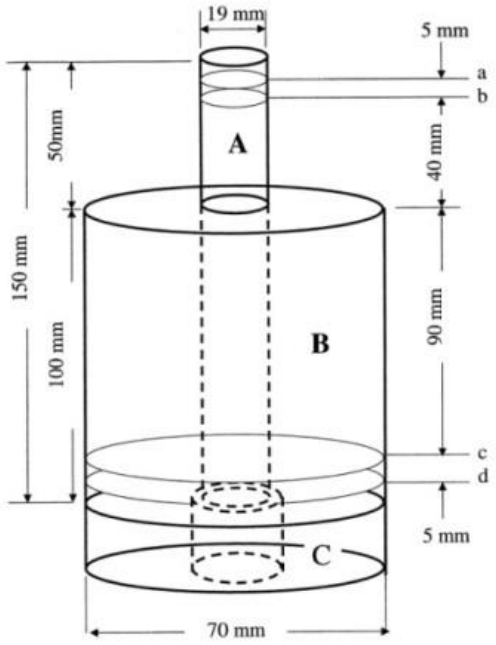

Figure A. 51 Configuration for measuring contact electrical resistance during shear loading of joint between steel rebar (A) and concrete (B). Steel support (C) (Cao and Chung, 2001)

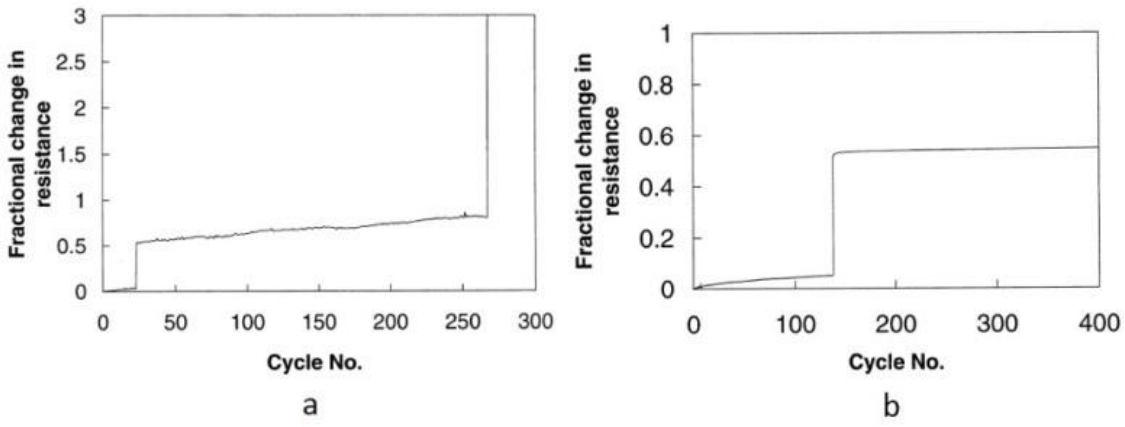

Figure A. 52 Variation of the fractional contact resistance change versus cycle number during cyclic shear loading at shear stress amplitude of: (a) 3.73MPa and (b) 0.75 MPa (Cao and Chung, 2001)

A.2.4 X-ray Tomography

X ray CT imaging employs the right combination of imaging variables to provide clear images of interior damage in reinforced concrete element. The current energy sources are adequate for imaging up to 6 inches of concrete. X-ray CT images of two typical bond test specimens, a pull-out test specimen and a uniform tension test specimen, were analysed to investigate local damage and global behaviour Sprague 2006. They calculated the bond displacement zone by the motion estimation algorithm for 3D images generated for both types of tests. Regarding two specified images at different load steps of a specimen, the motion estimation algorithm seeks the displacement field that minimizes the difference in the grey scale intensity. Gradient of the grey scale intensity and gradient of the displacement field are considered as the global objective.

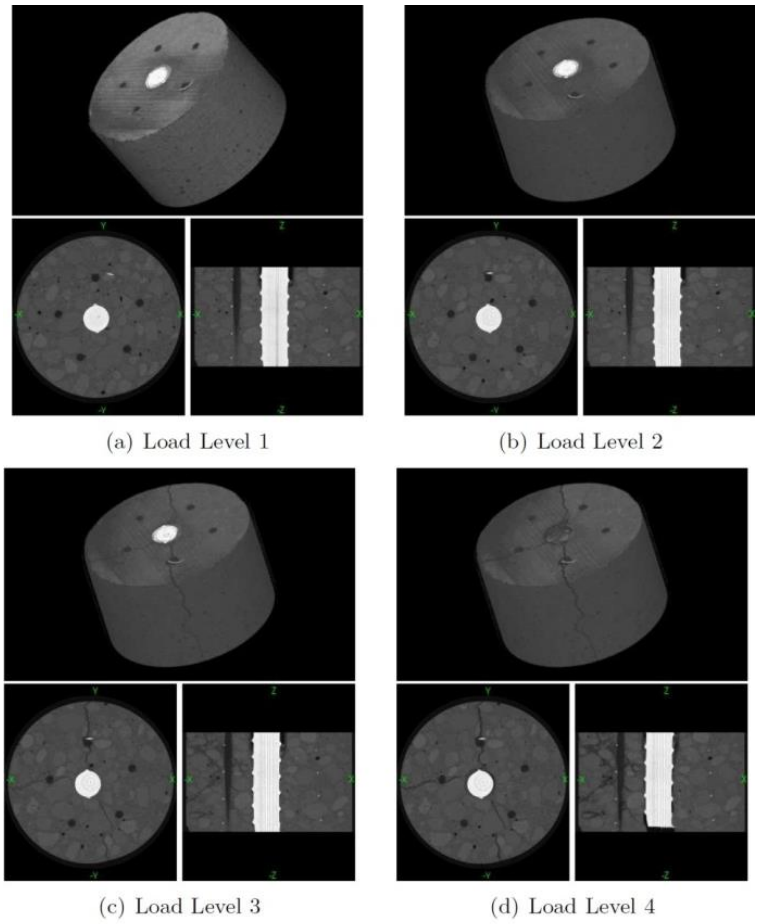

Figure A. 53 Volumetric Images of Pull-out Test Specimen (Li, 2010)

A.3 References

A944, A. S. (2010). "Standard Test Method for Comparing Bond Strength of Steel Reinforcing Bars to Concrete Using Beam-End Specimens."

ACI "Test Procedure to Determine Relative Bond Value of Reinforcing Bars (AC1 208-58)." *Proc., ACI Journal Proceedings*, ACI, 1-16.

Balázs, G., Grosse, C., Koch, R., and Reinhardt, H. (1993). "Acoustic emission monitoring on steel-concrete interaction." *Otto Graf Journal*, 4, 56-90.

Balazs, G., and Koch, R. (1995). "Bond characteristics under reversed cyclic loading." *Otto Graf Journal*, 6, 47-62.

Balazs, G. L. (1989). "Bond Softening Under Reversed Load Cycles." *Studi e ricerche—Corso di perfezionamento per le costruzioni in cemento armato Fratelli Pasenti*, 11, 503-524.

Balázs, G. L. (1986). "Bond behaviour under repeated loads." *Studi e ricerche—Corso di perfezionamento per le costruzioni in cemento armato Fratelli Pasenti*, 8, 395-430.

Broms, B. B. "Technique for investigation of internal cracks in reinforced concrete members." *Proc., ACI Journal Proceedings*, ACI, 35-44.

Cao, J., and Chung, D. (2001). "Degradation of the bond between concrete and steel under cyclic shear loading, monitored by contact electrical resistance measurement." *Cement and concrete research*, 31(4), 669-671.

Chana, P. (1990). "A test method to establish realistic bond stresses." *Magazine of Concrete Research*, 42(151), 83-90.

Chiang, C.-H., Tsai, C.-L., and Kan, Y.-C. (2000). "Acoustic inspection of bond strength of steel-reinforced mortar after exposure to elevated temperatures." *Ultrasonics*, 38(1), 534-536.

Edwards, A., and Yannopoulos, P. (1978). "Local bond-stress–slip relationships under repeated loading." *Magazine of Concrete Research*, 30(103), 62-72.

Edwards, A., and Yannopoulos, P. "Local bond-stress to slip relationships for hot rolled deformed bars and mild steel plain bars." *Proc., ACI Journal Proceedings*, ACI, 405–420.

Eligehausen, R., Popov, E. P., and Bertero, V. V. (1983). "Local bond stress-slip relationships of deformed bars under generalized excitations." Earthquake Engineering Research Center, University of California, Berkeley, California.

Ferguson, P. M., Breen, J. E., and Jirsa, J. O. (1988). *Reinforced concrete fundamentals*, John Wiley, New York.

Fu, X., and Chung, D. (1995). "Linear correlation of bond strength and contact electrical resistivity between steel rebar and concrete." *Cement and concrete research*, 25(7), 1397-1402.

Gambarova, P. G., and Rosati, G. (1996). "Bond and splitting in reinforced concrete: test results on bar pull-out." *Materials and Structures*, 29(5), 267-276.

Goto, Y. "Cracks formed in concrete around deformed tension bars." *Proc., ACI Journal Proceedings*, ACI, 244–251.

Harajli, M., Hamad, B., and Karam, K. (2002). "Bond-slip response of reinforcing bars embedded in plain and fiber concrete." *Journal of Materials in Civil Engineering*, 14(6), 503-511.

Hungspreug, S. (1981). "Local bond between a steel bar and concrete under high intensity cyclic load."Ph.D. Dissertation, Cornell University, Ithaca, NY.

Ismail, M., and Jirsa, J. O. "Behavior of anchored bars under low cycle overloads producing inelastic strains." *Proc., ACI Journal Proceedings*, ACI, 433-438.

Kankam, C. (2003). "A routine method for measuring bond stress, steel strain and slip in reinforced concrete beams at service loads." *Magazine of Concrete Research*, 55(1), 85-93.

Kankam, C. K. (1997). "Relationship of bond stress, steel stress, and slip in reinforced concrete." *Journal of Structural Engineering*, 123(1), 79-85.

Kemp, E., and Wilhelm, W. "Investigation of the parameters influencing bond cracking." *Proc., ACI Journal Proceedings*, ACI, 47-72.

Kemp, E. L., Brezny, F., and Unterspan, J. "Effect of Rust and Scale on the Bond Characteristcs of Deformed Reinforcing Bars." *Proc., ACI Journal Proceedings*, ACI, 743-756.

Li, J., Gao, X., and Zhang, P. (2007). "Experimental investigation on the bond of reinforcing bars in high performance concrete under cyclic loading." *Materials and Structures*, 40(10), 1027-1044.

Lindorf, A., Lemnitzer, L., and Curbach, M. (2009). "Experimental investigations on bond behaviour of reinforced concrete under transverse tension and repeated loading." *Engineering structures*, 31(7), 1469-1476.

Malvar, L. (1992). "BOND OF REINFORCEMENT UNDER CONTROLLED CONFINEMENT." *ACI Materials Journal*, 89(6), 593–601.

Mo, Y., and Chan, J. (1996). "Bond and slip of plain rebars in concrete." *Journal of materials in Civil Engineering*, 8(4), 208-211.

Morimoto, H. K., Hiroyuki; Fujii, Shigeru; Morita, Shiro (1984). "Local Bond-Slip Behaviour Under Splitting Bond-Shear." *Transactions of the Japan Concrete Institute*, 6, 469-476.

Morita, S., and Kaku, T. "Local bond stress-slip relationship under repeated loading." *Proc., Proc., IABSE Symp.: Resistance and Ultimate Deformability of Structures Acted on by Well-Defined Repeated Loads*, 221-227.

Murcia-Delso, J., Stavridis, A., and Shing, P. B. (2013). "Bond Strength and Cyclic Bond Deterioration of Large-Diameter Bars." *ACI Structural Journal*, 110(4), 659-670.

Nilson, A. H. "Internal measurement of bond slip." *Proc., ACI Journal Proceedings*, ACI, 439–441.

Noakowski, P. J., K. (1978). "Vorschlag für ein allgemeingültiges Verbundprüfverfahren (Proposal for gerneric bond test)." Institutsbericht, Lehrstuhl für Massivbau, TU München

Oh, B. H., and Kim, S. H. (2007). "Realistic models for local bond stress-slip of reinforced concrete under repeated loading." *Journal of Structural Engineering*, 133(2), 216-224.

Perry, E. S., and Jundi, N. "Pullout bond stress distribution under static and dynamic repeated loadings." *Proc., ACI Journal Proceedings*, ACI, 377–380.

Raynor, D. J., Lehman, D. E., and Stanton, J. F. (2002). "Bond-slip response of reinforcing bars grouted in ducts." *ACI Structural Journal*, 99(5), 568-576.

Rehm, G. (1961). "Über die Grundlagen des Verbundes zwischen Stahl und Beton." 138.

Rehm, G., and Eligehausen, R. (1977). "Einfluß einer nicht ruhenden Belastung auf das Verbundverhalten von Rippenstählen."

Rehm, G., and Eligehausen, R. "Bond of ribbed bars under high cycle repeated loads." *Proc., ACI Journal Proceedings*, ACI, 297-310.

RILEM/CEB/FIP (1973). "Bond test for reinforcing steel: 1-Beam test(7-II-28 D). 2-Pullout test (7-II-128) Materials and Structures." *Materials and Structures*, 6(32), 96-105.

Roberts, N. (1973). "A limit state anchorage bond test for reinforcement in concrete." *Matériaux et Construction*, 6(2), 119-122.

Rteil, A., Soudki, K., and Topper, T. (2011). "Mechanics of bond under repeated loading." *Construction and Building Materials*, 25(6), 2822-2827.

Shima, H., Chou, L.-L., and Okamura, H. (1987). "Micro and macro models for bond in reinforced concrete." *Journal of the Faculty of Engineering*, 39(2), 133-194.

Snowdon, L. (1970). "Classifying reinforcing bars for bond strength." Building Research Station, Department of the Environment, Garston, England.

Soleymani Ashtiani, M., Dhakal, R., Scott, A., and Bull, D. (2013a). "Cyclic beam bending test for assessment of bond–slip behaviour." *Engineering Structures*, 56, 1684-1697.

Soleymani Ashtiani, M., Dhakal, R. P., and Scott, A. N. (2013b). "Post-yield bond behaviour of deformed bars in high-strength self-compacting concrete." *Construction and Building Materials*, 44, 236-248.

Sprague, T. (2006). "An X-Ray Tomography Investigation of Bond in Reinforced Concrete." MSCE Thesis, University of Washington, Seattle, WA.

Verderame, G. M., Ricci, P., Carlo, G. D., and Manfredi, G. (2009). "Cyclic bond behaviour of plain bars. Part I: Experimental investigation." *Construction and Building Materials*, 23(12), 3499-3511.

Wu, F., and Chang, F.-K. (2006a). "Debond detection using embedded piezoelectric elements for reinforced concrete structures-Part II: Analysis and algorithm." *Structural Health Monitoring*, 5(1), 17-28.

Wu, F., and Chang, F.-K. (2006b). "Debond detection using embedded piezoelectric elements in reinforced concrete structures-part I: experiment." *Structural Health Monitoring*, 5(1), 5-15.

Appendix B Specimen design

B.1 Description of prototype

As this experimental test is intended to assess the residual capacity of post-1982 RC member, the specimen is expected to simulate the real behaviour of a RC beam in an existing building designed to NZS 3101:1982. To this end, lab specimen was scaled and designed in a way to address a typical RC beam in a building tagged red in Christchurch. Test specimen is intended to represent the potential plastic hinge of a middle-rise (6-9 storeys) prototype frame. It is assumed that points of contra-flexure occur at mid-span of beams. The prototype Building was built in 1980-1989 on 86 Gloucester Street, Brannigans. The selected prototype building for the experimental investigation is given in Figure E-1.

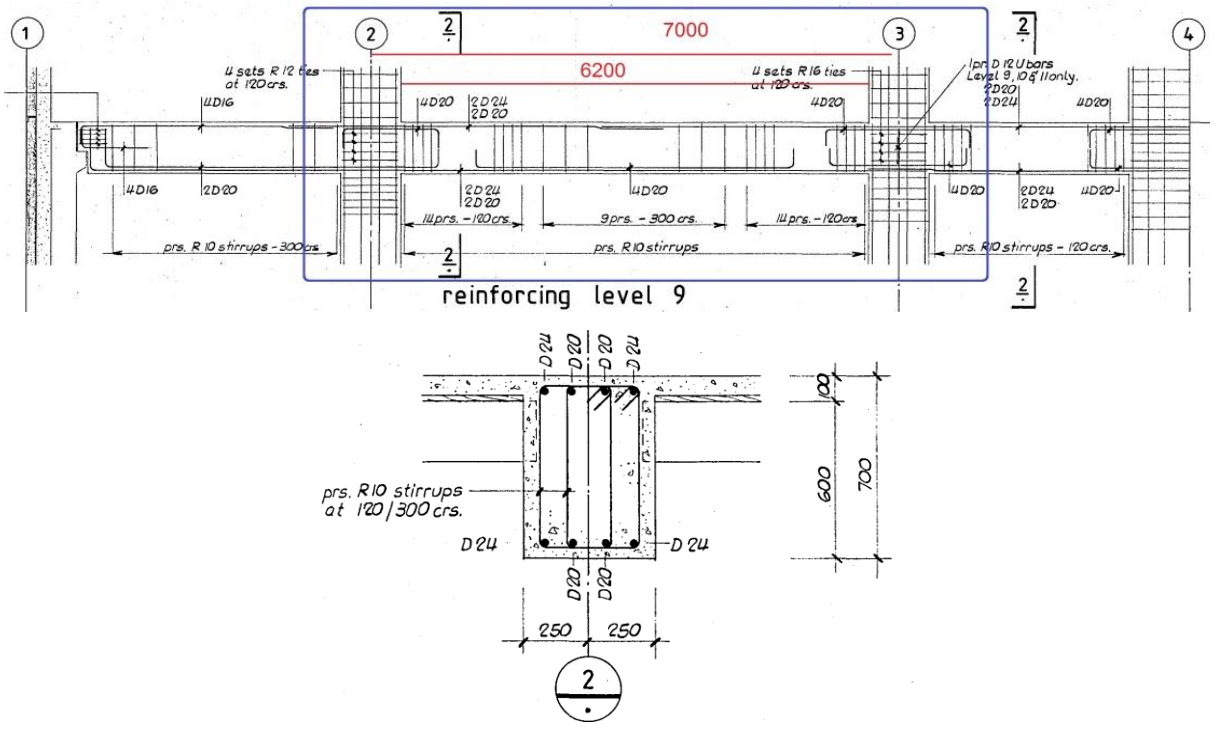

Figure B. 1 Reinforcement detail of a post-1980s RC beam (86 Gloucester Street, Brannigans, Christchurch, New Zealand; courtesy of Christchurch city council)

Appendix B Specimen design

Table B. 1 provides the summary of scale factors, prototype and specimen dimensions.

Table B. 1 summary of scale factors, prototype and specimen dimensions

	Prototype beam	**Test specimen**
Height (mm)	700	350
Width (mm)	500	250
Clear Span (mm)	6200*	3100
Point of contraflexure	3100	1550
Scale factor for dimension: 1/2 **Scale factor for shear forces: 1/4** **Scale factor for moment: 1/8** **Scale factor for area: 1/4** **ρ should be the same** *** clear span length is : 7000-2 × 40 = 6200 mm**		

Given information:

Top steel: (2D24+2D20) + (4D20)

d= 700-30-10-24/2= 648mm

d'= 30+10+24/2=52 mm

b=500 mm

$A'_{s,\,top} = (2 \times \pi \times 24^2/4 + 2 \times \pi \times 20^2/4) + (4 \times \pi \times 20^2/4) = 2790\ mm^2 \Rightarrow \rho'_s = 2790/(500 \times 648) = 0.0086$

Bottom steel: (2D24+2D20) + (4D20)

$A_{s,\,bot} = (2 \times \pi \times 24^2/4 + 2 \times \pi \times 20^2/4) + (4 \times \pi \times 20^2/4) = 2790\ mm^2 \Rightarrow \rho_s = 2790/(500 \times 648) = 0.0086$

$f'_{c,\,28\ days}$: 30MPa

Moment capacity, $M_n = 0.85\ f'_c\ ba\ (d-a/2) + A'_s\ f'_s\ (d-d')$

$f'_s = 600\ \frac{a \times \beta_1 d'}{a}$

$\Sigma f=0 \Rightarrow a = 48.5$ mm $\Rightarrow M_{n,prototype} = 461$ KN.m

D: deformed bar grade 275

R: plain bar grade 275

B.2 Design of test specimen (beam)

B.2.1 Design for flexure

B.2.1.1 Assumptions

Cover: 20mm (Regarding scale factor:1/2 × 40mm = 20mm)

D16: main longitudinal bars grade 300E

D10: stirrups grade 300E

d=350-30-10-16/2=302mm

$M_{n,specimen}$ = 1/8 $M_{n,prototype}$ = 58 KN.m

$\rho_{s,\ specimen} = \rho_{s,\ real\ beam}$ => $A_{s,\ specimen}$ = 0.0086 x 250 x 302 = 650 mm^2

Number of bars: 650/(π $x16^2$/4) = 3.23 => n_b = 4

Provided area by tension reinforcement: 4 x (π $x16^2$/4) = 804 mm^2

=> Σ f=0 => a = 39.5 mm => $M_{n,specimen}$ = 67 KN.m

B.2.1.2 Minimum thickness of beam (NZS3101:1982, 4.4.1.3)

For f_y = 300MPa and cantilever beam: $d > \frac{L}{10}$ => d > 3100/10 = 310 mm

B.2.1.3 Minimum concrete cover (NZS3101:1982, 5.3.33.1)

No problem as the specimen is in lab conditions

B.2.1.4 Dimension check for the cantilever beam end (NZS3101:1982, 6.5.2.2)

$\frac{L_n}{b_w} = \frac{3100}{250}$ = 12.4 < 15 O.K

$\frac{L_n h}{{b_w}^2} = \frac{3100 \times 350}{250^2}$ =17.3 < 60 O.K

B.2.1.5 Minimum reinforcement ratio (NZS3101:1982, 6.5.3.2)

$\rho_{min} = \frac{?}{f_y}$ = numerator is disappeared in the available copy, hence on the basis of C6.5.3.2, 0.0051 is considered as the minimum value.

$\rho_{min} = \frac{A_{s,min}}{b_w d}$ => $A_{s,\ min}$ = 0.0051 x 250 x 302 = 385 mm^2

=> $A_{s,\ prvd} > A_{s,\ min}$ O.K

B.2.1.6 Maximum reinforcement ratio (NZS3101:1982, 6.5.3.2)

$\rho_{max} = \frac{7}{f_y} = 0.023$

$\rho_{max} = \frac{A_{s,max}}{b_w d}$ => $A_{s,\,max} = 0.023 \times 250 \times 302 = 1761\ mm^2$

=> $A_{s,\,prvd} < A_{s,\,max}$ O.K

B.2.1.7 Maximum beam bar size (NZS3101:1982, 5.5.2.5)

$d_b \leq \frac{12 h_c}{f_y} = \frac{12 \times 400}{300} = 16$ => D16 is O.K

B.2.1.8 Potential plastic hinge region in beam (NZS3101:1982, 6.5.3.1)

The PPHR length at the face of the supporting column: 2 x beam depth= 2 x 350 = 700mm

B.2.1.9 Antibuckling and confinement (NZS3101:1982, 6.5.3.3)

(Width) – (2 x cover to centroid of longitudinal bar) = 250 - 2 x (30+10+16/2) = 154 mm < 200 mm O.K

=> No need for extra stirrups

B.2.1.10 Area of one leg of a stirrup-tie (NZS3101:1982, 6.5.3.3(b))

$A_{te} = \frac{\sum A_b f_y}{16 f_{yt}} \frac{s}{100} = \frac{(1 \times 201) \times 300 \times s}{16 \times 300 \times 100} = 0.125s\ mm^2$

B.2.1.11 Maximum space in potential plastic hinge zone (NZS3101:1982, 6.5.3.3(d))

Min ($\frac{d}{4}$, $6d_b$, 150mm) = min ($\frac{302}{4}$, 6 x 16, 150) = 75 mm

A_{te} = 0.125 x 75 = 9.42 mm^2

A_{te} < R10 O.K

The first stirrup-tie shall not be further than 50mm from the column face

B.2.2 Design for shear

B.2.2.1 Assumption

Shear strength provided by shear reinforcement in specimen should be proportional to prototype. Thus, taking into account scale factor for shear, the specimen should provide following shear strength.

$V_{S,\,specimen} = 1/4 \times V_{S,\,prototype}$

$V_S = A_v f_{yt} \frac{d}{s}$

$\Rightarrow (A_v) \times (300) \times (\frac{302}{75}) = (1/4)\ x\ (4\ x\ \pi\ x\ 10^2/4)\ x\ (300)\ x\ (\frac{648}{120}) \Rightarrow A_v = 105\ mm^2$

B.2.2.2 Checks on maximum permissible total shear stress (NZS3101:1982, 7.3.1.8)

Total shear stress $v_i \leq (0.2f'_c, 6Mpa)$

$\leq (0.2)(30) = 6$ MPa

≤ 6 MPa

B.2.2.3 Shear reinforcement in PPHR (NZS3101:1982, 7.3.6.3)

The concrete shear contribution within the PPRH is assumed to be zero because of concrete degradation.

$A_{v,prvd}$ = 2 legs R10@75c/c : $157mm^2$

B.2.2.4 Maximum spacing of shear reinforcement (NZS3101:1982, 7.3.5.4)

$S_{max} = 0.5d = 0.5\ x\ 302 = 150mm$

B.2.2.5 Minimum shear reinforcement (NZS3101:1982, 7.3.4.3)

$A_{v,min} = \frac{0.35 b_w s}{f_y} = \frac{0.35 \times 250 \times 150}{300} = 43.7\ mm^2$

Placing stirrups 2 legs R10@ 125mm within the beam off plastic hinge

B.3 Capacity assessment of the section

For this purpose, Cumbia has been employed to provide both force-displacement and moment-curvature relationships of the test specimens, as it is illustrated in Figure B. 2 and Figure B. 3.

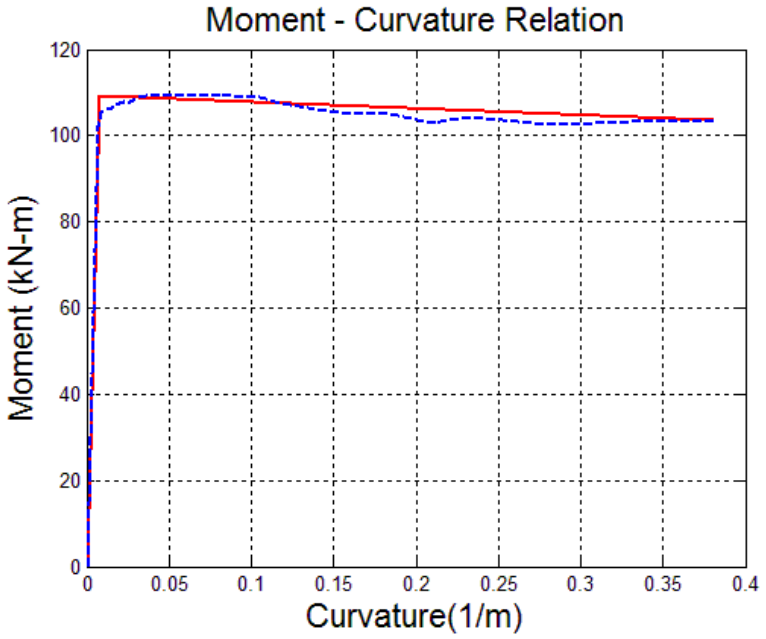

Figure B. 2 Moment-Curvature response of the test specimen

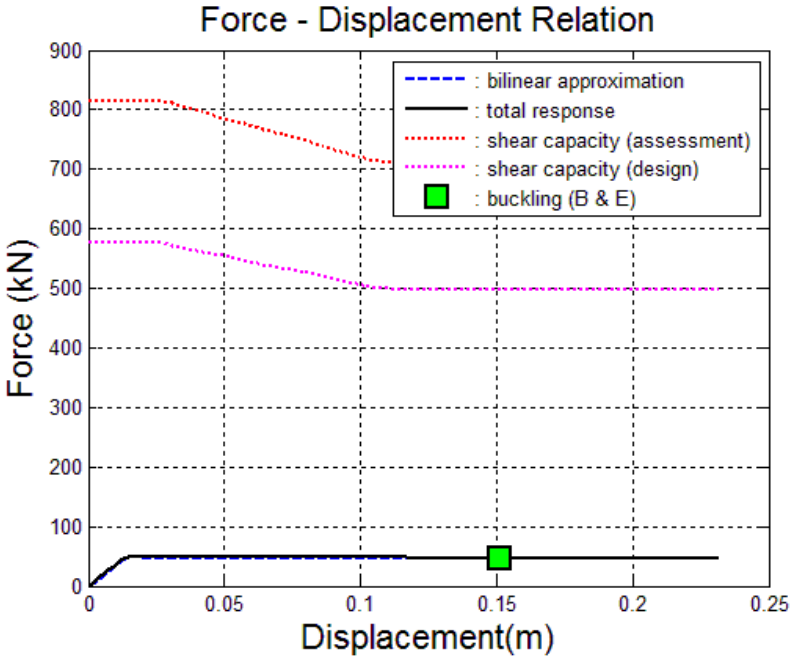

Figure B. 3 Force- Displacement response of the RC beam member

Appendix C Test set-up design

C.1 Design of top connections

The test set-up consists of steel connections at top and bottom of the specimen (i.e., loaded and unloaded ends).

C.1.1 Design of fitting connection

For the design of fitting connection, LRFD design approach has been used. All concepts and formulas are adopted from AISC specification, 2005, steel design manual (AISC) 14th edition and NZS 3678. The fitting is comprised of two components; fitting plate and T stem plate as it is illustrated in the figure 1.

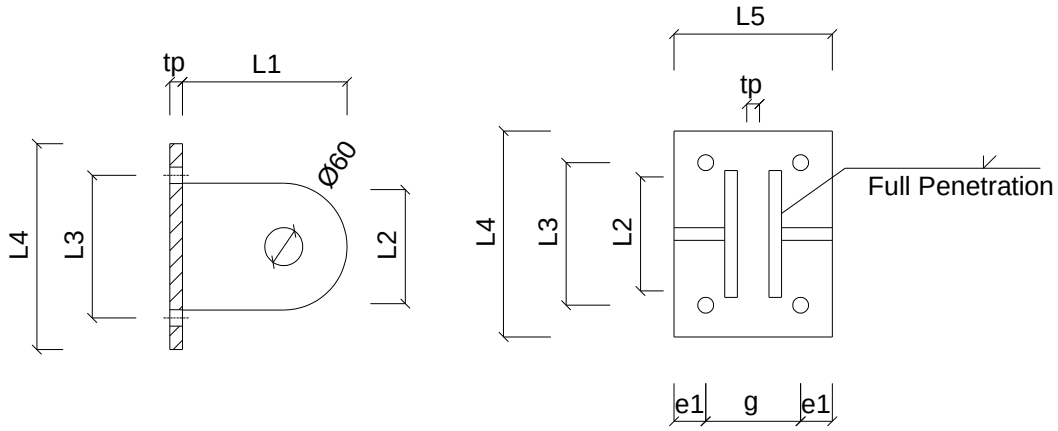

Figure C. 1 Schematic details of fitting connection

Geometrical properties

L_1 = 250 mm L_5 = 250 mm

L_2 = 200 mm t_p = 20 mm

L_3 = 225 mm g=150 mm

L_4 = 325 mm e_1 = 50 mm

Mechanical properties (NZS 3678)

Hot rolled plates

Grade 300

13mm <thickness <20mm

Appendix C Test set-up design

F_y: 300 MPa

F_u: 430 MPa

Design of T stem plate

M_r = 110 kN.m

Tensile force (lateral pull) applied during testing, F=Mr / h = 110 kN.m / 2.1 m = 52.3 KN

Safety factor: 4

$F_{max,applied}$ =4 × 52.3 KN = 209 kN

Tensile yielding of tee stem plate

$P_n = F_y A_g$

$A_g = L_3 \times t_{p,stem}$

Using L_3 = 200 mm & $t_{p,stem}$ =20 mm

⇨ A_g = 200 mm × 20 mm = 4000 mm^2

P_n =280 MPa × 4000 mm^2 = 1120 kN AISC Specification Equation D2-1

Ø = 0.9

$Ø P_n$ = 0.9 × 1120 KN = 1008 KN > 209 kN O.K

Welding stem to end-plate

*Stem should be welded to end plate according to full penetration requirements by a certified welder

Tensile rupture strength of the tee's stem plate

U = 1 (shear lag factor from AISC Specification, table D3-1)

$A_e = U A_n$

$A_n = A_g - \Sigma(d \times t)$ = 4000 – (Ø × $t_{p,stem}$) = 4000 – (60 × 20) = 2800 mm^2

$P_n = F_u A_e$ = 440 MPa × 2800 mm^2 = 1232 KN AISC Specification Equation D2-2

$Ø_t$ = 0.75

$Ø_t P_n$ = 0.75 × 1232 = 924 KN > $F_{applied}$ o.k

C.1.2 Design of end-plate for fitting

Bolt design

Appendix C Test set-up design

Try 4 M24 Grade 8.8 bolts

Required strength per bolt, T = $F_{applied}$ / No. of bolts = 209 KN / 4 = 52 kN

Design tensile strength per bolt, B = Ø r_n = 40.6 kips = 180.5 kN AISC Manual Table. 7-2

⇨ B > T o.k

Determination of tributary length per pair of bolts, p.

Maximum effective length: 2 x g = 2 x 150 mm = 300 mm AISC Manual part 9& figure 9-4

Assuming bolt gage length, g = 150 mm

Assuming L_3 = 225 mm

$P = \frac{300\ mm - L_3}{2} + \frac{g - t_{p,stem}}{2} = \frac{300\ mm - 225}{2} + \frac{150 - 20}{2}$ = 102.5 mm AISC Manual page 9-11

Check 1: p < 2b => 102.5 mm < 2 x65 mm o.k

Check 2: p < s => 102.5 mm < 225 mm o.k

<u>Prying action calculations in accordance with AISC Manual part 9</u>

The thickness of RC beam (dimension perpendicular to end-plate) is significantly thicker than the end-plate thickness attached to: thus prying in end-plate will control prying action.

b = $\frac{g - t_{p,stem}}{2} = \frac{150\ mm - 20\ mm}{2}$ = 65 mm

⇨ check if b > C_1 (entering and tightening clearance) => 65 mm > 1 3/8 in o.k

a = $\frac{b_f - g}{2} = \frac{250\ mm - 150\ mm}{2}$ = 50 mm AISC Manual Fig. 9-4

b' = $b - \frac{d_b}{2} = 65 - \frac{24\ mm}{2}$ = 53 mm AISC Manual Equation 9-21

a' = $a + \frac{d_b}{2} \leq 1.25b + \frac{d_b}{2} = \left(50 + \frac{24}{2}\right) \leq \left(1.25 \times 65 + \frac{24}{2}\right)$ AISC Manual Equation 9-27

⇨ 62 mm ≤ 93.2 mm

ρ = $\frac{b\prime}{a\prime} = \frac{53\ mm}{62\ mm}$ = 0.854 AISC Manual Equation 9-26

$\beta = \frac{1}{\rho} - \left(\frac{B}{T} - 1\right) = \frac{1}{0.854} - \left(\frac{180.5\ KN/Bolt}{52\ KN/Bolt} - 1\right)$ = -1.3 AISC Manual Equation 9-25

Ratio of the net area at the bolt line to the gross area at the face of the stem, $\delta = 1 - \frac{d\prime}{p}$

Width of the hole, d' = 27 mm AISC Specification, Table J3.3M

$\delta = 1 - \frac{d'}{p} = \frac{27}{102.5} = 0.73$ AISC Manual Equation 9-24

If: $\beta \geq 1 \Rightarrow \alpha' = 1.0$ AISC Manual page 9-12

If: $\beta < 1 \Rightarrow \alpha' = \text{Min}\left(1.0, \frac{1}{\delta}\left(\frac{\beta}{1-\beta}\right)\right)$

⇨ In this case: $\beta < 1 \Rightarrow \alpha' = \text{min}\left(1.0, \frac{1}{0.73}\left(\frac{-1.3}{1-(-1.3)}\right)\right) = -0.66$

$t_{min} = \sqrt{\frac{4 \times T \times b\prime}{\phi \times p \times F_u \times (1+\delta\alpha')}}$ AISC Manual Equation 9-23a

F_u: minimum tensile strength of connecting element

$F_{u,\ tee\ stem}$ = 440 MPa (NZS3679, Grade 300)

$\sqrt{\frac{4 \times 52\ \times 10^3\ N \times 53mm}{0.9 \times 102.5mm \times 440MPa \times (1+0.73 \times -0.66)}}$ = 22.9 mm < 25 mm o.k

USE Plates **325mmx225mmx25mm as fitting plate**

& 250mmx200mmx25mm as stem

C.1.3 Design of fillet weld to connect fitting stem plate to end-plate

Assuming a 10 mm fillet weld is used on each side of the stem plate.

Fillet weld design strength,

$\emptyset R_n = F_w A_w$ AISC Spec. Equation J2-4

Ø = 0.75

$A_{w,eff}$ = effective throat size x effective length = $t_{w,eff}$ x $L_{w,eff}$

Considering the total length of L_2 as effective weld length for the first trial

⇨ $A_{w,eff}$ = 0.707 D × $L_{w,eff}$ = (0.707 × 10 mm) × 200 mm = 1414 mm^2

Nominal strength of the weld metal per unit area (MPa),

$F_w = 0.6\ F_{EXX}\ (1 + 0.5\ sin^{1.5}\theta)$ AISC Spec. Equation J2-5

To be more conservative, the increasing term ignored, so

Using E 60 as weld electrode, weld electrode strength, F_{EXX} *is equal to 413MPa*

$F_w = 0.6\ F_{EXX}$ = 0.6 × 413 MPa = 247 MPa

⇨ $R_n = F_w\ A_w$ = 247 MPa × 1414 mm^2 = 349 KN

Limitation checks according to AISC Spec. section J2-2b

1. Max/Min weld size

Table C. 1 shows the limitations for maximum and minimum weld size.

Table C. 1 the criteria for maximum and minimum weld size

Maximum weld size of fillet weld (D_{max})	Material thickness - 2 mm	If material thickness ≥ 6 mm	AISC Spec. section J2-2b
Minimum weld size of fillet weld (Dmin)	8 mm		AISC Spec. Table J2.4

Material thickness = t_p = 20mm

⇨ D_{max} = 20 mm – 2 mm = 18 mm

⇨ D_{min} < Weld size < D_{max} => 8 mm < 10 mm < 18 mm

2. Distance between fillet weld

For longitudinal fillet welds used alone in end connections of flat-bar tension members, the length of each fillet weld shall be not less than the perpendicular distance between them.

Length of weld (L_2): 200 mm

200 mm > 50 mm o.k

3. Weld length/weld size ratio

For end-loaded fillet welds:

If: $\frac{Length\ of\ weld}{Size\ of\ weld} < 100$ => effective length = actual length

If: $\frac{Length\ of\ weld}{Size\ of\ weld} > 100$ => effective length = less than actual length

⇨ effective length = β × actual length

β = 1.2 – 0.002 (L/W) ≤ 1 AISC Spec. Equation J2-1

In this case:

$$\frac{Length\ of\ weld}{Size\ of\ weld} = \frac{200\ mm}{10\ mm} = 200$$

⇨ β = 1.2 – 0.002 (200) = 0.8
⇨ effective length, L_{eff} = 0.8 x 200 mm = 160 mm

Re-calculate R_n

$A_{w,eff}$ = 0.707 D x $L_{w,eff}$ = (0.707 x 10 mm) x 160 mm = 1131 mm^2

$R_n = F_w A_w$ = 247 MPa x 1131 mm^2 = 279 kN

Design strength, $ØR_n$ = 0.75 x 279 KN = 209 kN

For 4 sides, the total design strength which could be sustained by for 4 weld lines:

$ØR_n$ = 4 x 209 KN = 836KN

836 KN > 300 KN (Actuator capacity) o.k

C.1.4 Design of extension component

To fill the gap between actuator and fitting which is connected to reaction frame we need an extension piece.

Demand = ram capacity = 300KN

Using a 100x100x6 SHS (Steel and Tube Company)

A = 2130 mm^2

F_y: 350 MPa

⇨ axial capacity= 2130 mm^2 × 350 MPa = 745 kN
⇨ S.F = 745 / 300 = 2.4

C.2 Design of base connection

C.2.1 Control of base beam

Section: 500 WC 414

Z_x = 8800 x 10^3 mm^3

Capacity: $M_x = Z_x \times F_y$ = 8800 x 10^3 mm^3 × 280 MPa = 2464 kN.m

Demand: Ram capacity × lever arm = 300 KN × 2.663 = 798 kN

⇨ S.F = 2464 KN.m / 798 KN.m = 3 o.k

C.2.2 End-plate design for welded column section

The procedure used for design of flush moment end-plate connection herein, is completely in accordance with Design procedure 1, described in steel design guide 16, chapter 3, published by AISC. The end-plate, connected to base support is classified under Two-bolt flush unstiffened moment connection. Base support is made up of two separated high capacity welded-column (500WC 414) which are tied together using threaded rods and will be fixed to strong floor by 8 anchor bolts.

Geometric design data

500WC 414 (based on OneSteel company designation format)

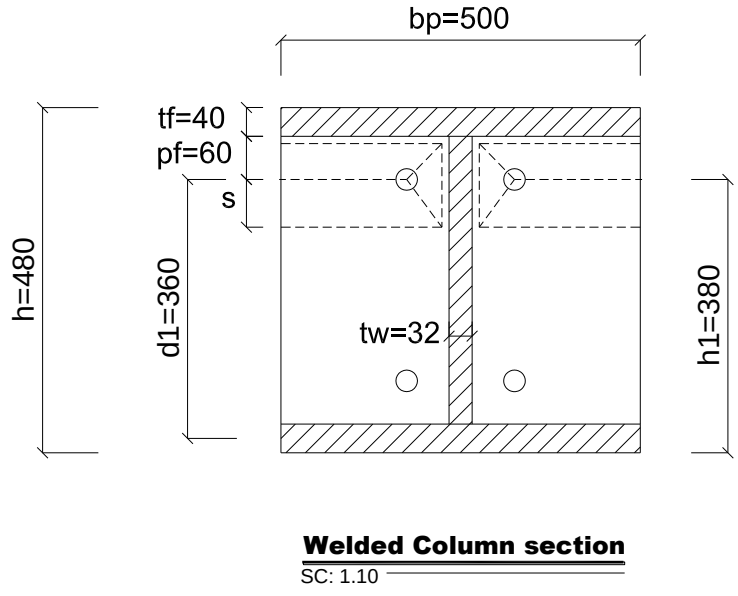

Figure C. 2 section of end moment connection

b_p = 500 mm

t_f = 40 mm

Appendix C Test set-up design

g = 150 mm

p_f = 60 mm

h = 480mm

d_1= h - t_f - p_f - t_f/2= 480 - 40 – 60 – 40/2 = 360 mm

h_1= h - t_f - p_f - t_f/2= 480 - 40 – 60 = 380 mm

Required bolt diameter assuming no prying action,

$d_{b,\ reqd} = \sqrt{\frac{2\ M_u}{\pi \phi F_t\ (\sum d_n)}}$ AISC Steel Design Guide 16. Equation 2-4

M_u = 110 KN.m x 3 = 313 kN.m

Ø = 0.75

F_t: nominal tensile strength (Table J3.2 AISC, 2005).

In this design, we will use grade 8.8 high strength bolts, so the tensile strength in accordance with AS/NZS 4291. 2: 1995 Table A. 1, F_t = 830 MPa

$\Sigma d_n = d_1$ =360mm

$= \sqrt{\frac{2 \times 313 \times 10^6 N.mm}{\pi \times 0.75 \times 830 MPa \times 360\text{mm}}}$ = 29.8 mm

⇨ **Use M30**

Required end-plate thickness

$t_{p,\ reqd} = \sqrt{\frac{1.11\ \gamma_r(\phi M_{np})}{\phi_b F_{py}\ Y}}$ AISC Steel Design Guide 16. Equation 2-7

γ_r = 1.25

This coeeficient is considered as a load factor to limit connection rotation at ultimate moment to 10% of simple span rotation. It takes 1 and1.25 for extended and flush end-plates, respectively.

$Ø_b$ = 0.9

F_{py} = 280 MPa (end-plate material yield stress)

Using Grade 300 (NZS 3678; hot rolled plates) and thickness 21-150mm

$s = \frac{1}{2}\sqrt{b_p g}$ = $\frac{1}{2}\sqrt{500 \times 150}$ = 137 mm AISC Steel Design Guide 16. Table 3-2

p_f = 60 mm < s O.K => p_f = 60 mm

$Y = \frac{b_p}{2}\left[h_1\left(\frac{1}{p_f}+\frac{1}{s}\right)\right] + \frac{2}{g}\left[h_1(p_f + s)\right]$ AISC Steel Design Guide 16. Table 3-2

$Y = \frac{500}{2}\left[380\left(\frac{1}{60}+\frac{1}{137}\right)\right] + \frac{2}{150}[380(60+137)]$ = 3275 mm

$P_t = \left(\frac{\pi {d_b}^2}{4}\right) \times F_t$

$P_t = \left(\frac{\pi \times 30^2}{4}\right) \times 620$= 438 KN

$ØM_{np}$ = Ø (2 P_t (Σd_n)) AISC Steel Design Guide 16. Table 3-2

$ØM_{np}$ = 0.75 (2 × 438 KN × 360 mm) = 236.5 kN.m

$t_{p,\ reqd} = \sqrt{\frac{1.11 \times 1.25 \times 236.5 \times 10^6 N.mm}{0.9 \times 280 MPa \times 3275 mm}}$ = 19.9 mm

This required thickness is over-design since the $ØM_{np}$ used in radical has been calculated for M30. The M30 was already determined for ultimate moment (S.F × Mr).

⇨ Use Plate 500x480x30 mm
⇨ S.F = 30 mm / (19.9 / $\sqrt{S.F}$) = 2.6 O.K

C.2.3 Control of tensile strength for anchor bolts

In this section we will check the capacity of anchor bolts to resist applied moment (demand).

Taking moment and using the distribution of forces as it can be seen in the figure 7 (assuming linear distribution in elastic range) we can write following relationships.

M_r: 110 kN.m

S.F:3 => $M_{ultimate}$: 330 KN.m

F_1 × 1143 mm + F_2 × 1905 mm = 330 × 10^6 kN.m

$\frac{F_2}{1905/2} = \frac{F_1}{1143/2}$ => F_1 =0.6 F_2

⇨ 0.6 F_2 × 1143 +F_2 × 1905 = 330 × 10^6 kN.m
⇨ F_2 = 127.3 KN

⇨ F_1 = 76 KN

Capacity: T = $A_b \times F_y = \frac{\pi \times 36^2}{4} \times 300MPa = 300$ kN

127.3 KN < 300 kN o.k

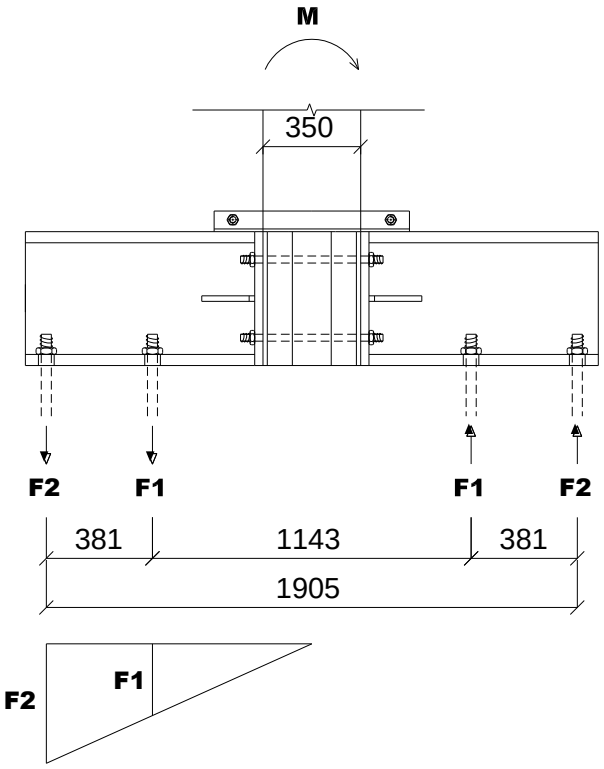

Figure C. 3 Base connection and stress distribution

C.2.4 Control of shear strength for anchor bolts

Since the specimen is supported by two sided beams, so the huge shear force will be generated in floor level. Taking moment about fulcrum:

F_{max} = 65 × S.F = 65 × 3 = 195 kN

Σ M = 0 => F_{max} × (2.18m + 0.48m) = V_2 × 0.48 => V_2 = 1080 kN

Bearing strength of bolts:

$R_n = 1.2\ l_c\ t\ F_u \leq 2.4\ d\ t\ F_u$ AISC Spec Equation J3-6a

l_c = lesser (140mm , 341mm) = 140 mm

Appendix C Test set-up design

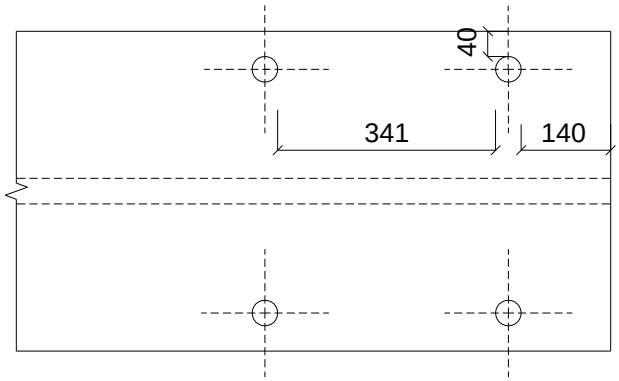

Figure C. 4 Determination of clear distance

$R_n = (1.2)(140mm)(40mm)(280MPa) \leq (2.4)(36)(40)(280)$

⇨ 1881 KN > 967 KN => R_n = 967 kN

⇨ For LRFD: Ø R_n = (0.75)(967) = 725 kN

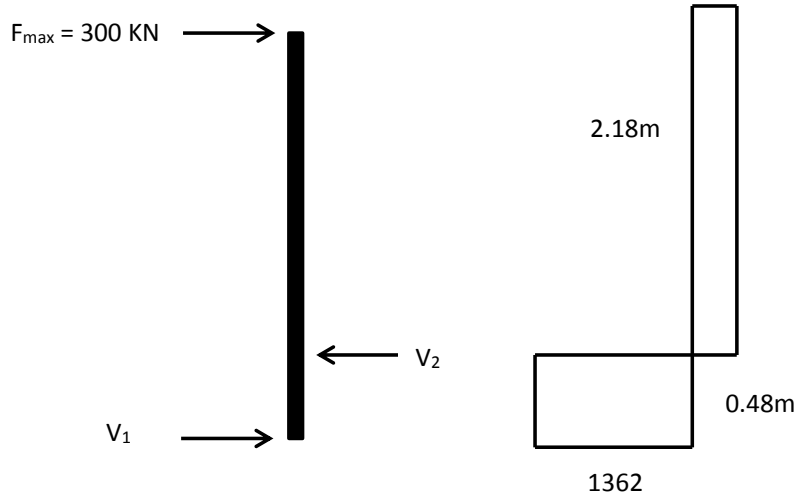

Figure C. 5 Forces diagram

Shearing strength of bolts:

$R_n = F_{nv} A_b$

F_{nv} = 68 KSI (469 MPa)

$A_b = \pi \times 36^2/4 = 1017\ mm^2$

$R_n = F_{nv} A_b$ = (469 MPa)(1017 mm^2) = 477 KN/per bolt

In the worst case scenario, each side acts separately,

4 × 477 KN/per bolt = 1908 KN > 1080 KN O.K

S.F = 1908/1080 = 1.7

C.2.5 Control of sliding

It has been assumed that anchor rods act similar to shear lug. To be more conservative, the friction between bottom flange of base beams and strong floor ignored. The procedure described here is in accordance with AISC Design guide 1 (Design for shear).

$A_{lug} = \frac{V}{0.85\ \varphi\ f'_c} = \frac{1362\ KN}{(0.85)(0.6)(40MPa)} = 66764\ mm^2$

Height of bearing portion:

H-G = $\frac{A_g}{W}$

G: grout height =0

⇨ H = $\frac{66764\ mm^2}{(8\ )\times 36\ mm} = 231$ mm

Cantilever end moment acting on a unit length of the shear lug:

$M_{lug} = \frac{V}{W}\left(\frac{H+G}{2}\right) = \frac{1362\ KN}{288\ mm}\left(\frac{231mm+0}{2}\right) = 1092 \times 10^3$ N.mm

The shear lug thickness is then determined.

$t_{lug} = \sqrt{\frac{4\times M_{lug}}{0.9\ F_Y}} = \sqrt{\frac{4\times 1092\times 10^3\ N.mm}{0.9\times 280}} = 131$mm => 8 (bolts) x (36 mm, width) = 288 mm

S.F = 288 / 131 = 2.19

C.2.6 Control for out of plane instability

In order to prevent from any out of plane movement/instability, 4 angles will be considered on 4 corners of RC beam. One angle leg will be connected to end-plate moment connection of beam (using bolts) and the other leg on to RC beam (no fastener) as it is illustrated in Figure C. 6 and Figure C. 7. The idea behind designing these angles adopted from design of unstiffened seated connection. The concentrated forces which are supposed to be resisted by angles are taken from lateral force generated by actuator in direction perpendicular to test set up plane.

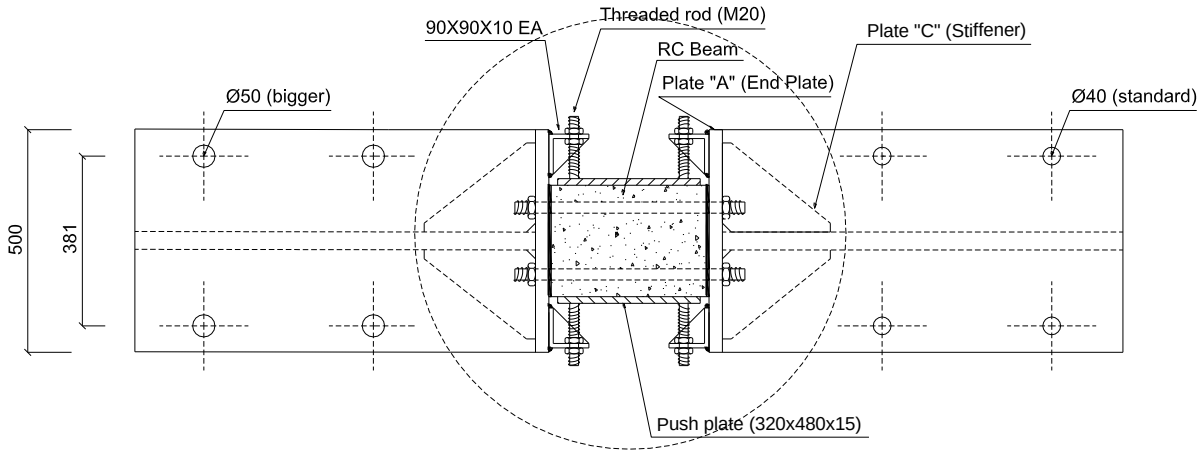

Figure C. 6 Base connection configuration

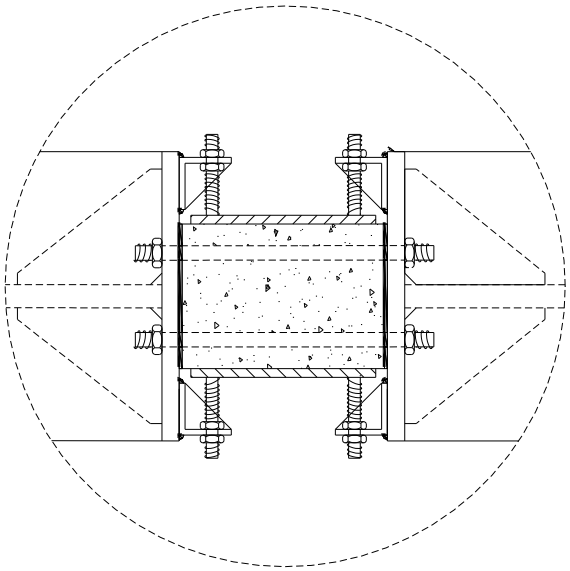

Figure C. 7 Magnified end-plate connection to RC beam

Step 1 (Determining bearing length)

The required bearing length, $l_{b,\,reqd}$,is determined as the larger value of l_b required for the limit state of local yielding and crippling of the beam web.

$l_{b,\,reqd} = \max (l_{b,\,local\ yielding}, l_{b,\,crippling}) \geq k_{des}$

k_{des}: distance from outer face of flange to the web toe of fillet used for design

To determine $l_{b,\,local\ yielding}$ and $l_{b,\,crippling}$, we need to check web yielding and crippling, respectively.

Check local web yielding

$l_{b,\ reqd} = \frac{\emptyset R_n - \emptyset R_1}{\emptyset R_2}$ AISC

Manual Equation 9-45a

In general, to pick the right value for $\emptyset R_1$ and $\emptyset R_2$ from AISC manual 14th edition, Table 9-4, the steel beam section designation should be given.

*No need to control this criterion as angles will support a RC beam, so no local web yielding will occur.

Check local web crippling

$l_{b,\ reqd} = \frac{\emptyset R_n - \emptyset R_3}{\emptyset R_4}$ AISC

Manual Equation 9-47a

For this control, we need to determine how far the force is applied at the with respect to member end. In general, to pick the right value for $\emptyset R_2$ and $\emptyset R_4$ from AISC manual 14th edition, Table 9-4, the steel beam section designation should be given.

*No need to control this criterion as angles will support a RC beam, so no local web crippling will occur.

=> **Use 90 x 90 x t EA**

Step 2 (Determining thickness of angle)

From AISC Manual table 10.5

Min angle leg =3*1/2 in* => 90 mm > 8.9 mm o.k

Assuming angle length = 8 in. (in this design L=480 mm which is much more than 8")

Assuming angle thickness = 3/8 in. (=10 mm)

Assuming required bearing length = 2 in.

Assuming t = 10 mm

⇨ Outstanding angle leg strength = 9.11 kips = 9.11 kips × 2 × 4.44 = 80 kN
Adding extra capacity due to using 2 angles on top of the top flange: 9.11 × 4.44 = 40 kN

The lateral force, F=Mr / h = 110 kN.m / 2.1 m = 52.3 kN

S.F. = 2 => $F_{out\ of\ plane}$ = 104 kN

80 kN + 40 kN > 104 kN O.K

=> **Using 90 x 90 x 10 EA is acceptable.**

Step 3 (Determining weld/bolt available strength)

Appendix C Test set-up design

From AISC Manual table 10.5

Assuming a bolt diameter = 3/4 in (M22)

Connection type: D

Bolt group: A/N

Bolt available strength = 53.7 kips = 53.7 kips × 4.44 = 238 kN

Use 6 bolts M22 connect angles to end-plate

Appendix D compressive and tensile behaviour of concrete

ε_c	σ_c	ε_{0c}^{el}	$\tilde{\varepsilon}_c^{in}$	$\tilde{\varepsilon}_{c,shifted}^{in}$	d_c
0	0.00	Elastic range			
0.00005	1.43				
0.00025	6.95				
0.0005	13.20				
0.00075	18.62	0.000648	0.000102	0	0
0.001	23.23	0.000809	0.000191	0.000090	0
0.00125	27.09	0.000943	0.000307	0.000205	0
0.0015	30.30	0.001055	0.000445	0.000343	0
0.00175	32.95	0.001147	0.000603	0.000501	0
0.002	35.12	0.001223	0.000777	0.000675	0
0.00225	36.89	0.001284	0.000966	0.000864	0
0.0025	38.32	0.001334	0.001166	0.001064	0
0.00275	39.48	0.001374	0.001376	0.001274	0
0.003	40.40	0.001406	0.001594	0.001492	0
0.00325	41.12	0.001432	0.001818	0.001717	0
0.0035	41.68	0.001451	0.002049	0.001947	0
0.00375	42.11	0.001466	0.002284	0.002182	0
0.004	42.43	0.001477	0.002523	0.002421	0
0.00425	42.65	0.001485	0.002765	0.002663	0
0.0045	42.80	0.001490	0.003010	0.002908	0
0.00475	42.88	0.001493	0.003257	0.003156	0
0.005	42.90	0.001494	0.003506	0.003405	0
0.00525	42.88	0.001493	0.003757	0.003655	0.001
0.0055	42.82	0.001491	0.004009	0.003908	0.002
0.00575	42.73	0.001488	0.004262	0.004161	0.004
0.006	42.61	0.001483	0.004517	0.004415	0.007
0.00625	42.47	0.001479	0.004771	0.004670	0.010
0.0065	42.31	0.001473	0.005027	0.004925	0.014
0.00675	42.13	0.001467	0.005283	0.005181	0.018
0.007	41.95	0.001460	0.005540	0.005438	0.022
0.00725	41.75	0.001454	0.005796	0.005695	0.027
0.0075	41.54	0.001446	0.006054	0.005952	0.032
0.00775	41.33	0.001439	0.006311	0.006209	0.037
0.008	41.11	0.001431	0.006569	0.006467	0.042
0.00825	40.89	0.001424	0.006826	0.006725	0.047
0.0085	40.67	0.001416	0.007084	0.006982	0.052
0.00875	40.44	0.001408	0.007342	0.007240	0.057
0.009	40.22	0.001400	0.007600	0.007498	0.063
0.00925	39.99	0.001392	0.007858	0.007756	0.068
0.0095	39.76	0.001384	0.008116	0.008014	0.073
0.00975	39.53	0.001376	0.008374	0.008272	0.079
0.01	39.30	0.001368	0.008632	0.008530	0.084
0.01025	39.08	0.001360	0.008890	0.008788	0.089
0.0105	38.85	0.001353	0.009147	0.009046	0.094
0.01075	38.63	0.001345	0.009405	0.009303	0.100
0.011	38.41	0.001337	0.009663	0.009561	0.105
0.01125	38.19	0.001330	0.009920	0.009819	0.110
0.0115	37.97	0.001322	0.010178	0.010076	0.115
0.01175	37.76	0.001314	0.010436	0.010334	0.120
0.012	37.54	0.001307	0.010693	0.010591	0.125
0.01225	37.33	0.001300	0.010950	0.010849	0.130
0.0125	37.12	0.001292	0.011208	0.011106	0.135
0.01275	36.92	0.001285	0.011465	0.011363	0.139
0.013	36.72	0.001278	0.011722	0.011620	0.144
0.01325	36.52	0.001271	0.011979	0.011877	0.149
0.0135	36.32	0.001264	0.012236	0.012134	0.153
0.01375	36.12	0.001258	0.012492	0.012391	0.158
0.014	35.93	0.001251	0.012749	0.012647	0.162
0.01425	35.74	0.001244	0.013006	0.012904	0.167
0.0145	35.55	0.001238	0.013262	0.013161	0.171
0.01475	35.37	0.001231	0.013519	0.013417	0.176
0.015	35.18	0.001225	0.013775	0.013673	0.180

0.01525	35.00	0.001219	0.014031	0.013930	0.184
0.0155	34.82	0.001212	0.014288	0.014186	0.188
0.01575	34.65	0.001206	0.014544	0.014442	0.192
0.016	34.48	0.001200	0.014800	0.014698	0.196
0.01625	34.31	0.001194	0.015056	0.014954	0.200
0.0165	34.14	0.001189	0.015311	0.015210	0.204
0.01675	33.97	0.001183	0.015567	0.015466	0.208
0.017	33.81	0.001177	0.015823	0.015721	0.212
0.01725	33.65	0.001171	0.016079	0.015977	0.216
0.0175	33.49	0.001166	0.016334	0.016232	0.219
0.01775	33.33	0.001160	0.016590	0.016488	0.223
0.018	33.17	0.001155	0.016845	0.016743	0.227
0.01825	33.02	0.001150	0.017100	0.016999	0.230
0.0185	32.87	0.001144	0.017356	0.017254	0.234
0.01875	32.72	0.001139	0.017611	0.017509	0.237
0.019	32.57	0.001134	0.017866	0.017764	0.241
0.01925	32.43	0.001129	0.018121	0.018019	0.244
0.0195	32.29	0.001124	0.018376	0.018274	0.247
0.01975	32.14	0.001119	0.018631	0.018529	0.251
0.02	32.00	0.001114	0.018886	0.018784	0.254
0.02025	31.87	0.001109	0.019141	0.019039	0.257
0.0205	31.73	0.001105	0.019395	0.019294	0.260
0.02075	31.60	0.001100	0.019650	0.019548	0.263
0.021	31.46	0.001095	0.019905	0.019803	0.267
0.02125	31.33	0.001091	0.020159	0.020057	0.270
0.0215	31.20	0.001086	0.020414	0.020312	0.273
0.02175	31.08	0.001082	0.020668	0.020566	0.276
0.022	30.95	0.001078	0.020922	0.020821	0.279
0.022	30.95	0.001078	0.020922	0.020821	0.279

ε_t		σ_t	ε_{0t}^{el}	$\tilde{\varepsilon}_t^{ck}$	$\tilde{\varepsilon}_{t,shifted}^{ck}$	d_t
0		0.00	Elastic range			0
0.00005		1.12				0
0.00025		1.78	0.0000392	0.000211	0.000193	0.368
0.0005		1.126	0.0000297	0.000470	0.000453	0.521
0.00075		0.853	0.0000253	0.000725	0.000707	0.593
0.001		0.726	0.0000225	0.000977	0.000960	0.637
0.00125		0.647	0.0000206	0.001229	0.001212	0.668
0.0015		0.592	0.0000191	0.001481	0.001463	0.691
0.00175		0.550	0.0000180	0.001732	0.001715	0.710
0.002		0.517	0.0000171	0.001983	0.001965	0.725
0.00225		0.490	0.0000163	0.002234	0.002216	0.737
0.0025		0.468	0.0000156	0.002484	0.002467	0.748
0.00275		0.448	0.0000150	0.002735	0.002717	0.758
0.003		0.432	0.0000145	0.002985	0.002968	0.766
0.00325		0.417	0.0000141	0.003236	0.003218	0.773
0.0035		0.404	0.0000136	0.003486	0.003469	0.780
0.00375		0.392	0.0000133	0.003737	0.003719	0.786
0.004		0.381	0.0000129	0.003987	0.003970	0.791
0.00425		0.371	0.0000126	0.004237	0.004220	0.796
0.0045		0.363	0.0000123	0.004488	0.004470	0.801
0.00475		0.354	0.0000121	0.004738	0.004720	0.805
0.005		0.347	0.0000118	0.004988	0.004971	0.809
0.00525		0.340	0.0000116	0.005238	0.005221	0.813
0.0055		0.333	0.0000114	0.005489	0.005471	0.816
0.00575		0.327	0.0000112	0.005739	0.005721	0.820
0.006		0.321	0.0000110	0.005989	0.005972	0.823
0.00625		0.316	0.0000108	0.006239	0.006222	0.826
0.0065		0.311	0.0000106	0.006489	0.006472	0.828
0.00675		0.306	0.0000105	0.006740	0.006722	0.831
0.007		0.301	0.0000103	0.006990	0.006972	0.833
0.00725		0.297	0.0000102	0.007240	0.007222	0.836
0.0075		0.293	0.0000101	0.007490	0.007472	0.838
0.00775		0.289	0.0000099	0.007740	0.007723	0.840

0.008		0.285	0.0000098	0.007990	0.007973	0.842
0.00825		0.282	0.0000097	0.008240	0.008223	0.844
0.0085		0.278	0.0000096	0.008490	0.008473	0.846
0.00875		0.275	0.0000095	0.008741	0.008723	0.847
0.009		0.272	0.0000094	0.008991	0.008973	0.849
0.00925		0.269	0.0000092	0.009241	0.009223	0.851
0.0095		0.266	0.0000091	0.009491	0.009473	0.852
0.00975		0.263	0.0000091	0.009741	0.009723	0.854
0.01		0.260	0.0000090	0.009991	0.009974	0.855
0.01025		0.257	0.0000089	0.010241	0.010224	0.857
0.0105		0.255	0.0000088	0.010491	0.010474	0.858
0.01075		0.253	0.0000087	0.010741	0.010724	0.860
0.011		0.250	0.0000086	0.010991	0.010974	0.861
0.01125		0.248	0.0000086	0.011241	0.011224	0.862
0.0115		0.246	0.0000085	0.011492	0.011474	0.863
0.01175		0.243	0.0000084	0.011742	0.011724	0.864
0.012		0.241	0.0000083	0.011992	0.011974	0.866
0.01225		0.239	0.0000083	0.012242	0.012224	0.867
0.0125		0.237	0.0000082	0.012492	0.012474	0.868
0.01275		0.235	0.0000081	0.012742	0.012724	0.869
0.013		0.234	0.0000081	0.012992	0.012974	0.870
0.01325		0.232	0.0000080	0.013242	0.013225	0.871
0.0135		0.230	0.0000080	0.013492	0.013475	0.872
0.01375		0.228	0.0000079	0.013742	0.013725	0.873
0.014		0.227	0.0000078	0.013992	0.013975	0.874
0.01425		0.225	0.0000078	0.014242	0.014225	0.875
0.0145		0.223	0.0000077	0.014492	0.014475	0.875
0.01475		0.222	0.0000077	0.014742	0.014725	0.876
0.015		0.220	0.0000076	0.014992	0.014975	0.877
0.01525		0.219	0.0000076	0.015242	0.015225	0.878
0.0155		0.217	0.0000075	0.015492	0.015475	0.879
0.01575		0.216	0.0000075	0.015743	0.015725	0.879
0.016		0.215	0.0000074	0.015993	0.015975	0.880
0.01625		0.213	0.0000074	0.016243	0.016225	0.881
0.0165		0.212	0.0000073	0.016493	0.016475	0.882
0.01675		0.211	0.0000073	0.016743	0.016725	0.882
0.017		0.209	0.0000072	0.016993	0.016975	0.883
0.01725		0.208	0.0000072	0.017243	0.017225	0.884
0.0175		0.207	0.0000072	0.017493	0.017475	0.884
0.01775		0.206	0.0000071	0.017743	0.017725	0.885
0.018		0.205	0.0000071	0.017993	0.017975	0.886
0.01825		0.204	0.0000070	0.018243	0.018225	0.886
0.0185		0.202	0.0000070	0.018493	0.018476	0.887
0.01875		0.201	0.0000070	0.018743	0.018726	0.888
0.019		0.200	0.0000069	0.018993	0.018976	0.888
0.01925		0.199	0.0000069	0.019243	0.019226	0.889
0.0195		0.198	0.0000069	0.019493	0.019476	0.889
0.01975		0.197	0.0000068	0.019743	0.019726	0.890
0.02		0.196	0.0000068	0.019993	0.019976	0.890
0.02025		0.195	0.0000068	0.020243	0.020226	0.891
0.0205		0.194	0.0000067	0.020493	0.020476	0.892
0.02075		0.193	0.0000067	0.020743	0.020726	0.892
0.021		0.192	0.0000067	0.020993	0.020976	0.893
0.02125		0.191	0.0000066	0.021243	0.021226	0.893
0.0215		0.190	0.0000066	0.021493	0.021476	0.894
0.02175		0.190	0.0000066	0.021743	0.021726	0.894
0.022		0.189	0.0000065	0.021993	0.021976	0.895
0.022		0.188				